ISAS - INTERNATIONAL SCHOOL
FOR ADVANCED STUDIES

X-ray Variability of Blazars

Thesis submitted for the degree of
Doctor Philosophiæ

Astrophysics Sector

Candidate:

You Hong Zhang

Supervisors:

Dr. Annalisa Celotti

Prof. Aldo Treves

October 2000

SISSA - SCUOLA INTERNAZIONALE SUPERIORE DI STUDI AVANZATI

TRIESTE
Via Beirut 2-4

TRIESTE

SISSA ISAS
SCUOLA INTERNAZIONALE SUPERIORE DI STUDI AVANZATI
INTERNATIONAL SCHOOL FOR ADVANCED STUDIES

X-ray Variability of Blazars

Thesis submitted for the degree of
Doctor Philosophiæ

Astrophysics Sector

Candidate:

You Hong Zhang

Supervisors:

Dr. Annalisa Celotti

Prof. Aldo Treves

October 2000

To

♡ **little Tianli** ♡

Abstract

This thesis is dealing with the X-ray variability characteristics of blazars, using data obtained mostly with *Beppo*SAX. First we performed a comprehensive variability analysis on two TeV sources, MKN 421 and PKS 2155−304, respectively. We then studied possible variability trend in the blazars class as a whole.

MKN 421 and PKS 2155−304, monitored with *Beppo*SAX between 1996 and 2000, showed very similar variability characteristics. The light curves are characterized by recurrent flares with durations of $\sim$ 1 day. The quasi-symmetric structure of the flares is seen in most cases. In general, the variability amplitude is larger and time scale shorter with increasing energy, but do not correlate with the luminosity. The structure functions are characterized by a steep slope of $\sim$ 1.2 at short time scales, with a clear turn-over at a characteristic time scale of $\sim$ 0.5 days. A probable flare periodicity of $\sim$ 1 day was present in the 2000 observations of MKN 421. Soft lags, hard lags, and zero lags between different X-ray energies were detected in MKN 421, but in PKS 2155−304 only soft and zero lags

were found. The energy-dependence of time lags is well determined when a flare showed pronounced time lags. Our analysis shows that the relative changes of values in the dominant time scales involved in the emission region are necessary to account for complex energy-dependent variability behaviors observed in these two sources. The fact that both the quasi-symmetric structure and time lags were detected in some flares indicates that the sizes of the emission regions are energy-dependent.

X-ray variability trends of blazars are qualitatively consistent with a scenario postulating continuity in the spectral energy distributions in blazars. The variability amplitude and photon indices in the 2–10 keV inversely correlate with the radio luminosities, and sources with steeper X-ray spectra show larger amplitude of variability.

$\star \quad \star \quad \star \quad \star \quad \star \quad \star$

Acknowledgements

The first "special" thanks are for Tianli, just born here when I started writing this thesis. I have shared a lot of pleasure time with him, but I will always be indebted to him and his mother for the very short time with them during which this thesis was written.

My deep thanks go to Annalisa Celotti and Aldo Treves, they have been my supervisors during these years. They are not only striking scientists but also really good supervisors, and I am greatly indebted to them for their stimulating discussions, constant encouragements, and teaching me how to unlock the problems. I mostly thank Annalisa, the most influential scientist for me. She always supported and encouraged me in both the research and daily life, and in particular convinced me what was good to do. Annalisa is also specially thanked for carefully reading this thesis, and for a lot of constructive comments. Aldo is really thanked for choosing the "timing" topic as the thesis project.

I then would like to thank Gianpiero Tagliaferri, who guided me into the field of data analysis. He has given me so much help that I cannot describe it here.

Laura Maraschi and Gabriele Ghisellini are greatly thanked for stimulating discussions on my research during these years.

I wish to thank Giovanni Fossati, Elena Pian, Fabrizio Tavecchio, Lucio Chiapetti, Rita Sambruna, Marco Chiaberge, and Ilaria Cagnoni for a lot of help, in particular for providing me with the data. Elena is greatly thanked for the use of some codes.

Dennis Sciama and Luigi Danese, the previous and present head of the Astrophysics sector, and John Miller are thanked for constant help and discussions. They all are very kind and striking scientists. The persons who gave the stimulating lectures during the first year are greatly thanked. I would also like to thank other members of the

sector, in particular those who sent a gift to Tianli, and Lia Cesario, Andrea Martocchia and Francesca Perrotta, they enrolled the sector at the same time as me, and gave me a lot of help.

Guangzhong Xie is deeply thanked for constant references during these years, he also was my supervisor at the time of the work for the Master thesis, and I learned a lot from him in many aspects. I would like to thank many nice friends during my staying in Kumning, a beautiful plateau town.

I would like to thank the Astrophysics sector and SISSA for granting me a fellowship to undertake this research. I thank greatly each member of scientific and administrative staffs at SISSA, they make SISSA alive everyday. I cannot forget the secretariats, Alex, Andrea, Claudia, Giuliana and Riccardo, and the system managers and the librarians for their efficiency and availability, in particular for their kind help.

Anyway, I thank everybody, either inside or outside SISSA, whom I met and talked to in this beautiful gulf town, Trieste.

This research has made use of the *Beppo*SAX data archive which is operated by the *Beppo*SAX Science Data Center.

I keep the final thanks to my parents, and also to myself.

$\star \quad \star \quad \star \quad \star \quad \star \quad \star$

Preface

Blazars represent the most extreme subclass of radio-loud Active Galactic Nuclei (AGNs), and are thought to be the "simplest" AGNs, being dominated by (a few) nonthermal radiative processes and overall (jet) symmetry, so that many of the complications of other AGNs can be neglected to the first order. Observationally blazars exhibit the most special properties among AGNs (e.g., Angel & Stockmann 1980), as characterized by high luminosity, rapidly and violently variable non-thermal continuum from radio to γ-ray wavelengths, high and variable polarization, and superluminal motion of VLBI components (e.g., Vermeulen & Cohen 1994). They are core-dominated, flat spectrum radio sources. More importantly, all the 66 extragalactic γ-ray sources detected so far by the EGRET instrument on board the Compton Gamma-Ray Observatory (CGRO) are blazars, and a few blazars have been identified as strongly variable extragalactic TeV sources. These extreme properties are generally interpreted in terms of synchrotron emission of relativistic particles residing in a jet of plasma moving relativistically towards the line of sight, and inverse Compton upscattering of soft photons responsible for the high energy γ-ray emission (Blandford & Rees 1978; Blandford & Königl 1979). As such, blazars generally represent the most extreme phenomenon (apart from Gamma-ray Bursts, GRBs) in the Universe, and provide fortuitous natural laboratories to study the central region of AGNs, jet processes, and ultimately shed light on how energy is extracted from the putative central massive black hole.

$\star \quad \star \quad \star \quad \star \quad \star \quad \star$

This thesis is dealing with the energy-dependent X-ray variability characteristics of blazars, especially focusing on the bright TeV-emitting blazars, MKN 421 and PKS 2155−304.

Chapter 1 is a brief introduction, illustrating what blazars are, blazars properties, and blazar-related topics.

Chapter 2 briefly summarizes the current blazar radiative models, including an overview of the temporal-dependent diffusive particles acceleration models.

In Chapter 3 we present an overview of blazar variability, emphasizing variations in the high energy bands.

The data analysis techniques used in this thesis are summarized in Chapter 4.

In Chapter 5 and 6, we perform a detailed temporal X-ray analysis of MKN 421 and PKS 2155−304, respectively, using data observed with *Beppo*SAX. The physical insights of our results on blazar models are also discussed.

Chapter 7 is aiming at finding some trends of X-ray variability among various blazar classes, in terms of correlations of the variability parameters with the luminosity and spectral index, using public *Beppo*SAX archival data for blazars.

Conclusions and perspectives arising from our work are summarized in the last chapter, Chapter 8.

* * * * * *

Contents

Chapter 1

Introduction

1.1 What blazars are

1.1.1 Birth of blazars era

Although BL Lacertae itself was found as an irregularly variable star in 1929, the "true" BL Lac objects era began in 1968, when an unusual variable radio source (VRO 42.22.01) was found to coincide with the BL Lacertae optical position (MacLeod & Andrew 1968; Schmitt 1968). This firstly prompted observational attention in radio and optical bands, and BL Lacertae was characterized as optically featureless, violently variable radio and optical continuum, high optical polarization, and optical spectrum smoothly connecting with radio spectrum. All these features indicate the nonthermal origin of the radio–optical emission from this source, and MacLeod et al. (1971) summarized the special properties of this prototype of BL Lac objects, BL Lacertae. By 1972, another four objects were found to be similar to BL Lacertae. These observations suggested the existence of a new class of objects, and Strittmatter et al. (1972) for the first time discussed these objects as a class and called them BL Lacertae (type) objects, and defined the following somewhat "extreme" properties of this type objects:

- Rapid variations of intensity in radio, infrared, and visual bands;
- Spectral energy distributed in a manner such that most of the energy is emitted at infrared wavelengths;
- Absence of discrete features in low dispersion optical spectra;
- Strong and rapidly varying polarization at visual and radio wavelengths.

At that time the determination of the distance of BL Lac objects was of great relevance, since they must have been incredibly luminous if they were at distances similar to quasars, and it was hard to understand how such a large flux was produced from a very small region, as inferred from rapid variations. Theoretical models to explain such sources received particular attention. The first conference on BL Lac objects held in Pittsburgh in 1978 summarized observational and theoretical progresses for the first ten years of BL Lac objects studies, and especially relativistic jet model was proposed by Blandford & Rees (1978).

One interesting point is how the word "blazar" came. Since at that time many Flat Spectrum Radio Quasars (FSRQs) were found to show remarkably similar characteristics to BL Lac objects, it was suggested that a common physical process is at work in these objects and then should treat all as a single group. In a memorable banquet speech at the Pittsburgh meeting Ed Spiegel suggested the name "blazar" for this class of object. Angel & Stockmann (1980) formerly took the name "blazar", and summarized and discussed a large sample of blazars available at that time. Now we refer to blazar as a combination of BL Lac objects and FSRQs, characterized phenomenologically by the importance of relativistic beaming. As we will see later, BL Lac objects and FSRQs indeed share common extreme characteristics, the important difference between them is that these FSRQs have strong and broad optical emission lines.

1.1.2 XBLs vs RBLs

The last section gives us an impression that these classic BL Lac objects were firstly discovered as strong, variable radio sources, and then were identified with optical counterparts, i.e., that they were exclusively discovered through radio selection. However this changed when MKN 421 and MKN 501 were found to be strong, variable X-ray sources (Ricketts, Cooke & Pounds 1976; Mushotzky et al. 1978), significantly in contrast to the non-detection of other four radio-selected BL Lac objects (Margon et al. 1976). These two X-ray sources were also suggested to be BL Lac objects based on the unusually bright, variable optical nucleus and the featureless continuum spectrum (Ulrich 1973), similar to those of BL Lac objects found through radio method. More interestingly these strong X-ray sources are weaker radio sources compared to BL Lac objects found through radio surveys. These data therefore suggested that there are systematically differences, possibly intrinsic, between objects discovered by radio and X-ray selections, respectively. This led to a classification of BL Lac objects into radio-selected (RBLs) and X-ray-selected (XBLs) BL Lac objects, following the band of discovery. More and more obser-

vations confirmed the systematic differences between XBLs and RBLs, i.e., XBLs are weaker radio but stronger X-ray sources, less variable, with lower optical polarization and core dominance (relative to the extended radio lobe emission) (e.g., Kollgaard et al. 1992; Permann & Stocke 1993; Jannuzi, Smith & Elston 1994). The most striking difference is manifested by the broad-band spectra of the two classes (e.g., Ledden & O'Dell 1985; Stocke et al. 1985; Maraschi et al. 1995; Sambruna, Maraschi & Urry 1996). XBLs and RBLs occupy separate regions on the color-color diagram (normally α_{ro} vs α_{ox} diagram). These differences naturally pose a question: are RBLs and XBLs just a single class or two classes? Furthermore under this classification, XBLs seemed generally to outnumber RBLs, and this could be understood for example if the X-ray jet opening angle were broader than the radio one.

1.1.3 HBLs vs LBLs

As we have shown in last section, systematic differences are quite clear between XBLs and RBLs. The division of BL Lac objects into RBLs and XBLs is however not satisfactory, since it is based on the selection band (radio or X-ray) rather than intrinsic physical properties and thus depends on survey details. In addition, many BL Lac objects have been defined as both RBLs and XBLs in different surveys (e.g., Laurent-Muehleisen et al. 1993; Brinkmann et al. 1995). With substantial accumulations of well sampled broadband spectral data of BL Lac objects (either simultaneous or not), especially in the X-ray band, it emerged that BL Lac objects are a single population characterized by a smooth spectral energy distribution (SED; synchrotron) from radio to infrared frequencies followed by a cutoff, i.e., show a peak in a νf_ν versus ν plot, at infrared/optical wavelengths for most RBLs, and at ultraviolet/X-ray (even higher energies) for most XBLs (e.g., Giommi, Ansari & Micol 1995). This led to reclassify BL Lac objects in a more objective way into "High energy peak" and "Low energy peak" (referring to the synchrotron emission component) BL Lac objects (i.e., HBLs and LBLs), respectively (Giommi & Padovani 1994; Padovani & Giommi 1995a). Due to obvious selection effects, most XBLs are HBLs and most RBLs are LBLs, and objects which appear in different surveys have proper classification. A quantitative distinction has been done on the basis of the ratio between radio and X-ray fluxes, the dividing value being $\log F_{1keV}/F_{5GHz} = -5.5$ (e.g., Fossati et al. 1998).

Note also that HBLs are probably dominated by a (steep) synchrotron emission in the soft X-ray band, while LBLs have a flat inverse Compton component which emerges.

1.1.4 BL Lacs vs FSRQs

Apart from the presence of a strong UV "bump", FSRQs show remarkably similar properties to BL Lac objects. The spectra of FSRQs show, by definition, strong, broad emission lines, having typical equivalent widths much larger than 5 Å, the value below which objects are generally classified as BL Lac objects (e.g., Stickel et al. 1991; Stocke et al. 1991). These quasars are identified as various types, including Optically Violently Variable (OVVs) quasars, Highly Polarized Quasars (HPQs), and Core-Dominated Quasars (CDQs), but the most striking property is their flat radio spectrum at a few GHz, with a radio spectral index $\alpha_r < 0.5$ ($f_\nu \propto \nu^{-\alpha_r}$). Therefore they are defined together as FSRQs. Since growing evidence suggests that rapid variability, high polarization, and radio structures dominated by compact radio cores closely correlate with each other (e.g., Fugmann 1988; Impey & Tapia 1990), it is reasonable that BL Lac objects and FSRQs are collectively called blazars (Angel & Stockmann 1980).

However the different relationships between the two classes have been suggested. Padovani (1992), based mostly on their different isotropic properties, has argued that BL Lac objects and FSRQs represent examples of similar relativistic beaming phenomena hosted by radio galaxies of different power (see §1.1.9). A tighter connection has also been proposed through evolution (e.g., Vagnetti, Giallongo & Cavaliere 1991) or gravitational lensing (e.g., Ostriker & Vietri 1985).

The current idea about the relationship between FSRQs and BL Lac objects is that all of them are manifestations of the same physical process, differing in some critical parameters, such as the central massive object, or the accretion rate, as inferred from the "continuous" distribution of their SEDs (Sambruna, Maraschi & Urry 1996; Fossati et al. 1997, 1998; Ghisellini et al. 1998).

1.1.5 High energy γ-ray emission

In recent years, high energy γ-rays have come to play an important role in the study of AGNs. Prior to the launch of CGRO in 1991, the only known extragalactic source of high energy γ-rays was 3C 273 which had been discovered by the COS-B satellite 20 years ago (Swanenburg et al. 1978). Since then, sixty-six AGNs have been detected by the EGRET instrument on board the CGRO as extragalactic sources of high energy γ-rays at energies above 100 MeV (Hartmann et al. 1999). Interestingly, these γ-ray loud AGNs are all identified as blazars, and a substantial fraction of the unidentified high-latitude EGRET sources are likely to be blazars as well. The strong, variable γ-ray radiation from blazars impose strong constraints on origin of

γ-rays, the structure, energetics and matter content of the jets (and environments). Here we summarize some of the main results and physical constraints:

- One of the most remarkable characteristics of EGRET observations is that often the γ-ray luminosity dominates the bolometric power of blazars, and during flaring episodes, the γ-ray emission can greatly exceed the energy output of blazars at all other wavelengths. The inferred isotropic luminosities can be as large as 3×10^{49} ergs s^{-1} in the most extreme sources (e.g., Mukherjee 1999), indicating that blazar jets are very powerful. Thus, any attempt to understand the physics of these objects must include consideration of the γ-ray emission.

- Blazars are more variable in the γ-rays than in any other wavelengths. Some blazars exhibit variability on very short time scale of one day or less.

- The combination of high luminosities and short time scales variations indicates very high compactness of γ-rays, providing an independent evidence that blazar radiation must be highly beamed, being produced by a relativistic jet oriented to the line of sight, in order to avoid catastrophic reprocessing of high energy γ-rays into X-rays through the $\gamma\gamma$ pair production.

- Currently γ-ray producing mechanisms involve both leptonic and hadronic models, although the former being more popular. In leptonic models, where electrons are the primary accelerated particles, γ-ray emission is believed to be due to inverse Compton upscattering of low energy photons, both internal and external to the jets. Proton-initiated cascades (PIC) is the main mechanism in hadronic models to produce high energy γ-rays of blazars (e.g., Mannheim et al. 1991).

1.1.6 Blazars SED sequence

It is well known that the SEDs of blazars are dominated by the nonthermal emission throughout the whole electromagnetic spectrum. It is now clear, thanks to EGRET and ground-based Cherenkov telescopes, that the overall SEDs of blazars show two distinct components, typically characterized by two broad peaks in a νf_ν versus ν representation. The first component, peaking anywhere from mm to X-ray wavelengths, is thought to be due to synchrotron radiation of relativistic electrons in a relativistic jet towards our line of sight. In general, this component is more variable with increasing energies, and polarized (Ulrich, Maraschi, & Urry 1997). The second component, peaking at GeV–TeV energies, but less well determined compared

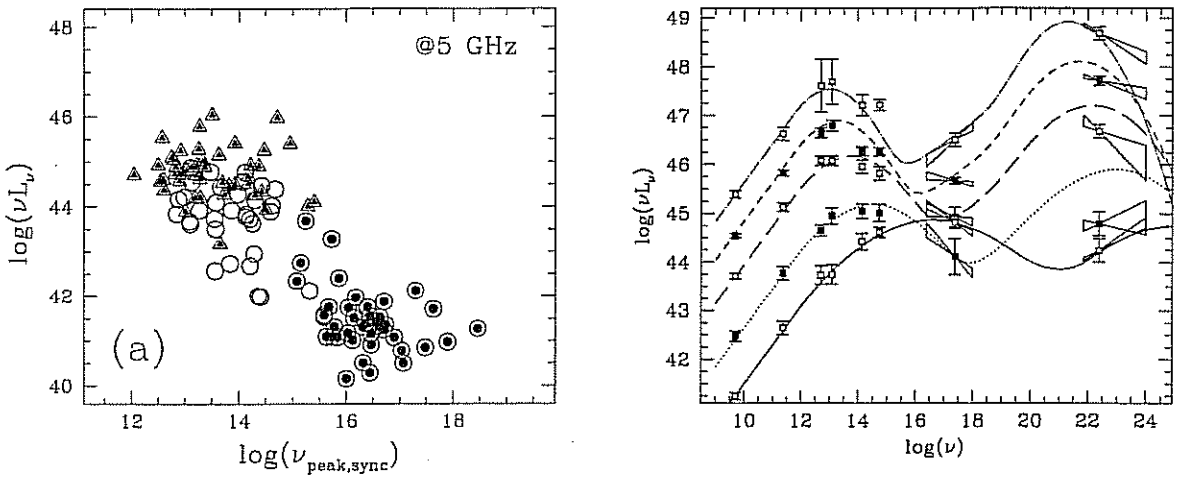

Figure 1.1: Left: the peak frequency of the synchrotron component, $\nu_{\rm peak,syn}$, as derived with the polynomial fits to the synchrotron components, plotted against the radio luminosity L_{5GHz}; Right: average SEDs for the "total blazar sample" binned according to radio luminosity irrespective of the original classification. The overlaid curves are analytic approximations obtained according to the one–parameter–family definition described in the text of Fossati et al. 1998. Quoted from Fossati et al. 1998.

to the first peak, most likely originates from the same population electrons via inverse Compton upscattering of soft (peaking at IR–UV) photons, either internal (synchrotron photons) or external (ambient soft photons) to the jet.

The blazar family has begun to be ordered according to the global shape of the observed SEDs from radio to γ-rays (e.g., Giommi, Ansari & Micol 1995; Sambruna, Maraschi & Urry 1996). This is mainly due to more and more simultaneous observations conducted at multiwavelengths, allowing us to understand well the whole electromagnetic spectrum of at least part of blazars. Fossati et al. (1998) ordered the blazar "zoo" from three complete subsamples of blazars (1Jy, EMSS and 2Jy for LBLs, HBLs, and FSRQs, respectively), and Ghisellini et al. (1998) physically modeled the SEDs of γ-ray loud blazars. The quite well ordered blazar SED sequence, the current blazar paradigm, represents the intrinsic unification of all blazars. The most striking feature of the blazar SED sequence is that blazars change SED shape systematically with the bolometric luminosity (Figure 1.1), typically characterized by the following trends: (1) the position of the two peaks decrease in frequency with increasing luminosity; (2) the ratio between the luminosities of the two SED components, L_C/L_S — often called the "Compton dominance" — increases, from ~ 1 or even less for the extreme low luminosity BL Lac objects to as much as 100–1000

for some luminous FSRQs. Moreover, the luminosity in emission lines also increases with bolometric luminosity.

This trend is becoming increasingly apparent from recent multi-color surveys (Laurent-Muehleisen et al. 1998; Perlman et al. 1998) which find sources with intermediate spectral shapes.

1.1.7 From viewing angle to peak energy

A striking improvement in our knowledge about blazars is that the blazar diversity can be unified in a coherent picture, where blazars form a continuous sequence with SED. This suggests that the nonthermal continuum emission of blazars can be characterized by one parameter, and previous unified schemes for XBLs and RBLs (e.g., increasing viewing angle from RBLs to XBLs) encountered serious difficulties in interpreting the continuity of blazars SED properties (Sambruna, Maraschi & Urry 1996). In fact, if the differences between XBLs and RBLs are determined by the angle of the jet with respect to the line of sight, the important parameter is the relativistic Doppler factor δ: the observed peak frequency shifts to $\delta\nu_{peak}$, and observed luminosity amplified by a factor of δ^{3-4}. In general, δ can change a factor ~ 10 from a typical XBL to RBL (assuming a typical jet bulk Lorentz factor $\Gamma = 10$). This means that the peak position can shift up by just one decade, while luminosity will increase by at least a factor 1000. This is completely opposite to the observed SED sequence, in which peak position moves to lower frequency with increasing observed luminosity. There is another serious difficulty, that is, the whole observed range of synchrotron peak frequencies (from IR to X-ray bands) shown by blazar can not be accounted for with only a change of Doppler factor δ (i.e., viewing angle) without changing in a coherent way any other intrinsic physical property of the source (Fossati et al. 1998). Indeed, by physically fitting the SED of all blazars detected in the γ-rays, Ghisellini et al. (1998) found a tight correlation between the energy of the electrons ($\gamma_{\rm peak} m_e c^2$) emitting at the peaks of the spectrum and the total energy density U (both in radiation and in magnetic field): $\gamma_{\rm peak} \propto U^{-0.6}$. This indicates that in less powerful sources (with weak magnetic field and weak emission lines) the radiative cooling is less severe and electrons can be accelerated up to very high energies, producing a SED typical of a HBL. Furthermore because of the shortage of external photons, the SSC process dominates producing high energy γ-ray emission. With increasing energy density U, electrons will be accelerated up to decreasing energies (because of the higher radiative cooling), and both peaks of the SED move towards lower frequencies. Also the dominance of inverse Compton process in producing high energy γ-rays will increase because of the amplification

of external radiation relative to the jet.

So the continuity of blazar SEDs is accounted for in terms of a systematic change of intrinsic physical conditions in the emitting environment, i.e., the importance of external photon field relative to the magnetic field.

1.1.8 TeV emission from blazars

The Whipple Observatory γ-ray telescope has discovered three nearby BL Lac objects which emit at energies above 300 GeV and there are recent detections of two other BL Lac objects with Cherenkov telescopes. In 1992 MKN 421 (z=0.031) was detected as the first extragalactic sources of Very High Energy (VHE) γ-rays at photon energies around 1 TeV using the Whipple Observatory γ-ray telescope (Punch et al. 1992). Since then many efforts have been devoted to detect VHE γ-ray emission from extragalactic sources. MKN 421 has been confirmed as a source of VHE γ-rays by the HEGRA Collaboration (Petry et al. 1996), the Telescope Array Project (Aiso et al. 1997), and the SHALON telescope (Sinitsyna et al. 1997). MKN 501 (z=0.033) was significantly identified as a TeV emitting source at the Whipple Observatory in March 1995 (Quinn et al. 1996), and confirmed as a source of VHE γ-rays in 1996 by the HEGRA telescopes (Bradbury et al. 1997), the CAT telescope (Punch et al. 1997), the Telescope Array Project (Hayashida et al. 1998), and TACTIC (Bhat et al. 1997).

In addition to the confirmed detections of MKN 421 and MKN 501, two other objects have recently been reported as sources of VHE γ-rays, but remain to be verified by detections from independent γ-ray telescopes. 1ES 2344+514 ($z = 0.044$) was detected at energies about 350 GeV by the Whipple Observatory in 1995 (Catanese et al. 1998), and PKS 2155−304 ($z = 0.117$), was detected at energies above 300 GeV by combining observations from 1996 and 1997 by the Durham group (Chadwick et al. 1999).

These findings impose strong constraints on the radiation mechanism of blazars. All these TeV sources are HBLs and not the strong MeV-GeV sources detected by EGRET, and they are barely detectable even during flaring states seen from other bands. Vice versa many other blazars, such as 3C279 (z=0.538), are strong at MeV bands but still none is detected above 1 TeV. Thus the TeV observations have significantly affected our understanding of blazars, and the nature of the differences between HBLs, LBLs and FSRQs:

- The >100 MeV fluxes are near (MKN 421, MKN 501) or below (1ES 2344+514) the EGRET sensitivity limit, meaning that the γ-ray power output does not

peak in that energy range as it does for many of the EGRET-detected blazars (von Montigny et al. 1995).

- The rapid variability and TeV extent of the emission from HBLs point to the differences between the sub-classes being more fundamental, as originally proposed by Padovani & Giommi (1995a): the HBLs have higher maximum electron energies and lower intrinsic luminosities.

- The rapid variability indicates either very low accretion rates and photon densities near the nucleus (Celotti, Fabian & Rees 1998) or, conversely, requires the γ-ray emission region to be located relatively far from the nucleus to escape the photon fields (Protheroe & Biermann 1997).

- Correlated synchrotron and VHE γ-ray spectra also constrain the magnetic field strength (B) and Doppler factor (δ) of the jet (e.g., Buckley et al. 1996, 1997; Tavecchio, Maraschi & Ghisellini 1998; Catanese 1999 for MKN 421; Samuelson et al. 1998; Tavecchio, Maraschi & Ghisellini 1998; Hillas 1999 for MKN 501).

- The VHE observations have constrained the types of models that are likely to produce the γ-ray emission.

- Measurements of the VHE spectra of blazars provide an indirect means of investigating the background IR radiation (Stecker, de Jager & Salamon 1992)

1.1.9 Blazars unification schemes

It is now well established that the appearance of AGN depends strongly on orientation. Apparently various AGN classes might actually be intrinsically similar, only viewed at different angles with respect to the line of sight (see Antonucci 1993 and Urry & Padovani 1995 for reviews of AGN unification schemes). Here we only touch the aspects of this topic relevant to blazars.

As already discussed, the emission characteristics of blazars are believed to arise from relativistic jets oriented at relatively small angles to the line of sight. If so, the observed radiation will be strongly amplified by relativistic beaming (Blandford & Rees 1978). Direct evidence for relativistic beaming of the radio emission comes from Very Long Baseline Interferometer (VLBI) observations of apparent superluminal motion in many blazars (e.g., Vermeulen & Cohen 1994). The rapid variability and very high luminosities of the detected high energy γ-ray sources imply that the γ-rays are also beamed (e.g., Maraschi, Ghisellini & Celotti 1992).

If blazars are indeed "beamed" toward us, their isotropic, unbeamed properties should be identical to those of the substantial population seen at large angles between the jet and the line of sight, the so-called *parent population* of blazars. The strong dependence of some observables on the viewing angle will cause blazars and their parent population to show a significantly different phenomenology. However, the isotropic observables, such as extended radio emission and its morphology, host galaxies, cluster environments, and emission lines, have to be still similar. The current studies based on these isotropic properties suggest that radio galaxies classified as Fanaroff-Riley I (low luminosity) and II (high luminosity) (FR I and FR II; Fanaroff and Riley 1974) are the parent populations for BL Lac objects and FSRQs, respectively. This "basic" form of unification was also supported by other studies: the distribution of superluminal speeds in radio sources (Vermeulen & Cohen 1994); ratios of jets to counter-jets in radio galaxies (e.g., Giovannini et al. 1994); the correlation between core and total powers (Morganti et al. 1995); the number count and luminosity functions (Urry & Padovani 1995).

1.2 Blazar properties

We highlight the most striking properties of blazars as follows:

- Radio loudness: compact, core-dominated flat-spectrum radio sources;
- Variability: rapid and large amplitude (i.e., high $\Delta L/\Delta t$) in any observed frequency;
- Polarization: high ($P_{\rm opt} > 3\%$ and $P_{\rm rad} > 1-2\%$) and variable optical and radio linear polarization;
- Continuum: dominated by smooth, broad, non-thermal emission over the whole measured energy bands;
- Superluminal motion of VLBI components, indicating relativistic jets;
- Strong γ-ray sources: all extragalactic sources detected by EGRET are blazars;
- TeV sources: all confirmed and potential extragalactic TeV sources are nearby BL Lac objects.

Moreover, crucial information from blazars are:

- SEDs from radio to gamma-rays (Gev and TeV energies), and their trends with bolometric luminosities;

- Correlated variability properties at various energies, with measured time lags.

1.3 Beyond blazars

Needless to say, there are still a lot of issues about blazars we can not discuss at all within this short introduction. However there is an aspect from which we expect to achieve a lot in the future, that is studying similar physical processes taking place in blazars, and in Galactic black hole candidates (GBHCs) (more specifically microquasars with relativistic jets) and Gamma-ray bursts (GRBs).

Both AGNs and GBHCs are variable X-ray sources, and they show on different scales two relevant aspects of relativistic astrophysics, i.e., mass accreting onto black holes identified as thermal emission from surrounding accretion disks and relativistic jets observed by their synchrotron emission. Indeed, simple scaling laws govern the physics of flows around black holes, with length and time scaling proportional to the mass of the black holes. Thus there is an underlying unity in the physics of accreting black holes over an enormous range of scales, from stellar-mass black holes in binary systems, to supermassive black holes at the center of distant galaxies.

Galactic X-ray binaries mimic the AGNs, i.e., radio-loud vs radio-quiet. At present, there are about 200 galactic X-ray binaries, of which about 10 percent are radio-loud. Similarly, 15%–20% AGNs are radio-loud (e.g, Urry & Padovani 1995). It is of great importance to compare their X-ray properties, as this might open a new way to better understand the radio-loud/quiet AGNs dichotomy. Moreover one of main progress in studying GBHCs is the discovery of *microquasars* (Mirabel & Rodríguez 1999): stellar-mass black-holes with relativistic jets which mimic, on a much smaller scale, many of the phenomena seen in radio-loud quasars. Their study might shed light on the connection between the accretion of matter onto black holes and the origin of relativistic jets seen in blazars. It is interesting to note that up to now all microquasars have θ (the angle between the line of sight and the axis of jets) larger than 60°. Therefore, we expect *microblazars*, that is a galactic source with relativistic jets and small θ, to be found. Microblazars should appear as sources with fast and large amplitude variations in the observed flux up to very high photon energies. Again this will give us information of similar physical processes operating on different scales.

One more important point should be stressed, that is, because of the relative short timescales of the phenomena associated with the flows of matter around stellar mass black holes, one can sample phenomena that we have not been able to observe in AGNs.

GRBs and blazars display many similarities in terms of their SEDs and light curves, but with times appropriately scaled by the corresponding factors. The light curve of GRBs is extremely variable and spiky, with the shortest spikes lasting for 1 ms. Indeed, if one stretches a GRBs light curve by a factor $\sim 10^8$, one obtains light curves very similar to the blazar ones, with the shortest timescales of the order of hours-days (Ghisellini 1999). In addition, by examining GRB light curves through Fourier analysis and adding up the resulting power spectra, a remarkably well defined power law (in frequency space) is found, with slope $-5/3$ (Beloborodov, Stern & Svensson 2000). This may be also the case for blazars. Our primary channel of information about blazars and GRBs derives from the nonthermal radiation produced by the relativistic plasma expelled from a central engine. We might thus expect unification in terms of the underlying physical processes which produce the radiation from the relativistic outflows in blazars and GRBs.

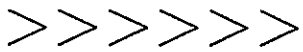

Chapter 2

Blazar Models

On the previous chapter we have briefly shown the observational properties of blazars, and introduced the fundamental frame for the radiative models of blazars. However, it is not clear yet whether in jets the electrons (and positrons) are accelerated directly and produce the emission via synchrotron and inverse Compton upscattering with various target photon fields either internal or external to the jets (i.e., *leptonic models*), or protons are the primarily accelerated particles which then produce the high energy γ-ray via photo-pair and photon-pion production, followed by π^0 decay and synchrotron emission by secondary particles (i.e., *hadronic models*, e.g., Mannheim 1993).

In this chapter, we try to present an overview of the leptonic models: the relativistic beaming scenario, the radiative processes operating in blazars, the observational constraints on the emitting region, the origin of blazar variability, the acceleration mechanisms of particles, and the time-dependent homogeneous SSC model which interprets multiwavelength temporal and spectral variations of TeV blazars. A very brief description of hadronic jet models is also presented.

2.1 Relativistic beaming effects

If the emitting material (blob) is moving at close angles to the line of sight at a relativistic speed βc, some special relativistic effects become important, and the observed radiative characteristics are modified with respect to those measured in the blob rest frame. These are generally named relativistic beaming effects. Hereinafter we will use the primed quantities for those measured in the blob frame. The basic quantity describing beaming effects is the Doppler factor:

$$\delta = \frac{1}{\Gamma(1 - \beta \cos\theta)} \tag{2.1}$$

where $\Gamma = (1 - \beta^2)^{-1/2}$ is the bulk Lorentz factor of the blob and θ is the angle between the velocity of the blob and the line of sight. The Doppler factor peaks at $\theta = 0$ with value of $\delta \sim 2\Gamma$, and most of the radiation is seen within angle $\theta = 1/\Gamma$. For $\Gamma \gg 1$, we have

$$\theta \simeq 1/\Gamma \simeq 1/\delta \tag{2.2}$$

The basic relationships for frequency, time, flux and luminosity are the following:

$$\nu = \delta\nu' \tag{2.3}$$

$$\Delta t = \frac{\Delta t'}{\delta} \tag{2.4}$$

$$F_\nu(\nu) = \delta^p F'_{\nu'}(\nu) \tag{2.5}$$

$$L_\nu = \delta^p L'_\nu \tag{2.6}$$

where $p = 2 + \alpha$ or $p = 3 + \alpha$ for a continuous jet or a spherical isotropic source, respectively, in which α is the spectral index in the considered spectral band. If the flux, luminosity and energy density are integrated over a frequency band, then

$$F = \delta^q F' \tag{2.7}$$

$$L = \delta^q L' \tag{2.8}$$

$$U = \delta^q U' \tag{2.9}$$

where $q = 3$ or $q = 4$ for a continuous jet or a spherical isotropic source, respectively, and the integration limits should be transformed on the basis of equation 2.3.

2.2 Overview of leptonic jet models

The particles involved in this scenario are electrons, which are directly producing the low energy component by synchrotron radiative process, as suggested by the nonthermal spectrum as well as its polarization observed at IR–UV or even X-ray bands.

For the high-energy component, most current models invoke the *inverse Compton* process due to upscattering of the lower energy target photons scattered by the same electrons responsible for the low energy synchrotron component, as originally discussed by Jones, O'Dell & Stein (1974a,b). The various leptonic models are discriminated by two main factors: (i) the nature of target photons fields (either internal or external to the jet), and (ii) the jet geometry adopted (either homogeneous or inhomogeneous emitting region).

2.2.1 SSC model

The most direct process producing high energy radiation is synchrotron-self-Compton (SSC) as suggested many years ago (Königl 1981; Marscher & Gear 1985). In this process, the same electron population produce low energy synchrotron radiation and upscatter some of synchrotron photons to higher energies (X-rays and γ-rays). The homogeneous SSC model is successful in interpreting the TeV emission (high energy Compton component) and its close correlation with X-ray emission (low energy synchrotron one) for a few extreme HBLs (e.g., Mastichiadis & Kirk 1997; Chiaberge & Ghisellini 1999). The SSC models give good overall fits to the multiwavelength spectra of MKN 421, MKN 501 and PKS 2155−304.

2.2.2 ERC model

Although the SSC process is a very plausible mechanism responsible for the high energy emission, it cannot be the unique one since high density of external radiative field may exist in the blazar nuclei, which may also be upscattered to high energies. This competing process, the Comptonization of external radiation, is called ERC (external radiation Compton) model. There are many variants based on various target soft photon fields external to the jet:

- UV–soft–X-ray radiation from the accretion disk, either entering the jet directly, the ECD (External Comptonization of Direct disk radiation) process (Dermer, Schlickeiser & Mastichiadis 1992; Dermer & Schlickeiser 1993), or after reprocessing in the broad line regions (BLR) or other circumnuclear material, the ECC (External Comptonization of radiation from Clouds) process (Sikora, Begelman & Rees 1994; Blandford & Levinson 1995; Dermer, Sturner & Schlickeiser 1997).

- IR radiation from a dusty torus surrounding the blazar nucleus (Wagner et al. 1995; Sikora et al. 1997).

2.2.3 MC model

There is also a hybrid of the SSC and ERC models, the Mirror Compton (MC) model (Ghisellini & Madau 1996; Bednarek 1998), in which some synchrotron photons from the jet may be reflected by nearby circumnuclear material (e.g., the BLR) back to the jet itself where are then upscattered to high energies.

2.2.4 Inhomogeneous and homogeneous models

There are two different scenarios regarding the emitting region: the 'inhomogeneous' and the 'homogeneous' models. In the inhomogeneous model, the emitting part of the jet is assumed to be cylindrically symmetric with a cross-section which varies with distance from the central object. The magnetic field is also taken to vary with distance from the central source. It is usually assumed that relativistic electrons are 'injected' at a shock front which moves through the emission region, starting close to the central source. These electrons also move outwards with the jet material, and undergo energy losses due both to radiation and to the adiabatic expansion of the jet. The observed radiation is a superposition of emission by integrating over the different emission region, within which both the magnetic field and the particle distribution is inhomogeneous (e.g., Ghisellini, Maraschi, & Treves 1985; Marscher & Gear 1985; Celotti, Maraschi, & Treves 1991; Maraschi, Ghisellini, & Celotti 1992; Marscher & Travis 1996).

In the homogeneous model, both the magnetic field and the particle distribution function are assumed not to vary throughout the emission region (e.g., Inoue & Takahara 1996; Mastichiadis & Kirk 1997; Chiaberge & Ghisellini 1999). The relativistic electrons are injected with a specified distribution and are assumed to escape on a time scale $t_{\rm esc}$. The homogeneous model with escape corresponds approximately to the plausible physical situation in which particles are accelerated at a shock front, and there is a region of relatively high magnetic field just behind the shock. In this case, radiation from this volume may be expected to dominate the observed emission. The simultaneous variations in the X-rays and TeV γ-rays observed in MKN 421 (Maraschi et al. 1999) suggest that a single population of electrons in a homogeneous volume is responsible for the observed emission. However, a problem arises in the homogeneous model concerning time variability: only if the physical dimensions of the source are such that the light crossing time is short compared to the synchrotron cooling time is it reasonable to assume homogeneity. If this condition is not fulfilled, the observed variability is dominated by the shape and orientation of the source, rather than the intrinsic cooling and acceleration time scales. Until recently, models for the rapid variability of blazars have either fulfilled this condition or have made specific assumptions about the source geometry.

2.2.5 Comments on leptonic models

These various mechanisms have been tested on specific sources with simultaneous multiwavelength monitorings. The current situation is that often more than one

model can reproduce the same data with similar accuracy (e.g., see von Montigny et al. 1997 for 3C 273; Ghisellini et al. 1996 for 3C 279; Comastri et al. 1997 for 0836+710). Although the relative importance of these components could be estimated by comparing the energy densities of the respective target photon fields in different sources on the basis of the intensities of broad emission lines or UV bump, the main diagnostic technique is the time lags between the low and high frequency emissions and their relative amplitude of variability (e.g., M^{c}Hardy 1999).

However in general it appears that the SSC model may be adequate to explain the γ-ray emission for BL Lac objects, while the ERC models are probably more applicable for FSRQs, as also suggested by the relative importance of the energy densities of the external radiation fields with the energy density of the synchrotron radiation field (both as measured in the jet comoving frame) due to strong line emission and UV bump as seen in FSRQs, but not in many BL Lac objects (e.g., Ghisellini et al. 1998).

It is also worth noting that various Compton components could dominate in different high energy bands because of the different energy distribution of the seed photon fields. M^{c}Hardy et al. (1999) successfully modeled simultaneous IR and X-ray variations by SSC process in the case of 3C 273, while high energy γ-ray are believed to be due to the ERC mechanism.

When comparing the relative importance of ERC and SSC radiation components with the synchrotron one, the different angular distribution of these radiation fields also plays an important role. Since the SSC and synchrotron radiation fields have the same angular distribution (they both are produced isotropically in the source comoving frame), the predicted high-energy to low-energy luminosity ratio does not depend on θ. In contrast, the ERC model predicts this ratio to drop very rapidly with viewing angle outside the $1/\Gamma$–cone because the ERC radiation is much more strongly collimated than synchrotron and SSC, this could explain why a significant fraction of FSRQs do not show γ-ray activity (Dermer 1995).

2.2.6 Hadronic jet models

The term "hadronic models" is used for a large variety of scenarios for the gamma-ray production in blazars. They all propose energetic protons as the main carriers of dissipated energy in the jet, different from the so-called "leptonic models", which assume the bulk of the energy available for radiation is in electrons or $e^{\pm}$ pairs. Energetic protons can lead to emission of gamma-rays via pp interactions with surrounding gas, or $p\gamma$ interactions with ambient photons. This produces secondary $e^{\pm}$ pairs, or mesons like $\pi^{\pm}$ and π^{0}, which eventually decay into $e^{\pm}$ pairs, photons and

neutrinos. Electrons or pairs can then produce high energy photons by synchrotron (or Compton) processes. The photons can either escape from the jet or produce new pairs in $\gamma\gamma \rightarrow e^+e^-$ processes, which subsequently radiate a new generation of photons. In particular *synchrotron-pair cascades* of this kind are important if interactions of ultra-high energy (UHE) protons in AGN jets are considered, where they shift the energy in secondary radiation down from the extreme proton energies to the observable gamma-ray regime. This mechanism has been coined PIC for "proton induced cascades" (Mannheim et al. 1991).

There are several kinds of hadronic jet models. (i) Protons have been suggested to be responsible just for the injection of energetic electrons, which then produce the observed emission by a synchrotron-self Compton (SSC) mechanism (Kirk & Mastichiadis 1992; Kazanas & Mastichiadis 1999). (ii) Some hadronic models assume gamma-ray production in *pp* interactions during the collision of jets with surrounding gas clouds, or in a very massive jet itself (Dar & Loar 1997). (iii) A different kind of hadronic models in which UHE cosmic rays in the jet interact with low energy target photons. They are split into two classes: (a) target photons are produced by synchrotron-radiating electrons co-accelerated with the protons (Mannheim 1993; 1996), and (b) external target photons are present in the vicinity of the jet, as for example thermal photons emitted from an accretion disk or a warm dust torus (Protheroe 1997). For the discussion of TeV blazars, we can therefore concentrate on so-called *synchrotron-self proton induced cascade* (SS-PIC) models, in which UHE protons interact with synchrotron photons emitted by electrons accelerated *in the same process* as the protons. One clear consequence of scenarios is that the gamma-ray emission due to the PIC process is in competition with the SSC emission of the electrons.

2.3 Basic formulae for radiative processes

In this section we summarize some basic equations which are necessary to understand the main features of the synchrotron and various inverse Compton emissions produced from the leptonic jets.

The discussion is restricted to the *homogeneous* single blob with size R tangled in a magnetic field B, emitting isotropically in the comoving frame. The blob may move through an external (isotropic) radiation field of energy density $U_{\rm ext}$, resulting from a fraction ξ of the observed $L_{\rm ext}$ (disk emission, BLR emission and so on) which is reprocessed/scattered and "available" to the blob, within a "reprocessed/scattering volume" of radius $R_{\rm ext}$. This external radiation field is assumed to have a peaked

(νf_ν) spectrum, at a characteristic frequency $\nu_{\rm ext}$. It is important to note that in the blob reference frame the external radiation will be boosted as $U'_{\rm ext} = \Gamma^2 U_{\rm ext}$, and the frequency blueshifted as $\nu'_{\rm ext} = \Gamma \nu_{\rm ext}$.

2.3.1 Radiative frequencies

Assuming isotropic momentum distribution of relativistic electrons moving in an isotropic magnetic field, the electrons with random Lorentz factor γ emit at a (averaged) monochromatic synchrotron and inverse Compton photon frequencies:

$$\nu_{\rm syn} = \frac{4}{3}\gamma^2 \nu_L \simeq 3.7 \times 10^6 \gamma^2 B \quad \text{Hz} \tag{2.10}$$

$$\nu_{\rm com} \simeq \frac{4}{3}\gamma^2 \nu^{\rm in} \tag{2.11}$$

where $\nu_L = \frac{e}{2\pi m_e c} B \simeq 2.8 \times 10^6$ Hz is the electron Larmor frequency.

2.3.2 Radiative powers

The emitted powers, i.e., electron cooling rates $\dot{\gamma}$, for synchrotron, SSC and ERC (Rybicki & Lightman 1979; Sikora et al. 1996) are:

$$\dot{\gamma}_{\rm syn} m_e c^2 = \frac{4}{3}\sigma_T c \gamma^2 U'_B \tag{2.12}$$

$$\dot{\gamma}_{\rm SSC} m_e c^2 = \frac{4}{3}\sigma_T c \gamma^2 U'_{\rm syn} \tag{2.13}$$

$$\dot{\gamma}_{\rm ERC} m_e c^2 \simeq \frac{16}{9}\sigma_T c \gamma^2 U'_{\rm ext} \tag{2.14}$$

where σ_T is the Thomson scattering cross section. The integration of powers over the electron energy distribution gives rise to the total luminosity emitted, and is proportional to the energy density involved.

2.3.3 Radiative field energy density

The respective radiative field energy density is specified as:

$$U'_B = \frac{B^2}{8\pi} \tag{2.15}$$

$$U'_{\rm syn} = \frac{L'_{\rm syn}}{4\pi R^2 c} = \frac{1}{\delta^4}\frac{L_{\rm syn}}{4\pi R^2 c} \tag{2.16}$$

$$U'_{\rm ext} \simeq \Gamma^2 U_{\rm ext} = \Gamma^2 \frac{\xi L_{\rm ext}}{4\pi R_{\rm ext}^2 c} \tag{2.17}$$

2.3.4 Cooling time scales

The cooling time scale is the crucial quantity to compare the importance of different processes and acceleration time scales at work in the emitting blob. It is defined as:

$$\tau = \frac{\gamma}{\dot{\gamma}} \propto \gamma^{-1} \tag{2.18}$$

that is, higher energy electrons will cool first. Then the total cooling time is

$$t'_{\rm cool} \simeq \left[\frac{\sigma_T c}{mc^2}\gamma(\frac{4}{3}U'_B + \frac{4}{3}U'_{\rm syn} + \frac{16}{9}U'_{\rm ext})\right]^{-1} \tag{2.19}$$

Clearly the cooling time is dominated by the fastest of the three cooling processes, which in turn is determined by the respective energy density. Under the assumption of Thomson regime, in the case in which the magnetic field energy density, SSC and external radiation fields dominates, respectively, we can express respective cooling time as (in the observer's frame):

$$t_{\rm cool} \simeq (t_{\rm cool})_{\rm syn} = 1.49 \times 10^{12} B^{-3/2}\delta^{-1/2}\nu^{-1/2} \tag{2.20}$$

$$t_{\rm cool} \simeq (t_{\rm cool})_{\rm SSC} = C_{\rm SSC} B^{1/2}\delta^{7/2}\nu^{-1/2} \tag{2.21}$$

$$t_{\rm cool} \simeq (t_{\rm cool})_{\rm ERC} = C_{\rm ERC} B^{1/2}\delta^{-5/2}\nu^{-1/2} \tag{2.22}$$

where $C_{\rm SSC}$ and $C_{\rm ERC}$ relates to the nature of the SSC and external fields, respectively.

2.3.5 Relationships between frequencies

If both the high-energy and low-energy spectral components are produced by the same population of relativistic electrons, then the synchrotron and inverse Compton frequencies are related to each other. We have the following relationships between observed frequencies of both components:

$$\nu_{\rm syn} = (1+z)\delta\nu'_{\rm syn} \simeq 3.7 \times 10^6 (1+z)\delta\gamma^2 B \tag{2.23}$$

$$\nu_{\rm SSC} \simeq \frac{4}{3}\gamma^2\nu_{\rm syn} \tag{2.24}$$

$$\nu_{\rm ERC} \simeq (1+z)\delta(\frac{4}{3}\gamma^2\nu'_{\rm ext}) \simeq \frac{4}{3}(1+z)\delta\gamma^2\Gamma\nu_{\rm ext} \tag{2.25}$$

The ratio of the observed Compton and synchrotron frequencies are:

$$\left(\frac{\nu_{\rm com}}{\nu_{\rm syn}}\right)_{\rm SSC} \simeq \frac{4}{3}\gamma^2 \tag{2.26}$$

$$\left(\frac{\nu_{\rm com}}{\nu_{\rm syn}}\right)_{\rm ERC} \simeq \frac{\Gamma\nu_{\rm ext}}{B} \tag{2.27}$$

2.3.6 Luminosities ratios

The ratio of the total Compton and synchrotron luminosities, $L_{\rm com}/L_{\rm syn}$, usually referred to as *Compton dominance*, traces the ratio between the radiation field and magnetic energy densities. In the frame of a single electron population, we have

$$\left(\frac{L'_{\rm com}}{L'_{\rm syn}}\right)_{\rm SSC} = \frac{\dot{\gamma}_{\rm SSC}}{\dot{\gamma}_{\rm syn}} = \frac{U'_{\rm syn}}{U'_{\rm B}} = \frac{1}{\delta^4}\frac{2L_{\rm syn}}{B^2R^2c} \tag{2.28}$$

$$\left(\frac{L'_{\rm com}}{L'_{\rm syn}}\right)_{\rm ERC} = \frac{\dot{\gamma}_{\rm ERC}}{\dot{\gamma}_{\rm syn}} \simeq \frac{U'_{\rm ext}}{U'_{\rm B}} = \Gamma^2\frac{2\xi L_{\rm ext}}{B^2R_{\rm ext}^2c} \tag{2.29}$$

then the ratio between SSC and ERC luminosities is

$$\frac{L'_{\rm ERC}}{L'_{\rm SSC}} = \frac{\dot{\gamma}_{\rm ERC}}{\dot{\gamma}_{\rm SSC}} \simeq \frac{U'_{\rm ext}}{U'_{\rm syn}} \simeq \delta^4\Gamma^2\frac{\xi L_{\rm ext}}{L_{\rm syn}}\frac{R^2}{R_{\rm ext}^2} \tag{2.30}$$

The above formulae hold also for the ratio of the observed synchrotron, SSC and ERC luminosities, provided that the angular distributions of radiation fields are the same (e.g., isotropic in the blob frame). For an isotropic magnetic field, the synchrotron and SSC radiation in the blob frame are isotropic, and transforms with δ^4, so

$$\frac{L_{\rm SSC}}{L_{\rm syn}} = \frac{L'_{\rm SSC}}{L'_{\rm syn}} \tag{2.31}$$

However, this is not the case for the ERC process ($\propto \delta^6$), but provided we are looking at the source within the aperture angle of the beaming pattern $\theta = 1/\Gamma$ we can consider an approximate equality and assume that

$$\frac{L_{\rm ERC}}{L_{\rm syn}} \simeq \frac{L'_{\rm ERC}}{L'_{\rm syn}} \tag{2.32}$$

$$\frac{L_{\rm ERC}}{L_{\rm SSC}} = \frac{L'_{\rm ERC}}{L'_{\rm SSC}} \tag{2.33}$$

2.4 Diagnosing the emitting blob

After having the summarized fundamental quantities regarding radiative process, we can derive or constrain the physical parameters (or range) for the emitting blob on the basis of the observables. We restrict to the *homogeneous* case.

2.4.1 Variability time scales

The emitting blob dimension R is constrained by the observed variability time scale due to the causality condition:

$$R \leq ct_{\rm var}\delta(1+z)^{-1} \tag{2.34}$$

and thus the determination of the minimum time scales is of particular relevance. Daily variability is quite common among blazars, and this gives $R \sim 10^{16}$ cm.

2.4.2 Peak frequencies

One of the most important features of the SED are the peak frequencies and their ratio of the synchrotron and inverse Compton components, from which we can get the electron energies which are emitting at the peak frequencies, and the relationship between B and δ.

SSC case

In the SSC case, from equation (2.26), by just substituting the peak frequencies, we have,

$$\gamma_{\rm peak} = \left(\frac{3\nu_{\rm com}}{4\nu_{\rm syn}}\right)^{1/2} \tag{2.35}$$

$$B\delta = (1+z)\frac{\nu_{\rm syn}^2}{(e/2\pi m_e c)\nu_{\rm com}} \tag{2.36}$$

The last formula shows that for fixed $\nu_{\rm syn}$ and $\nu_{\rm com}$, B and δ are inversely proportional. However in the Klein-Nishina (KN) regime this situation is reversed (see Tavecchio, Maraschi & Ghisellini 1998).

ERC case

For $\theta = 1/\Gamma(\delta \simeq \Gamma)$, from equations (2.25) and (2.23), we get,

$$\gamma_{\rm peak}\delta \simeq \left(\frac{3\nu_{\rm com}}{4\nu_{\rm ext}}\right)^{1/2} \tag{2.37}$$

$$\frac{B}{\delta} = (1+z)\frac{\nu_{\rm syn}\nu_{\rm ext}}{(e/2\pi m_e c)\nu_{\rm com}} \tag{2.38}$$

2.4.3 Peak luminosities

Along with peak frequencies, another important property of the SED is the ratio of the total luminosity of the synchrotron and inverse Compton peaks, which is directly related to the ratio of the radiation and the magnetic field energy density.

SSC case

The total luminosity can be expressed through the peak luminosity (see Tavecchio, Maraschi & Ghisellini 1998), which is more accessible to observations:

$$L_{\rm S,C} = f(\alpha_1, \alpha_2)\nu_{\rm S,C}L_{\rm s,c}(\nu_{S,C}) \tag{2.39}$$

where $f(\alpha_1, \alpha_2)$ is given by

$$f(\alpha_1, \alpha_2) = \frac{1}{1-\alpha_1} + \frac{1}{\alpha_2 - 1} \tag{2.40}$$

where α_1 and α_2 are the approximated power law spectral indices below and above the two SED peaks. Therefore, from equations (2.28) and (2.34), we have,

$$B^2\delta^6 \geq (1+z)^2 \frac{2(\nu_S L_S(\nu_S))^2 f(\alpha_1, \alpha_2)}{c^3 t_{\rm var}^2 \nu_C L_C(\nu_C)} \tag{2.41}$$

ERC case

We can only write the ratio of peak frequencies as a function of parameters of external radiation field and of the Compton dominance:

$$\frac{\nu_C}{\nu_S} \simeq (1+z)c^{3/2}\nu_{\rm ext}R_{\rm ext}(\xi L_{\rm ext})^{-1/2}\left(\frac{L_C}{L_S}\right)^{1/2} \tag{2.42}$$

2.4.4 Time lags

The fact that cooling time of relativistic electrons is inversely proportional to its energy implies that the lower energy emission will lag the higher energy emission. The lag is defined as the difference of cooling time scales of electrons emitting at low and high frequencies. Therefore the measurement of time lags of variations in various energy bands provides a strong constraint on the physical parameters of the source.

If the electron cooling is dominated by the synchrotron process, from equation (2.20) we can derive

$$B\delta^{1/3} = 300\left(\frac{1+z}{\nu_{1,17}}\right)^{1/3}\left[\frac{1-(\nu_1/\nu_0)^{1/2}}{\tau_{\rm obs}}\right]^{2/3} \text{Gauss} \tag{2.43}$$

where ν_0 and ν_1 are the low and high observed frequencies in unit of 10^{17} Hz, respectively, and τ_{obs} is the measured lag (in seconds) between them.

In the SSC cooling dominated region (Tavecchio, Maraschi & Ghisellini 1998),

$$B\delta^{11} = \frac{3.7\cdot 10^{-8}}{1+z}\nu_{1,17}\left[\frac{2\nu_s L_s(\nu_s)f(\alpha_1,\alpha_2)}{c^3 t_{\rm var}^2}\frac{\tau_{\rm obs}}{1-(\nu_1/\nu_0)^{1/2}}\right]^2 \text{Gauss} \tag{2.44}$$

2.4.5 Characteristics of the electron population

Information on the electron population can be inferred by the SED features and would be given by the balance between acceleration, cooling and escape of the emitting electrons. The most useful parameters include:

- the minimum injected electron energy, $\gamma_{\rm min}$
- the maximum injected electron energy, $\gamma_{\rm max}$ (cooling = acceleration)
- the "cooling" break energy, $\gamma_{\rm break}$ (cooling = escape)
- the spectral slope of the injected electron population, s

Cooling break energy, $\gamma_{\rm break}$

The equilibrium between cooling and escape time scale of electrons from the source, $t_{\rm cool} = t_{\rm esc}$, determine the characteristic electron energy, $\gamma_{\rm break}$, below which radiative cooling of electrons is inefficient and the electron spectrum unchanged. If we assume that electrons escape at the speed of light c ($t_{\rm esc} = R/v_{\rm esc} \simeq R/c$), and electrons cool via synchrotron and inverse Compton scattering (both SSC and REC), we can get

$$\gamma_{\rm break} = \frac{3m_e c^2}{4(U'_{\rm B} + U'_{\rm syn} + U'_{\rm ext})\sigma_T R} \tag{2.45}$$

The electrons at $\gamma_{\rm break}$ leave their signature in the synchrotron radiation spectra at energies $\nu \propto \gamma_{\rm break}$, which is usually recognized as the synchrotron peak frequency in the SED.

Maximum injected energy, $\gamma_{\rm max}$

The maximum energy of the injected electrons can be constrained by the balance between the efficiency of the acceleration and of the cooling, and thus value may reflect the properties of the acceleration mechanism. The most promising scenario for particles acceleration in blazars relativistic jets is acceleration at shocks (see §2.6.2), and can yield a maximum electron energy (Inoue & Takahara 1996):

$$\gamma_{\rm max} \simeq \left[\frac{9eB}{80(U'_{\rm B} + U'_{\rm syn} + U'_{\rm ext})\sigma_T \xi}\right]^{1/2} \tag{2.46}$$

where ξ is the electron mean free path in units of the Larmor radius (see equation 2.54).

Minimum injected energy, $\gamma_{\rm min}$

The nature of $\gamma_{\rm min}$ is less clear and its role is assumed to be unimportant in most simulations. For an extensive discussion of $\gamma_{\rm min}$ we refer to Fossati (1998).

Electron spectrum

The spectral shape of the electron distribution is another important parameter, and is assumed to be a power law $\propto \gamma^{-s}$, extending from $\gamma_{\rm min}$ to $\gamma_{\rm max}$. Furthermore, the observed SED requires that the electron spectrum steepens with increasing energy. For optically thin synchrotron emission, the spectral index of radiation is determined by that of the emitting electron through $\alpha = (s-1)/2$, and the peak in the νf_ν spectrum occurs where $s = 3$. In a stationary case, there are a few basic "rules" telling how the electron energy distribution is, and there are only a few possible combinations (e.g., Ghisellini 1989). In the range of electron energies where cooling is dominant the spectrum steepens to $s_{\rm inj}+1$, due to radiative losses, while where escape is dominant the spectrum keeps its injection slope, and finally below $\gamma_{\rm min}$ it is $s = 2$.

Of course, the relative importance of $\gamma_{\rm min}$, $\gamma_{\rm max}$, and $\gamma_{\rm break}$, depends also on the slope of the injected electron spectrum, and one of them is going to correspond to the observed peak frequency, $\nu_{\rm peak}$ (see Ghisellini et al. 1998; Fossati 1998) (such electrons have energy $\gamma_{\rm peak} m_e c^2$).

2.5 Variability mechanisms and predictions of models

2.5.1 Variability mechanisms

There are a large variety of ways to cause intrinsic variability at any particular frequency:

- changes in the size, geometry and beaming (i.e., the velocity vector of a particular sub-volume of the jet fluid) of jet flow;
- the magnetic field may change with time in both strength and direction;
- changes in the radiating particles properties, injection rate (density), maximum energy of the particles, electron distribution, all can alter the intensity at each location within the jet;

- changes of the intensity of the ambient radiation (in the ERC model);
- the opacity may change with time and will modulate the intensity produced *in-situ*;
- changes of various time scales may modify the relationship between different frequencies.

It is very plausible that not all of these parameters may change significantly on all sort of time scales, but neither the fluid dynamics of the jet flow, nor the particle acceleration mechanisms or the emission processes are sufficiently well understood to predict which of these parameters are more likely to vary and thus cause changes on a particular time scale. The main aim of multiwavelength monitoring is to disentangle those ambiguities by characterizing temporal patterns and relationships between variations seen at different frequencies.

2.5.2 Predictions of models

Time scales

The current blazar models assume that emission originates from the inner jet, the size of the source being limited by optical depth effects, lying in the range between 10^{-3} to about 1 pc for γ-rays and IR to X-rays emission photospheres (e.g., Blandford & Levison 1995; Levinson 1996). The corresponding light-crossing times, as measured by a distant observer at a small viewing angle, then range from a few minutes to several weeks, assuming that the emitting plasma moves with Lorentz factor $\Gamma \sim 10$. The radio-spheres are typically located at much larger radii. This range of time scales is in accord with the rapid variability frequently observed in blazars, e.g., variations has been observed in many bands, with changes on time scales as short as a few minutes in the optical and X-ray bands and a few hours in γ-rays.

Variability amplitude

The various emission models make different predictions regarding the relative amplitude of the low (synchrotron) and high (inverse-Compton) energy variations, because changes in any parameter affect synchrotron and Compton components in different way. Under the assumption that $\theta = 1/\Gamma$, the dependencies of luminosities of the various emission components on the magnetic field B, electron density N_e, jet bulk Lorentz factor Γ, and external photon energy density $U_{\rm ext}$ can be written as

$$L_{\rm syn} \propto \Gamma^4 N_e B^2 \tag{2.47}$$

$$L_{\rm SSC} \propto \Gamma^4 N_e^2 B^2 \tag{2.48}$$

$$L_{\rm ERC} \propto \Gamma^6 N_e U_{\rm ext} \tag{2.49}$$

$$L_{\rm MC} \propto \Gamma^8 N_e^2 B^2 \tag{2.50}$$

From these relationships we can make the following predictions:

- In the SSC and MC models, if the observed variability is due to variations in the electron density, the Compton variations should be proportional to the square of the synchrotron variations, i.e., $L^{\rm high}_{SSC,MC}/L^{low}_{\rm SSC,MC} = (L^{\rm high}_{\rm syn}/L^{\rm low}_{\rm syn})^2$. However in the ERC model, the Compton and synchrotron variations should be linearly related, i.e., the ratio $L_{\rm ERC}/L_{\rm syn}$ is predicted to be constant during a flare.

- Variability caused by magnetic field irregularities usually produces linear relationships.

- The strongest dependence on the jet bulk Lorentz factor occurs in the MC model (Ghisellini & Madau 1996).

3C 279, one of the best studied FSRQs, whose high energy Compton radiation is usually thought due to ERC, shows much higher amplitude of variability in the γ-ray band than in the optical/UV band (e.g., Wehrle et al. 1998). Such variability patterns cannot be predicted by the ERC model but by the SSC; However, the amplitude ratio observed in the January 1996 flare of 3C 279 was even larger than that predicted by the SSC model (Wehrle et al. 1998). This behavior can be instead reconciled with the one zone ERC model (either pure or in its mirror varieties) if the increased injection rate of relativistic electrons is accompanied by an increase of the bulk Lorentz factor, upon which synchrotron and Compton components have a different dependence (for an application of the *mirror* model to this case see Bednarek 1998). This example indicates that the dominant emission may well change in different states of a single source.

Time lags

- In the synchrotron cooling dominated frequencies range, higher energy photons are expected to lead low energy ones because of faster cooling time scale of higher energy electrons. This is quite a common phenomenon observed in different bands for various blazars.

- In the SSC model, the lag of the Compton component with respect to the synchrotron one will be approximately the light crossing time across the emitting region, since most of synchrotron photons will travel across the bulk of this region before being scattered. In the case of variability caused by small compressions, it is possible that Compton photons lead the synchrotron photons by a time scale of approximately the rising time of any flare.

- In the ERC model, if variations of external soft photon field cause Compton flare, the low energy synchrotron photons would lead the Compton scattered photons by a time scale which is roughly equal to the light crossing time of the extra distance traveled by synchrotron photons. For target photons originating in the accretion disc or broad line region, this time scale might be of order days. In contrast, if the density of scattering electrons changes, exactly simultaneous synchrotron and Compton scattered flares would be expected as an electron in the jet could equally well scatter an external photon (producing a high energy photon) or a lump of magnetic field (producing a synchrotron photon).

- In the MC model, synchrotron photons from the jet are reflected back to the jet from a nearby cloud before being Compton scattered and so, again, any synchrotron flare would lead the Compton scattered one by the extra light travel time, which might be of $\sim$ days, but which might be expected to vary from flare to flare.

Synchrotron peak shift

- In a HBL, in which the external radiation field is believed to be quite weak, the overall SED up to TeV is reasonably thought to be dominated by the SSC radiative process, both the synchrotron and the γ-ray component shift toward higher frequencies during the flare state.

- The synchrotron νF_ν peak in FSRQs is expected to shift toward lower frequencies during a flare states if Comptonization of external radiation field (ERC model) is the dominant electron cooling and radiation mechanism at γ-ray energies (Böttcher 1999).

2.6 Time-dependent SSC model

Blazars are characterized by rapid and strong time variability, indicating that the properties of the emitting electron distribution is rapidly changing, possibly over

time scales shorter than the light crossing time through the emitting region, which is sufficiently compact to let radiative losses dominate the cooling of high energy electrons. The high energy electrons cool so fast that (re-)acceleration or injection must frequently occur. Accordingly, time-dependent radiative models from a time-dependent electron population, due to electron cooling, escape and acceleration, are necessary in order to reproduce observed temporal and spectral features of blazars. Within the homogeneous SSC assumption, current time-dependent models can be globally divided into two types: one only involves electron cooling after episodic electron injection, and another considers both acceleration and cooling of electrons. The time-dependent model generally starts from seeking parameters that could fit specific blazar spectra in steady (low) state, and then tries to induce a flare by changing some parameters of the fit.

2.6.1 Homogeneous SSC model

The observed emission is assumed to be produced by a blob moving relativistically toward us. The blob is a spherical and uniform cloud with typical radius R, embedded in a tangled isotropic homogeneous magnetic field B. The relativistic electrons with a specific distribution are instantaneously injected into the blob at a rate $Q(\gamma)$ [$\mathrm{cm^{-3}\ s^{-1}}$]. Electrons then lose energy by emitting synchrotron and SSC. Furthermore electrons can also escape from the emitting region before cooling over a time scale $t_{\rm esc}$, generally assumed to be independent of electron energies. Other effects are generally neglected, like synchrotron self-absorption, heating effect, photon–photon collisions. The model is then constrained by the following 7 parameters: the blob size R and Doppler factor δ, the magnetic field strength B, the maximum injecting electron energy $\gamma_{\rm max}$, the spectral slope s and compactness l_e of injection, and the effective escape time scale $t_{\rm esc}$ of relativistic electrons. The minimum energy $\gamma_{\rm min}$ of the injected electron is unimportant and usually set to 1. These seven parameters are strongly constrained by the observables (see §2.4).

The continuity equation describing the temporal evolution of the electrons distribution $N(\gamma,t)$ [$\mathrm{cm^{-3}}$] under the above assumptions can be expressed as

$$\frac{\partial N(\gamma,t)}{\partial t} = \frac{\partial}{\partial \gamma}\left[\dot{\gamma}(\gamma,t)N(\gamma,t)\right] - \frac{N(\gamma,t)}{t_{\rm esc}} + Q(\gamma,t) \tag{2.51}$$

where $\dot{\gamma} = \dot{\gamma}_{\rm syn} + \dot{\gamma}_{\rm SSC}$ is the total cooling rate, given by the summation of equations (2.12) and (2.13). The properties of the radiated spectrum and light curves at different energies are determined by the comparative results of the three time scales: cooling and escape time of the electrons, and the light-crossing time.

There are a few works dealing with the time-dependent (homogeneous) SSC models. The earlier paper is Kardashev (1962), which solves the continuity equations for the particle distribution in cases where the cooling time $t_{\rm cool}$ can be considered longer than the light crossing time R/c for any energy band.

Recently, Mastichiadis & Kirk (1997) solved the kinetic equations of electrons and photons simultaneously, by injecting power-law electrons with an exponential cutoff. They studied various possibilities to explain the time variations, such as the changes in the magnetic field, injection compactness and the maximum Lorentz factor $\gamma_{\rm max}$ of nonthermal electrons, and proved that the time dependence of the keV/TeV flare in MKN 421 observed in April and May 1994 (Macomb et al. 1995, 1996) could have been the result of a sudden increase in the maximum energy of the injected electrons. It is important to note that only the variability on time scales longer than R/c were studied, due to neglecting the light-crossing effects.

In contrast, Chiaberge & Ghisellini (1999) showed the important role of light travel time effects on variability on the very short time scales often detected in highly luminous (and compact) objects. This implies that the cooling time for the highest energy electron may well be shorter than the light-crossing time R/c. Moreover, the quasi–symmetric flares in the X-rays , with rise and decay time scales approximately equal (e.g., Urry et al. 1997, Ghisellini et al. 1997, Giommi et al. 1998), also indicate that both times are controlled by the light-crossing time R/c, and suggest that the cooling times of the emitting electrons are very short. This in turn implies that the distribution of electrons, at least at high energies, is significantly changing on time scales shorter than R/c. As a result, the observer would see, at any given time, the sum of photons produced in different parts of the source, due to different light-crossing times and characterized by an electron distribution of different ages even though the electrons are injected uniformly throughout the blob. Then even a homogeneous source can resemble an inhomogeneous one. Time lags between the light curves at different frequencies are expected, but the time profile of each time variation is not necessarily observed clearly. They successfully reproduced the multiwavelength spectra of MKN 421 in different states, particularly the $\sim$ 1 hour lag between soft and hard X-rays during an X-ray flare (Takahashi et al. 1996). By using similar mechanism, Kataoka et al. (2000) also modeled similar variability behavior of PKS 2155−304 observed in May 1994 by ASCA.

2.6.2 Diffusive particle acceleration

The fact that the spectra of synchrotron components of blazars extend up to optical, UV, and even X–ray bands indicates that the jets contain highly relativistic

electrons/positrons, with Lorentz factors up to $10^4 - 10^6$. Energy losses of such electrons are so rapid that they must be accelerated/injected *in situ*, i.e., at the location where they radiate. These locations are the sites of the energy dissipation events, which propagate along the jet at moderate ($\Gamma \sim 10$) relativistic speeds. The dissipation events can result from interaction of the jet with external obstacles, annihilation of magnetic fields, and/or collisions of inhomogeneities in a jet (Blanford & Königl 1979). During such events, a part of the dissipated energy is converted into relativistic electrons and protons.

The most popular particles acceleration mechanism is *shock acceleration*, according to which particles gain energy by being scattered by magnetic "disturbances", repeatedly crossing the shock front (e.g., Kirk 1997). In some scenarios, shock acceleration can give rise to a maximum acceleration rate on the order of gyro-frequency of the accelerated particles (e.g., Inuoe, & Takahara 1996; Kirk 1997). Now we consider a time-dependent model with particle acceleration included.

Let us then consider a blob which includes a moving accelerating region which is presumably a thin shock front moving down a cylindrically symmetric jet (Marscher & Gear 1985; Kirk, Rieger & Mastichidis 1998) with a velocity u_s in the rest frame of the jet. Particles are accelerated by the shock through a first order Fermi scheme and subsequently escape downstream where they radiate. The assumptions about particles acceleration are

- The acceleration region (AR) and the cooling region (CR) are spatially separated. Shocks in the blob are expected to be the site of electron acceleration and electrons cool mainly outside the shock regions. The spectra of both the electrons and the photons in the blob are calculated for the AR and the CR separately.

- The spatial volume of the AR is much smaller than the size of the blob itself (i.e., acceleration time scale $t_{\rm acc} \ll R/c$), and the AR is a slab with thickness $R_{\rm acc}$.

- In the AR, electrons are injected at low energy and continuously accelerated, and cooling is unimportant except for the highest values of γ. Thus very little radiation is emitted by a particle in the AR.

- Electron acceleration time, $t_{\rm acc}$, and escape time, $t_{\rm esc}$, in the AR are assumed to be energy independent.

- With these assumptions, the spectrum of electrons in the AR is a power law with a power-law index -2, i.e., $N(\gamma) \propto \gamma^{-2}$, which is expected from the theory

of shock acceleration and confirmed analytically (e.g., Drury 1983; Blandford & Eichler 1987; Kirk, Rieger & Mastichiadis 1998). The maximum energy of electrons is determined by a detailed balance between the acceleration and cooling rates at the Lorentz factor $\gamma_{\rm max} = 1/(A_{\rm cool} t_{acc})$, where A_{cool} is the cooling coefficient.

- The variability features therefore do not depend only on the electron cooling time scale but on the interplay between acceleration and cooling time scales (see below). For $\gamma < \gamma_{\rm max}$ the acceleration rate exceeds the cooling rate while for $\gamma > \gamma_{\rm max}$ the distribution vanishes.

- In the CR, electrons with a nonthermal spectrum are injected from the AR. The escape rate of electrons from the AR is equal to the injection rate of electrons in the CR because of the number conservation.

- The shock front provides a moving source of electrons, which subsequently suffer energy losses, but are assumed not to be transported in space. This is valid when ARs and CRs are more or less uniformly distributed in a cloud, but it is expected to be a fair approximation to the case where a single shock propagates in a jet.

The continuity equation describing the time-evolution of the number density of particles $N(\gamma, t)$ with Lorentz factors between γ and $\gamma + d\gamma$ in the AR can be written

$$\frac{\partial N(\gamma,t)}{\partial t} = -\frac{\partial}{\partial \gamma}\left[\left(\dot{\gamma}_{\rm acc} - \dot{\gamma}_{\rm cool}\right) N(\gamma,t)\right] - \frac{N(\gamma,t)}{t_{\rm esc}} + Q\delta(\gamma - \gamma_0) \qquad (2.52)$$

where monochromatic electrons with Lorentz factor γ_0 are injected in the AR. Electrons are then accelerated and lose energy. The energy loss rate $\dot{\gamma}_{\rm cool}$ may include synchrotron radiation and inverse Compton scattering. Particles are also assumed to escape from the AR at an energy independent rate $t_{\rm esc}^{-1}$. Finally the acceleration term is approximated by

$$\dot{\gamma}_{\rm acc} = \frac{\gamma}{t_{\rm acc}} \qquad (2.53)$$

In the framework of diffusive shock acceleration (e.g., Drury 1983; Blandford & Eichler 1987), $t_{\rm acc}$ can be approximated as

$$t_{\rm acc} = \frac{20\lambda(\gamma)c}{3u_s^2} \sim 3.79 \times 10^{-6} \left(\frac{0.1{\rm G}}{B}\right) \xi\, \gamma \quad {\rm sec}, \qquad (2.54)$$

where $u_s \approx c$ is the shock speed, and $\lambda(\gamma) = \gamma m_e c^2 \xi/(eB)$ is the mean free path assumed to be proportional to the electron Larmor radius with ξ being a parameter. For the convenience of numerical calculations, $t_{\rm acc}$ is usually assumed to be independent on γ, and used as parameter of fit.

The electron spectrum in the CR is calculated by equation (2.51), with $Q(\gamma)$ replaced by the escaping electrons from the AR.

Diffusive shock acceleration has provided a method to treat high energy flares including particle acceleration processes. Kirk, Rieger & Mastichiadis (1998) restrict the analysis only to synchrotron losses to fit MKN 501. The interplay between the acceleration and energy loss time scales provides us with the different flare behaviors. When the system is observed at frequencies where the acceleration time scales is smaller than the cooling time scales, i.e., cooling dominated, the behavior of spectral index against the intensity exhibits a characteristic clockwise pattern and lower photons lag the higher ones. This type of behavior is well-known and has been observed at different wavelengths in several sources, e.g., OJ287 (Gear, Robson & Brown 1986), PKS 2155–304 (Sembay et al. 1993, Zhang et al. 1999, Kataoka et al. 2000) and MKN 421 (Takahashi et al. 1996). It arises whenever the system is controlled by the cooling with any cooling process which is faster at higher energy so that information about injection propagates from high to low energies (Tashiro et al. 1995). If the system is observed closer to the maximum emitted frequency, where the cooling and acceleration times are equal, the picture changes. Here information about the occurrence of a flare propagates from lower to higher energy, as particles are gradually accelerated into the radiating window. This time the loop (spectral slope against the intensity) is traced anticlockwise. Such behavior, although not as common, has occasionally been observed in the X-rays of PKS 2155-304 (Sembay et al. 1993) and MKN 421 (Fossati et al. 2000a).

Kusunose, Takahara & Li (2000) derived, with both synchrotron and Compton cooling, the dependence of variations on the acceleration time scale, the electron injection rate, and the strength of magnetic fields. The value of $\gamma_{\max}$ and the ratio of the synchrotron to the Compton luminosity depend on such parameters. Particularly, they stressed that at the early stage of the evolution, i.e., $t = 0 - R/c$, the synchrotron component dominates the spectrum. The energy flux of soft X-rays starts to rise earlier than that of hard X-rays. Later ($t > R/c$), the Compton luminosity gradually increases. At the same time, the peak energy of the synchrotron component decreases because of radiative cooling. They next simulated a flare by simply changing the value of $t_{\rm acc}$ for a certain time span. With a shorter acceleration time scale, more energetic electrons, and consequently more hard photons are produced. The relation between the energy flux and the photon index during a flare was obtained. This is similar to the results by Kirk, Rieger & Mastichiadis (1998), with only synchrotron cooling considered.

>>>>>>

Chapter 3

Blazar Variability

We have discussed in the previous chapter radiative models, variability mechanisms, particle acceleration and the time-dependent SSC model in blazar jets. In this chapter, we will give a brief review of blazar variability.

3.1 Overview

Rapid and large amplitude variability at all observed frequencies is a hallmark of blazars. Intensity variations on a time scale of hours to days are quite common, indicating that blazar emission comes from a very compact region, and is likely Doppler-boosted towards us as a result of relativistic motion of the emitting blob of plasma (e.g., Mattox et al. 1993; 1997).

Both theoretically expected and observationally confirmed, the most strong variations of blazars occur at above peak frequencies in both the SED components, and variability is approximately correlated between the two peaks with larger amplitude seen in the high energy (Compton) γ-ray component than in the synchrotron component. The variations between different energies are correlated, usually with low energy emission lagging the high energy one. The lags at high energy bands are short, e.g., typically hours in the X-rays of HBLs and in the IR-optical of LBLs, and wavelength-dependent. The correlated variability suggests that the same electrons could be radiating both components.

Historically, it has long been noted that HBLs are much less variable and polarized in the optical than LBLs. This has led to a common interpretation that they are relatively less active since their jets are viewed off the line of sight. It is now becoming clear, from the SED-based perspective, that the difference is just an accident of where the SED peak occurs relative to the optical band: in LBLs, optical frequencies lie above the synchrotron peak, i.e., the region of maximum variability,

whereas in HBLs this is well below the synchrotron peak frequency, where variability is typically small. In fact, HBLs are at least as variable, in terms of large amplitude and short time scales, as LBLs, but at the corresponding part of the SED, i.e., at the UV/X-ray energies. By the same argument, one would predict high EUV/X-ray polarization in HBLs, comparable to the optical polarization in LBLs. FSRQs are very similar to LBLs.

3.2 Variability from TeV to GHz

Variability of substantial amplitudes is detected throughout the entire electromagnetic spectrum on all time scales which have up to now been probed.

VHE γ-rays

Variations in the TeV band, the highest energy end of the electromagnetic spectrum accessible with current technology, have received great attention in recent years. This band is probed with the ground-based Cherenkov telescopes, which are rapidly growing in number.

Extreme variability on time-scales from minutes to years is the most distinctive feature of the VHE emission from TeV-detected BL Lac objects. Variability is a surprising feature in some respects because it implies a small emission region. If low energy photons (e.g., infrared, optical, and ultraviolet) are produced in the same region, the VHE photons would pair produce with these photons and would not escape. Also, if the variability occurs near the base of the jet, there is likely to be considerable ambient radiation present which can attenuate the γ-ray signal. This opacity problem is reduced considerably if the emission is beamed toward us (e.g., Dermer & Gehrels 1995; Buckley et al. 1996), and this has been one of the main arguments for γ-ray beaming in these objects.

Several years of observations of MKN 421 by the Whipple Observatory revealed many distinct episodes of flaring activity, and more importantly, indicated that the VHE emission from MKN 421 was best characterized by a succession of day-scale or shorter flares with a baseline emission level below the sensitivity limit of the Whipple detector (Buckley et al. 1996), since the flux levels measured each night varied fairly randomly with no evidence of a smooth pattern. The most spectacular event took place in 1996, with the observations of two flares by the Whipple Collaboration (Gaidos et al. 1996). In the first flare, observed on May 7, the flux increased monotonically during the course of $\sim$2 hours of observations. This flux is the highest observed from any VHE source to date. The doubling time of the flare was $\sim$1

hour. The second flare, observed on May 15, lasted approximately 30 minutes with a doubling and decay time of less than 15 minutes. *These two flares are the fastest time-scale variability, by far, seen from any blazar at any γ-ray energy.*

Systematic observations of MKN 501 sensitive to day-scale flares have been conducted since 1995 with the Whipple Observatory γ-ray telescope (Quinn et al. 1999) and since 1997 with the telescopes of the HEGRA (Aharonian et al. 1999a), CAT (Punch et al. 1997), and Telescope Array (Hayashida et al. 1998) collaborations. The results of these observations indicate a wide range of emission levels and some very interesting similarities and differences with the VHE emission from MKN 421. The observations in 1995 indicate a flux which is constant, with the exception of one night (Quinn et al. 1996; Quinn et al. 1999). Observations in 1996 by the Whipple Observatory show that the average flux of MKN 501 had a two-fold increase in the average flux over the 1995 observations (Quinn et al. 1999). The Whipple observations show no flaring episodes but clearly indicate that the emission is varying on at least month-scales (Quinn et al. 1999). There is no significant evidence for day-scale variations within each month in 1996. In 1997, the VHE emission from MKN 501 changed dramatically. Significant hour-scale variations were seen. Two clear episodes of hour-scale variability were detected with the Whipple Observatory telescope. In addition to the establishment of the flaring itself, the Telescope Array Collaboration performed a periodicity search with their VHE observations of MKN 501 in 1997 (Hayashida et al. 1998). They show evidence for a quasi-periodic signal in the data which has a period of approximately 12.7 days. Similar to MKN 421, the HEGRA detected rapid intra-hour variability at TeV energies during June 1998, with doubling time is approximately 20 min (Sambruna et al. 2000).

The other unconfirmed sources are also variable emitters of VHE γ-rays. 1ES 2344 +514 was only detected with high statistical significance on one night, but has never been detected on the other occasions (Catanese et al. 1998; Aharonian et al. 1999b). PKS 2155−304 has also been claimed to be variable (Chadwick et al. 1999).

The significance of detected VHE γ-rays variability in BL Lac objects is that they parallel well the variability of FSRQs in the GeV γ-rays (see below), as predicted by the overall SED characteristics of blazars.

High energy γ-rays

The shortest time-scale variations detected for blazars with EGRET are for PKS 1622 −297 (Mattox et al. 1997) and 3C 279 (Wehrle et al. 1998). For both objects the flux was found to increase by a factor of two or more in less than 8 hours. Other objects that have shown flux variations over the period of a few days are 3C 279

(Kniffen et al. 1993), 3C 454.3 (Hartman et al. 1993), 4C 38.41 (Mattox et al. 1993), PKS 1406–076 (Wagner et al. 1995), and PKS 0528+134 (Hunter et al. 1993; Mukherjee et al. 1996). All these sources which show significant variations around the GeV bands are FSRQs, since their high energy (Compton) component peaks there.

Low energy γ-rays

Blazars tend to vary around MeV frequencies as well (Colmar 1996), which have been studied by the COMPTEL telescope on board CGRO but for only a small number of sources. However the larger errors in the flux determinations do not allow any detailed studies of the variability properties.

X-rays

In the keV regime, fast variations down to time scales of a few seconds have been detected in some brighter HBLs. Down to time scales of a few hours changes in the X-ray spectral indices have been found to accompany (and slightly lag behind) changes in total flux. The X-ray variations have been used successfully to derive quantitative SSC models. The significant variations in the X-rays of HBLs match the one in the optical of LBLs. More information about blazar X-ray variability will be reviewed in §3.4.

UV

IUE measurements of a sample of blazars were studied by Edelson (1992). It was found that significant variability correlates with luminosity. Among blazars PKS 2155−304 is the source best observed with IUE, which was variable on time scales of 1 day and a few hours (Maraschi et al. 1986; Edelson et al. 1991), and a doubling time scales of 10 days is common (Urry et al. 1993). In particular, the observed UV flux in PKS 2155−304 doubled in 1 hour (Pian et al. 1997). Evidence for spectral variations in the UV band is generally marginal, MKN 421 and PKS 2155−304 showed weak evidence for spectral hardening with increasing intensity and weak energy-dependence UV variability amplitude (Ulrich et al. 1984, Maraschi et al. 1986; George, Warwick, & Bromage 1998; Urry et al. 1988). LBLs are generally faint in the UV and their variability and spectra were difficult to measure with IUE. OJ 287 showed variability on time scale of 2 days (Maraschi et al. 1986).

Optical

In the optical blazars are known to vary on time scales from years to seconds. For a subsample of blazars optical variations have been investigated over 100 years. The spectral indices change on similar time scales as well. In general the source follows the common trend of becoming harder during brighter states.

The flares of total flux are accompanied by dramatic variations of the degree of polarization as well as position angle. There is no trivial correlations of the polarization characteristics with the total flux in any band, possibly due to the superposition of different, polarized components.

As expected from the SED differences, extensive studies showed: (a) the short time scales variations of LBLs are systematically larger in amplitude and have higher duty cycles than those of HBLs (Heidt 1996); (b) HBLs are in general less polarized than LBLs (Jannuzi et al. 1993).

Infrared

The near infrared variability shows similar amplitudes and time scales to the optical emission, and in some cases sources get bluer as they brighten.

In the mid- and far-IR wavelengths IRAS observations of LBLs/FSRQs have shown rapid (time scales of weeks) large amplitude (factors of two) variations (Impey & Neugebauer 1988 and references therein), since the synchrotron component peaks around this range (e.g., 3C 345; Bregman et al. 1986). Significant information of mid- and far-infrared variations are being expected from ISO. The ISO observations of PKS 2155−304 in May and June 1996 showed no detectable time variability (Bertone et al. 2000) because its IR emission is at frequencies lower than the synchrotron peak.

Radio

For a review of blazars variability at radio wavelengths see Wagner & Witzel (1995). Radio emission in the GHz (cm) range generally shows intraday variability (IDV) characteristic. It is now clear that even in the cm range blazars may vary fast. Kraus et al. (1997) and Kedziora-Chudcer et al. (1997) find that flux densities may change within two hours, and polarizations and spectral indices change equally fast as well.

Variability at mm wavelengths is important because these are the lowest frequencies which are still unaffected by scattering of electromagnetic waves in the interstellar plasma. It has become possible in the last years to get sufficient accuracy to investigate variations on short time scales. Significant variations have been

detected in PKS 0405−385 (Wagner 1997).

3.3 Multi-wavelength variability

Simultaneous multi-wavelength monitoring has received more and more attention, despite of difficulties in arranging this kind of observations, since it is the best probe of the physics of blazars.

Because they are very bright at optical/UV/X-ray wavelengths, MKN 421, MKN 501 and PKS 2155−304 are the best-monitored blazars. Each has been the target of multiple well-sampled, long-duration monitoring campaigns. For MKN 421 both the high-energy synchrotron emission and the gamma-ray component have been well monitored because it is consistently bright at TeV energies. MKN 501 has been well monitored more recently, following a dramatic TeV and X-ray flare in April 1997. PKS 2155−304 has been observed with better sampling at optical through X-ray wavelengths but without simultaneous TeV monitoring (Chadwick et al. 1999).

Of great interest is the correlated variability between synchrotron and Compton components at corresponding points on the SED, in particular at the two peaks. For TeV blazars, the spectral peaks are in the X-ray and TeV bands. One of the most exciting progress is the detection of correlated TeV/X-ray variations. Two confirmed strongly and rapidly variable TeV sources, MKN 421 and MKN 501, showed remarkably correlated X-ray and TeV variations, strong evidence for a common production mechanism for both synchrotron and γ-ray Compton components. Measuring the time lags accurately between the SED peaks, a good determination of which requires detailed monitoring over a large wavelength range, should distinguish between Compton scattering models and alternatives like PIC. The relation between X-rays and TeV emission in TeV sources corresponds to the relation between optical and GeV emission in radio-selected blazars. Here we summarize recent developments on this topic.

The observations to date reveal that the X-ray and TeV emission vary quasi-simultaneously to within a day (e.g., Maraschi et al. 1999), and the emission in the other bands does not, showing that the increase of the maximum energy in the electron distribution is the critical parameter (Mastichiadis & Kirk 1997). As yet the exact TeV/X-ray time lags are not well defined due to, to some extent, the lack of sensitivity in both the X-ray and TeV observations. There are hints, particularly in the well studied source MKN 501 that sometimes the X-rays may lead and sometimes the TeV emission leads (Lamer and Wagner 1999). The clarification of time lag properties is clearly an important future observational task.

MKN 421

The first evidence of correlated variability between VHE γ-rays and lower energy emission came from a multi-wavelength campaign on MKN 421 in 1994 April/May (Macomb et al. 1995,1996). Correlated variations in the VHE γ-ray and X-ray energies were claimed, but detailed comparisons of the variability in those wavebands are not possible because of the offset in time of the observations between the VHE γ-rays and the X-rays. The observations at MeV, UV, IR, mm, and radio wavelengths showed no evidence of variability during this period.

The multiwavelength campaign, organized in 1995 to better measure the multi-wavelength properties of MKN 421, revealed, for the first time, correlations between VHE γ-rays and X-rays (Buckley et al. 1996). MKN 421 underwent a large amplitude flare in VHE γ-rays during the observations. The flare is also clearly seen in the *ASCA* and *EUVE* observations. The X-rays and VHE γ-rays appear to vary together, limited to the one day resolution of the VHE observations, and the amplitude of the flares is similar, $\sim$ 400% difference between the peak flux and that at the end of the observations. The EUVE and optical data (assuming it is also correlated) are consistent with the flare being delayed by approximately 1 day relative to the X-rays and VHE γ-rays. The amplitude of the flare also decreases with decreasing energy. The EUV flux varies by $\sim$ 200% during the observations and the optical flux varies by about 20%. The B-band polarization varies by nearly a factor of two in the observations.

The observations of MKN 421 in 1994 and 1995 were clearly undersampled, limiting the conclusions that could be drawn concerning correlations between wavelengths and emission models. Two multiwavelength campaigns organized in 1998 attempted to improve these results through more dense observations in X-rays and VHE γ-rays. The first campaign, conducted in late April 1998, was centered at X-ray wavelengths on observations with the *BeppoSAX* satellite and established the first hour-scale correlations between X-rays and VHE γ-rays in a blazar (Maraschi et al. 1999). A flare is clearly detected in X-rays and TeV γ-rays on the first day of observations. The peaks in the light curves occur at the same time, within 1 hour, but the fall off in the X-ray flux is considerably slower than the TeV γ-rays. Also, the TeV γ-rays have a larger variability amplitude ($\sim$ 4-fold ratio between average and peak) than the X-ray ($\sim$ 2-fold). Both the faster VHE flux decrease and the larger amplitude variability have not been seen previously in MKN 421. These observations provide the first clear indication that X-ray and VHE γ-rays may not be completely correlated on all time-scales.

The second multiwavelength campaign started in late 1998 April, immediately

after the observations discussed above, and was centered around a seven day continuous observation of MKN 421 with ASCA (Takahashi et al. 2000). This campaign revealed that similar variability time scale between the X-ray and VHE γ-rays and some sub-day time scale X-ray variability with amplitude too low to be resolved with the Whipple observations. Instead, the X-ray observations revealed the complete cycle of about 8 flares, the first time this has been done for MKN 421. Also, these observations seem to confirm the supposition of Buckley et al. (1996) that the VHE emission from MKN 421 is primarily the result of flares, with little steady emission evident. Finally, the combination of VHE data from these telescopes confirms the sub-day-scale correlations seen in the Whipple/*Beppo*SAX observations.

MKN 501

The first multi-wavelength observations of MKN 501, which included VHE γ-rays data were conducted in 1996 (Kataoka et al. 1999). The observations were too undersampled to clearly establish any correlation.

Multiwavelength observations of MKN 501 during its high emission state in 1997 revealed, for the first time, clear correlations between its VHE γ-ray and X-ray emission (Catanese et al. 1997). The results of this campaign show that for MKN 501, like MKN 421, the VHE γ-rays and the soft X-rays vary together and the variability in the synchrotron emission increases with increasing energy. However, OSSE has never detected MKN 421 despite several observations (McNaron et al. 1995), while the MKN 501 detection had the highest 50–150 keV flux ever detected by OSSE from a blazar. A likely explanation of the OSSE detection is that the synchrotron emission in MKN 501 extends to $\sim$ 100 keV, compared with the $\sim$1 keV cutoff seen in MKN 421. This explanation was first confirmed by the observations with *Beppo*SAX (Pian et al. 1998). In addition, the day scale variations for MKN 501 are larger in γ-rays than in X-rays. So, despite the similarity of MKN 421 and MKN 501 in some respects, these multi-wavelength campaigns are beginning to reveal differences in the two objects.

Petry et al. (2000) studied the medium-timescale variability of the broadband spectra, averaged over weekly intervals, which shows correlation between X-rays and TeV energies (HEGRA), while the source shows only minor variability at radio and optical wavelengths.

Sambruna et al. (2000) studied exactly simultaneous X-ray (RXTE) and TeV (HEGRA) monitoring of MKN 501 during 15 days in 1998 June. The source underwent a remarkable flare in the TeV and in the X-ray energy bands, lasting for about six days and with a larger amplitude at TeV energies than in the X-ray band, with

no lags of more than one day.

3.4 X-ray variability

For blazars different emission components are competitive in the X-ray region, possibly depending on their luminosity in terms of both from differences between source to source and from state to state of a source. The various emission components and their reasonable mixture may well be represented by their spectral characteristics. It is now clear that in the soft and medium X-ray bands (0.1−10 keV), HBLs have steep, LBLs intermediate, and FSRQs flat X-ray spectra. From the point view of spectral properties, the main difference between HBLs, LBLs and FSRQs is that we are observing the high energy tail of the synchrotron component in HBLs while in FSRQs we are detecting the low energy end of the Compton scattered component, and X-ray emission of LBLs is a mix of synchrotron and Compton emission. These are supported by multiwavelength observations: in HBLs the X-ray spectrum can be extrapolated smoothly from optical-UV and comprising part of the downward gradually curving spectrum, this is signature of synchrotron emission. However in LBLs and FSRQs the extrapolation of IR-optical spectrum is well below the X-ray one, a concave optical-X-ray continuum, which is dominated by a much flatter Compton component in the X-rays. Intermediate objects which have received much attention recently, may have both components contributing in the X-ray range with the steep synchrotron component prevailing in the soft X-rays.

Notably, not only different components exhibit characteristic spectral features, but also have strikingly different variability properties. In this section we briefly review X-ray variability properties of blazars, and the especially exciting results from recent ASCA, RXTE and *Beppo*SAX observations.

3.4.1 Temporal and spectral Variability

A blazar (radio-loud AGNs) typically spends the majority of its time at the quiescent level, upon which are superposed large outbursts. The light curve is non-linear, i.e., the variability is not symmetric about the mean (e.g., M^{c}Hardy 1996). There is not much evidence for very short time scales ($\sim$ 100–1000s) large amplitude flickering which is seen in Seyfert galaxies.

In TeV BL Lac objects and some other bright HBLs, rapid and large amplitude X-ray variability is a hallmark, with flux doubling on time scales of hours, and the variability amplitude generally increasing with photon energies (e.g., Takahashi

et al. 1996; Zhang et al. 1999; Fossati et al. 2000a). The spectra harden systematically with increasing intensity (e.g., Urry et al. 1986; Treves et al. 1989; Giommi et al. 1990; Sembay et al. 1993; Sambruna et al. 1994). Muti-waveband variability (mainly in UV and X-ray) of HBLs suggests that spectral changes and variability amplitude are greater at or above the synchrotron peak frequency, which is in the soft X-rays or even in the hard X-ray range during flares. One of the most important properties of HBLs is that rapid and large intensity variations in the X-ray band affect the entire SED, with the peak frequency of synchrotron emission shifting to higher energy with increasing intensity. Moreover, shifts of up to 2 orders of magnitude in the position of synchrotron peak have been detected in a few extreme cases (e.g., MKN 501, Pian et al. 1998; 1ES 2344+514, Giommi, Padovani & Perlman 2000). This behavior, in turn, affects systematic comparisons of variability in the fixed X-ray bands due to various parts of the synchrotron component moving in or out this band which refer to different cooling time scales.

RXTE performed monitoring over long time scales. The RXTE ASM light curve of MKN 501 reveals an active period lasting for over a year during 1997, with detectable flares of tens of days. During the rising side of this outburst the *Beppo*SAX showed the X-ray spectrum hardened considerably, with the synchrotron component peaking up to $\sim$ 100 keV, rather than at a few keV as normally (Pian et al. 1998). Interestingly, this behavior is confirmed by RXTE during the decaying side of the outburst (Lamer & Wagner 1999).

PKS 2005–489, a TeV source candidate, was monitored by RXTE during October-December 1998 (Perlman et al. 1999). The source underwent a spectacular flare with remarkably simple and symmetrical structure, lasting about a month at half-maximum and nearly three months from the start to end. The X-ray spectrum hardened considerably and steepened rapidly during the flare's rising and declining phase, respectively.

On very short time scales, RXTE detected a vary fast flare (1998 May) of MKN 501 in which 2–10 keV flux increased by $\sim$ 60% in less than 200 seconds, followed by a drop-off of $\sim$ 40% in less than 600 seconds (Catanese & Sambruna 2000).

In fact most observations were carried out over time scale of days with good sampled light curves by ASCA and *Beppo*SAX. The most exciting observations of X-ray variability are recently performed with *Beppo*SAX and ASCA for MKN 421 and PKS 2155−304 due to their brightness. In Chapter 5 and 6 we will perform a detailed temporal analysis for most of these observations and compare them with the results from other observations.

LBLs show, in general, flatter spectra than HBLs and different variability behavior as well. In some cases there are "inverse" spectral changes, that is, a softening of the spectrum with increasing intensity (Cappi et al. 1994; Urry et al. 1996). This can be understood in terms of the relative variation of two spectral components that intersect each other in the X-ray range: a soft, highly variable one that swamps (high soft intensity) or uncovers (low hard intensity) a less variable flatter component. Such objects should be intermediate between LBLs and HBLs.

ON 231 was observed with *Beppo*SAX in May and June 1998, with about one day duration in each observation (Tagliaferri et al. 2000). The spectrum from 0.1 up to 100 keV had a concave shape in both cases, with a break detected at about 4 and 2.5 keV, respectively. The interesting results from these observations is that the variability amplitude above the break is much smaller than that below it. In particular, during the May observation a flare below 4 keV was detected as a fast variability event increasing by about a factor of three in 5 hours. In contrast, no variability was detected above 4 keV. This behavior of X-ray variability is accounted for by a steep synchrotron component below the break and a flat Compton component above the break.

The *Beppo*SAX monitoring of S5 0716+714 showed spectral steepening with increasing intensity during events of rapid variability, a behavior rarely observed in BL Lac objects. The transition between synchrotron and inverse Compton emission has been clearly detected as sharp X-ray spectral breaks at around 2–3 keV. Significant variability is present only at low energies (Giommi et al. 1999). These findings are probable consequence of a shift of the synchrotron peak emission from IR/optical band to higher energies, causing the synchrotron tail to push into the soft X-ray band more and more as the source brightens.

As FSRQs, the emission line blazars, less is known about the X-ray variability properties because they are relatively faint X-ray sources, with the exception of 3C 273. They generally show extremely hard spectra in the 0.2–4 keV band (Worrall & Wilkes 1990), much flatter than the extrapolation of the optical-UV spectrum.

In summary, the observations show that when a flat component is present in the X-ray band (as for LBLs and FSRQs), it appears to vary on longer time scales and with lower amplitude than the steep X-ray component (as for HBLs) that is thought to be an extension of the longer wavelength synchrotron emission. However this statement may be partly biased by the lower X-ray fluxes of LBLs and FSRQs compared to those of the better-observed HBLs, although the theoretical predictions are consistent with the observations.

3.4.2 Time lag

The energy-dependent X-ray variations is a powerful tool to constrain the blazar radiative models. The lag/lead between different energies is the most important one, which can be studied by two independent techniques: cross-correlation analysis and spectral (or identically hardness ratio) evolution against intensity.

Soft lag

In HBLs, the synchrotron component dominates out to at least a few keV. The lower energy photons are expected to lag the higher energies ones due to longer cooling time scale of lower energy electrons relative to higher energy ones. This phenomenology has been extensively observed in both MKN 421 and PKS 2155–304, the soft X-rays lagging hard X-rays by $\sim$ hours (Sembay et al. 1993; Takahashi et al. 1996; Urry et al. 1997; Zhang et al. 1999; Kataoka et al. 2000), roughly as expected from a homogeneous source, where the lag time is roughly the radiative time scale at the lower energy. We call this pattern a "soft lag". Similarly the optical/UV variations lag the X-ray variations by $\sim$ day. In the well studied case of PKS 2155−304 the lags approximately follow a $\nu^{-0.5}$ relationship, suggesting that radiating losses are the dominant process. Such behavior can be explained by the injection of high energy electrons, raising the upper cutoff energy of the electron distribution, followed by radiative cooling so that the number of high energy electrons decreases, and those cooled electrons then add to the emission at lower energies.

Hard lag

The opposite behavior is also seen with the lower energy photons leading the higher energies ones. We call it "hard lag". The hard lag has been rarely seen in previous BL Lac objects observations, and it was firstly seen in PKS 2155−304 (Sembay et al. 1993). However recently it has been seen in several X-ray observations of TeV BL Lac objects (Fossati et al. 2000a,b for MKN 421; Lamber & Wagner 1998; Catanese & Sambruna 2000 for MKN 501; Sambruna 1999 for PKS 2155−304). This is an important information, since the hard lag is consistent with a flare dominated by the acceleration time scale in a simple relativistic shock model.

3.5 Why to study blazar variability?

Here we emphasize the importance of blazar variability studies and list what we would like to know about their variations.

- The variability relationships among all observed wavelengths: relative amplitudes, time scales, time lags, similarities and differences and, chiefly, regularities (trends). Variations (especially complete flares) from radio to γ-ray frequencies should exhibit frequency-dependent characteristics that can test models for both the low- and high-energy components and the nature of the inner jet in blazars.

- To identify any possible variability continuity among blazars in terms of wavelength and luminosity. This should deepen our understanding of the blazar unification schemes.

3.5.1 Importance of X-ray variability studies

Synchrotron emission followed by inverse Compton scattering (with various photon seeds) in a relativistic jet close to the line of sight is generally thought to be the mechanisms responsible for the strong and rapidly variable nonthermal radiation over the entire electromagnetic spectrum in blazars (e.g., Kollgaard 1994; Urry & Padovani 1995). We have understood that in different subclasses of blazars the X-ray emission could be pure synchrotron/Compton components or a combination of both. So different X-ray variability characteristics are predicted for different blazar subclasses, and accordingly, X-ray studies are crucial in discriminating different emission models. Recently, the *Beppo*SAX satellite, thanks to its wide X-ray band pass (0.1–200 keV) has made direct measurements of the Compton part of the spectrum for a number of LBLs (e.g., Giommi et al. 2000), and the very variable tail of synchrotron component of several HBLs (e.g., Pian et al. 1998; Wolter et al. 1998, 2000; Giommi, Padovani & Perlman 2000; Chiappetti et al. 1999; Fossati et al. 2000a,b). In particular, *Beppo*SAX has detected for the first time both spectral components in the case of the two intermediate BL Lac objects, S5 0716+714 and ON 231, which clearly show that the soft X-ray synchrotron radiation varies in a different way compared to the hard Compton components (Giommi et al. 1999; Tagliaferri et al. 2000).

The limited SED data, either simultaneous or not, on most blazars prevent us from being able to discriminate among the various models on the basis of the spectra alone. For example, both the SSC and ERC models can reproduce the SED of 3C 279 rather well (e.g., Maraschi, Ghisellini & Celotti 1992; Hartman et al. 1996). Similarly the SSC model fits well the data of the March 1993 flare of PKS 0528+134 (Mukherjee et al. 1996), while its August 1994 low state was fitted with the ERC model by Sambruna et al. (1997). Particularly the SSC, ERC, and PIC models well

reproduce the SED of 3C 273 (von Montigny et al. 1997). It is then important to consider the opportunity offered by comparison of different "snapshots" of the same source at different levels of activity and brightness. The characteristics of the correlations among the fluxes at different energies over a broad energy range may actually be anticipated from the basic properties of the different (time-dependent) emission mechanisms. As stated above, the correlations between X-rays and other wavelengths play a key role for this kind of studies. For example, the SED of the two intermediate BL Lacs S5 0716+714 and ON 231 indicate that the variability of the Compton component (harder X-rays) may be correlated with the radio flux and not with the optical and soft X-ray synchrotron emission and possibly confirm that the harder X-rays measured by *Beppo*SAX are just the beginning of Compton emission. M^{c}Hardy et al. (1999) showed that the medium energy X-ray (3–20 keV) and near infrared fluxes in the quasar 3C 273 are highly correlated, with the infrared leading the X-rays by 0.75 ± 0.25 days, and further estimated that each decade of the seed photon distribution from the mm to IR waveband contributes roughly equally to the medium energy X-ray flux in this source. These observations rule out the 'External Compton' emission process and support SSC model for the production of the X-rays in 3C 273.

However, compared to the X-ray spectral understanding which we have achieved, we are still in a situation of shortage of systematic comparisons of temporal variability among different classes of blazars, and even within a single class. Needless to say, a systematic temporal X-ray analysis is necessary in order to fully understand the physical differences among HBLs, LBLs and FSRQs. The main diagnostic techniques to distinguish the different temporal variability are the time lags between the low and high energy photons, and their relative amplitude of variability (M^{c}Hardy 1999). In the X-ray bands, we have recognized variable soft lags in the HBL PKS 2155–304 and MKN 421, but hard lags have also been detected in these sources. It is thus quite evident that we need to measure time lags between photons of different energies in many occasions, and in a number of different blazars, to see whether the results found for PKS 2155–304 and MKN 421 are typical or not. Moreover by searching for variations of time lags in similar flares on different occasions in the same source, we would be able to distinguish between different emission models and determine how the particles are injected or accelerated.

The current X-ray observations show that acceleration and cooling are the dominant physical mechanisms responsible for the observed variability properties from TeV blazars' jets. It would also be interesting to perform similar studies in the IR-optical ranges for typical LBLs and FSRQs, since it is important to compare the

nature of the acceleration and cooling in the different ranges of electron's energies (i.e., radiated frequencies). Of course, our ultimate goal should be trying to find out a systematic trend of the acceleration and cooling mechanisms in blazars, like the SED trend.

Another aspect which we have not examined for blazars is the luminosity dependence of the X-ray variability amplitude at fixed time scales, while several studies have been performed for different samples of Seyfert galaxies and radio-quiet quasars (see § 7.1).

3.5.2 Scientific justification

X-ray astronomy is one of the most active and rapidly advancing field in astrophysics. Past and currently working X-ray satellites have increased our understanding of the universe. New X-ray satellites (e.g., Chandra and XMM) with larger receiving areas and higher temporal/spectral resolution will significantly improve our knowledge.

It is predicted that X-ray variability studies will have a good progress on two fronts. First, the availability of uniform data archives like ASCA, RXTE and *Beppo*SAX has made systematic studies and statistical comparisons possible among different classes of blazars (more generally AGNs). Second, the new satellites like Chandra and XMM with high resolution (in spectrum, time and space) will permit deeper studies. For example, long enough observation (e.g., one week duration of observations) has freshed our understanding on the physical processes at working in TeV BL Lac objects (e.g., Sambruna 1999 for PKS 2155−304; Takahashi et al. 2000 for MKN 421). In particular, we have just seen information on relativistic electrons acceleration in the jet from both temporal and spectral evolution (e.g., Fossati et al. 2000a,b).

>>>>>>

Chapter 4

Data Analysis Techniques

It is well known that the variability is one of the fundamental characteristics of blazars. One brief overview on this issue have been presented in the previous chapter, and the importance of variability analysis is also stressed. While the SED is extensively used to constrain blazar models, there are relatively very few attempts to use their variability properties as a starting point of a model, in spite of the large effort put in monitoring campaigns. One of the main reasons for this asymmetry is that it is very difficult to quantify the properties of the variability.

The best techniques to characterize variability include the power density spectrum (PDS) and inter-band correlations: the PDS slopes and the measured time lags impose strong constraints on radiation models. Before starting our temporal analysis, it is useful to study firstly the data analysis techniques which are necessary to define blazar variability characteristics. In this chapter, we summarize and develop the techniques that are relevant to our analysis.

4.1 Some terminology

A history of the intensity of a source of radiation over time is referred to as a **light curve**, $x(t)$. The representation of a light curve in terms of observation is often **binned** (or **resolution**) from a X-ray detector, and **rebinned** when doing pratical timimg analysis as requested by improving **statistic confidence**. The average intensity, $x(t_i)$, over a particular time range, Δt, referred to as the **binning time**, is calculated by integrating the instantaneous intensity $x(t)$ — in an astrophysical setting, this usually means **counting photons**, and represent in a unit time (e.g., s), this is so-called **count rate**. The **bins** are typically of constant time width, equally spaced, with no space between them. This procedure of operation is called **sampling**, in which the instantaneous value of a signal is measured at a series of

discrete times:

$$x_i = x(t_i) \tag{4.1}$$

where the t_i are typically evenly spaced, $t_i = i\Delta t$, and x_i has an assigned measurement errors, σ_i. However the **exposure** properties of a detector will cause a bin to be **fully-, partly- or non-exposured**, of which the rejected partly- and non-exposured bins form the "normal" **gaps** of a time series, this will cause the time series to be **unevenly** sampled. We choose, throughout our analysis, that the bins which are less than 25% exposured are rejected. The selected and rejected bins are generally named **good** and **bad** bins respectively.

When studying some computed properties of a light curve which is believed to have some well-defined (at least locally) average values, the light curve is often segmented into several **intervals**, with equal **interval length**, usually an integer multiple of the binning time: $t_I = n\Delta t$, and the intervals, usually the last one, of which the length is less than t_I (also depending the specific selection as do in selecting bin exposure), is also rejected. The parameter of interest is then calculated for each interval, and the results averaged over intervals.

4.2 χ^2 test for variability

The first piece of information that we need to know is whether a light curve is variable. For this purpose a simple χ^2 test is performed on each light curve to test for variability against the null hypothesis that the flux remains constant. We label the light curve as "variable" if the hypothesis of constant flux is rejected at greater than 95% confidence level. Otherwise sources are classed as "constant". The reduced-χ^2, χ^2_ν, is defined as

$$\chi^2_\nu = \frac{1}{\nu}\sum_{i=1}^{N}\frac{(x_i - \bar{x})^2}{\sigma_i^2} \tag{4.2}$$

Where $\bar{x}$ is the unweighted mean count rate over a light curve x_i, $i = 1, ..., N$, and σ_i is the measurement uncertainties associated with x_i. $\nu = N - 1$ is the degree of freedom.

4.3 Variability amplitude

4.3.1 Fractional *rms* variability amplitude

It has been demonstrated that blazars show a rich diversity of variability characteristics. For example, the individual sources exhibit different amplitudes of variability, which may also be energy- and/or brightness-dependent. The first fundamental quantity to characterize blazar variability is to define the amplitude of variability of a light curve.

We first point out that a rigorous approach would be to define the amplitude and slope of the power density spectrum (PDS) of a light curve (see §4.5). Unfortunately, however, unlike the well studied EXOSAT light curves, such an analysis is extremely difficult with unevenly sampled data, as afforded by low-earth satellites such as *Beppo*SAX. In addition, most blazars studied in Chapter 7 are too faint to obtain variability amplitudes by detailed PDS analysis. A simpler method is to estimate the intrinsic variance in the light curve, since this quantity is proportional to the amplitude of the PDS.

The fractional (i.e., normalized by the mean count ratio) *root mean square (rms)* variability parameter, $F^2_{\rm var}$, is a general parameter to quantify the variability amplitude of an unevenly sampled light curves. It is defined as the so-called *excess variance* (or intrinsic variance) which is calculated by taking the difference between the standard variance of a light curve and the expected variance due to measurement errors, normalized by the square of the unweighted average count rate. We clarify this definition as follows.

The standard total variance, $\sigma^2_{\rm total}$, and the expected measurement variance, $\sigma^2_{\rm noise}$ are, respectively, defined as

$$\sigma^2_{\rm total} = \frac{1}{N}\sum_{i=1}^{N}(x_i - \bar{x})^2 \tag{4.3}$$

$$\sigma^2_{\rm noise} = \frac{1}{N}\sum_{i=1}^{N}\sigma_i^2 \tag{4.4}$$

The fractional *rms* variability parameter is then defined as:

$$F^2_{\rm var} = \frac{\sigma^2_{\rm total} - \sigma^2_{\rm noise}}{\bar{x}^2} \tag{4.5}$$

The error on $F^2_{\rm var}$, asymptotically for large N, is given by $s_{\rm D}/(\bar{x}^2\sqrt{N})$ (Nandra et al. 1997) where:

$$s^2_{\rm D} = \frac{1}{N-1}\sum_{i=1}^{N}\{[(x_i - \bar{x})^2 - \sigma_i^2] - F^2_{\rm var}\bar{x}^2\}^2 \tag{4.6}$$

i.e., the variance of the quantity $(x_i - \bar{x})^2 - \sigma_i^2$.

It should be noted that this parameter depends on the observation length and particular sampling (Lawrence & Papadakis 1993; Fossati et al. 2000a). Since $F_{\rm var}^2$ is a simple measurement of the variability amplitude, we assume that it is reasonable to compare this parameter when the individual observations are not radically different in duration.

4.3.2 A maximum likelihood estimator

It is, however, important to note that an intrinsic assumption in the above method is that each point in the light curve has equal weight, which will break down in cases where the errors differ significantly from point to point. In fact, many blazars studied in Chapter 7 are too faint to obtain a meaningful variability amplitude, and $F_{\rm var}^2$ will be negative values, this demonstrate that the above definition to measure the intrinsic variations will break down in light curves with low ratio of signal to noise. We therefore take a maximum likelihood technique (Almaini et al. 2000) to extract the best estimate of the intrinsic (noise subtracted) variance given a set of data values x_i with differing measurement errors σ_i. In particular, although most light curves will be too faint to enable a significant detection of variability, this method can nevertheless place upper limits on the amplitude of variability which could be present.

In the following we describe in detail the maximum likelihood estimator for separating the intrinsic variance from the scatter due to measurement errors.

The total variance $\sigma_{\rm total}^2$ in a light curve should include two components: the fluctuations due to noise ($\sigma_{\rm noise}^2$) and probable intrinsic variations from a source ($\sigma_{\rm source}^2$):

$$\sigma_{\rm total}^2 = \sigma_{\rm noise}^2 + \sigma_{\rm source}^2 \tag{4.7}$$

If we assume Gaussian statistics, for a light curve x_i with assigned measurement errors σ_i and a mean value $\bar{x}$, the probability density for obtaining the N data of the light curve is given by:

$$p(x_i|\sigma_i, \sigma_{\rm source}) = \prod_{i=1}^{N} \frac{\exp\left\{-\frac{1}{2}(x_i - \bar{x})^2/(\sigma_i^2 + \sigma_{\rm source}^2)\right\}}{(2\pi)^{1/2}(\sigma_i^2 + \sigma_{\rm source}^2)^{1/2}} \tag{4.8}$$

This is simply a product of N Gaussian functions representing the probability distribution for each bin. We may use Bayes' theorem to obtain the probability distribution for $\sigma_{\rm source}$ for given measurements:

$$p(\sigma_{\rm source}|x_i,\sigma_i) = p(x_i|\sigma_i,\sigma_{\rm source})\frac{p(\sigma_{\rm source})}{p(x_i)} \quad (4.9)$$

$$\propto L(\sigma_{\rm source}|x_i,\sigma_i) \quad (4.10)$$

where $L(\sigma_Q|x_i,\sigma_i)$ is the likelihood function for the parameter $\sigma_{\rm source}$. This general form for the likelihood function can be calculated if one assumes a Bayesian prior distribution for $\sigma_{\rm source}$ and x_i. In the simplest case of a uniform prior one obtains:

$$L(\sigma_{\rm source}|x_i,\sigma_i) \propto p(x_i|\sigma_i,\sigma_{\rm source}) \quad (4.11)$$

$$= \prod_{i=1}^{N}\frac{\exp\left\{-\frac{1}{2}(x_i-\bar{x})^2/(\sigma_i^2+\sigma_{\rm source}^2)\right\}}{(2\pi)^{1/2}(\sigma_i^2+\sigma_{\rm source}^2)^{1/2}} \quad (4.12)$$

By differentiating the above, the maximum likelihood estimate for $\sigma_{\rm source}$ can be shown to satisfy the following, which (for a uniform prior) is mathematically identical to a least χ^2 solution:

$$\sum_{i=1}^{N}\frac{\{(x_i-\bar{x})^2-(\sigma_i^2+\sigma_{\rm source}^2)\}}{(\sigma_i^2+\sigma_{\rm source}^2)^2}=0 \quad (4.13)$$

With zero measurement errors, this reduces to the standard form:

$$\lim_{\sigma_i\to 0}\sigma_{\rm source}^2 = \frac{1}{N}\sum_{i=1}^{N}(x_i-\bar{x})^2 \quad (4.14)$$

In the case of identical measurement errors ($\sigma_i = constant = \sigma_c$) this reduces to the definition 4.5 after normalized by the mean $\bar{x}$,

$$\lim_{\sigma_i\to\sigma_m}\sigma_{\rm source}^2 = \frac{1}{N}\sum_{i=1}^{N}\left\{(x_i-\bar{x})^2-\sigma_c^2\right\} \quad (4.15)$$

In general however, Equation 4.13 can only be solved analytically for the case where $N \leq 2$. For a larger number of bins we must find the maximum likelihood estimate numerically, from which maximum likelihood estimates for $\sigma_{\rm source}^2$ can be evaluated with suitable error bounds. The maximum likelihood estimate for $\sigma_{\rm source}^2$ is obtained by locating the peak of the likelihood curve, while the error bounds are obtained in the standard way by assuming that the likelihood curve has a Gaussian shape.

As $F_{\rm var}^2$, when comparing values of $\sigma_{\rm source}^2$ from the maximum likelihood estimate, it is also important to be aware of the effects of different total integration times and sampling. We further justify that $F_{\rm var}^2$ and $\sigma_{\rm source}^2$ are identical in a light curve with enough high signal-noise-ratio, but the errors are different due to the definitions.

4.4 Time scales

The measurement of the variability amplitude can only characterize the mean variability of a light curve. However, a direct measurement of the fastest time scale on which the intensity can change is crucial as it may constrain the source size, and thus luminosity density, accretion efficiency or beaming parameters, and black hole mass. This requires to identify rapid variability events rather than the average variability properties. One often considers the so-called "doubling time" as a reasonable measure of the fastest and meaningful time scale of a source (e.g., Edelson 1992). More precisely, here we define the "doubling time" as

$$T_2^{ij} = \left| \frac{x_{ij} \Delta T_{ij}}{\Delta x_{ij}} \right| \tag{4.16}$$

where $\Delta T = t_j - t_i$, $\Delta x_{ij} = x_j - x_i$, and $x_{ij} = (x_j + x_i)/2$, and consider the minimum value of T_2^{ij} over any data pairs as the shortest time scale for each observation,

$$T_2 = \min_{\forall i,j}(T_2^{ij}) \tag{4.17}$$

keeping in mind that this quantity is ill-defined, strongly depending on sampling rate, length and signal-to-noise ratio of the observation (Press 1978). The error on T_2^{ij} is propagated through the errors on the fluxes x_i and x_j, i.e., σ_i and σ_j respectively, and *a priori* we neglect the value of T_2^{ij} if the error is larger than 20%. Although the criterion used here to gauge the minimum time scale of variability in a light curve is somewhat arbitrary, it does provide a way to compare the numbers obtained. As we will show in the next two sections, the best ways to determine the characteristic time scale of a light curve are PDS and stucture function (SF).

4.5 Power density spectrum

It is well known that the best way to measure the characteristic variability time scale and variability amplitude at a given frequency (or time scale), and to characterize source variability in general, is to determine the fluctuation power density spectrum (PDS), since PDS represents the amount of variation at any given frequency present in a signal, and any pattern and change of the PDS over some frequency region will reflect information of a physical process.

A common method of estimating the PDS is computing the periodogram, which is calculated as the modulus squared of the (discrete in fact) Fourier transform of a signal:

$$P(f_i) = \frac{\Delta t}{N} \sum_{j=1}^{N} \left| x(t_j) e^{-i2\pi f_i t_j} \right|^2 \tag{4.18}$$

where $f_i = i/(N\Delta t)$, $i = 1, 2, ..., (N/2) - 1$ (e.g., Deeming 1975) are the discrete Fourier frequencies.

The PDS analysis is carried out with the direct Fourier transform algorithm which is included in the timing series analysis package XRONOS. Here we further describe some details to derive a "true" PDS when using this package:

1. The average count rate, $\bar{x}$, is subtracted from all temporal bins before PDS calculation.

2. To obtain an intrinsic PDS of a light curve, the expected white noise power caused by the uncertainty in measuring the flux (Poisson statistics) must be subtracted, which is $\sigma^2_{\rm noise}$ (see equation [4.4]).

3. Due to the wide and nonnormal distribution of the PDS calculated by the above equation for a single measurement, averaging of several PDS estimates is often performed. The estimates may be for the same frequency component in different intervals or for nearby frequencies (e.g., logarithmically rebinned) in the same interval, or both (our case). This can reduce the variance and approximate their probability distribution function to a normal (Gaussian) distribution.

4. PDS is normalized so that its integral gives the squared *rms* fractional variability, $F^2_{\rm var}$, therefore the power spectrum is in unit of $F^2_{\rm var}/Hz$, which is in turn normalized to the squared average count rate. This kind of normalization is useful when comparing the PDS of a source in different epochs and of different sources.

5. The error bars represent the standard deviation of the average power in each rebinned frequency interval, where the power in each bin is χ^2 distributed with $2N$ degrees of freedom, where $N = ML$ is the total number of points used to produce the mean power in each frequency bin (from M intervals and L independent Fourier frequencies).

A more important issue, discussed in detail by Tagliaferri et al. (1991), is the data gap filling, which is unavoidable for a low orbit X-ray satellite. The gap-filling procedure could strongly affect the derived PDS slope, artificially increasing the power at high frequencies and introducing spurious quasi-periodic oscillations

(QPOs) (Tagliaferri et al. 1996). In order to decrease the effect of data gaps in determining the PDS, we adopt the gap filling procedure defined as "running mean gap filling" in XRONOS. This method replaces the data gaps with the moving average of the light curve calculated in our cases over a duration of about 1.5 hour. In this way, the gaps are bridged in a smooth way, which not only simulates real events but also reduces the bias introduced by the window function. We also determined *a posteriori*, by considering a somewhat different duration (e.g., 2 hours), that the slope of the PDS is rather insensitive to the filling duration over which the running mean is calculated. This indicates that the running mean could follow the light curve behavior on time scales of hours as long as the gap filling duration is substantially shorter than the whole interval and longer than the data gaps, so that the gap center could be "linked" with the running mean from a relatively high number of points and the statistical fluctuations are reduced.

4.6 Structure function

The calculation of the PDS is in fact extremely difficult with unevenly sampled data, in particular when large gaps are unavoidable in a low-Earth satellites such as *Beppo*SAX and, in particular, interruption during observations. We thus would like to take another method, structure function (SF) which gives information similar to PDS but have advantages with unevenly sampled and nonperiodic data, to characterize the variability of a light curve.

Simonetti, Cordes & Heeschen (1985) firstly introduced the concept of SF into the field of astronomy. The first order SF of a time series $x(t)$ at a time scale "τ" is defined as:

$$SF(\tau) = \frac{1}{N}\sum_{i=1}^{N}[x(t+\tau) - x(t)]^2 \tag{4.19}$$

In fact, the SF is a measurement of the mean value of the flux differences, $x(t+\tau) - x(t)$, of all pairs, N, with time difference τ over a interval of $\tau - \Delta t/2 < \tau < \tau + \Delta t/2$ for a specific binning pattern Δt (equally or logarithmically binned). Thus a SF will be a function of time scale τ. The errors are simply calculated by the standard deviation of flux differences of all pairs in a bin (but see Simonetti, Cordes & Heeschen 1985 and Cagnoni, Papadakis & Fruscione 2000 for the problem of such errors).

The SF analysis is a very simple, convenient tool to analyze a time series and determine several important properties of a light curve. While it suffers from the

same limitations as the PDS analysis, it has nevertheless some advantages, and presents some important features of the time series in a very intuitive way. It can therefore provide some simple quantitative information on the time series. Any deviation from a plateau is indeed a signature of true variability in the light curve, In particular the SF can give an indication that all time scales may be resolved by the curve "turning over". We recall here its most important features, with emphasis on the parameters brought up by the SF:

1. A "typical" SF is characterized by two time scales at short and long time scales, namely minimum and maximum time scales, $\tau_{\rm min}$ and $\tau_{\rm max}$, respectively, and the region between them is linked by a curve, $SF(\tau) \propto \tau^{\beta_{\rm SF}}$, whose slope depends on the nature of the intrinsic variation of the source.

2. Below $\tau_{\rm min}$ the SF is a plateau, and its value is $2\sigma^2_{\rm noise}$. It thus provides an experimental estimation of the measurement noise.

3. Above $\tau_{\rm max}$ the SF flattens again, and its value is $2 \times (\sigma^2_{\rm source} + \sigma^2_{\rm noise})$.

The SF of a time series is related to its total variance $\sigma^2_{\rm total}$ and autocorrelation function (ACF):

$$SF(\tau) = 2 \times \left(\sigma^2_{\rm total} - ACF(\tau)\right) \tag{4.20}$$

More importantly, there are simple correspondences between the SF and the PDS. If the PDS has a cutoff frequence $f_{\rm max}$ at high frequency, and a break frequency $f_{\rm min}$ at low frequency, and $P(f) \propto f^{-\alpha_{\rm PDS}}$ between them, then there are relationships:

$$f_{\rm min} = \frac{1}{\tau_{\rm max}} \tag{4.21}$$

$$f_{\rm max} = \frac{1}{\tau_{\rm min}} \tag{4.22}$$

$$\alpha_{\rm PDS} = \beta_{\rm SF} + 1 \tag{4.23}$$

4.7 Cross correlation function

The intensive monitorings with high time resolution and long duration allow detailed measurements of the inter-band cross correlation properties, and in particular to make quantitative estimates of the degree of correlation and of any lags between variations at different X-ray wavelengths. Two cross correlation methods, namely

the Discrete Correlation Function (DCF) and Modified Mean Deviation (MMD), are applied. Throughout the thesis, a positive lag indicates the lower energy X-rays lagging the higher energy ones (**soft lag**), while negative one indicates the opposite (**hard lag**).

4.7.1 DCF

The DCF is analogous to the classical correlation function (e.g., Press et al. 1992, which requires evenly sampled data) except it can work with unevenly sampled data. The DCF technique was described in detail by Edelson & Krolik (1988). Here we show how it works in our code.

We assume that the two unevenly sampled light curves, $x_1(t_i)$ and $x_2(t_j)$, have the mean, $\bar{x}_1$ and $\bar{x}_2$, and standard deviation, σ_1 and σ_2, respectively. First, we compute unbinned DCF (UDCF) between each data pair from the two light curves. This is calculated and weighted by the observational errors, $\sigma_1(i)$ and $\sigma_2(j)$, and standard deviation, σ_1 and σ_2, in the time domain as

$$UDCF_{ij} = \frac{(x_1(t_i) - \bar{x}_1)(x_2(t_j) - \bar{x}_2)}{\sigma_1(i)\sigma_2(j)\sigma_1\sigma_2} \tag{4.24}$$

The $UDCF_{ij}$s are then binned with width τ in a way such that all UDCF$_{ij}$s, of which the time difference $\Delta t_{ij} = t_i - t_j$ belong to $[T_{\rm lag} - \tau/2, T_{\rm lag} + \tau/2]$, are averaged to a DCF($T_{\rm lag}$) at each time lag $T_{\rm lag}$:

$$DCF(T_{\rm lag}) = \frac{1}{N} \sum UDCF_{ij} \tag{4.25}$$

The DCF advantages are that it uses all the data points available, does not introduce new errors through interpolation, and calculates a meaningful error estimate:

$$\sigma_{DCF(T_{\rm lag})} = \frac{1}{N-1} \sum_{i=1}^{N} \{[UDCF_{ij} - DCF(T_{\rm lag})]^2\}^{1/2} \tag{4.26}$$

4.7.2 MMD

In order to check the results suggested by the DCF technique, we perform a similar analysis by using the MMD method introduced by Hufnagel & Bregman (1992). The MMD considers the mean deviation of the two cross correlated time series as the correlation estimator and the minimum value of the MMD should correspond to the best correlation point (lag). Thus, unlike the DCF, it cannot be used to estimate the significance of the correlation between different wavelengths. For comparison, we show MMD along with DCF under the terminology of cross-correlation function,

while itself is not a true cross-correlation function. The MMD is calculated in a similar way as DCF.

First unbinned MMD (UMMD) is calculated between any pairs from the two light curves:

$$UMMD_{ij} = \frac{(x_1(t_i) - \bar{x}_1) - (x_2(t_j) - \bar{x}_2)}{\sigma_1(i)\sigma_2(j)\sigma_1\sigma_2} \tag{4.27}$$

$UMMD_{ij}$s are then binned in the same way as $UDCF_{ij}$s but computed as follows:

$$\Delta MMD(T_{\rm lag}) = \frac{1}{N}\sum UMMD_{ij} \tag{4.28}$$

$$MMD(T_{\rm lag}) = \left[\frac{1}{N}\sum(UMMD_{ij} - \Delta MMD(T_{\rm lag}))\right]^{1/2} \tag{4.29}$$

where N is the number of matching pairs. The error on MMD($T_{\rm lag}$) is similarly obtained by

$$\sigma_{MMD} = \frac{1}{N-1}\left[\sum(UMMD_{ij} - \Delta MMD(T_{\rm lag})\right]^{1/2} \tag{4.30}$$

4.7.3 More on DCF and MMD

We bin the original light curves and fix the DCF/MMD resolution according to the following general criteria:

1. The bin sizes in both the light curves and the DCF/MMD are in general 3 times smaller than any possible lag;
2. The bin size should also be as large as possible to reduce the error on the DCF/MMD.

In order to quantify any time lag, we fit the DCF/MMD with a Gaussian function plus a constant, and take the Gaussian centroid, rather than the DCF/MMD peak/dig, as the lag between the two energy bands (see arguments by Edelson et al. 1995 and Peterson et al. 1998). The error on the time lag is normally determined from the 1σ uncertainties (68% confidence level) of the Gaussian peak/dig parameter obtained by minimum χ^2 of the DCF and MMD to a Gaussian plus constant functions. The two main advantages of this are:

1. The Gaussian fit takes into account the overall symmetry of the DCF/MMD distribution around the peak/dig, reducing the possibility of spurious lags due to a particular DCF/MMD point that could originate from statistical errors;

2. We found that – under the two conditions mentioned above – the lag and its uncertainty derived from a Gaussian fit are insensitive to the bin sizes of both the light curves and the DCF/MMD.

It should also be noted that a Gaussian fit – although representative of the peak/dig position and dispersion for the DCF/MMD – does not necessarily provide a statistically adequate fit to these functions. In particular this will happen when the DCF/MMD distribution is not well represented by a Gaussian, the lag and its error determined from the DCF/MMD are sometimes ambiguous. A non-smooth DCF/MMD distribution will accompany serious changes of the Gaussian peak/dig (i.e., lag) when fitting range changes. This will not happen when fitting to a smooth distributed DCF/MMD, and we believe the fitting results.

4.7.4 Monte Carlo simulations

As suggested by Peterson et al. (1998), the uncertainty on the cross-correlation lag is dependent on both the flux uncertainties in individual measurements and the observational sampling uncertainties of the light curves. So, the statistical significance of the detection of a lag can not be assessed just by a cross-correlation analysis. In order to test the dependence of our findings on photon statistics, in this section we apply to our data the model-independent Monte Carlo simulation method introduced by Peterson et al. (1998). Because of the uncertainties just mentioned, the method considers "flux randomization" (FR) and "random subset selection" (RSS). FR assumes that the errors on fluxes resulting from the total photon number in a bin (several hundred photons in our cases) are normally distributed. Thus FR just takes each real flux x_i and modifies it by adding a random Gaussian deviation based on the quoted error σ_i for each data point of the light curves. So, the modification of each data point is statistically independent of each of the others, and therefore the dependence of lags on flux errors can be easily assessed through the FR simulations. RSS tests instead the sensitivity of a cross correlation lag by considering only subsets of the original light curves with no dependence on previous selection but still preserving the temporal order of the data points. The probability of random removal of any data point is $\sim 1/e \simeq 0.37$ which is a Poisson probability. Thus each RSS realization is based on a randomly selected subset which is typically $\sim 37\%$ smaller than the real data set. Peterson et al. (1998) argue that RSS gives a fairly conservative estimate of the uncertainties due to sampling. We thus take the combination of FR and RSS in a single simulation to test together the sensitivity of the cross-correlation lags on flux uncertainties and sampling characteristics. We

apply the DCF and the MMD to each FR/RSS Monte Carlo realization to determine individual lags obtained from the centroid of the Gaussian fit to each independent realization. The same process is repeated 1000 times to build up a cross-correlation peak distribution (CCPD; Maoz & Netzer 1989), which is not necessarily a normal distribution (e.g., Peterson et al. 1998). From the CCPD we can determine the probability that a given lag falls in some particular likelihood range, e.g., 68% or 90% confidence ranges. In addition, we tested that the results are insensitive to the bin sizes of both the light curves and DCF/MMD.

4.8 X-ray spectral analysis

We do not intend to do a comprehensive X-ray spectral analysis for our data, but we indeed compute the mean flux when comparing variability parameters among individual observations from different detectors and various sources. The X-ray spectrum is simply modeled as a single power law plus a free absorbing column N_H. We are aware that this is not a physical model in most cases, nontheless, this model is a convenient representation of the curved spectrum which may significantly reduce the fitting χ^2 compared to the model of a single power law plus the fixed Galactic N_H, and can produce a reliable flux estimation.

4.9 Fitting

It will be stated that a model (either a power law or Gaussian) has been **fit** to the dataset of the PDS, SF, DCF/MMD and X-ray spectrum (also §4.2). This refers to the processes of parameter estimation and model selection in which the data are compared to a prediction calculated with a parameterizable mathematical model, usually through a numerical **fit statistic**. The model is often derived from some physical theory, but is sometimes a strictly empirical description of the data.

The model parameters then are varied to find the values of parameters that give the most desirable fit statistic. These values are referred as the **best fit parameters**, and the model made up of the best-fit-parameters is considered to be the **best fit model**.

χ^2 statistic is the most common fit statistic, appropriate for measurements which are drawn from a normal (Gaussian) distribution, and defined as follows:

$$\chi^2 = \sum_{i=1}^{N} \frac{(x_i - m_i)^2}{\sigma_i^2} \tag{4.31}$$

where x_i with uncertainty σ_i is the dataset to be fitted, and m_i is the predicted value of a model at the corresponding point of x_i.

Once a "best fit" model is obtained, one must ask two questions:

1. How confidence one dataset is produced by the best-fit-model, known as the **goodness-of-fit**. As a general rule, one wants the **reduced** χ^2, $\chi^2_\nu = \chi^2/\nu$, to be approximately equal to one ($\chi^2 \sim \nu$). A χ^2_ν much greater than one indicates a poor fit, while a χ^2_ν much less than one indicates that the errors on the dataset have been over-estimated.

2. For a given best-fit parameter, one must determine the range of values within which one can be confident the true value of the parameter lies. The answer to this question gives on the **confidence interval** for the parameter. The confidence interval for a given parameter is computed by varying the parameter value until the χ^2 increase by a particular amount above the minimum, or "best-fit" value. For example, $\Delta\chi^2$ is 1.00 and 2.71 for one given parameter at 68% and 90% **confidence level** (Press et al. 1992).

4.10 Software

The light curves and PDS are analyzed with the time analying package XRONOS, and all other analyses are calculated with the home-made codes. Most fits are performed with package QDP, and spectral fits are performed with package XSPEC. We do not discuss the details of these softwares and would like to refer to the relevant references.

4.11 *Beppo*SAX overview

For a detailed description of the Italian/Dutch *Beppo*SAX mission we refer to Boella et al. (1997a) and references therein.

The *Beppo*SAX payload (Boella et al. 1997a) consists of four Narrow Field Instruments (NFIs) which point in the same direction, namely one Low Energy Concentrator Spectrometer (LECS) sensitive in the 0.1−10 keV range (Parmar et al. 1997), and three identical Medium Energy Concentrator Spectrometers (MECS) sensitive in 1.5−10 keV band (Boella et al. 1997b). Both the LECS and MECS detectors are Gas Scintillation Proportional Counters (GSPC) and are in the focus of the four identical X-ray telescopes. There are two more collimated instruments: the High Pressure Gas Scintillation Proportional Counter (HPGSPC) (Manzo et al. 1997)

and the Phoswich Detector System (Frontera et al. 1997), which are not however suitable to perform temporal analysis because of the high background and limited statistics. Therefore, for the timing analysis, only LECS and MECS data are used.

The MECS was composed at launch by three identical units. On 1997 May 6 a technical failure caused the switch off the unit MECS 1. All observations after this date are performed with two units (MECS2 and MECS3).

The starting point of our analysis is based on linearized events files for the LECS and the MECS experiments, and the events from the two or three units of MECS are merged together to improve the photon statistic. These events files, together with appropriate background event files, are produced at the *Beppo*SAX Science Data Center (REV 0.2, 1.1 AND 2.0).

>>>>>>

Chapter 5

MKN 421

In the previous chapter we have discussed the data analysis techniques related with our temporal analysis. The long and uninterrupted light curves of blazars with high time resolution observations by *Beppo*SAX are rather suitable to carry on comprehensive temporal studies. Moreover the energy band (0.1–10 keV) achieved by *Beppo*SAX is broader than previous observations (e.g., Sembay et al. 1993), this allow us to conduct temporal analysis for "real" soft X-rays. Starting from this chapter, followed by the other two chapters, we will perform a comprehensive temporal analysis on MKN 421, PKS 2155−304, and blazars as a class, respectively.

We first perform in this chapter detailed timing analysis for MKN 421, which is one of the well-observed sources by *Beppo*SAX. First is a short introduction to MKN 421 in §5.1; we briefly summarize the observations in §5.2; the light curves and fundamental variability analysis are presented in §5.3, followed by the SF analysis in §5.4; Probable variability periodicity is examined in §5.5; in §5.6 we carry out comprehensive cross-correlation analysis with detailed Monte Carlo simulations to determine the uncertainties on inter-band lags, and energy-dependence of time lags is studied in §5.7; We probe the physical implications from the results in §5.8.

5.1 Introduction

MKN 421 ($z = 0.031$) is the brightest blazar at UV, X-ray and TeV wavelengths, and also the first blazar detected in these high energy bands. MKN 421 have received particular attention as an ideal source for a detailed temporal and spectral variability studies in the broadest spectral ranges, which provide a good chance to understand the physical processes operating in blazar jets. Extensive multiwavelength monitoring campaigns have been conducted in 1994, 1995, and 1998 (see §3.3 for details). The main findings are the close correlations among light curves at dif-

ferent energies and, in particular, the pronounced temporal and spectral evolution during multiple flares seen in the X-rays by ASCA and *Beppo*SAX (Takahashi et al. 1996, 2000; Fossati et al. 2000a,b).

5.2 Observations

MKN 421 has been observed by *Beppo*SAX for four years between 1997 and 2000, with several days pointing for each year. In particular, a long look was performed in 2000, which revealed unprecedented activity of MKN 421. The journal of the observations is given in Table 5.1.

Table 5.1: Observational Journal

Date(UTC)	Net Exposure(ks)		Archive #
	LECS	MECS	
1997			
1997/04/29 04:02:27–1997/04/29 14:42:06	11.6	21.8	50032001
1997/04/30 03:19:29–1997/04/30 14:42:06	11.4	24.1	50032002
1997/05/01 03:17:56–1997/05/01 14:42:06	11.2	23.8	50032003
1997/05/02 04:10:33–1997/05/02 09:41:06	4.4	11.4	50016002
1997/05/03 03:24:43–1997/05/03 09:41:06	4.3	11.7	50016003
1997/05/04 03:25:08–1997/05/04 09:45:06	4.9	12.2	50016004
1997/05/05 03:32:21–1997/05/05 09:45:06	5.0	11.9	50016005
1997/05/07 04:47:45–1997/05/07 10:27:06	6.0	...	50016006[a]
1998			
1998/04/21 01:52:32–1998/04/22 03:13:48	23.6	29.6	50686002
1998/04/23 00:27:12–1998/04/24 06:37:04	27.2	34.7	50686001
1998/06/22 07:16:21–1998/06/23 02:21:52	11.1	32.5	50765001
1999			
1999/05/04 18:16:57–1998/05/08 03:21:50	50.0	111.2	50918001
2000			
2000/04/26 17:36:35–2000/04/28 23:17:33	49.9	57.6	512820011
2000/04/28 23:17:34–2000/04/30 03:04:14	22.2	25.7	512820012
2000/04/30 03:04:14–2000/05/03 02:13:02	58.9	33.0	512820013
2000/05/09 03:53:30–2000/05/12 08:08:42	62.3	131.6	512820014

[a]On 7 May 1997 MECS 1 had a fatal failure, only LECS data are available, and they are not studied in this chapter.

1997: *Beppo*SAX daily pointed MKN 421 for several hours between April 29 and May 7 in the 1997 campaign. MECS data are not available for May 7 because of the failure of the MECS detector unit 1 on May 6. Here we will not consider the LECS data of this last day of the 1997 campaign, because unfortunately LECS data alone do not provide useful spectral and variability information. The total *net* exposure time (excluding the May 7 data) was $\sim$ 52 and $\sim$ 117 ks for LECS and MECS respectively, while the on-source time coverage calculated as the sum between each starting and stopping time is $\sim$ 58 hrs, and the observational duration is $\sim$ 7 days in this campaign.

1998 April: on April 21–23 *Beppo*SAX observed MKN 421 as part of a long monitoring campaign involving *Beppo*SAX, ASCA, *Rossi*XTE, EUVE, and ground based TeV observatories (Maraschi et al. 1999; Takahashi et al. 2000). The *Beppo*SAX observation comprised two distinct long pointings, about one day each, started respectively on April 21 and 23, respectively. The total *net* exposure time for MECS telescopes has been of 64.3 ks and the LECS one adds up to 50.8 ks, while actual on-source time coverage is $\sim$ 55.5 hrs.

1998 June: on 1998 June 22, *Beppo*SAX also observed MKN 421. The on-source time coverage is $\sim$ 19 hrs, while the *net* exposure time is 11.1 and 32.5 ks in the LECS and MECS respectively.

1999: *Beppo*SAX continuosly monitored MKN 421 for about three days between May 4 and 8 in 1999, yielding a *net* exposure time of 50.0 and 111.2 ks for the LECS and MECS respectively.

2000: the 2000 campaign for MKN 421 is a long look between April 26 and 12 May, including 4 separate pointings. There was about 6 days gap between the first three pointings and the last one. Furthermore, unfortunately, MECS data are not available during the most part of the third pointing. The total *net* exposure time is 193.3 and 247.9 ks for the LECS and MECS respectively.

* * *

Results on the 1997 and 1998 campaigns have been presented by Guainazzi et al. (1999), Malizia et al. (2000), and Fossati et al. (2000a,b), respectively, where the details and motivation of the observations are also given. In this chapter we reanalyzed those data along with the new ones, applying the same techniques, in order to obtain a homogeneous set of results, necessary for a direct comparison. Furthermore we also perform further timing analysis which the above analyses did not include.

5.3 Variability analysis

In this section we present in time order the light curves for the observations mentioned in last section and study the fundamental X-ray variability characteristics of MKN 421.

To study the temporal variability in detail, light curves have been accumulated for different energy bands over various time scales. The input photon lists were extracted from the full events list by selecting events in a circular region centered on the position of the point source. In the case of MKN 421 (bright and soft source), the used extraction radii are 8 and 6 arcmin for LECS and MECS respectively, to be sure that > 95 % of the photons are collected in the whole energy range (see, e.g., Fiore, Guainazzi & Grandi 1999 for details).

To test for confidence of the variability and compare the variability amplitude in the soft and hard X-ray bands, the light curve is binned over 1000 s in the 0.1–2 keV (from the LECS) and 2–10 keV (from the MECS). This ensure that sufficient counts are obtained in each time bin for Gaussian statistics to be appropriate. We are then able to test for variability by means of a χ^2 test against the hypothesis that the flux is constant, and quantify the variability amplitude and the minimum time scale.

1997

The light curves in the 0.1–1.5 keV (LE), 1.5–3.5 keV (ME1) and 3.5–10 keV (ME2) bands with their hardness ratio, ME1/LE (HR1) and ME2/ME1 (HR2) are shown in Figure 5.1 from top to bottom panels, respectively. To study clearly variability characteristics, the 7 single pointings in 1997 are shown together with time order preserved. It is clear that the source showed a high degree of flux variability, while there are no complete flares detected because of the observational constraints, i.e., a few hours each pointing, which is smaller than the characteristic time scale of MKN 421 day-to-day flare events as estimated from the SF analysis which we will study in §5.4. It is worth noticing, however, that the fluxes offsets are evident from one to another pointing, suggesting daily flare events of the source, with possibly a major flare between the third and fourth pointing.

The χ^2 calculated is 44.9 and 127.4 in the 0.1–2 keV and 2–10 keV bands respectively, this shows variability at greater than 99.9% confidence. The *rms* fractional variability amplitude $F_{\rm var}$ is 0.20±0.08 and 0.29±0.10 for the light curve in the 0.1–2 keV and 2–10 keV bands respectively, showing that the amplitude of variability is larger at higher energies, as commonly observed in blazars synchrotron component at energies above the synchrotron peak frequency (e.g., Ulrich, Maraschi & Urry 1997). We also search the minimum doubling time scale T_2 from the whole light

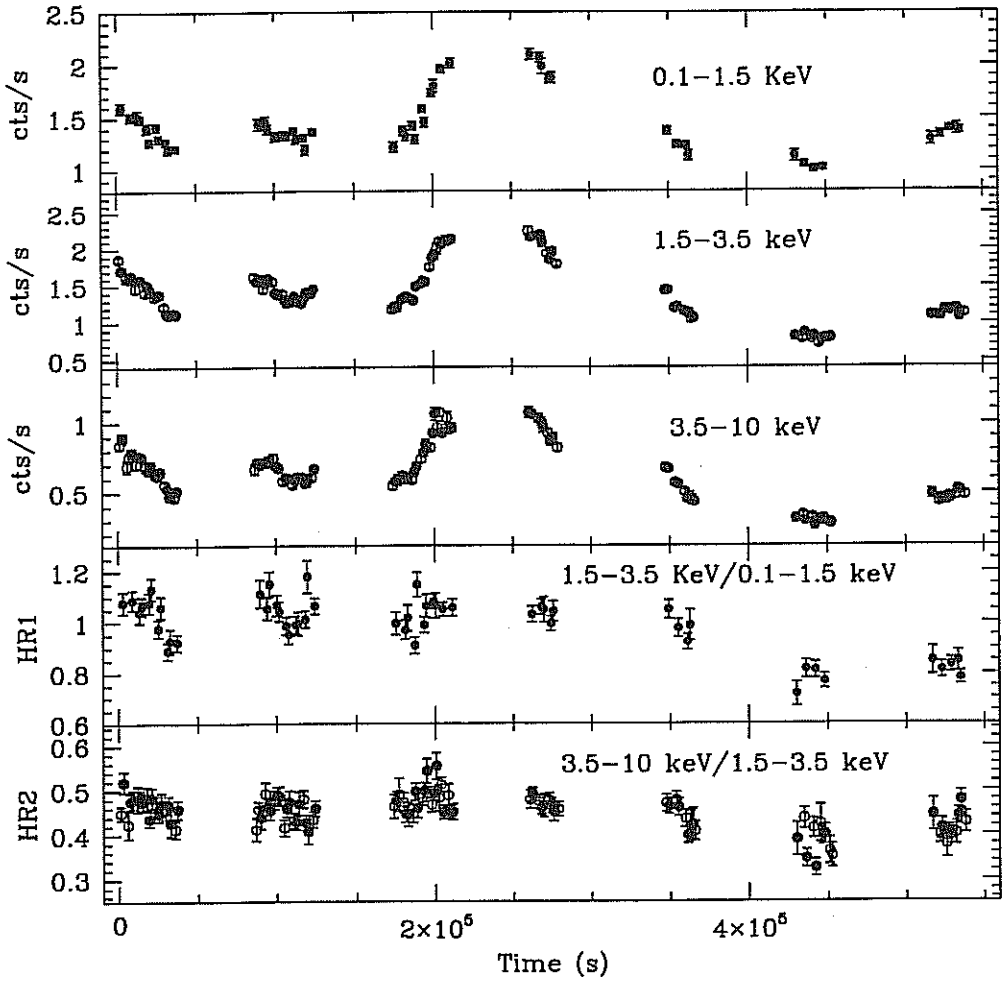

Figure 5.1: Light curves and hardness ratios of *Beppo*SAX 1997 April 29 – May 5 observations. Data are rebinned in 1500 s. The reference time is 1997/04/29 (TJD=10567) 04:00:00 UT. From top to bottom panel: light curve in the 0.1−1.5, 1.5−3.5 and 3.5−10 keV bands, respectively, and hardness ratio between the 1.5−3.5 and 0.1−1.5 keV bands (HR1) and between 3.5−10 and 1.5−3.5 keV bands (HR2). Note that the temporal coverage of the LECS is much more sparse than that of the MECS. The simultaneous data points between LECS and MECS are indicated by filled symbols.

curve, which is 16.9±3.3 ks and 16.1±2.9 ks in the 0.1–2 keV and 2–10 keV band respectively, showing that the time scales in both bands are statistically compatible.

The temporal evolution of hardness ratios normally track the behavior of the light curves, while some exceptions are clear, possibly due to weak photon statistics in much less exposured bins. We also performed a detailed analysis for the spectral evolution in this campaign by using a continuously curved spectral model (see Fossati et al. 2000b). The analysis shows that there is a clear relation between the flux variability and the spectral parameters. Moreover, important result is the correlation between changes in the brightness (even the small ones) and shifts of the synchrotron peak position, as the latter carries direct information on the source physical properties.

The spectral analysis shows a factor of $\sim$ 2 flux variations in the 0.1–2 keV band, and a factor of $\sim$ 3 flux variations in the 2–10 keV band. The average flux is 1.83×10^{-10} and 0.83×10^{-10} erg cm^{-2} s^{-1} in the 0.1–2 keV and 2–10 keV band respectively.

1998

The light curves in the LE, ME1 and ME2 bands with their hardness ratios are shown in Figure 5.2 and 5.3 for the April and the June campaign, respectively.

April campaign: the April observation comprise two different parts. The source is very bright, the average fluxes during this campaign is 4.20×10^{-10} and 2.53×10^{-10} erg cm^{-2} s^{-1} in the 0.1–2 keV and 2–10 keV band respectively, at least doubling the 1997 average fluxes. A single complete flare is well defined at the beginning of the campaign (#1), and after about one day observational gap, the source is characterized by a long time scale flux decaying with some flickers superimposed (#2). It is again worth noticing, however, that the positive flux offset of the beginning of April 23 with respect to the end of the April 21 suggests the presence of a second flare occurring between the two pointings. This seems to be also confirmed by the *Rossi*XTE All Sky Monitor (ASM) light curve (Fossati et al. 2000a).

The concave feature of decay phase is visible in both #1 and #2. We further performed a detailed decay time scale analysis by fitting the post–flare light curves with an exponential decay superimposed to a constant (quasi–steady) flux level, see Fossati et al. (2000a) for more details. We summary here the main conclusions obtained: (1) the decay time scales depend on the presence/absence of a contribution by a non variable component. In the cases with baseline, the decay time scales range between 30 and 45×10^3 s, and *do not* show a clear (if any) relationship with the energy, suggesting an achromatic post–flare evolution. On the contrary, in the case

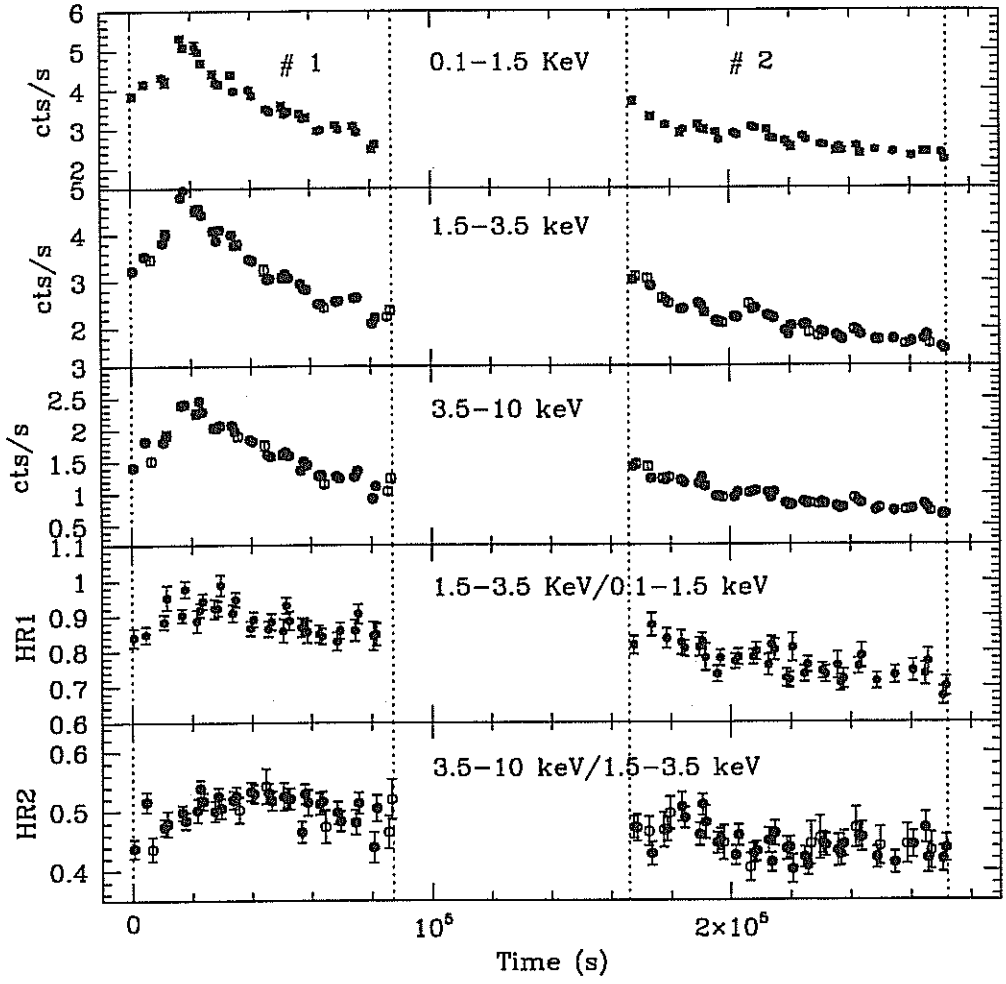

Figure 5.2: Light curves and hardness ratios of *Beppo*SAX 1998 April observations. Data are rebinned in 1000 s. The reference time is 1998/04/21/ (TJD=10924) 02:00:00 UT. The symbols have the same meaning of those in Figure 5.1.

of pure exponential decay the time scales follow a weak inverse relationship with the energy, $\tau \propto E^{-0.18\pm0.02}$; (2) the variability amplitude estimated from the fitting positively correlates with the energy, as reported in many cases for HBLs (e.g., Sambruna et al. 1994; Ulrich, Maraschi & Urry 1997); (3) Possible asymmetry in the rise/decay phases: the flare seems to be symmetric at the energies corresponding (roughly) to the peak of the synchrotron component, while it might have a faster rise at higher energies.

The χ^2 computed is 148.6 and 245.8 in the 0.1–2 keV and 2–10 keV bands respectively, strongly showing variability at greater than 99.9% confidence. The *rms* fractional variability amplitude $F_{\rm var}$ is 0.25±0.11 and 0.34±0.13, and the minimum doubling time scale T_2 is 30.3±2.9 and 17.7±2.2 ks for the 0.1–2 keV and 2–10 keV band light curve respectively, showing again that the source is more variable with shorter time scale at higher energies.

The temporal evolution of hardness ratios correlates well with the one of the light curves, but with a clear delay in #1 between the maximum of the hardness ratios with respect to the maximum of the flux, this is an evidence that the hard X-ray photons lag the soft ones (hard lag), which will be quantified by the detailed cross-correlation analysis (see §5.6 and 5.7). It is worth noticing that this is *opposite* to the normal variability behavior expected in the synchrotron cooling case, that is, a soft lag is expected in a way that the hardness ratios reach the maximum before the flux does. This normal behavior is clearly seen in the 1997 campaign of PKS 2155−304 by *Beppo*SAX (see the # 2 flare of Figure 6.2 in next chapter).

The behavior that the flux variability at higher energies lag the one at lower energies can be well identified by the "anti-clockwise loop" in the flux–spectral plane. This was done by the detailed spectral fitting by using an intrinsic curved spectral model (see Figure 5 of Fossati et al. 2000b). Conversely, a soft lag is identified by the "clockwise loop" in the flux–spectral plane (see Takahashi et al. 1996 for MKN 421; Kataoka et al. 2000 for PKS 2155−304).

June campaign: the June state is very close to the April one. The average June fluxes is 3.47×10^{-10} (0.1–2 keV) and 1.69×10^{-10} erg cm^{-2} s^{-1} (2–10 keV). The variability characteristics can be summarized in three parts. #1 is a decay phase with a time scale of $\sim 2 \times 10^4$ s, followed by a low amplitude flare (a factor of 25%) with similar time scale (#2). A relative steady phase (#3) is detected at the end of the campaign.

The variability during this short period is dominated by the relatively weak variations. To quantify it, we compute the χ^2, 5.0 and 11.3 in the 0.1–2 keV and 2–10 keV energies, but still at greater than 99.9% confidence level. The corresponding

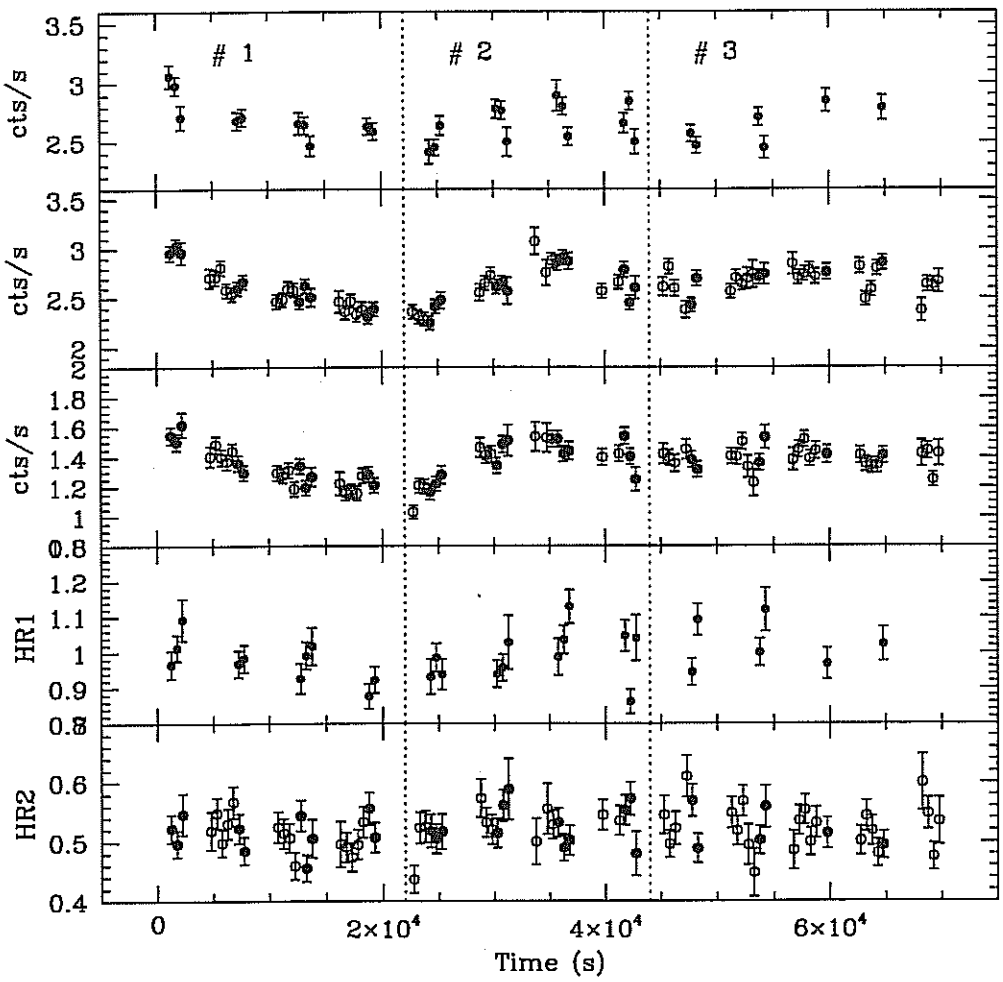

Figure 5.3: Light curves and hardness ratios of *Beppo*SAX 1998 June observations. Data are rebinned in 500s. The reference time is 1998/06/22 (TJD=10986) 07:00:00. The symbols have the same meaning of those in Figure 5.1.

rms fractional variability amplitude $F_{\rm var}$ is 0.040±0.03 and 0.06±0.03, and minimum doubling time scale is 83.6±15.8 and 32.5±5.5 ks. These values show that MKN 421 is much less variable with longer time scales in June than in April, while both periods have the similar brightness level.

The temporal evolution of hardness ratios HR1 correlate with the light curves, which is not clear in the HR2.

1999

We show the light curves and their hardness ratios in Figure 5.4. The source is in a relative faint state during this period, and have the steepest average spectra when compared with those in 1997, 1998 (and 2000, see below).

The variability can be characterized by three different parts, stated as #1, 2 and 3 in Figure 5.4. A flare with low amplitude is possible for #1, but the "actual" flare part was lost due to the observational gap. #2 part starts from a weak "recovery" from the minimum of #1 decay phase, then characterized by a relative "stable" phase with fluctuations superimposed. It is interesting to note that these flickers are increasing more defined as the energy increasing. A very pronounced complete flare was detected at the end of the period, i.e., #3 part. This flare includes the rising (with a gap at the middle of the rising phase) and decaying phase; but with different time scale: $\sim 6 \times 10^4$ s for the rising phase, and $\sim 4 \times 10^4$ s for the decay one. Moreover this flare seems to be different from that of 1998 #1, in particular the decay phase shows "convex" features.

The energy-dependent variability characteristics are compared by calculating the same variability parameters as above. The χ^2 is 132.1 and 199.4; $F_{\rm var}$ 0.28±0.11 and 0.42±0.15; and minimum T_2 22.1±4.2 and 10.4±2.0 ks for the 0.1–2 keV and 2-10 keV energy bands. These values indicate the same variability behavior as the above analysis: the source is variable at greater than 99.9% confidence level, the amplitude of variability is larger and time scales shorter at higher energy than at the lower energy.

Another clear feature of this campaign is that the temporal evolution of both the HR1 and HR2 hardness ratio correlate well with the light curves, as seen from the last two panels of Figure 5.4, indicating that the X-ray spectrum tends to steepen as the source becomes fainter. The comparison of hardness ratio shows that the spectra are steeper than those in previous campaigns.

2000

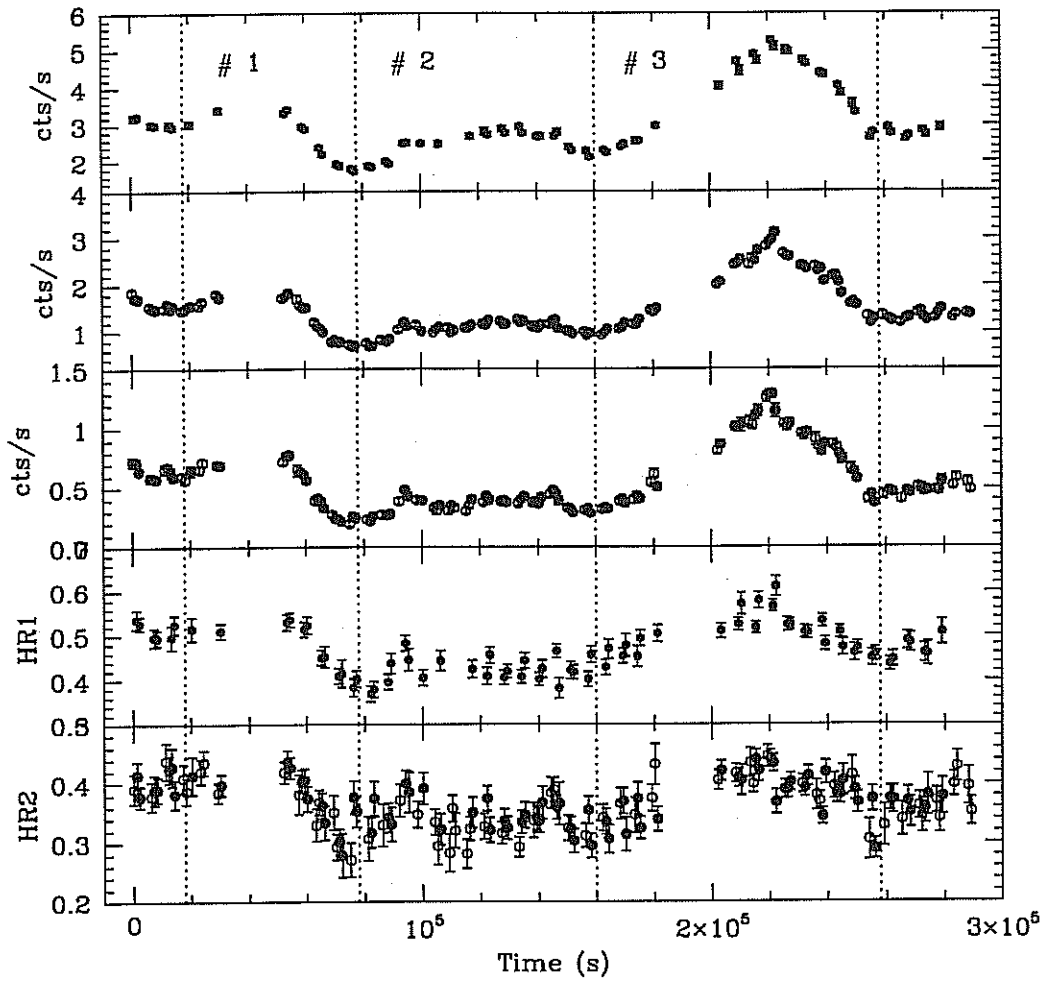

Figure 5.4: Light curves and hardness ratios of *Beppo*SAX 1999 observations. Data are rebinned in 1000s. The reference time is 1999/05/04/ (TJD=11302) 19:00:00 UT. Panels and symbols have the same meaning of those in Figure 5.1.

To show clearly the extreme variability details obtained in the 2000 campaign, we show the light curves and hardness ratio in Figure 5.5 and Figure 5.6 for the first and second part of the 2000 observations.

2000a: The source is much brighter than any previous periods between 1997 and 1999.

The source showed very high degree of activity throughout the campaign. The most important is that multiple pronounced flares were detected, occurring on time scale of about one day or less, confirming the same extreme phenomena occurred in 1998 observed by ASCA (Takahashi et al. 2000). The flares are almost symmetric for most of cases, implying that the dominant time scale is the light-crossing time through the emitting region. However the various shapes are also present among these flares and light curves in the different energies, possibly indicating a various convolution of cooling and light-crossing time scales. The decay phase of #1 flare shows a convex feature, which is increasingly more defined as the energy increases. A double peak is clear in the #2 flare, again more increasingly defined with higher energies. The dip between #1 and #2 is clear in the ME1 and ME2 bands, but not present in the LE band, which is a long steady phase in a high state (above the half count rate of the maximum count rate). The shape of rising and decay phase of #3 flare is different, with convex and concave feature, respectively. The flare amplitude of these three flares are similar.

Unfortunately, the much more pronounced flare (perhaps two) was lost because of problem occurred during the observations. The gap between #4 and #5 prevent us from defining the "true" variability characteristics for this extreme outburst events. It seems that both #4 and #5 comprise a major flare, but an abrupt drop following the #4 maximum make it an isolated flare. If it were true, a rapid increase should proceed the observed #5, constructing another major flare. There is still another possibility that #4 and #5 belong to one major flare, but with double peaks superimposed. This phenomenon have been also observed in #2, (and #6 and #7 in 2000b, the second part in the 2000 campaign, see below and Figure 5.6).

More badly, the observations between #6 and #7 parts are only available for the LECS, which can not provide useful information as we have stated in the 1997 campaign. A low amplitude flare in #6 and fluctuations in #7 is present in the LE band. The negative offset at the beginning of #6 relative to the end of #5 suggests another "event" occurred. Finally, a flare (#8) with medium amplitude (within this campaign) is detected at the end of the first part of 2000 campaign.

We calculated χ^2 for this part observation, which is 74.2 and 254.3 for the 0.1–2 keV and 2–10 keV energy, clearly showing the variations at larger than 99.9%

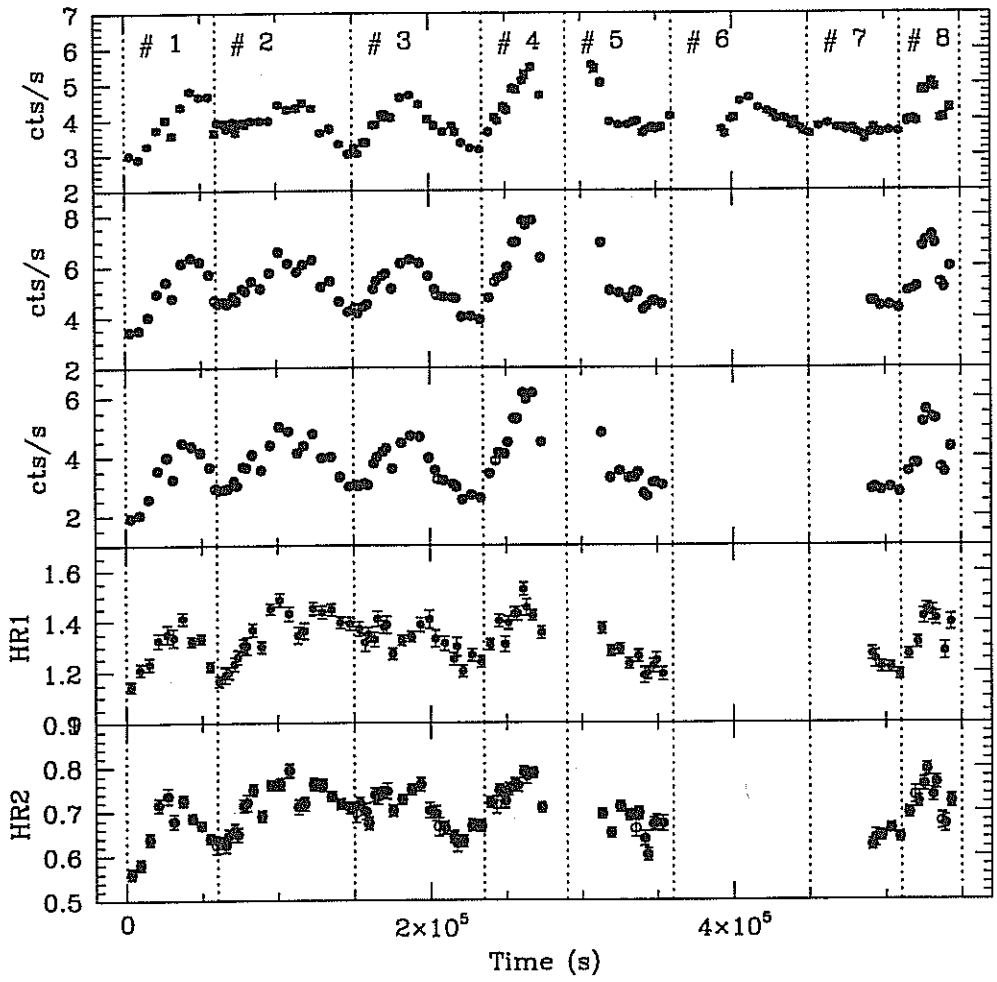

Figure 5.5: Light curves and hardness ratios of *Beppo*SAX 2000 observations (the first part). Data are rebinned in 2000s. The reference time is 2000/04/26/ (TJD=11660) 18:00:00 UT. The symbols have the same meaning of those in Figure 5.1.

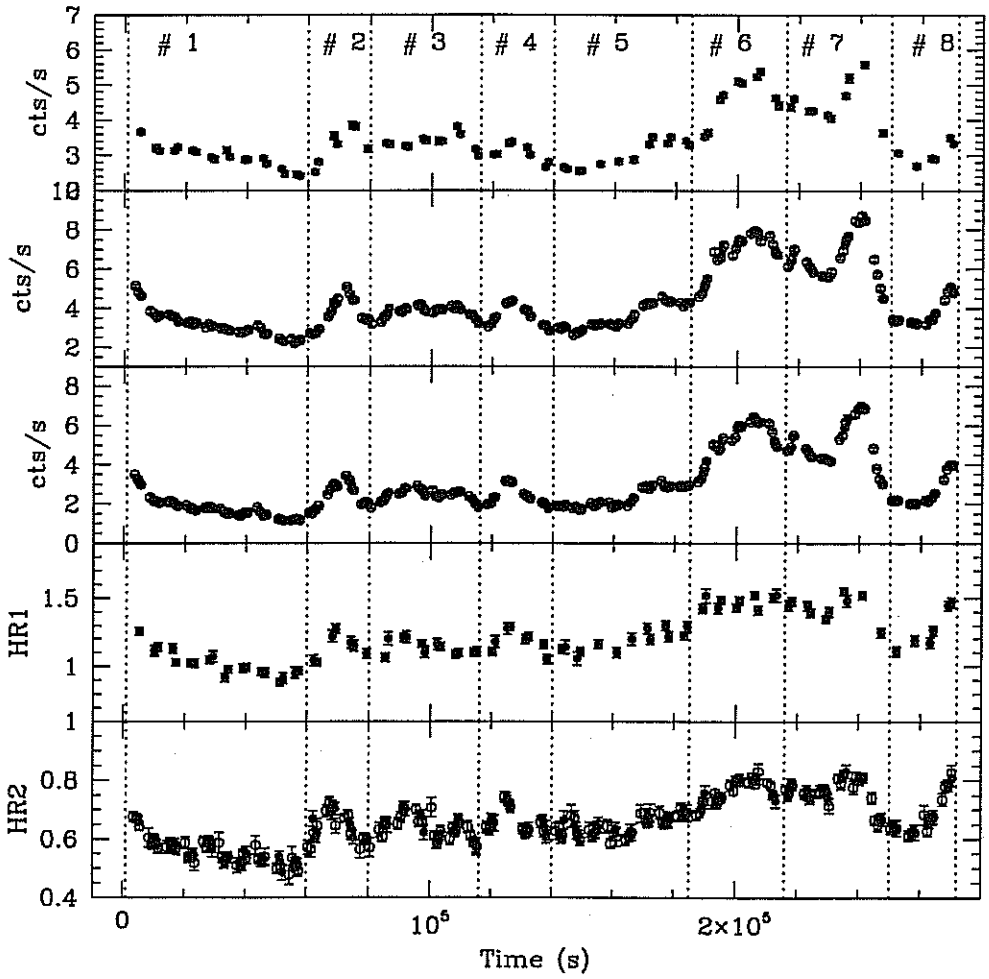

Figure 5.6: Light curves and hardness ratios of *Beppo*SAX 2000 observations (the second part). Data are rebinned in 2000s. The reference time is 2000/05/09/ (TJD=11673) 04:00:00 UT. The symbols have the same meaning of those in Figure 5.1. Note that there is a $\sim$ 6 days gap between this light curve and that of Figure 5.5.

confidence. The variability amplitude $F_{\rm var}$ is 0.14±0.05 and 0.21±0.07, and minimum T_2 14.1±1.5 and 12.3±1.7 ks in the 0.1–2 keV and 2–10 keV energy band, respectively. The characteristics of larger variability and smaller time scale with higher energy is confirmed by this long duration observations.

The temporal evolution of the hardness ratio generally follows that of the light curves, but many exceptions are present.

Finally we mention here a visible variability periodicity as seen from Figure 5.5, this issue will be analyzed in §5.5.

2000b: The second part of 2000 campaign lasting about 3 days is conducted after about 6 days of the end of the first part. This part of data just come, we will not studied them any more in this thesis. Here we show just the light curve for the second half of the campaign to illustrate once again the extreme variability detail achievable and point out different variability properties from the first part. During this period MKN 421 was consistently above its historical maximum X-ray flux, and the sharp flare in flare #7 marks the top flux, 1.2×10^{-9}ergcm^{-2}s^{-1} in the 2–10 keV band.

* * *

In this section the fundamental X-ray variability characteristics of MKN 421 from the *Beppo*SAX campaigns have been studied, focusing on the temporal evolution behavior of both the light curves and hardness ratios, and the χ^2, variability amplitude and time scale analysis in different energy bands. To compare the variability properties in various campaigns and conclude this section, the main results are parameterized in Table ??.

5.4 Structure function analysis

In last section, we have quantified the possible minimum variability time scale of MKN 421 by searching for the minimum values among the time scales over which the fluxes double. However there is still another important time scale to be determined, the maximum time scale above which the source will not show stronger variability. We call it as characteristic time scales of the source, T_c.

The long and uninterrupted *Beppo*SAX light curves (in the sense of time scale of days) present an excellent opportunity to study the temporal characteristics of the X–ray variability on time scale from the minimum detectable time scale to time scale of days, free of the possibly confusing effects of large gaps in the data. This range of time scale is very important, because the current monitorings have demonstrated

Table 5.2: Variability Parameters

band	Flux[a]	$\overline{F}$(cts/s)	F_{var}	χ^2_ν	T_2(ks)
			1997		
0.1–2	1.83	1.70	0.20±0.08	44.9(070)	16.9±3.3
2–10	0.83	1.60	0.29±0.10	127.4(136)	16.1±2.9
			1998 April		
0.1–2	4.20	3.94	0.25±0.11	148.6(067)	30.3±2.9
2–10	2.53	3.08	0.34±0.13	245.8(136)	17.7±2.2
			1998 June		
0.1–2	3.47	3.29	0.04±0.03	5.0(017)	83.6±15.8
2–10	1.69	3.14	0.06±0.03	11.3(041)	32.5±5.5
			1999		
0.1–2	....	2.60	0.28±0.11	132.1(072)	22.1±4.2
2–10	....	1.53	0.42±0.15	199.4(140))	10.4±2.0
			2000a		
0.1–2	....	5.20	0.14±0.05	74.2(189)	14.1±1.5
2–10	....	7.54	0.21±0.07	254.3(156)	12.3±1.7

[a]Flux in unit of 10^{-10} erg cm^{-2} s^{-1}.

that the variability of MKN 421 is characterized by recurrent flares on time scale of about or even less than one day.

We therefore in this section perform a structure function analysis for the light curves shown in last section. We first compute SFs of each single light curve to determine the characteristic time scales (roll-over point) and the slope of single SF. Then we combine all *Beppo*SAX observations to derive an average SF for MKN 421. We will not calculate SF at time scales larger than a few days, because the current observational campaigns were only carried out without "serious" interrupted monitoring for a few days each year. Thus any SF calculated over time scale larger than this time scale, i.e., 10^6 s, will become physically meaningless. Furthermore we do not consider very short time scale variability on time scale of less than 1000 s to avoid weak photons statistics in each actual time bin.

To compare the variability characteristics in the different X-ray bands, the SF is calculated in the 0.1–2 keV (LECS) and 2–10 keV (MECS) bands, respectively. Each light curve is binned over 1000 s and normalized by the average count rate before SF calculation, so we are investigating the variability characteristics on time scale between 10^3 and $\sim 5 \times 10^5$ s.

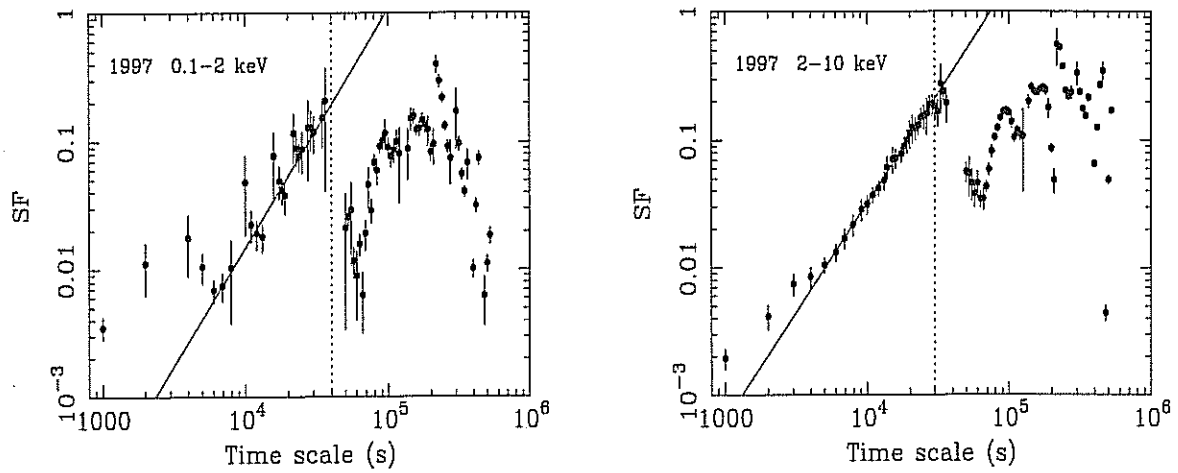

Figure 5.7: SF derived from the 1997 light curve (binned in 1000 s) in the 0.1–2 keV (left) and 2–10 keV (right) bands, respectively. Solid line indicate the best fit to a power law, and dotted line the position of roll-over point.

The SFs calculated are shown in Figure 5.7 (1997), 5.8 (1998 April), 5.9 (1998 June), 5.10 (1999), 5.11 (2000a), respectively. The average SFs calculated from combining all *Beppo*SAX light curves are shown in Figure 5.12.

To quantify the SF properties, we fit each SF with a power law to estimate the SF slop. The fitting is conducted only for the power law part of the SF. Furthermore we also experimentally determine the characteristic time scale (T_c from the turn-over point) of each SF. Both the best fits and T_c are shown in the corresponding figures. These parameters are also tabulated in Table 5.3.

Table 5.3: SF parameters

Date(UT)	**slope**		**T_c (10^4s)**	
	0.1–2 keV	2–10 keV	0.1–2 keV	2–10 keV
1997	1.86±0.13	1.71±0.07	4.0	3.0
1998 April	1.34±0.06	1.27±0.05	6.6	6.6
1998 June	0.85±0.28	0.76±0.12	2.0	2.0
1999	1.27±0.04	1.27±0.02	6.0	6.0
2000a	1.04±0.03	1.15±0.03	4.0	4.0
Average	1.10±0.03	1.28±0.03	4.0	4.0

The main results from the SF analysis are summarized in the following:

1. The SFs derived from different campaigns show similar structure, with a rel-

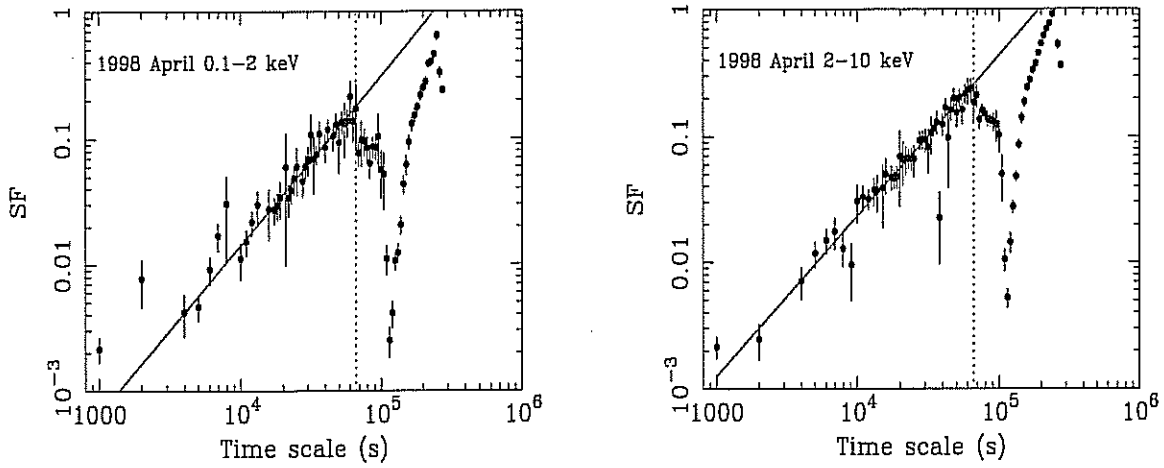

Figure 5.8: SF derived from the 1998 April light curve (binned in 1000 s) in the 0.1–2 keV (left) and 2–10 keV (right) bands, respectively. Solid and dotted lines have the same meaning as in Figure 5.7. A sharp dig at time scale of $\sim 10^5$ s is clear due to one day gap of the light curve.

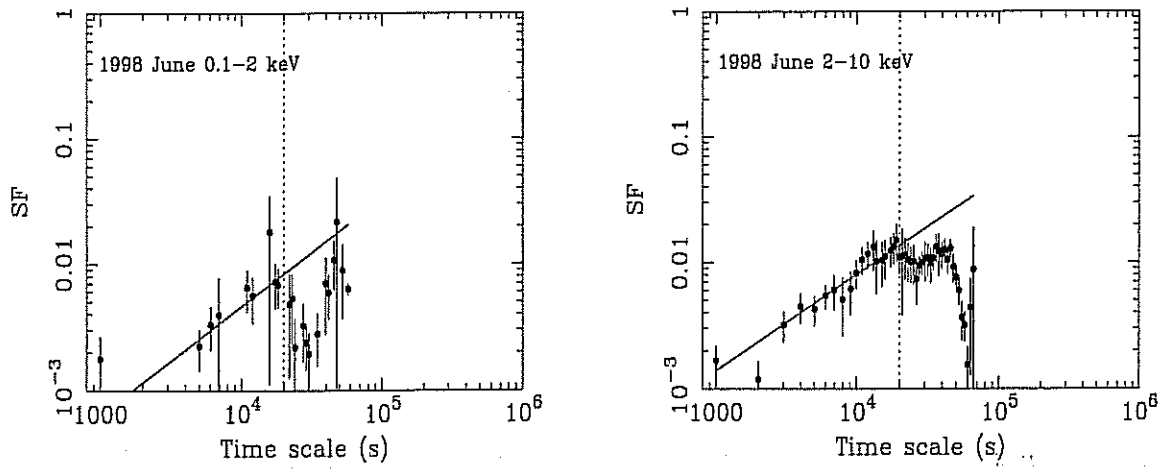

Figure 5.9: SF derived from the 1998 June light curve (binned in 1000 s) in the 0.1–2 keV (left) and 2–10 keV (right) bands, respectively. Solid and dotted lines have the same meaning as in Figure 5.7.

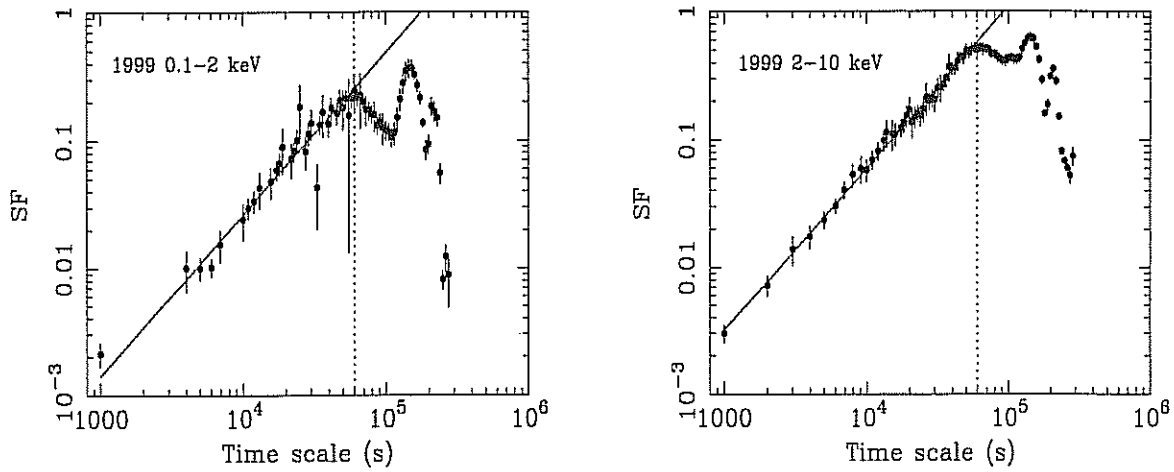

Figure 5.10: SF derived from the 1999 light curve (binned in 1000 s) in the 0.1–2 keV (left) and 2–10 keV (right) bands, respectively. Solid and dotted lines have the same meaning as in Figure 5.7.

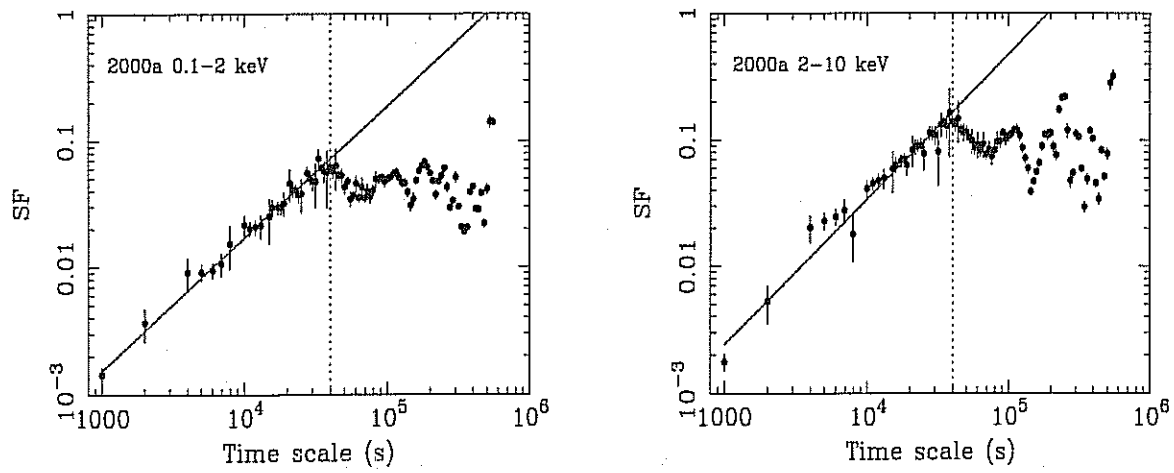

Figure 5.11: SF derived from the 2000 first part light curve (binned in 1000 s) in the 0.1–2 keV (left) and 2–10 keV (right) bands, respectively. Solid and dotted lines have the same meaning as in Figure 5.7.

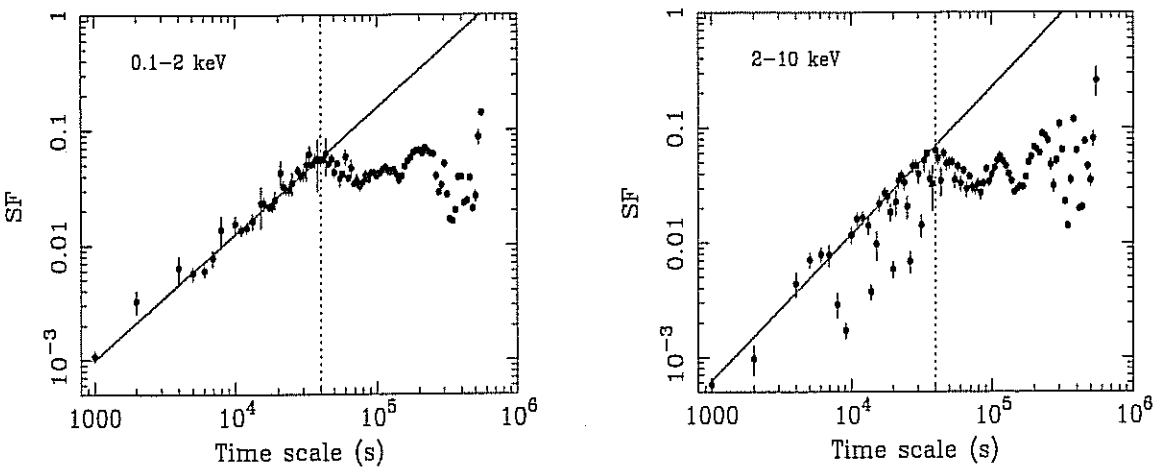

Figure 5.12: Average SF derived from *Beppo*SAX light curves (binned in 1000 s) in the 0.1–2 keV (left) and 2–10 keV (right) bands, respectively, but normalized to the mean count rate of 2000a. Solid and dotted lines have the same meaning as in Figure 5.7.

atively steep slope at high temporal frequencies (short time scales), i.e., the variability amplitude rising steeply logarithmically with time scale τ from 10^3 up to less than $\sim 10^5$ s, at which a roll-over occurrs.

2. The best fits to a power law show that the slope of the SFs, $\beta_{\rm SF}$, is larger than 1, this corresponds a slope of larger than 2 for the corresponding PDS (see equation 4.23), but the 1998 June SF is an exception, the slopes of both the soft and hard SF is flatter than 1.

3. The $T_{\rm c}$ estimated from the roll-over point is different from campaign to campaign, ranging from $\sim 2 \times 10^4$ to $\sim 7 \times 10^4$ s.

4. The shape of SFs is also roughly independent of photon energies when comparing the soft and hard band SFs in each campaign, in the sense of both the slope and roll-over point, while the 0.1–2 keV SFs are poorly defined than the 2–10 keV ones because of much less exposure time of LECS detector compared to MECS one.

This is an important result from the SF analysis, which shows MKN 421 shows a typical time scale of around half days, indicating that MKN 421 flare events usually take place repeatedly on time scales of less than one day. The symmetric shape for most flares is in agreement with the light-crossing time throughout the emitting region, and the size of radiating blob is not significantly different (within a factor of 3, possibly maximum at $\sim$ 0.5 days light-crossing time. On the time scale shorter

than this typical time scale, variability of MKN 421 sharply decreases towards very short time scale. This means that MKN 421 will not significantly show very rapid variability, unlike Seyfert galaxies; On the time scales of larger than this typical time scale the variability characteristics are not generally well defined due to constraint of observation duration. However there is tendency that the SFs will become flatter on time scales larger than this characteristic time scale. This flattening cannot be due to the uneven sampling of the light curves but it is what we would expect that MKN 421 will not show further stronger variations on time scale of days if the blob properties ejected each time from the central black hole are similar.

5.5 Periodicity in 2000a

From the light curve of the first part observation in the 2000 campaign (2000a, Figure 5.5), there is a visible evidence that the variations during this long period show possible periodicity. To check this visible variability periodicity, the best way is to perform a detailed PDS analysis (e.g., Tagliaferri et al. 1996). However, the obvious unevenly sampling pattern of the light curve make it impossible to do such an analysis. We thus take the advantage of the DCF technique suited to the unevenly sampled light curve to calculate the auto-correlation function (ACF) of the 0.1–2 keV and 2–10 keV light curves, respectively. The resulting ACFs are presented in Figure 5.13. The first peak, indicating the possible variability periodicity, occurs at $\sim 7.0 \times 10^4$ s, then ACF peaks again at roughly integer folds of this periodicity time scale, confirming the existence of the periodicity. It is interesting to compare this periodicity with the characteristic time scale, T_c, deduced from th SF analysis of the same light curves, we find that T_c is roughly half the periodicity time scale. This is not occasional, but it is what we would expect: the symmetric shape of most flares indicate that the variability time scale is dominated by the light-crossing time, which is the characteristic time scale T_c estimated from the SF analysis, that is, half the mean flare duration. The periodicity means the recurrence of the flares and the periodicity time scale is the average flare duration.

5.6 Cross correlation analysis

In this section we search for any possible time lag between LE and ME2 bands, with FR/RSS simulation performed on them. In §5.7 the energy-dependence of time lags will be studied in detail by dividing the energy band into smaller ranges.

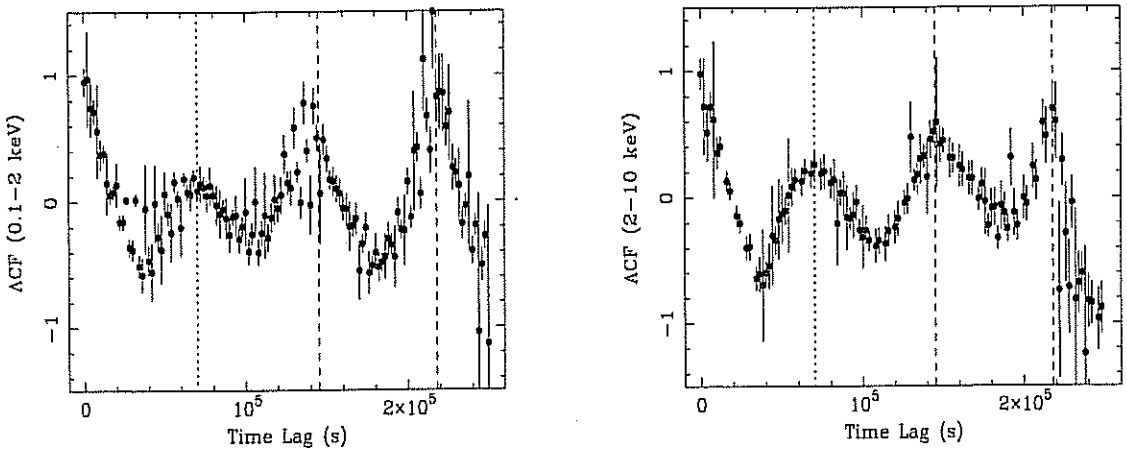

Figure 5.13: Auto-correlation function (ACF) of 2000a light curve in the 0.1–2 keV (left) and 2–10 keV (right) bands, calculated by using the DCF technique. The first ACF peak (dotted line) indicates the possible variability periodicity, confirmed by the recurrent ACF peaks at roughly integer folds of the first peak (two dashed lines).

The sampling pattern in 1997 prevent us from conducting a detailed cross-correlation analysis to study the energy-dependent variability characteristics during this period. Each pointing is insensitive to DCF/MMD analysis because of the constraints of sampling length. We then calculate the DCF/MMD from the whole campaign between LE and ME2 band, no significant lag is found, with a upper limit of $\sim$ 500 s. FR/RSS simulations are studied, which confirm the above result. We further point out that these results do not have any physical insights to shed light on the "true" energy-dependent variability attributes residing in the "possible isolated" flares.

1998 April

The observation in 1998 April comprise a complete flare (#1) and a pure decay (#2), while the latter is insensitive to cross-correlation analysis (resulting very broad DCF peak). Below we just performed a detailed cross-correlation analysis for the flare #1. The importance of this flare is that we first detect a pronounced hard lag in the X-ray bands in this source, i.e., hard X-ray photons lagging the soft ones, imposing new clues on the particle acceleration operating in blazar jets.

The DCF and MMD calculated between the LE and ME2 band is shown in Figure 5.14. A negative time lag is quite pronounced, this means that variations in the 3.5–10 keV band lag those in the 0.1–1.5 keV. We notice that this behavior is *opposite* to the previous findings for this source and other HBLs. A negative lag of -2.94 ± 0.20 and -2.16 ± 0.29 ks is derived from the best Gaussian fit to the "core"

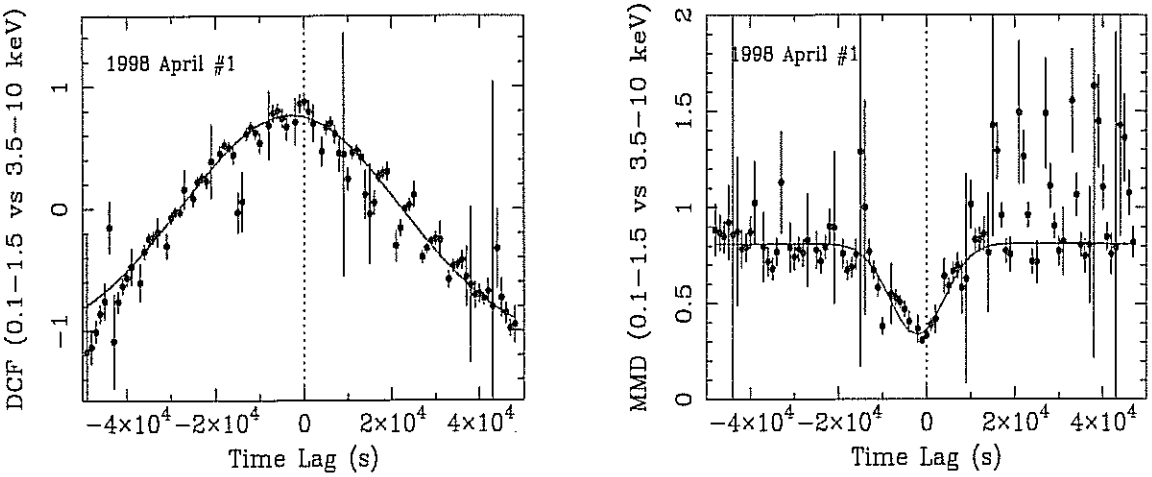

Figure 5.14: DCF (left) and MMD (right) between the 0.1–1.5 keV and the 3.5–10 keV derived from the 1998 April # 1 flare. The best fit consists of a Gaussian function plus a constant. The "estimated" time lag is taken from the time lag axis at which the Gaussian peaks.

of DCF and MMD functions, respectively. To check the significance of this finding, FR/RSS Monte Carlo simulation is performed for the same light curves for 1000 times, from which the CCPD is built (left panel of Figure 5.16). The average lags resulting from CCPD are $-2.70^{+1.55}_{-1.58}$ ks for DCF, and $-2.23^{+0.93}_{-0.10}$ ks for MMD (1 σ confidence intervals, two sided with respect to the average), confirming the significance of the above results with high confidence. The total integral probabilities for a negative lag (that would be the actual measure of the confidence of the "discovery" of the hard lag) are $\simeq 95.0\%$ (DCF) and $\simeq 98.7\%$ (MMD).

1998 June

Both the DCF and MMD analysis for the whole light curve show that time lag between the LE and ME2 bands is consistent with zero, with upper limit of several hundred seconds. We also carry out DCF and MMD calculation for the small flare #2, and the results are identical to the ones for the whole light curve.

1999

#1: time lag of flare #1 can not be well constrained due to data lack around the peak, though DCF and MMD analysis suggest small soft lag for this flare, which are 1.92±0.50 ks (DCF) and 1.73±0.6 ks (MMD) between the LE and ME2 bands.

#2: compared to the two other flares in this campaign, the variability during this part is characterized by small "fluctuations", so time lag is weakly determined due

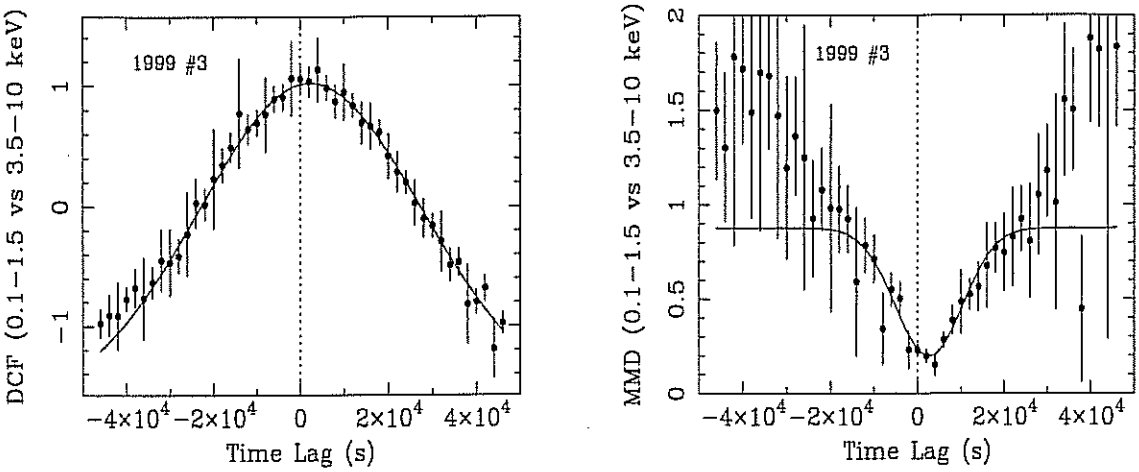

Figure 5.15: DCF and MMD between the 0.1–1.5 keV and the 3.5–10 keV from the 1999 #3 flare. The best fit consists of a Gaussian function plus a constant.

to small variability amplitudes. The estimated soft lag is 1.34±0.61 ks (DCF) and 1.16±1.02 ks (MMD) respectively, between the LE and ME2 bands.

#3: #3 is a very neat complete flare. Figure 5.15 shows the DCF and MMD calculated between LE and ME2 bands, which clearly shows the soft lag. The lag estimated from the best Gaussian fit to the DCF and MMD distribution is 2.20 ± 0.5 ks and 2.60 ± 0.5 ks respectively. The results from FR/RSS simulations (right panel of Figure 5.16) is $1.73^{+2.78}_{-2.73}$ ks (DCF) and $3.17^{+1.21}_{-1.78}$ ks (MMD). The total integral probabilities for a positive lag (that would be the actual measure of the confidence of the "discovery" of the soft lag) are $\simeq$ 95.8% (DCF) and $\simeq$ 94.8% (MMD).

2000a

The long length observations with multiple flares obtained in 2000 provide us a good opportunity to study the detail of the energy-dependent variability characteristics from a continuous sequence of flares, which will give us new clues about the continuous acceleration processes taking place in blazar jets.

#1: the DCF and MMD between the LE and ME2 band are presented in Figure 5.17. A positive lag is quite clear, which suggest a soft lag of 5.1 ± 0.6 ks (DCF) and 2.9 ± 0.9 ks (MMD), but note that there is ~ 2 ks difference for the values from these two methods. The CCPD built from the FR/RSS Monte Carlo simulations is shown in the left panel of Figure 5.19. The statistical average values of the soft lag with 68% confidence range is $5.54^{+2.41}_{-2.78}$ ks (DCF) and $4.22^{+1.21}_{-3.62}$ (MMD) ks. This

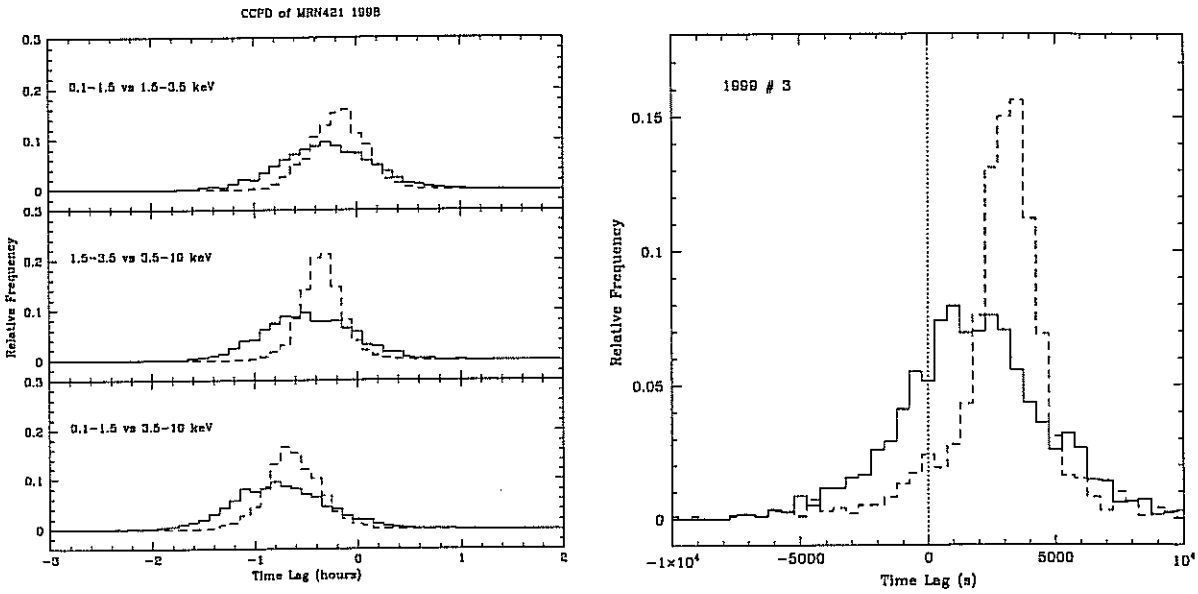

Figure 5.16: CCPD derived from the FR/RSS Monte Carlo simulations for the 1998 April #1 flare (left) and 1999 #3 flare (right). The solid and dashed lines refer to DCF and MMD results, respectively. Note that the time unit of the left panel is hour, and CCPDs are derived from 3 cases.

confirms the results from the direct DCF and MMD analysis. The total integral probabilities for a positive lag are $\simeq 100\%$ for both DCF and MMD.

#2: this complete flare comprise a double peaks. To increase significance of our analysis, we assume that both peaks are produced by a "single" flare event. We put the DCF and MMD results into Figure 5.18, and the corresponding CCPDs into the right panel of Figure 5.19. Interestingly, we find another clear negative lag (hard lag) from this flare, while the DCF does not show a regular distribution (the Gaussian fit to the "very core" of the distribution still suggest a hard lag of ~ 1000 s). The resulting hard lags are listed in the following for comparison: -2.9 ± 0.9 ks from DCF; -3.9 ± 1.2 ks from MMD; $-5.41^{+4.91}_{-4.63}$ ks from CCPD of DCF; and $-3.78^{+2.92}_{-3.07}$ ks from CCPD of MMD. The total integral probabilities for a negative lag are $\simeq 88.8\%$ (DCF) and $\simeq 88.7\%$ MMD.

#3: the DCF and MMD calculated between LE and ME2 bands are presented in Figure 5.20, which suggest a very small soft lags between these two bands: 0.2 ± 0.6 ks (DCF) and 1.2 ± 0.9 ks (MMD). In fact, DCF suggest "zero" lag within the error, which is confirmed by the CCPD of DCF: $-0.56^{+2.85}_{-2.96}$ ks (Figure 5.21), while the CCPD from MMD suggest a soft lag of $2.06^{+2.16}_{-2.88}$ ks. The total integral probabilities of DCF is 40.4% and 59.6% for a positive and a negative lag, respectively, an "actual" measurement of the confidence of the "discovery" of the "zero" lag. However, the

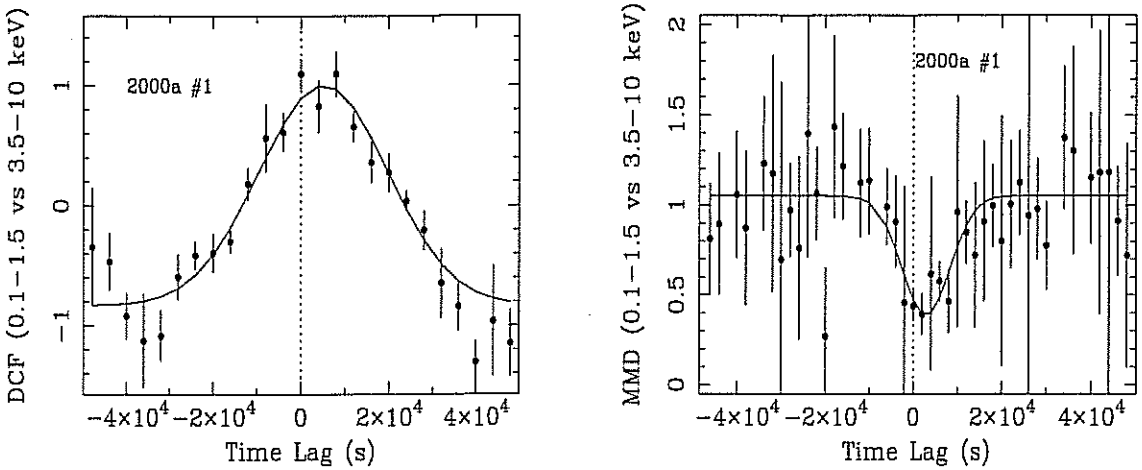

Figure 5.17: DCF and MMD between the 0.1–1.5 keV and the 3.5–10 keV from 2000 #1 flare. The best fit consists of a Gaussian function plus a constant.

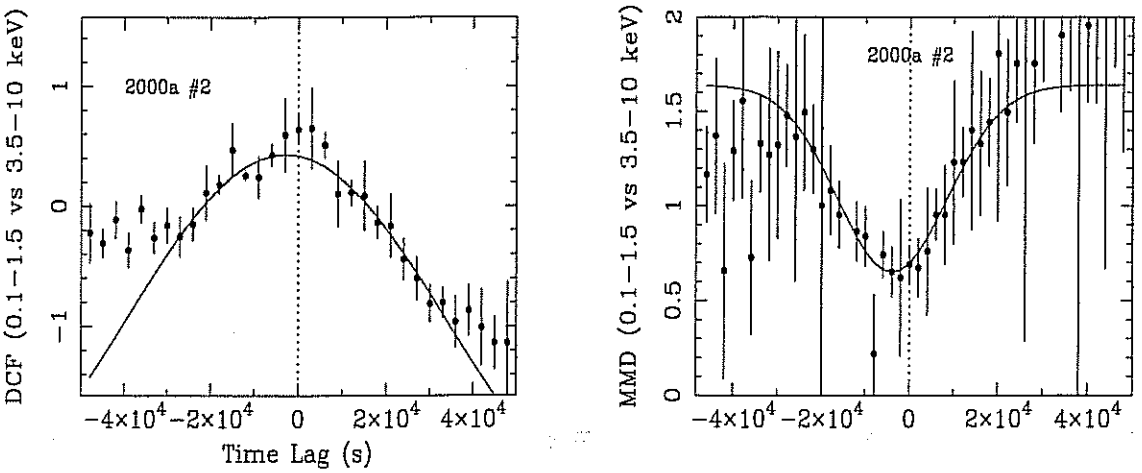

Figure 5.18: DCF and MMD between the 0.1–1.5 keV and the 3.5–10 keV from the 2000a # 2 flare. The best fit consists of a Gaussian function plus a constant.

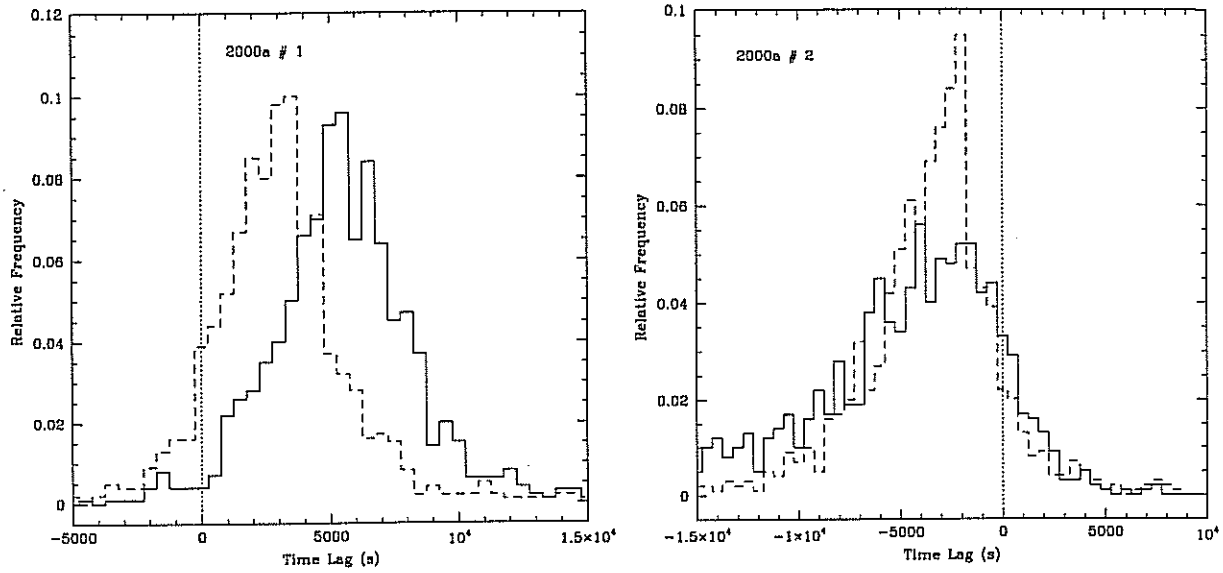

Figure 5.19: CCPD derived from the FR/RSS Monte Carlo simulations for the 2000 #1 (left) and #2 (right) flare. The solid and dashed lines refer to DCF and MMD results, respectively.

total integral probabilities of MMD for a positive lag (76.5%) is significantly larger than for a negative lag (23.5%).

#4: this flare is possibly incomplete for the decay phase. DCF analysis suggest time lag is consistent with zero, while MMD results in a small soft lag of $\sim$ 1600 s.

#8: this flare duration is short. Both the DCF and MMD suggest a very small soft lag of $\sim$ 1000 s.

* * *

To compare the time lags among different flares, we summarize cross-correlation analysis results in Table 5.4.

5.7 Energy-dependence of time lags

We have studied in last section any possible soft/hard lag between the 0.1–1.5 keV and the 3.5–10 keV bands residing in all isolated flares obtained by *Beppo*SAX during the four years' observations. Among the 10 complete flare events we have studied, 2 are found to show significant soft lags, and 2 significant hard lags, and other 6 flares are found to be no pronounced time lags. In this section, we further quantify the energy dependence of soft/hard lags, concentrating on these well defined flares. We divide the 0.1–10 keV energy range into 6 (for 1998 and 1999) and 8 (for 2000)

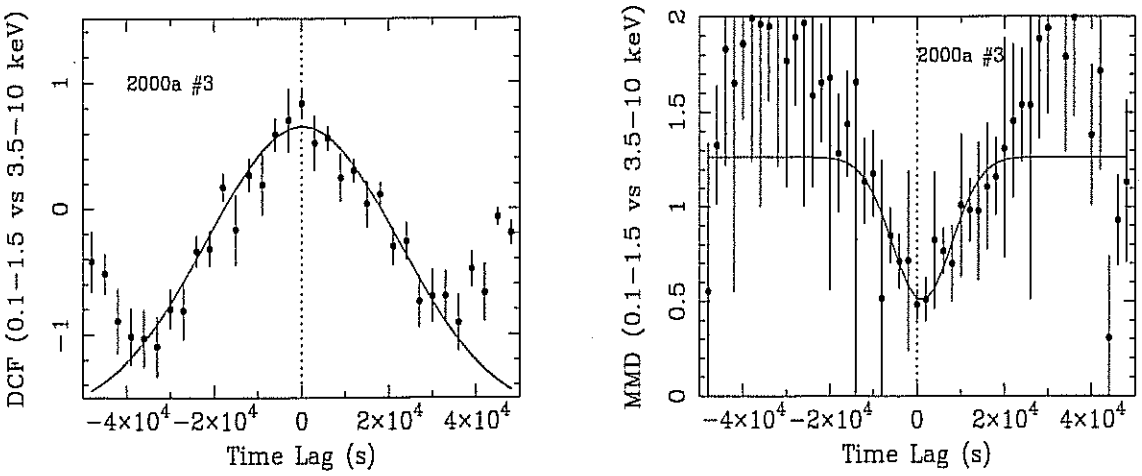

Figure 5.20: DCF and MMD between the 0.1–1.5 keV and the 3.5–10 keV from the 2000a # 3 flare. The best fit consists of a Gaussian function plus a constant.

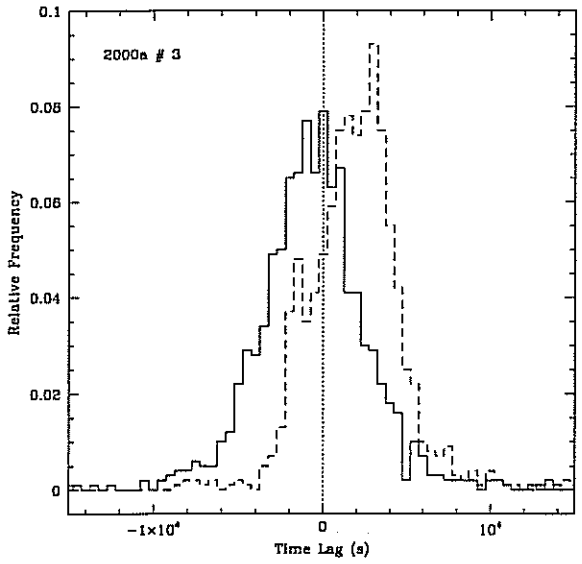

Figure 5.21: CCPD derived from the FR/RSS Monte Carlo simulations for the 2000a #3 flare. The solid and dashed lines refer to DCF and MMD results, respectively.

Table 5.4: Results of cross-correlation analysis (ks)

Flare #	DCF	MMD	CCPD	
			DCF	MMD
1998 Apr #1	-2.94 ± 0.20	-2.16 ± 0.29	$-2.70^{+1.55}_{-1.58}$	$-2.23^{+0.93}_{-1.10}$
1998 June	0.80±0.38	1.46±0.65	...	...
1999 #1	1.92±0.50	1.73±0.62	...	...
#2	1.34±0.61	1.16±1.02	...	...
#3	2.20±0.53	2.60±0.51	$1.73^{+2.78}_{-2.73}$	$3.17^{+1.21}_{-1.78}$
2000a #1	5.14±0.63	2.89±0.92	$5.54^{+2.41}_{-2.78}$	$4.22^{+1.21}_{-3.62}$
#2	-2.90 ± 0.91	-3.93 ± 1.23	$-5.41^{+4.91}_{-4.63}$	$-3.78^{+2.92}_{-3.07}$
#3	0.23±0.60	1.15±0.95	$-0.56^{+2.85}_{-2.96}$	$2.06^{+2.16}_{-2.88}$
#4	-0.90±0.41	1.61±0.72	...	...
#8	1.12±0.59	0.75±0.61	...	...

energy bands and measure the time lags of all low energy bands with respect to the 4–10 keV (for 1998 and 1999) and 7–10 keV energy band light curves using both the DCF and MMD methods. We will not show any actual DCF and MMD distributions and their fits to a Gaussian for these calculations, and the FR/RSS simulations will not perform on these results. However we would remind the reader that for a particular flare the DCF/MMD distributions with their CCPDs calculated here are quite similar to those studied in the previous section, but with a time shift of the peaks of the distributions.

The resulting energy-dependent lags are plotted against the energies in Figure 5.22 for the 1998 #1 (left panel: hard lag) and 1999 #3 (right panel: soft lag) flares, and in Figure 5.23 for the 2000a #1 (left panel: soft lag) and #2 (right panel: hard lag) flares. The results for the 2000a #3, #4 and #8 will not be shown here because these lags are quite small (consistent with the results obtained in last section) and the energy-dependence can not be well determined.

Interestingly, the 1998 April #1 flare (hard lag) and 1999 # 3 flare (soft lag) show similar energy dependence, which occurs again in the 2000a #1 (soft lag) and #3 (hard lag), where we probe into higher energy. However we remind the reader that the similarity of the energy dependence of both the soft and hard lag can not be caused by the same physical mechanism, as we discuss these issues in the following.

We assume that the soft and hard lags of the response of the soft X-rays variations compared with those of the hard X-rays respectively reflects the different synchrotron cooling time scale, $t_{\rm cool}$, and acceleration time scale, $t_{\rm acc}$, of the relativistic electrons

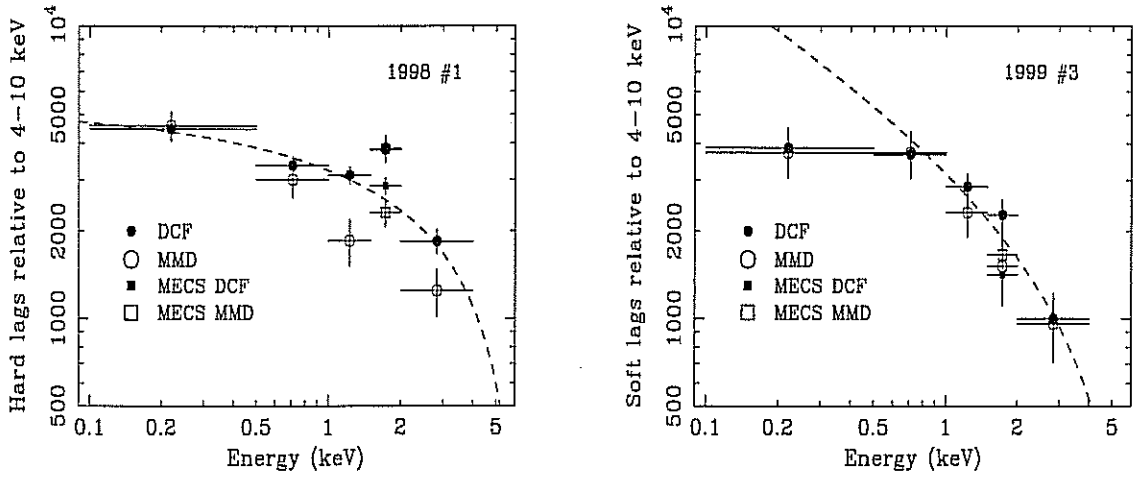

Figure 5.22: Energy dependent time lags of various X-ray energies compared to the 4–10 keV band photons, calculated from both the DCF (solid circles) and MMD (open circles). Left panel: 1998 #1 flare (hard lag); right panel: 1999 #3 flare (soft lag). The dashed line is the best fit with the energy dependence of the cooling (1999) and acceleration (1998) time scales respectively.

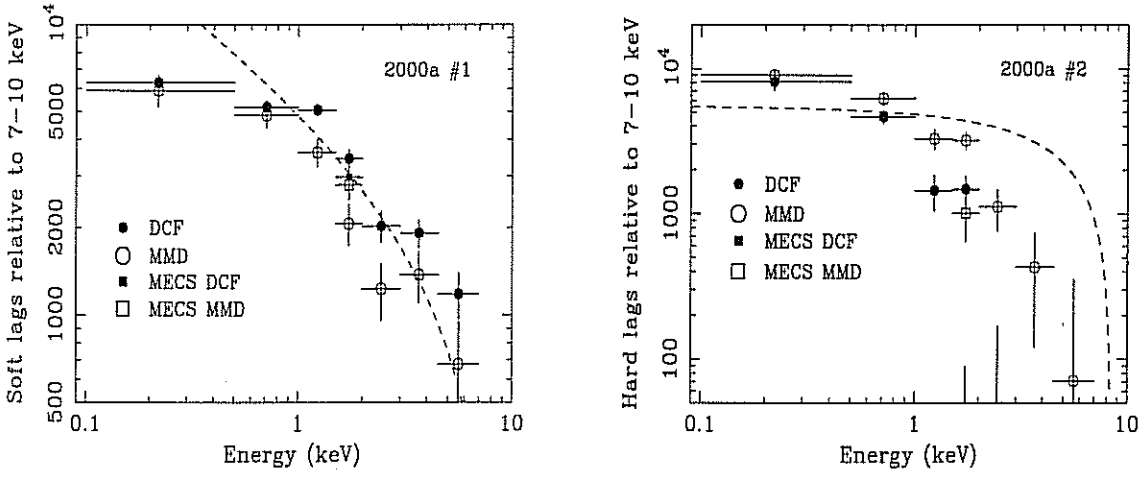

Figure 5.23: Energy dependent time lags of various X-ray energies compared to the 4–10 keV band photons, calculated from both the DCF (solid circles) and MMD (open circles). Left panel: 2000a #1 flare (soft lag); right panel: 2000a #2 flare (hard lag). The dashed line is the best fit with the energy dependence of the cooling (#1) and acceleration (#2) time scales respectively.

responsible for the emission in these studied energy bands. Here we rewrite $t_{\rm cool}$ (equation [2.20]) by synchrotron process, and $t_{\rm acc}$ (equation [2.54] in the framework of diffusive shock acceleration), in the observer's frame, as a function of the photon energies in keV,

$$t_{\rm cool}(E_{\rm keV}) = 3.04 \times 10^3 B^{-3/2}\delta^{-1/2}E_{\rm keV}^{-1/2} \quad \text{s} \tag{5.1}$$

$$t_{\rm acc}(E_{\rm keV}) = 9.65 \times 10^{-2}\xi B^{-3/2}\delta^{-3/2}E_{\rm keV}^{1/2} \quad \text{s} \tag{5.2}$$

where $E_{\rm keV}$ is the observed energy in keV. It is interesting to note that both the $t_{\rm cool}$ and $t_{\rm acc}$ have the "same" dependence with the photon energies (square root of the energy) for the synchrotron cooling and diffusive acceleration, but in the *opposite* way, i.e., the lower energy photons have longer cooling and shorter accelerating time scales than the higher energy photons, these properties are translated from the fact that the higher enrgy electrons cool faster and accelerate more slowly than the lower energy electrons. This qualitatively agree with the above findings.

We further assume that the significant soft/hard lag detected is controlled by the synchrotron cooling and diffusive acceleration processes, respectively. The soft/hard lag is then defined as the difference of $t_{\rm cool}/t_{\rm acc}(E_{\rm keV})$ and $t_{\rm cool}/t_{\rm acc}(E_0)$, which is approximately $t_{\rm cool}(E_{\rm keV})$ for the cooling dominated process, and $t_{\rm acc}(E_0)$ for the diffusive acceleration dominated processes when E_0 is at much higher energies. Here we take $E_{\rm keV}$ to be the logarithmic mean energy in the corresponding energy band used.

Having the above assumptions, we can fit the energy-dependence of time lags using the above two equations to constrain the magnetic field B and Doppler factor δ of the emitting blobs. It is clear that the cooling/acceleration time scale can not uniquely determine the magnetic filed B, Doppler factor δ and ξ. The practical model fits will only constrain a combination of the magnetic filed, Doppler factor and ξ. Here we take the form $B\delta^{1/3}$ and $B\delta\xi^{-2/3}$ for the soft and hard lag case, respectively. δ is usually well constrained by other methods, B can be thus constrained for the soft lag case. However in the hard lag case, ξ is very poorly constrained, so B can not be well determined.

In the following we discuss the fitting results for the energy-dependence of time lags we just showed.

1998 April #1: during this flare, a hard lag, hard photons lag the soft ones, is clearly detected. This is the first case that the X-ray variability behavior is *opposite* to what is normally expected in the X-rays of HBLs. We assume that this behavior most possibly provide clues on the particle acceleration process. We then fit the

energy-dependent hard lags with the (electron) energy-dependent acceleration time scale by using the equation [5.2]. The best fit means $B\delta\xi^{-2/3} = 1.42 \times 10^{-3}$ Gauss, and the fitting result is shown in Figure 5.22 (left panel, dashed line). It can be seen that the diffusive shock acceleration mechanism can well reproduce the variability behavior of MKN 421 during this flare. If we assume that $\delta = 20$ and $\xi = 10^5$ (see Inoue & Takahara 1996), we obtain that $B = 0.15$ Gauss.

1999 #3: this is a pronounced flare in a relative faint state of MKN 421, which showed a normally synchrotron cooling dominated X-ray variability behavior, producing the soft time lag which the soft X-ray photon lag the hard ones. We thus fit the energy-dependent soft lags (right panel of Figure 5.22) with the energy-dependent (electron) synchrotron cooling time scale by using equation [5.1]. The best fit suggests that $B\delta^{1/3} = 0.70$ Gauss, and the fitting result is shown in the same figure indicated by dashed line. If $\delta = 20$ is assumed, we get $B = 0.26$ Gauss, consistent with the value derived from the 1998 April # 1 within a factor two.

However, here we need to remind the reader that this fit does not include the first point of the energy-dependence of soft lags, i.e., the lowest energy band (0.1–0.5 keV) with respect to the 4–10 keV. This is because this point does not follow the general trend and it shows a flatten behavior of the energy-dependent soft lags towards the lowest energy band. The fit including this point can not produce a good result. It can be seen that there is a discrepancy between the observed energy-dependent soft lag trend and the simplified "theoretical" one, the latter does not show the flatten behavior towards the lowest energy band. Let us discuss further this issue. The comprehensive spectral fits to this flare show that the synchrotron peak frequency is $\sim$ 1 keV (the maximum value during the flux maximum of the light curve). The multiwavelength observations demonstrated that blazars are much less variable at the frequencies below the synchrotron peak frequency, then the energy-dependent cooling time scales below the synchrotron peak frequency can not be clearly discriminated from the observations. Therefore the behavior that the energy-dependent soft lag flatten at the energy below the synchrotron peak frequency is probably expected. This finding, firstly found in MKN 421, is confirmed by the 2000a #1 flare (see below).

2000a #1: this is another flare in which the pronounced soft lag is detected. The energy-dependent soft lag trend is very similar to that of the 1999 #3. Much higher brightness in 2000 campaign provide our good opportunity to divide the higher energy end of considered energy band here into smaller range without lost of good enough photon statistics. We thus correlate the lower energy photons with photons

in the 7–10 keV, which will probe the energy-dependent soft lags into higher energy compared with the previous two cases. From Figure 5.23 (left panel) we see that the correlation between the soft lag and the energy follows the same trend towards higher energy, and flatten again toward the lowest energy. Same as to the 1999 # 3 case, we fit the energy-dependent soft lag without the first point, and the fit result is shown in the same figure (dashed line). We obtain $B\delta^{1/3} = 0.55$ Gauss. If $\delta = 20$ is assumed, we get $B = 0.20$ Gauss, consistent with the above two values.

2000 #2: this is the second hard lag we detected with high confidence. More importantly, we find that the diffusive shock acceleration mechanism can not produce the observed correlation between the hard lag and the energy. We show the fitting result in Figure 5.23 (right panel) with the following parameters: $B = 0.30$ Gauss, $\delta = 20$ and $\xi = 10^5$ in the framework of diffusive acceleration mechanism. It can be seen that the shape of the energy-dependent hard lag obtained from equation (5.2) is significantly different from the observed one. Specifically, the observed hard lag decrease much steeper with the energy than the one expected from the simple diffusive shock acceleration case. This finding indicates that there might be other acceleration mechanisms operating in MKN 421 jets, with different slope of the energy-dependence of the accelerating time scales. However we are cautious of double peaks in this flare!

5.8 Discussion

The present X-ray monitoring campaigns by *Beppo*SAX (this chapter) and ASCA (Takahashi et al. 1996; 2000) have showed that MKN 421, the best observed blazar in the X-rays, is strongly variable, characterized by daily (or perhaps even more frequently) flares. The X-ray variability characteristics, and in particular, its energy and brightness dependence, is much more complex than anticipated. Therefore these high quality X-ray observations have provided our good opportunity to probe the physical processes taking place in the jets of MKN 421. MKN 421 is also an ideal source for the multiwavelength monitorings, and confirmation of the correlation in the X-ray and TeV energy bands within $\sim$ 1 hour have supported the idea that the same electron population in the same physical region is responsible for the emission in both energy bands by SSC process (Maraschi et al. 1999; see also §3.3).

Before discussing the physical insights from the results presented in this chapter, it is important to point out that the (intraday) X-ray variability of MKN 421 is similar to the intraday optical variability observed in FSRQs. This is expected with the recent results from blazar SED sequence, showing different synchrotron peak

frequencies for the various subclasses of blazars. In particular, the synchrotron peak frequencies locate in the keV X-ray range in HBLs, like MKN 421, and the eV optical (or even sub-eV IR) range in FSRQs, like 3C 279. As we have stated before, the most extreme variability observed in the synchrotron component of blazars occurs above the synchrotron peak frequency. Since the synchrotron emission is thought to be due to a single population of relativistic electrons characterized by a broken power law distribution, and the observed synchrotron peak frequency, $\nu_{\rm peak}$, relates to the electron broken energy, $\gamma_{\rm peak}$, by the following formula: $\nu_{\rm sync} = 3.7 \times 10^6 \frac{\delta}{(1+z)} \gamma_{\rm peak}^2 B$ Hz. Recent analyses have shown that $\gamma_{\rm peak}$ is lower for FSRQs ($\sim 10^3$–10^4) and higher for HBLs ($\sim 10^5$–10^6) (Ghisellini et al. 1998). The rapid, large-amplitude variability observed above $\nu_{\rm peak}$ is likely the result of the rapid change of the electron distribution above $\gamma_{\rm peak}$, in the regime where electron acceleration and cooling are approximately balanced (e.g., Inoue & Takahara 1996; Kirk, Rieger & Mastichiadis 1998). This sheds light on the particular differences when we study, in the same observed energy bands, blazars variability. At the present time, observations are much more better at the X-rays than at any other wavelengths, and can provide our good opportunity to study the physical processes operating in HBLs, like MKN 421, through dense sampling.

ASCA also observed MKN 421 in late of April 1998 for $\sim$ 7 days, just following 1998 April *Beppo*SAX observations. This long length monitoring by ASCA is very similar to the 2000a campaign by *Beppo*SAX, both showed that MKN 421 is very active, with continuous multiple flares, occurring on time scales of one day or even shorter. One visible difference between these tow long length campaigns is that the multiple flares observed by ASCA are superimposed on a general increasing trend, which is not seen in the *Beppo*SAX data. Of course, our *Beppo*SAX data, with obvious gaps, is inferior to the ASCA one because of problems during observations. We will compare our results with those from the ASCA data, which is shown in Figure 5.24 in the form of light curves, hardness ratios and time lags (Takahashi et al. 2000). An earlier ASCA observation in 1994 was presented in Takahashi et al. (1996), and a single complete flare was detected with $\sim$ 1 hour soft lag between the soft and hard X-rays. This is the time lag first definitely reported in blazars.

Structure of light curves: the first visible propeity from *Beppo*SAX (also ASCA) light curves of MKN 421 is that they are characterized by recurrent flares, and the dominant durations to be or less than one day. This indicates that injection or re-acceleration must frequently take place in the jets. The quasi-symmetric flare profiles seen in most cases imply that $t_{\rm acc}$ and $t_{\rm cool}$ are shorter than the source light-crossing time $t_{\rm crs}$, because faster time scales will always be smoothed out by $t_{\rm crs}$

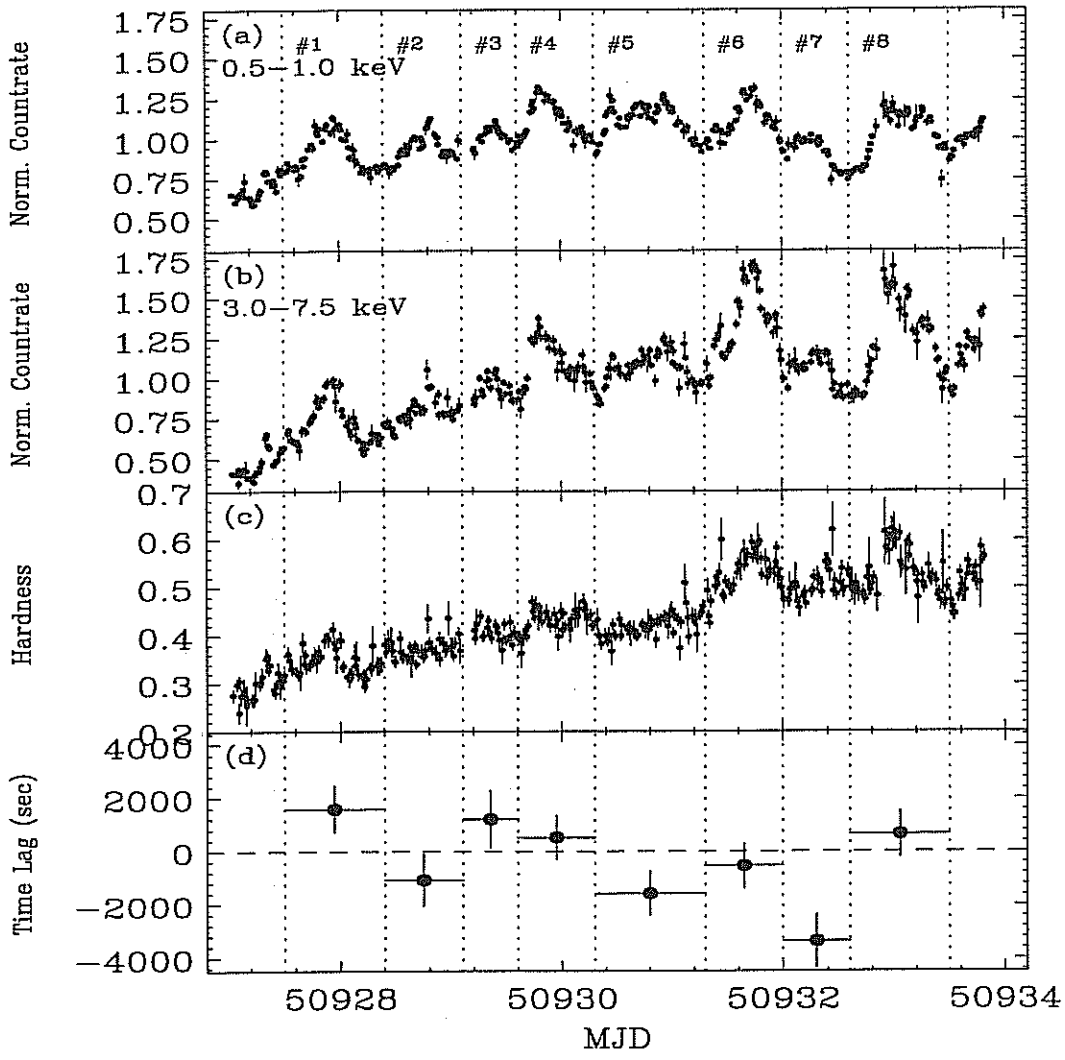

Figure 5.24: Temporal evolution of MKN 421 in the X-rays observed by ASCA in late April 1998. (a) Normalized count rate in 0.5–1.0 keV, and (b) in 3–7.5 keV band; (c) hardness ratio of count rates, defined as (3–7.5 keV)/(0.5–1.0 keV); (d) Time lags of photons of 0.5–1 keV band from 3–7.5 keV band calculated from Gaussian fit to the DCF. Quoted from Takahashi et al. (2000).

(Chiaberge & Ghisellini 1999). Furthermore the different structures from flare to flare and its energy-dependence are likely competitive effects between the different time scales among the electrons injection, acceleration, cooling, and light-crossing and escape from the emitting region. We discuss here some examples to show the complex features of the light curves. (a) A plateau may occurs during the maximum of the flare when the energetic electrons injection time scale, $t_{\rm inj}$, is longer than the cooling time scale, $t_{\rm cool}$, in which emission from individual slices does not fade as quickly after an increase, hence the observation of a plateau during a flare occurs when the entire volume is radiating. A plateau in ASCA #8 (Figure 5.24) is clear at low energies, but not seen at the higher energies. (b) The fact that the "convex" feature seen in the decay phase of 1999 #3 is increasingly more defined with the energy, is consistent with the convolution of cooling and light-crossing time scales: at energies corresponding to $t_{\rm cool} < t_{\rm crs}$ the "volume" should dominate, while at energies for which $t_{\rm cool}$ is comparable or longer than $t_{\rm crs}$ the flare would resemble more closely a simple cooling evolution. (c) Tow or more peaks may occur during a major flare if one mild injection come before completely fading from the previous injection. A double peaks is very clear at the high energies, but less defined at low energies due to slower decaying.

Variability amplitude: variability amplitude and its energy/brightness dependence carry precious information on the physics of the emitting region. In the context of MKN 421, the energy band (0.1–10 keV) discussed here is just the high energy part of the synchrotron component, and the highest amplitude of variability and its energy-dependence is expected. We have quantified the variability amplitude with the fractional *rms* variability parameter, $F_{\rm var}$, in the 0.1–2 keV and 2–10 keV energy bands for each single campaign, and the results are shown in Table ??. It can be seen that the variability amplitude is always higher at higher energies, independence of both the length of the observations and the brightness of the source. This is just what we would expect because the largest changes of the electron distribution always occur at the most energetic electrons due to the fastest cooling, this feature should be independent of the time length and population of electrons. When translating this feature about the electron distribution into the SED distribution, from the fact that higher electrons emit higher energy photons, higher variability is expected at higher energy.

However we do not find the brightness dependence of variability amplitude from these excellent *Beppo*SAX observations. The earlier statement, according to poor sampling and short observations, that the positive correlation between variability amplitude and the source brightness, *the higher variability amplitude accompanied*

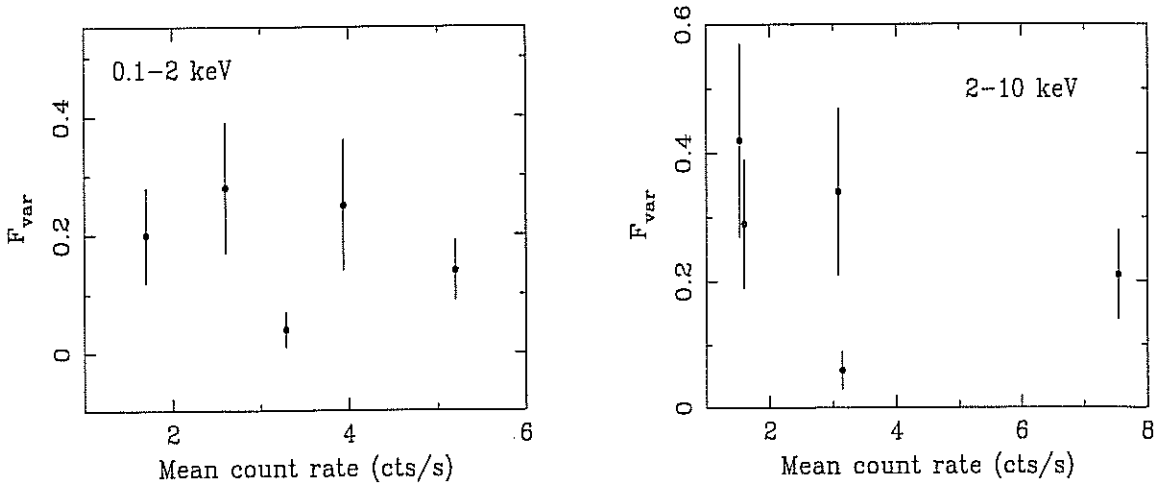

Figure 5.25: $F_{\rm var}$ is plotted against the mean count rate of each campaign.

by the higher flux, is not confirmed by these high quality observations by *Beppo*SAX, and in particular, it is possibly wrong. To clarify this point, we show in Figure 5.25 $F_{\rm var}$ against the mean count rate in the 0.1–2 keV and 2-10 keV respectively. It is obvious that the variability amplitude does not show any positive dependence on the source brightness, possibly anti-correlation, it is more pronounced in the 2–10 keV band. This finding is not fully explained, while sampling patterns (length, maximum, minimum and so on) may seriously affect the calculation of $F_{\rm var}$, which, of course, underline deeper analysis.

Variability time scales: variability time scales and its energy/brightness dependence is another important parameter which carry important information on the physics of the source. As explained above, the faster variability is expected at the higher synchrotron frequency. To quantify the variability time scale in different energy bands, we simply take the minimum doubling time scale, T_2, as an indicator (see Table ??), and we indeed find that the minimum doubling time scales are shorter in the higher energies than in the lower energies, also independent of both the length of sampling and the brightness of the source. This is the signature that higher energy electrons cool faster than lower energy ones.

As variability amplitude, we do not find the brightness dependence of the minimum doubling time scales, which is shown in Figure 5.26. If the point from 1998 June is excluded, the minimum doubling time scale at a given energy does not change too much with the brightness of the source.

We stress again that both the variability amplitude and the minimum doubling time scale do not depend on the source brightness, and this non-dependence may

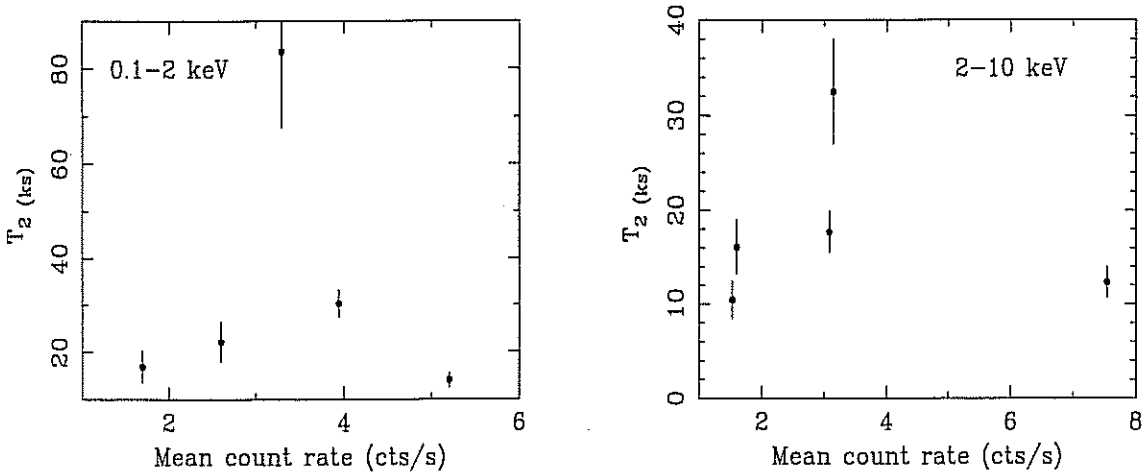

Figure 5.26: T_2 is plotted against the mean count rate of each campaign.

relate to the shifts of the synchrotron peak frequencies during different source brightness. This is a new finding although not fully explained yet.

SFs: the SFs of MKN 421 derived from the *Beppo*SAX light curves, in particular 2000a campaign which have similar sampling length, is very similar to the one derived from the ASCA 1998 light curves (compare Figure 5.11 with Figure 4 of Takahashi et al. 2000), with a break at a characteristic time scale of $\sim$ 0.5 day. Moreover, these X-ray SFs are also similar to those found in optical and radio studies of FSRQs, with a break at a characteristic time scale of $\sim$ 1 day (Wagner & Witzel 1995; Wagner et al. 1996).

The X-ray SFs of MKN 421 are characterized by a relatively steep slop, $\beta_{\rm SF} \sim 1.2$ (corresponding to $\alpha_{\rm PDS} \sim 2.2$), at high temporal frequencies (short time scales), this is much more steeper than those in other types of mass-accreting black hole systems, such as Seyfert galaxies, whose variability is well characterized by a fractal, flickering noise ($0 < \beta_{SF} < 1$) (e.g., Hayashida et al. 1998).

The most precious information from the SFs is the clear detection of the characteristic time scale of $\sim$ 0.5 days, just half the average duration of the flares. The quasi-symmetric structure in most flares and the fact that plateaus are rarely seen implies the dominant time scale is similar to the light-crossing time, which in turn supports the idea that the size of the emitting region is determined by diffusion and cooling. The dominant light-crossing time, $t_{\rm crs}$, should thus depend on the energy because the size of emitting region is determined by the cooling length, otherwise we can not see any time lags between different energy bands. Although there is preliminary evidence that suggests energy-dependence of $t_{\rm crs}$ from the present SF analysis,

e.g., the 1997 SFs, the further proper determination of the energy-dependent $t_{\rm crs}$ is clearly necessary and postponed to our future work.

The clear characteristic time scale from the SFs is thus a proper determination of the average size for the emitting region, which in turn may constrain the distance from the central black hole where the acceleration takes place. A simple conceptual scenario for particles acceleration is that a "blob" of plasma passes through the region where shock fronts are formed and electrons are accelerated. If we assume the opening angle of the jet is approximately equal to $1/\Gamma_j$, where the size of the blob at distance D from the base of the jet can be expressed as $R \sim D/\Gamma_j$. With this, the characteristic time scale of $T_{\rm c} \sim 0.5$ days implies that the emission region has size $R = cT_{\rm c}\Gamma_j \sim 10^{16}$ cm at distance $D \sim 10^{17}$ cm from the black hole, if we assume that $\Gamma_j \sim 10$. This is just distance where the two blobs with different initial velocity collide, *internal shock acceleration*; or the blob collide with BLR, *external shock acceleration.*

Time lags: the most important results from the comprehensive cross-correlation analysis presented in this chapter are the detection of time lags with various signs and values, indicating that soft, hard and zero lags are possible between the soft and hard X-rays in MKN 421. Specifically, among the 10 flares with different intensities at different epochs, two show pronounced soft lags, two show significant hard lags, and other 6 show smaller soft or zero lags. More importantly, current X-ray observations performed by *Beppo*SAX (and ASCA) have demonstrated that time lags observed in MKN 421 can be constrained to a small range, $\sim^{+}_{-}$ 1 hour between the 0.1–1.5 keV and the 3.5–10 keV bands, but dominated by the small time lags. Our results derived from *Beppo*SAX are completely consistent with those obtained from 9 isolated flares of ASCA (Takahashi et al. 1996; 2000), from which two soft and hard lags are clearly detected, respectively, and other 5 flares are dominated by very small or zero time lags.

To show the correlation between the time lags and the flare brightnesses, we plot in Figure 5.27 time lags between the 0.1–1.5 keV and the 3.5–10 keV bands against the maximum count rate of each flare in the 3.5–10 keV band. It is clear that no any correlation between time lags and flare intensities exist. Along with the independence of variability amplitude and time scales on source brightness, we can conclude that the variability characteristics in MKN 421 do not depend the source brightness, and probably relate to the synchrotron peak frequencies in different states. The dependence of the variability behaviors on the synchrotron peak frequencies is our future work, as comprehensive spectral analysis is needed.

We interpret the detected soft and hard time lags as the difference of the energy-

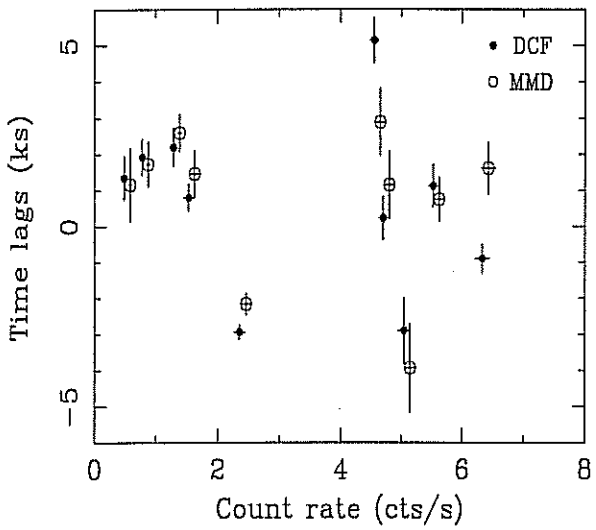

Figure 5.27: Time lags (0.1–1.5 keV vs 3.5–10 keV) are plotted against the maximum count rate of each flare in 3.5–10 keV energy band. A small shift is used for count rates in order to show clearly the results from DCF and MMD, respectively.

dependence of synchrotron cooling and acceleration time scales, respectively (see also §5.7). This in turn dictates negative or positive correlation of the light-crossing time on the energy in the case of soft or hard lag, respectively. The soft lag can be easily explained by the fact that $t_{\rm cool}$ is shorter for higher energy electrons (i.e., higher energy photons) (Rybicki & Lightman 1979). When energetic electrons are instantaneously injected into the emitting region and then cool radiatively, the soft photons lag the hard ones, by a time roughly equal to the cooling time at the soft energy. A pronounced soft lag can be seen by closely looking at the temporal evolution of the light curves at different energies, and their hardness ratios and/or spectral indices. Light curve at low energy usually peaks after the one at higher energy, and the hardness ratio will peak before both light curves. In the diagram of spectral index against the flux, a soft lag is identified by a *clockwise* loop. Conversely, the suggested hard lag can be explained, at least qualitatively at the present time, if the acceleration time scale is enough long, i.e., $t_{\rm acc} \sim t_{\rm cool}$, in this case electrons will appear first at low energies and gradually build up to higher energies (e.g., Kirk, Rieger & Mastichiadis 1998; Georganopoulos & Marscher 1998; Kusunose, Takahara & Li 2000). Although the shapes of two light curves are different from each other, a close look at the *Beppo*SAX and ASCA data for MKN 421 indicates the soft light curve rises and peaks ahead of the hard X-ray light curve, also suggested by the fact that the hardness ratio peaks after the light curves, consistent with a longer

acceleration time scale for the higher energy electrons. In the plane of spectral index against the flux, a hard lag behavior is shown by a *anti-clockwise* loop. The above behaviors for both the soft and hard lags will be not easily identified when a time lag is very small or consistent with zero given the specific sampling features of the light curves.

The detection of both pronounced soft and hard lags and of very small or zero lags implies that cooling is sometimes but not always the dominant process, and that acceleration is also important in some cases. More importantly, according to the detection of small range of time lags, both $t_{\rm cool}$ and $t_{\rm acc}$ are constrained, and this further indicates that both the magnetic field and Doppler factor will not significantly change from flare to flare. A factor of 2 changes of B are suggested by fitting the energy-dependent soft and hard lags from the four flares in which significant time lags, soft or hard lags, are detected.

The relatively small lags indicate $t_{\rm acc} \sim t_{\rm cool}$ at X-rays in MKN 421 at least from the present observations. This is consistent with the fact that the emission at X-rays is emitted by the highest energy end of the energetic electron distribution, where $t_{\rm acc}$ is approximately balanced with $t_{\rm cool}$. According to the shock acceleration scenario, $t_{\rm acc}$ depends on the energy in an *opposite* sense to $t_{\rm cool}$. It follows $t_{\rm acc}(\gamma) \propto \gamma$ for diffusive acceleration. Furthermore the good and bad fits to the hard lags detected in 1998 #1 and 2000a #2 respectively, by using the diffusive acceleration case, suggest that different acceleration mechanisms may operate in different flares.

Currently, the detection of both soft and hard and of zero lags in MKN 421 from present observations can be easily explained by a change in either $t_{\rm cool}$ or $t_{\rm acc}$, but too simplified. However, a large change of $t_{\rm cool}$ is unlikely, as it requires large change of B or δ associated with large-amplitude changes in the overall multi-frequency spectrum as the synchrotron luminosity is proportional to $B^2\delta^4$, which is not frequently observed. Hence we interpret that the various behaviors are caused by the changes of the acceleration time scale of electrons responsible for the emission in the X-rays. This predicts that the soft lag would be more pronounced in the lower frequency regions, where $t_{\rm cool}$ is much longer than $t_{\rm acc}$, and a change of sign of time lags may be expected at some frequencies according to relative changes between $t_{\rm cool}$ and $t_{\rm acc}$ over an energy range, e.g., in the optical. This behavior could be detected through much more intense multiwavelength monitoring campaigns from radio to X-ray wavelengths, but it is difficult to conduct.

In summary, the detection of various signs and values of time lags from the present 19 flares observed by *Beppo*SAX and ASCA clearly underlines the need for detailed time-dependent synchrotron models to explain the complex of the energy-

dependent variability characteristics, in which the time scales for electron acceleration and injection, and for radiative cooling and escape, are free to vary. Depending on the relative values of these time scales, a variety of behaviors can be expected. In addition, spectral evolution, in particular changes of synchrotron peak frequencies, is also necessary to explain the complex variability behavior. This is due to the fact that any intrinsic changes of time scales can be easily identified through pronounced variations, and smaller variations are detected below the peak frequency. We do see this phenomenon from the fact that the energy-dependence of soft lags flatten in the energy range of 0.1–1 keV, just the range of peak frequencies in MKN 421, and this behavior is not consistent with the one expected from the simple synchrotron cooling time scales.

To conclude the most important results, the richness of the unprecedented X-ray monitoring data for MKN 421 is a testimony to the fact that in different flares, the relevant time scales must have different relative values, but well constrained to a small range of changes, and light-crossing times are energy-dependent.

* * *

Finally, we show here an example to simulate the hard lag behavior detected in 1998 April #1 flare, while this example does not show the performance of relative changes of $t_{\rm acc}$ and $t_{\rm cool}$, but do simulate the behavior that the energetic electrons appear first at low energies, by a simple way to inject with time electrons from low to high energy (see Fossati et al. 2000b for details).

The time-dependent model is the one studied by Chiaberge & Ghisellini (1999) by introducing a (parametric) acceleration term in the particle kinetic equation (see equation 2.51) to account for the detected hard lag. The model includes the presence of a quiescent spectrum, which is assumed to be represented by and thus fitted to the broad band spectral distribution observed in 1994 (Macomb et al. 1995). A flaring component is added and this is constrained by the observed spectral and temporal evolution (the parameters for both the stationary and variable spectra are reported in Table 5 of Fossati et al. 2000b).

Clearly a parametric representation does not reproduce a priori a specific acceleration process, but we rather tried to constrain its form from the observed evolution. The main constraints on the form of the acceleration term are the following:

a) Particles have to be injected at progressively higher energies on the flare rise time scale to produce the hard lag.

b) Globally the range of energies over which the injection occurs has to be narrow, to give rise to a peaked spectral component.

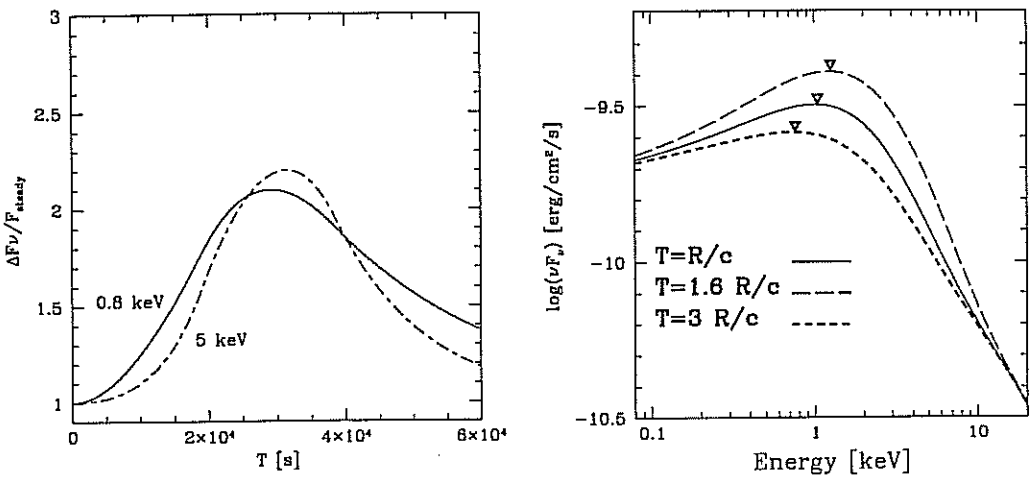

Figure 5.28: Left: Light curves computed from the model, at the centroid energies of the soft and hard band considered in the data analysis. The vertical axis represents the variations normalized to the flux of the stationary component; Right: X–ray spectra at different times, as derived from the model. On each spectrum we marked the position of the synchrotron peak with a symbol.

c) A quasi–monochromatic injection function for the flux at the highest energies to reach its maximum *after* that at lower ones (as opposed to, e.g., a power law with increasing maximum electron Lorentz factor).

d) The emission in the LECS band from the particles which have been accelerated to the highest energies (i.e., those radiating initially in the MECS band) should not exceed that from the lower energy ones, as after the peak no further increase of the (LECS) flux is observed; this in particular requires for the injection to stop after reaching the highest energies.

e) The total decay time scale might be dominated by the achromatic crossing time effects, although the initial fading might be determined by different cooling time scales.

The acceleration term has then been described as a Gaussian distribution in energy, centered at a typical particle Lorentz factor $\gamma_c(t)$ and with width $\sigma = 0.01\gamma_c(t)$, exponentially evolving with time: $\gamma_c(t) \propto e^{-(t_{max}-t)}$, where t_{max} corresponds to the end of the acceleration phase, when the maximum $\gamma_{c,max}$ is reached. The injected luminosity is assumed to be constant in time, thus number density of the injection electrons decrease with the energy.

The duration of the injection, assumed to correspond to the light-crossing time of the emitting region, is such that it mimics the passage of a shock front (i.e., a

moving surface passing through the region in the same time interval, see Chiaberge & Ghisellini 1999).

It should be also noted that, within this scenario, the symmetry between the rise and decay in the soft energy light curve seems to suggest that if the energy where most of the power is released is determined by the balance between the acceleration and cooling rates, at this very same energy the latter time scales are comparable to the light-crossing time of the region.

The predictions of the model are shown in Figure 5.28 in the form of light curves (left panel) and spectra (right panel) at different times, respectively. In particular, the light curves (normalized over the stationary component) at the two centroid energies of the soft and hard bands considered in the data analysis are reported. The presence of a hard lag is clearly visible as well as the larger variability amplitude at higher frequencies. Also the spectral evolution, reported in νF_ν in the observed energy range, seems to be at least in qualitative agreement with what observed (compare with Figure 3 of Fossati et al. 2000a).

* * *

Before leaving this chapter, we stress again that the unprecedented *Beppo*SAX (and ASCA) observations have revealed much more complex variability behaviors of MKN 421 than anticipated. To account for them, relative changes of values of different time scales, in particular energy-dependent light-crossing time, have to be carefully introduced when making a confident model that can reproduce well the observed flare behaviors. In next chapter we will see what happened in another HBL, PKS 2155−304, its SED is very similar to MKN 421.

>>>>>>

Chapter 6

PKS 2155−304

On the previous chapter, we have presented in a comprehensive way the X-ray variability characteristics for MKN 421 observed by *Beppo*SAX between 1997 and 2000. A lot of new results are achieved and their physical insights on the blazar jets are preliminarily probed. Another HBL, PKS 2155−304, can resemble MKN 421 in the temporal and spectral variability, especially in the X-rays, where the synchrotron emission peaks at the soft X-rays, $\sim$ 0.5 keV. Above the peak frequency, both are dominated by the rapid temporal and spectral variations. PKS 2155−304 is also very bright at UV and X-ray wavelengths, being another ideal source to study its X-ray variability characteristics. The similarity between PKS 2155−304 and MKN 421 dictate the great importance to compare in a systematic way their variability characteristics (in the X-rays), to show whether similar physical processes operate in these two sources and further present clues for other sources behaving like them. PKS 2155−304 is also monitored by *Beppo*SAX in three campaigns up to now, providing an excellent opportunity to compare in the same way its X-ray variability properties with those in MKN 421. This is main content of the present chapter.

A brief introduction to PKS 2155−304 is first given in §6.1; then the observations are briefly summarized in §6.2, followed by presenting the light curves and fundamental variability analysis in §6.3; we study the SF and PDS in §6.4 and §6.5, respectively; in §6.6 we further carry out comprehensive cross-correlation analysis with detailed Monte Carlo simulations to determine the uncertainties on inter-band lags, and energy-dependence of lags is discussed in §6.7; the physical implications of the results and comparisons with MKN 421 are discussed in §6.8.

6.1 Introduction

PKS 2155−304 was detected in gamma-rays by the EGRET experiment on CGRO, and showed a very hard gamma-ray spectrum in the 0.1−10 GeV region, with a power-law spectral index of $\alpha_\gamma \sim 0.71$ (Vestrand, Stacy & Sreekumar 1995; Sreekumar & Vestrand 1997). It is also one of the few BL Lac objects observed at TeV energies, with a time-averaged integral flux of 4.2×10^{-11} erg cm^{-2} s^{-1} above 300 GeV (Chadwick et al. 1999). Its broad band spectrum shows two peaks: the first one is synchrotron emission peaking at UV and/or soft X-rays. The other one is around the gamma-ray region and it is attributed to Compton scattering by the same high energy electrons which are radiating via synchrotron.

PKS 2155−304 has also been one of the best targets of multiwavelength campaigns because of its brightness. This kind of study has proved to be a powerful tool to constrain radiation models through the study of correlated variability among different bands. The first multiwavelength campaign was performed, from radio to X-ray wavelengths, in 1991 November, by ROSAT, IUE and ground-based telescopes, and correlated variability was observed between UV and soft X-rays with the UV lagging by $\sim$ 2 hours (Edelson et al. 1995). However, the source showed a definitely different variability behavior in the 1994 May campaign based on IUE, EUVE and ASCA data. Correlated variability was observed with larger amplitude at shorter wavelengths, and significant soft lags, i.e., the UV lagging the EUV by 1 day, and the EUV in turn lagging the X-rays by 1 day (Urry et al. 1997).

6.2 Observations

PKS 2155−304 has been monitored by *Beppo*SAX for three years between 1996 and 1999, with $\sim$ 2 days pointing each year. Moreover, one ASCA observation conducted in 1994 May is also included in our analysis for comparison with *Beppo*SAX observations. Table 6.1 shows the observational journal of PKS 2155−304.

SAX96: *Beppo*SAX NFIs observed PKS 2155−304 for $\sim$ 2.5 days during the Performance Verification phase of *Beppo*SAX on 20-22 November 1996. The *net* exposure time is $\sim$ 107 and $\sim$ 36 ks in the MECS and LECS respectively.

SAX97: slightly less than 1.5 days observation from 22 to 24 November 1997 was performed for PKS 2155−304. The *net* exposure times for MECS and LECS is $\sim$ 60 and $\sim$ 23 ks respectively.

SAX99: *Beppo*SAX continuously monitored PKS 2155−304 for $\sim$ 2.5 days between November 4 and 6 in 1999, yielding a *net* exposure time of $\sim$ 46 and $\sim$ 104 ks in

Table 6.1: Observational Journal

Date(UTC)	Net Exposure(ks) LECS	MECS	Archive #
*Beppo*SAX			
1996/11/20 00:15:58–1996/11/22 13:30:06	36.29	106.9	50016001
1997/11/22 16:03:00–1999/11/24 01:35:12	22.49	59.49	50160008
1999/11/04 04:27:27–1999/11/06 16:52:12	46.12	104.0	50880001
ASCA			
1994/05/19 04:38:21–1994/05/21 07:55:41	91.4		72012000[a]

[a]ASCA GIS2 data are studied in this chapter.

the LECS and MECS respectively.

* * *

Results on the 1996 and 1997 *Beppo*SAX campaigns have been presented by Giommi et al. (1998), Chiappetti et al. (1999) and Zhang et al. (1999), respectively, where the motivation and data reduction of the observations is also presented, but concentrating on the spectral analysis. In this chapter we re-analyzed those data along with the new one (SAX99), applying the same techniques, to accumulate a homogeneous set of results for PKS 2155−304.

ASCA94: PKS 2155−304 was previously monitored by the ASCA satellite for more than two days from 19 to 21 May in 1994 coordinated with a multiwavelength monitoring from radio to X-rays (Pesce et al. 1997; Pian et al. 1997; Urry et al. 1997). ASCA includes two SIS and two GIS focal-plane detectors (Tanaka, Inoue, & Holt 1994).

The X-ray light curve considered here – retrieved from the archive – was taken from the GIS2 detector. Preliminary results were presented by Makino et al. (1996), while detailed by Zhang et al. (1999) and Kataoka et al. (2000), where the motivation and data reduction details of the observation is also given. In this chapter we re-analyzed this dataset, applying the same techniques to the *Beppo*SAX datasets, to obtain a homogeneous set of results, necessary for a direct comparison with those from *Beppo*SAX. Furthermore we also perform further timing analysis which the above analysis did not include.

6.3 Variability analysis

In this section we show in time order the three light curves of the observations by *Beppo*SAX and present their preliminary variability properties. *Beppo*SAX light curves have been accumulated in the same way as MKN 421, as PKS 2155−304 is a bright and soft source as well. The ASCA light curve and its variability analysis is also shown.

As explained in §5 for MKN 421, the light curves is binned over 1000 s in the 0.1–2 keV (from the LECS) and 2–10 keV (from the MECS) to test for variability by means of a χ^2 test against the hypothesis that the flux is constant, and quantify the variability amplitude and the minimum time scale.

SAX96

The light curves and the hardness ratios are shown in Figure 6.1. A flare of low intensity is visible at the beginning of the observation, #1. An approximately symmetric flare was seen in the middle of the observation, #2, which is well resolved with rising ($\sim 5 \times 10^4$ s) and decaying ($\sim 3 \times 10^4$ s) time scales, but they will be same when extending the decay phase to the same level of count rate of the beginning of the rising phase. This major flare is followed by one more low amplitude flare, #3, superimposed on the decay phase of #2. A larger flare probably occurred towards the end of the observation, although the observation is incomplete. Some small-amplitude variability are also detected.

The χ^2 is 9.5 and 13.8 in the 0.1–2 keV and 2–10 keV energy band, showing the source is variable at greater than 99.9% confidence. The corresponding $F_{\rm var}$ is 0.10±0.04 and 0.12±0.04 respectively, and the estimated minimum "doubling times" are 99.3±19.6 and 56.4±9.7 ks respectively. These results show that the source is more variable with shorter time scale at higher energy.

The hardness ratio HR1 shows a behavior similar to that of the light curves, in the sense that the spectrum is harder at higher intensities, while again HR2 does not follow any trend (see Figure 6.1).

The average flux calculated is 1.39×10^{-10} and 0.57×10^{-10} erg cm^{-2} s^{-1} in the 0.1–2 keV and 2-10 keV band respectively.

SAX97

Figure 6.2 presents the light curves and hardness ratios. At the beginning of the observation PKS 2155−304 exhibited a large flare (#1), with a variation by a factor ~ 4, followed by a flare of smaller amplitude (#2), The rising phase of #1 is observationally incomplete, and the decay phase shows clear concave feature at the end

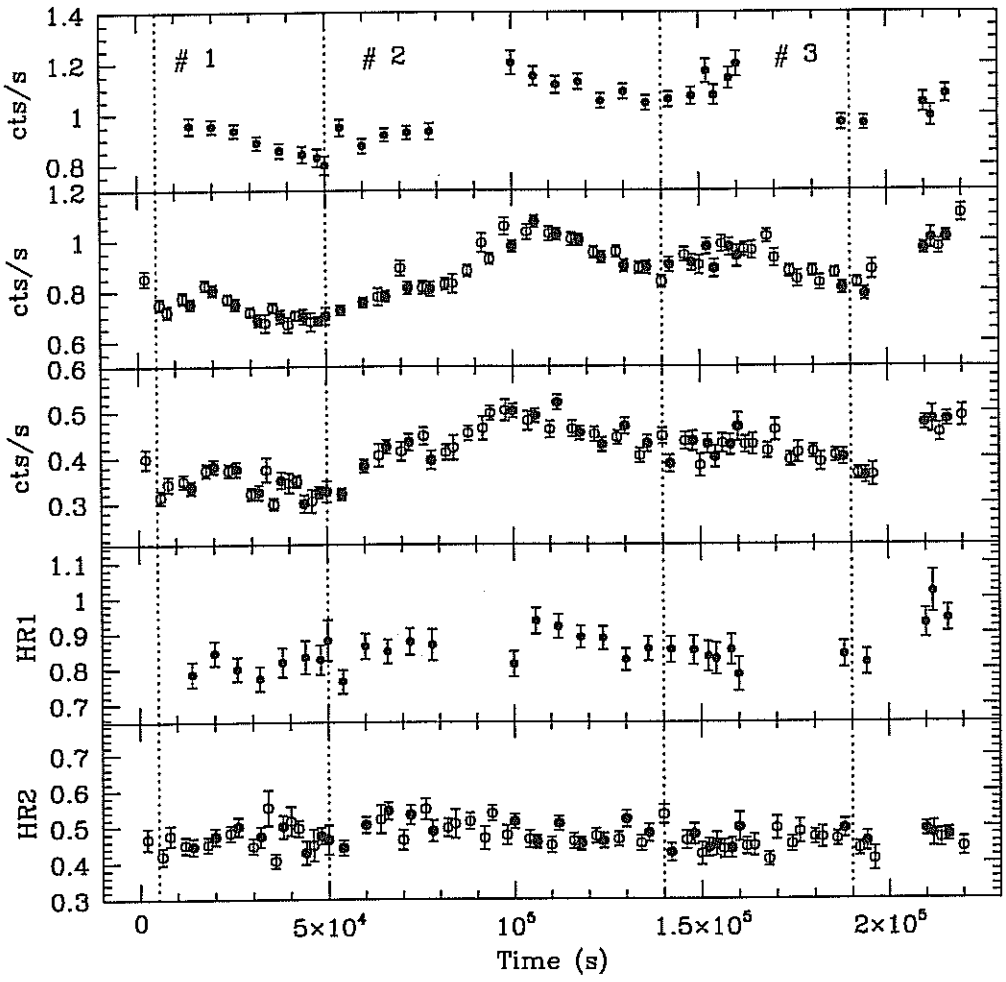

Figure 6.1: Light curves and hardness ratios of *Beppo*SAX 1996 November 22–24 observation. Data are rebinned in 2000 s. The reference time is 1996/11/20/ (TJD=10407) 00:00:00 UT. Panels and symbols have the same meaning of those in Figure 5.1.

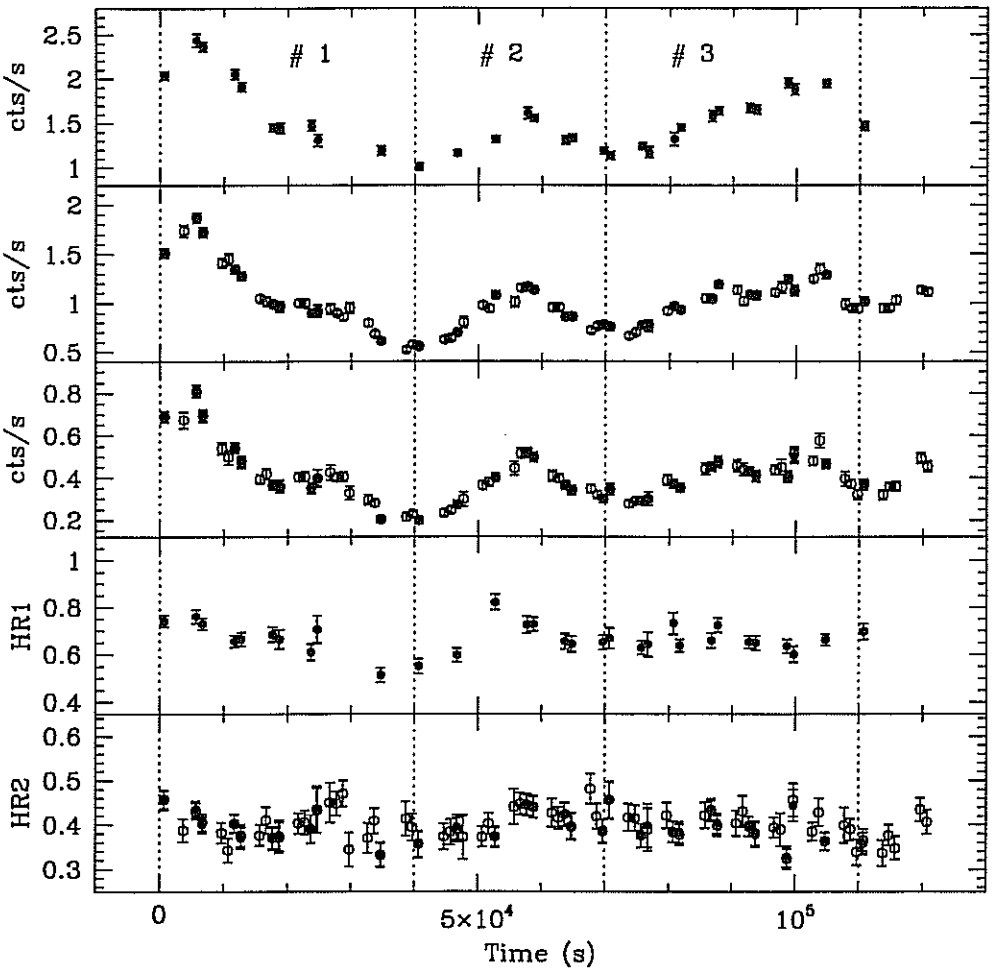

Figure 6.2: Light curves and hardness ratios of *Beppo*SAX 1997 observations. Data are rebinned in 1000s. The reference time is 1997/11/22/ (TJD=10774) 16:00:00 UT. Panels and symbols have the same meaning of those in Figure 5.1.

of the flare. In contrast, flare #2 presents similar rising and declining time scales. The variability of #3 is different from the first two, it did not show an isolated flare behavior, possibly from convolution of more than one "flare" events.

The variability amplitude is somewhat different in the soft and hard bands, increasing with increasing energy, $F_{\rm var}$ is 0.24±0.12 and 0.27±0.13 respectively, confirmed by their χ^2 value. The most rapid variation event – the fastest among the four observations – occurred during the first flare, with minimum values of T_2 of 16.4±1.6 and 10.8±1.5 ks in 0.1–2 and 2–10 keV bands, respectively. We notice that these time scales are much shorter and the fluxes about 50% higher than those of SAX96, indicating faster variability with higher intensity.

The average flux is 2.05×10^{-10} and 0.86×10^{-10} erg cm^{-2} s^{-1} in the 0.1–2 keV and 2–10 keV band respectively.

From the last two panels of Figure 6.2, one can see that the HR1 presents a global trend similar to that of the intensities (see Chiappetti et al. 1999 for more details). However, no statistically significant correlation seems to be present, as HR1 has the same value during the first two peaks which have significantly different intensities and is smaller during the end of the observation, although the average intensity is similar to that of the second peak. HR2 does not show any trend.

SAX99

PKS 2155−304 was very faint during $\sim$ 2.5 days *Beppo*SAX observation in 1999 November. Figure 6.3 shows the light curves and the hardness ratios. The average flux is 0.91×10^{-10} and 0.26×10^{-10} erg cm^{-2} s^{-1} in the 0.1–2 keV and 2–10 keV energy bands respectively, which are just half and one-fourth of the 1997 fluxes in the corresponding energy bands, indicating pronounced spectral steepening in 1999 period.

The light curves are dominated by two isolated flares with similar durations, possibly showing daily flare characteristics of the source. #1 flare, brighter and more pronounced than #2, showed faster decaying than the rising phase. In contrast, #2 flare showed faster rising phase than the declining phase.

The variability amplitude increases with increasing energy, the $F_{\rm var}$ is 0.13±0.05 (0.1–2 keV) and 0.18±0.06 (2–10 keV). The source did not show very fast variations during this period. The minimum "doubling times", obtained from probing the whole light curves, are 41.1±7.8 ks in the 0.1–2 keV and 38.5±7.4 ks in the 2–10 keV, respectively. In fact these time scales are quite confident to show the minimum time scales by doubling the fluxes, they are very similar to the whole rising time scales of both flares as the fluxes just doubled from the minimum to maximum fluxes, which are easily estimated by the eyes.

It is difficult to show the correlation between the evolution of the hardness ratio and that of the light curves due to very weak photon statistics in the high energy bands, resulting in larger error bars of hardness ratios.

ASCA94

The light curves and hardness ratios relative to this observation are plotted in Figure 6.4. A large amplitude flare (#1), with an approximately symmetric shape, is clearly seen at the beginning of the observation although the rising portion of the event is not fully sampled, both have a time scale of $\sim 3 \times 10^4$ s. The second

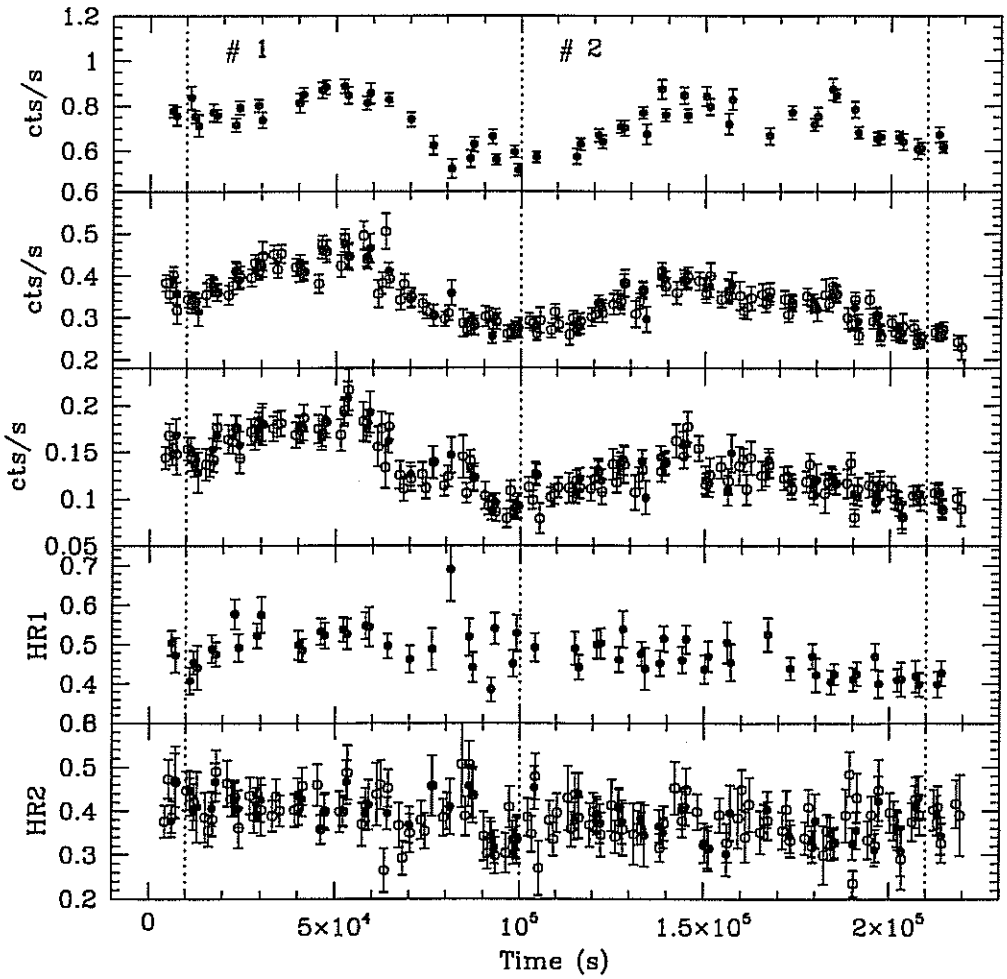

Figure 6.3: Light curves and hardness ratios of *Beppo*SAX 1999 observations. Data are rebinned in 1000s. The reference time is 1999/11/04/ (TJD=11486) 04:00:00 UT. Panels and symbols have the same meaning of those in Figure 5.1.

part of the observation (#2) is long slowly declining phase with some low amplitude fluctuations superimposed.

The source variability is somewhat different in different energy bands, and this is illustrated by separately plotting the light curves in the different energy bands from low to high energies, but the flare duration seems to be nearly the same. Notably, the amplitude of flux change is larger and the minimum time scale shorter at higher photon energies, as seen from Table 6.2. Also note that the peak of the light curve in the hard 3.5–10 keV band leads that in the soft 0.5–1.5 keV band by $\sim$ 4 ks, indicating that higher energy photons came earlier than low energy ones, this will be confirmed by a detail cross-correlation analysis in §6.6.

A significant characteristic of ASCA94 is that the hardness ratios present a trend of linear decrease over the whole period, which is a general signature that the spectra become softer when the source is fainter. Moreover, it is evident that the hardness ratios peaks before the light curves does, a signature of soft lag. The correlation between the flux and the photon index is shown by Kataoka et al. (2000), a "clockwise loop" is clearly seen for the flaring part #1. This clockwise motion in the flux versus photon index plane, indicating soft lag, has been seen in this source during earlier GINGA observations (Sembay et al. 1993), and similar behavior was clearly seen in MKN 421 in 1994 (Takahashi et al. 1996) and H 0323+022 in 1987 (Kohmura et al. 1994).

* * *

We have studied in this section the fundamental X-ray variability characteristics of PKS 2155−304 from four campaigns, including the temporal evolution behavior of both the light curves and hardness ratios, analysis of the χ^2, variability amplitude and time scale in various energy bands. To conclude this section and compare the variability properties in different source states, we summary main results, in the form of variability parameters, in Table 6.2.

6.4 Structure function analysis

We have quantified in last section the possible minimum variability time scale of PKS 2155−304 by searching for the minimum values among the time scales over which the fluxes double. As in §5.4, we probe in this section the characteristic time scale of this source, T_c, with SF technique.

The continuous and uninterrupted *Beppo*SAX and ASCA light curves performed on time scale of days are also suitable to do the SF analysis and derive the tempo-

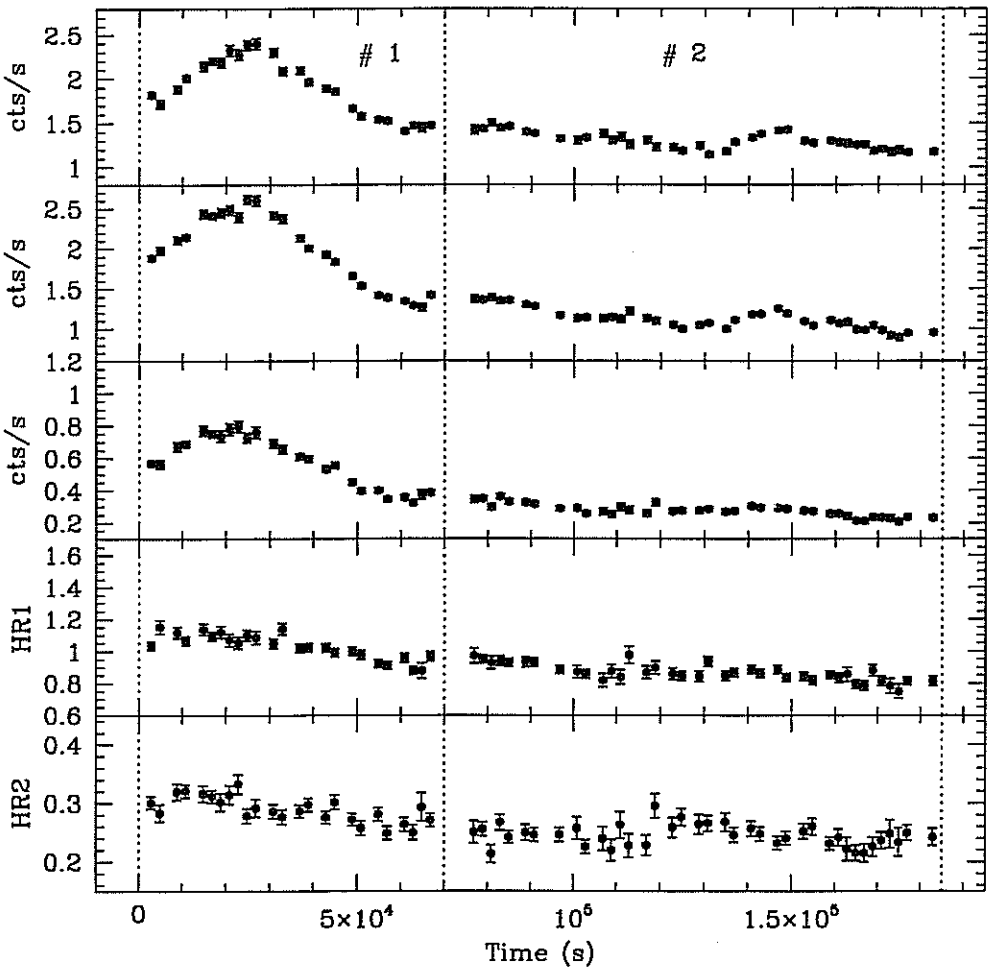

Figure 6.4: Light curves and hardness ratios of ASCA 1994 observations. Data are rebinned in 2000s. The reference time is 1999/05/19/ (TJD=9491) 05:00:00 UT. Panels and symbols have the same meaning of those in Figure 5.1, but for the ASCA GIS2 detector the lowest energy is set to 0.5 keV not 0.1 keV.

Table 6.2: Variability Parameters

band	Flux[a]	$\overline{F}$(cts/s)	F_{var}	χ^2_ν	T_2(ks)
			SAX96		
0.1–2	1.39	1.20	0.10±0.04	9.5(053)	99.3±19.6
2–10	0.57	1.01	0.12±0.04	13.8(135)	56.4±9.7
			SAX97		
0.1–2	2.05	1.85	0.24±0.12	67.2(031)	16.4±1.6
2–10	0.86	1.08	0.27±0.13	67.7(075)	10.8±1.5
			SAX99		
0.1–2	0.91	0.83	0.13±0.05	10.1(063)	41.1±7.8
2–10	0.26	0.35	0.18±0.06	9.7(126)	38.5±7.4
			ASCA94		
0.5–2	1.29	2.26	0.25±0.09	82.6(115)	29.8±4.2
2–10	0.71	1.07	0.39±0.14	94.7(115)	21.7±3.7

[a]Flux in unit of 10^{-10} erg cm^{-2} s^{-1}.

ral variability characteristics for PKS 2155−304 over time scale of days, similar to MKN 421 (see §5.4).

Same to MKN 421, we first calculate the SF of each light curve shown in last section to determine the characteristic time scale (from the roll-over point of SF) and the slop of the SF. The light curves are binned over 1000 s and normalized by their mean count rate before SF calculations. Then an average SF for PKS 2155−304 is derived by combining the light curves from three *Beppo*SAX campaigns, and we only calculate the average SF at time scale less than $\sim 5 \times 10^5$ s, as explained in the case of MKN 421 (§5.4).

The SFs are calculated in the 0.1–2 keV (LECS) and 2–10 keV (MECS) bands, respectively, for comparing the variability characteristics in the soft and hard X-ray bands. We present the SFs in Figure 6.5 (SAX96), 6.6 (SAX97), 6.7 (SAX99), and 6.8 (ASCA94), respectively. The average SF calculated from combining the three *Beppo*SAX light curves is also shown in Figure 6.9.

To quantify the SF features, we fit each SF within the power law region to estimate the SF slope, and experimentally determine the characteristic time scale (T_c from the turn-over point) of each SF. Both the best fits and T_c are shown in the corresponding figures. These parameters are also tabulated in Table 6.3.

We summarize the main results as following:

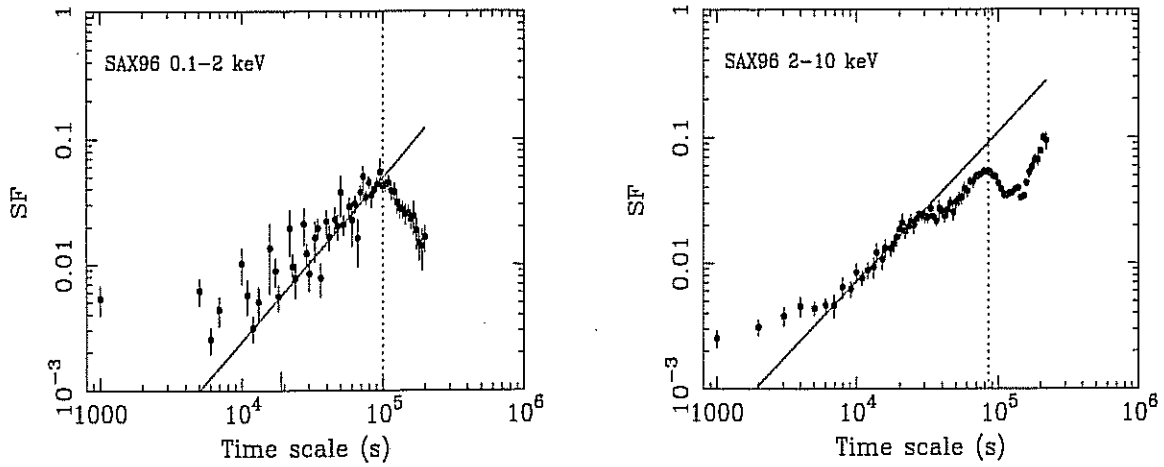

Figure 6.5: SF derived from the SAX96 light curve (binned in 1000 s) in the 0.1–2 keV (left) and 2–10 keV (right) bands, respectively. Solid and dotted lines have the same meaning as in Figure 5.7.

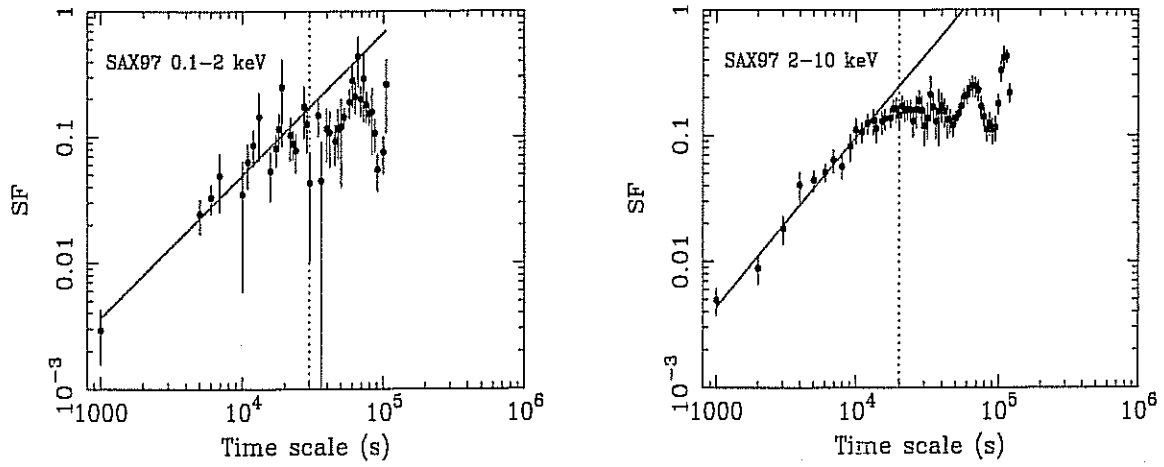

Figure 6.6: SF derived from the SAX97 light curve (binned in 1000 s) in the 0.1–2 keV (left) and 2–10 keV (right) bands, respectively. Solid and dotted lines have the same meaning as in Figure 5.7.

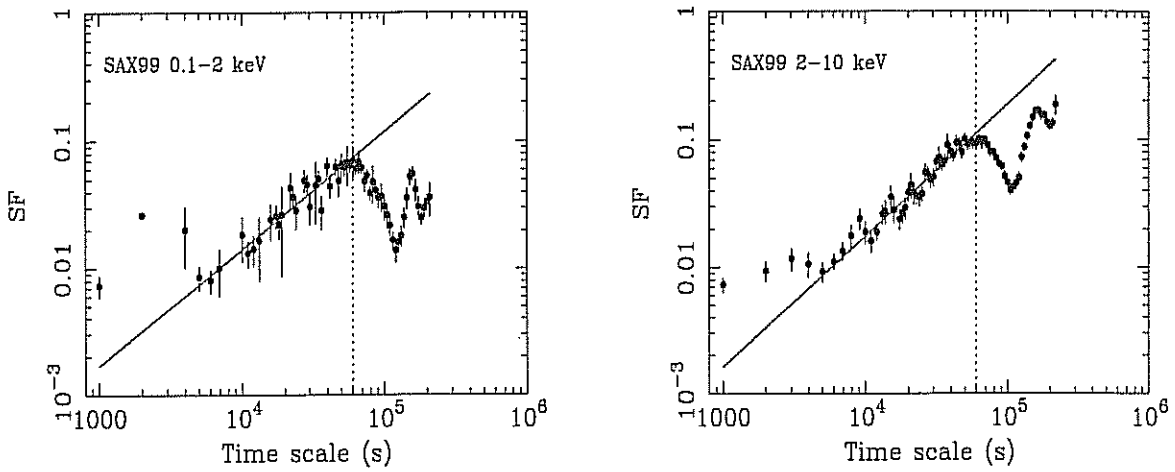

Figure 6.7: SF derived from the SAX99 light curve (binned in 1000 s) in the 0.1–2 keV (left) and 2–10 keV (right) bands, respectively. Solid and dotted lines have the same meaning as in Figure 5.7.

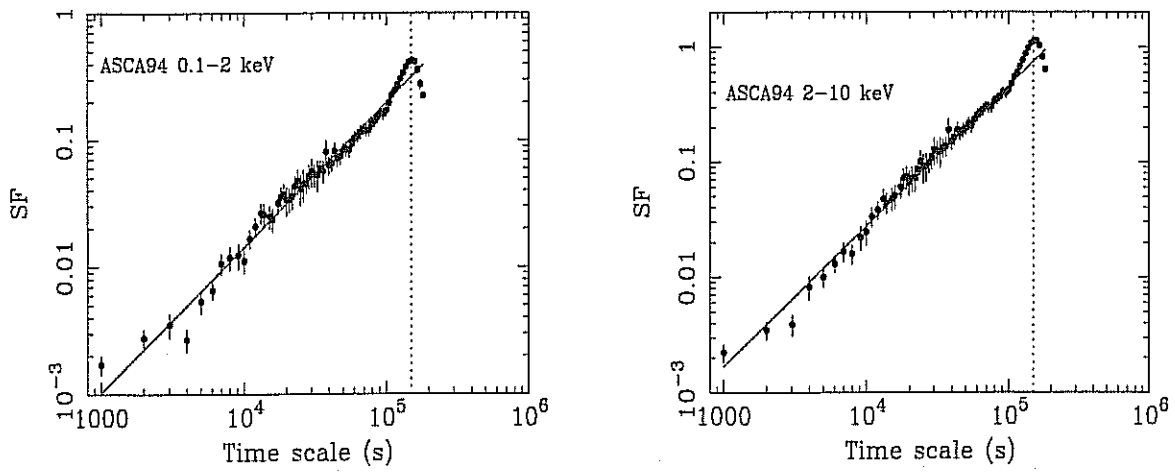

Figure 6.8: SF derived from the ASCA94 light curve (binned in 1000 s) in the 0.5–2 keV (left) and 2–10 keV (right) bands, respectively. Solid and dotted lines have the same meaning as in Figure 5.7.

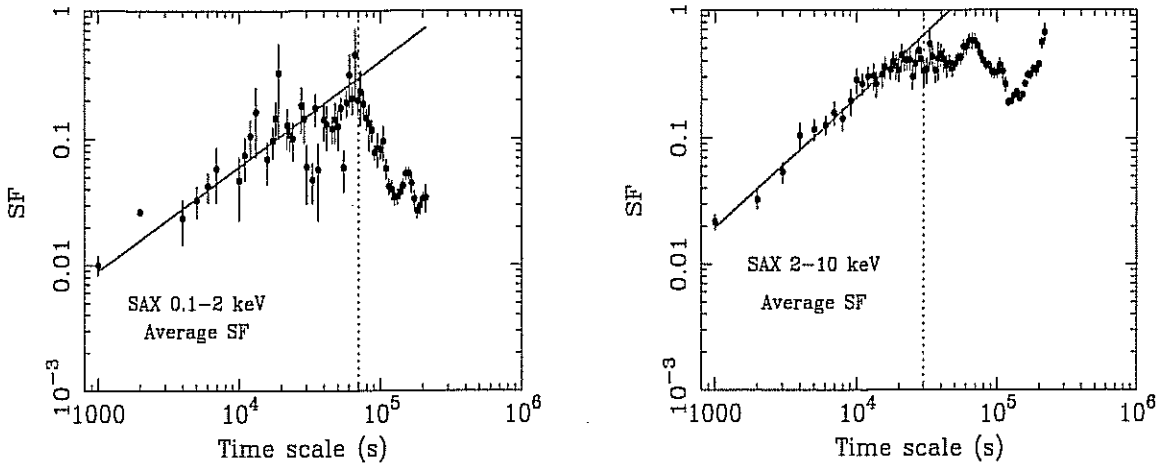

Figure 6.9: Average SF derived from the combined three *Beppo*SAX light curves (binned in 1000 s) in the 0.1–2 keV (left) and 2–10 keV (right) bands, respectively, but normalized to the mean count rate of 1999. Solid and dotted lines have the same meaning as in Figure 5.7.

Table 6.3: SF parameters

Date(UT)	slope		T_c (10^4s)	
	0.1–2 keV	2–10 keV	0.1–2 keV	2–10 keV
SAX96	1.26±0.24	1.17±0.10	10.	8.5
SAX97	1.13±0.13	1.13±0.06	3.0	3.0
SAX99	0.92±0.07	1.03±0.04	6.0	6.0
SAX mean	0.82±0.13	1.02±0.05	6.0	3.0
ASCA94	1.26±0.05	1.27±0.03	15.	15.

1. The SFs calculated from different campaigns show similar structures. A relatively steep slope at short time scales (high temporal frequencies) shows the variability decreasing quickly logarithmically with time scale from $\sim 10^5$ to 10^3 s, which is similar to those seen in MKN 421.

2. The fitting results show that the slope of the SFs, $\beta_{\rm SF}$, is larger than 1, this corresponds a slope of larger than 2 for the PDS.

3. The turn-over points range from $\sim 3 \times 10^4$ to $\sim 15 \times 10^4$ s.

4. It is of importance to note that, in the cases of SAX96 and ASCA94, one more time scale is clear before the characteristic time scale T_c where the pronounced turn-over occurs, indicating the source is not smoothly variable in some cases.

5. The shape of SFs is roughly independent of energy bands.

6.5 Power density spectrum analysis

AGN variability can be statistically characterized by its PDS. The PDS of very few Seyfert galaxies and PKS 2155−304 generally behave as power laws, proportional to $f^{-\alpha}$ over some temporal frequency range, where f is the temporal frequency (e.g., Edelson & Nandra 1999; Hayashida et al. 1998; Tagliaferri et al. 1991). For PKS 2155−304, the durations of the observations considered here are much longer ($\sim$ 2 days) than previous ones (e.g., EXOSAT), allowing us to determine the PDS over a range extending towards relatively lower frequencies. Because of low exposure efficiency of the LECS ($\sim$ 20%), here we focus on the SAX96 and SAX97 MECS and ASCA light curves in the 1.5−10 keV region.

For these observations, the PDS is calculated for the light curves with 10 s time resolution, as each PDS in our cases approaches (white) noise level before $\sim 10^{-2}$ Hz, clearly smaller than the Nyquist frequency of 5×10^{-2} Hz at 10 s bin size. The average count rate is subtracted from the bins before the PDS is calculated. In order to improve the signal-to-noise and study the mean variability properties of PKS 2155−304, the light curves are divided into several short intervals with each interval sampling 4096 points. The SAX97 light curve presents 3 good intervals; the SAX96 light curve has 4 good intervals, while we neglect the last part of the light curve which contains a long interruption towards the end of the observation; the ASCA94 observation is divided into 4 good intervals. For each light curve, the power spectra from each interval are then averaged.

The average PDS (after average noise subtraction) obtained in this way from each individual observation are shown in Figure 6.10a,b,c for SAX97, 96 and ASCA94 light curves, respectively. These are rebinned in logarithmic intervals of 0.18 (factor 1.5) to reduce the noise and allow the estimation of error bars. This means that the first point is still the lowest frequency point, but the second point is derived by averaging the next two points, etc. In such a way the PDS appear nearly equi-spaced in a log-log diagram. The expected (white) noise power level is subtracted (this level is about 1.5, 1.6 and 1.2 for SAX97, 96 and ASCA94 data, respectively) (see §4.5 for details about normalization, errors of PDS).

From Figure 6.10, one can see that each PDS shows a strong *red noise* spectral component which decreases with increasing frequencies, without any significant narrow feature that would be indicative of periodic or quasi-periodic variability. This component approaches the noise level at $\sim 6 \times 10^{-3}$ Hz for the SAX97, 96

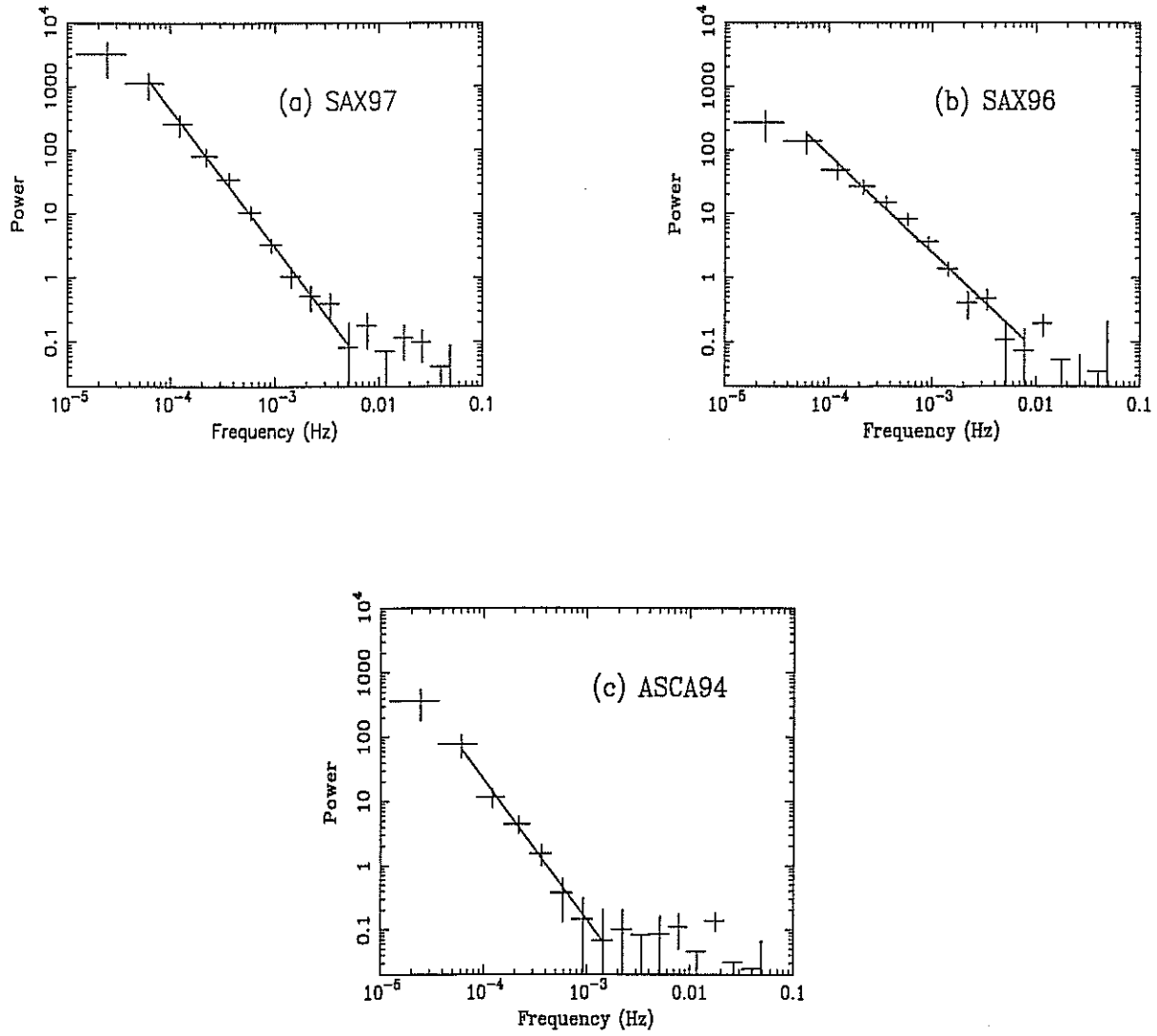

Figure 6.10: PDS with the best power-law fit (after average noise subtraction) in the 1.5–10 keV band. (a)SAX97; (b)SAX96; (c)ASCA94.

light curves, and at $\sim 1 \times 10^{-3}$ Hz for the ASCA94 data set. In addition, we note some differences among the three PDS. The SAX97 PDS clearly shows more power than the SAX96 one at lower frequencies, indicating a flatter PDS for SAX96 (this is easy to reconcile with the fact that $F_{\rm var}$ of SAX96 ($\sim$ 0.13) is much less than that of SAX97 ($F_{\rm var} \sim 0.3$)). The ASCA94 PDS has much less power than that of SAX97 over the whole range of temporal frequencies considered here, consistent with the fact that the ASCA94 PDS approaches the noise level at relatively lower frequencies. However, this does not agree with their corresponding $F_{\rm var}$ values. Let us consider the origin of this discrepancy. The SAX97, 96 light curves show more or less identical amplitude of variability over the whole observations, i.e., similar $F_{\rm var}$ for each interval, while the ASCA94 light curve does not present pronounced variability after the large flare at the beginning of the observation. Thus $F_{\rm var}$ for the ASCA94 dataset significantly changes from one interval to another, being about 0.23 and 0.11 for the flare and (almost) constant flux intervals of the ASCA94 light curve, respectively, but 0.35 when calculated over the whole duration. This makes the ASCA94 data set more variable if we consider it as a whole. For this reason we firstly compute the PDS in different intervals and normalized it so that the integral gives its own squared $F_{\rm var}$ value, and then obtained the average PDS by averaging the power spectra from each interval. Because the light curve of ASCA94 is characterized by different $F_{\rm var}$, we should use a mean value averaged from the (four) intervals considered in deriving the average PDS. This average $F_{\rm var}$, which is much smaller than those of the SAX97, 96 light curves, indeed agrees well with the average PDS. Note that instead, for the SAX97 and SAX96 light curves , the average $F_{\rm var}$ from each interval is identical to that of the whole observation.

Table 6.4: PDS parameters

Observation	**PDS slope**[a]	χ^2**(dof)**[a]
SAX97	2.17±0.10, 1.99±0.10	3.4(8), 9.0(8)
SAX96	1.54±0.07, 1.40±0.07	12.(9), 13.(9)
ASCA94	2.19±0.23, 2.15±0.49	1.1(5), 0.9(3)

[a]The fitting region is from $\sim 6 \times 10^{-5}$ to $\sim 6 \times 10^{-3}$ Hz (SAX97), $\sim 8 \times 10^{-3}$ Hz (SAX96) and $\sim 1.5 \times 10^{-3}$ Hz (ASCA94); the second values in this column refer to the PDS after the removal of a linear trend.

To quantify the slope of the PDS, power law model is fitted to each average power spectrum in the frequency interval $\sim 6 \times 10^{-5}$ to $\sim 6 \times 10^{-3}$ (SAX97, SAX96) or to $\sim 1.5 \times 10^{-3}$ Hz (ASCA94). The lowest frequency point of each PDS was

ignored because they tend to be more noisy, and also for comparison with previous PDS analysis. The best-fit power law slopes are $\sim 2.2, 1.5$ and 2.2 for SAX97, 96 and ASCA94 PDS, respectively. We also compute in the same way the average PDS after the removal of a linear trend from the light curves, in which the power law slopes for the "de–trended" PDS are consistent with the above values within 1σ, respectively. The fitting details are shown in Table 6.4.

6.6 Cross correlation analysis

As MKN 421 (§5.6), in this section we first perform cross-correlation analysis to find any possible time lag between the LE and ME2 bands, with FR/RSS Monte Carlo simulations performed on them. The energy-dependence of lag is postponed to §6.7.

SAX96

We first calculate the DCF and MMD for the whole observation. The resulting DCF and MMD between the LE and the ME2 band is shown in Figure 6.11, and the corresponding CCPDs are displayed in the left panel of Figure 6.13. These results suggest that PKS 2155−304 showed significant soft X-ray lags relative to higher energy X-rays. It is apparent from Figures 6.11 and 6.13 that the lags estimated with the DCF and MMD methods are compatible within the uncertainties of the FR/RSS Monte Carlo simulations, indicating the presence of a soft positive lag of $\sim$ 4 hours between the LE and ME2 bands. Soft lags of about 2 hours are also shown by the LE/ME1 and ME1/ME2 cross correlation functions. Note also that the soft X-ray lags in this case are the largest recorded so far for BL Lac objects in the X-rays.

To check time lag for the different parts as stated in Figure 6.1, we calculate again DCF and MMD between the LE and ME2 bands for the #1, #2 and #3 part of this observation. We can not determine well the time lags for the #1 and #3, though #1 suggest no time lag, and #3 indicate $\sim$ 1000 s soft lag. For the #2, the main flare during this campaign, pronounced soft lag is suggested: 5.60±0.64 ks (DCF) and 5.50±2.12 ks (MMD). Note that the soft time lag for this main flare is about half of time lag derived from the whole observation.

SAX97

We remind the reader that during SAX97 the source was in a relatively high state compared to SAX96, and variability was more pronounced. The DCF and MMD between the LE and ME2 bands derived from the whole observation is shown in

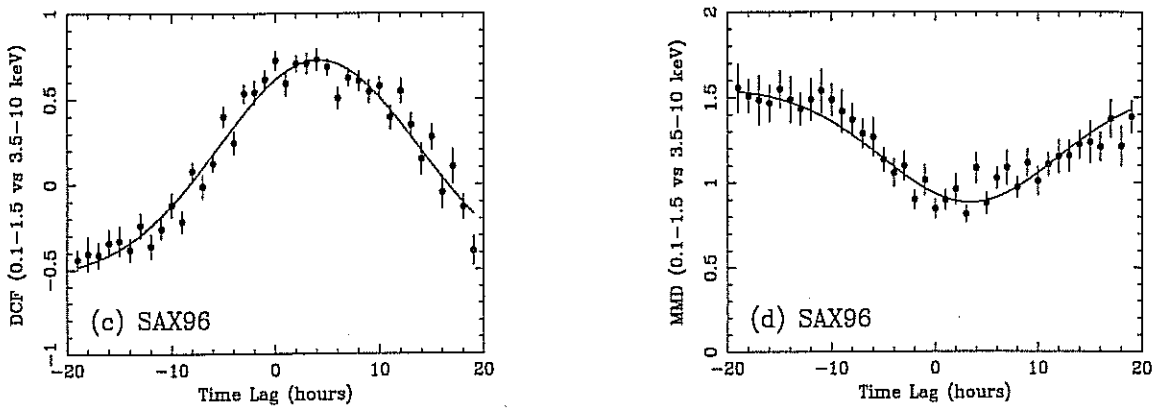

Figure 6.11: DCF and MMD between the 0.1–1.5 keV and the 3.5–10 keV band calculated from the whole observation of SAX96. The best fit consists of a Gaussian function plus a constant. The "true" time lag is taken from the time lag axis at which the Gaussian peaks.

Figure 6.12, and the corresponding CCPDs are displayed in the right panel of Figure 6.13. These analyses show a very short soft lag between the LE and ME2 bands ($\sim$ 1000 s), while the lags for LE/ME1 and ME1/ME2 are consistent with zero. The FR/RSS Monte Carlo simulations confirm these findings with high significance.

To determine the time lags for the different flares numbered in Figure 6.2, as in SAX96, we calculate again DCF and MMD functions between LE and ME2 bands for the three flares separately. The time lags of these three flares can not be well determined due to non-smooth DCF and MMD distributions, though the soft time lags can be constrained to be less than $\sim$ 2000 s for the three cases, which is consistent with those derived from the whole observations.

SAX99

Compared with the previous two campaigns, PKS 2155−304 is in a very faint period during 1999 campaign. However this observations comprise two isolated complete flares, give us a good opportunity to determine the time lags for the single flare in a faint state. We therefore perform a detailed cross-correlation analysis for the two flare separately, as numbered in Figure 6.3.

#1: We show DCF and MMD between the LE and ME2 bands in Figure 6.14, and the corresponding CCPDs are displayed in the left panel of Figure 6.16. It is clear that the source showed a pronounced soft lag, but suffering weak photon statistics. The estimated soft lag is 6.07±0.76 ks (DCF) and 4.93±1.28 ks (MMD), and the

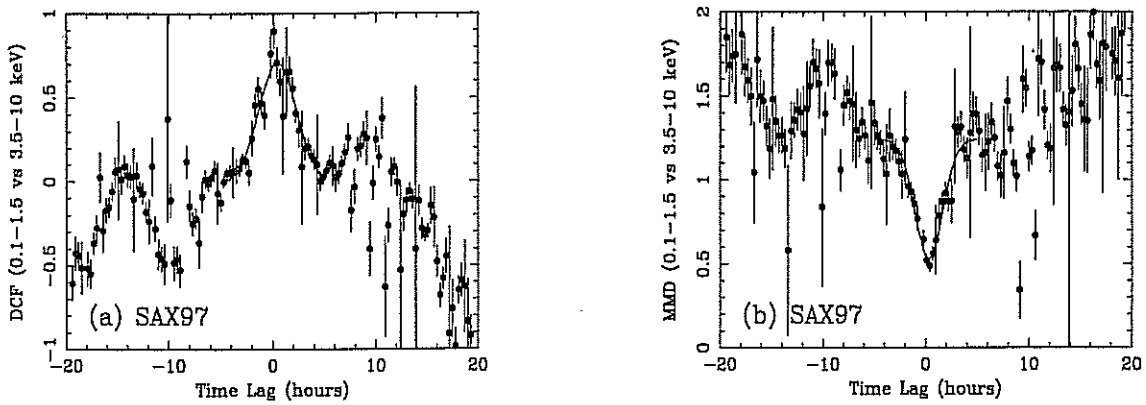

Figure 6.12: DCF and MMD between the 0.1–1.5 keV and the 3.5–10 keV derived from the whole SAX97 observations. The best fit consists of a Gaussian function plus a constant.

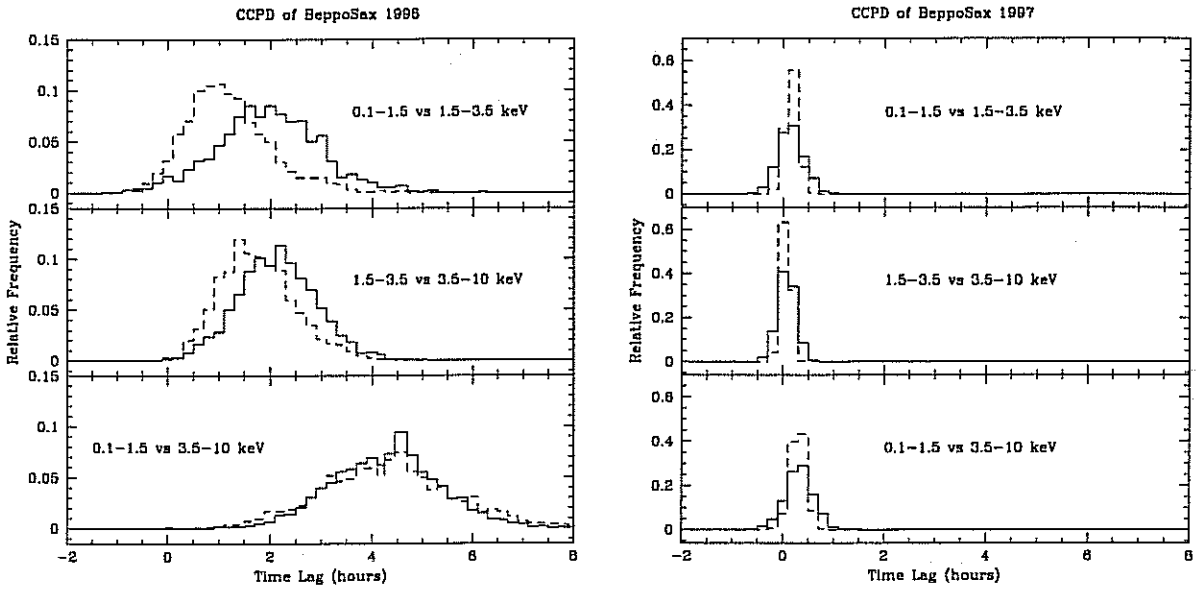

Figure 6.13: CCPD derived from the FR/RSS Monte Carlo simulations for the SAX96 (left) and SAX97 (right). The solid and dashed lines refer to DCF and MMD results, respectively.

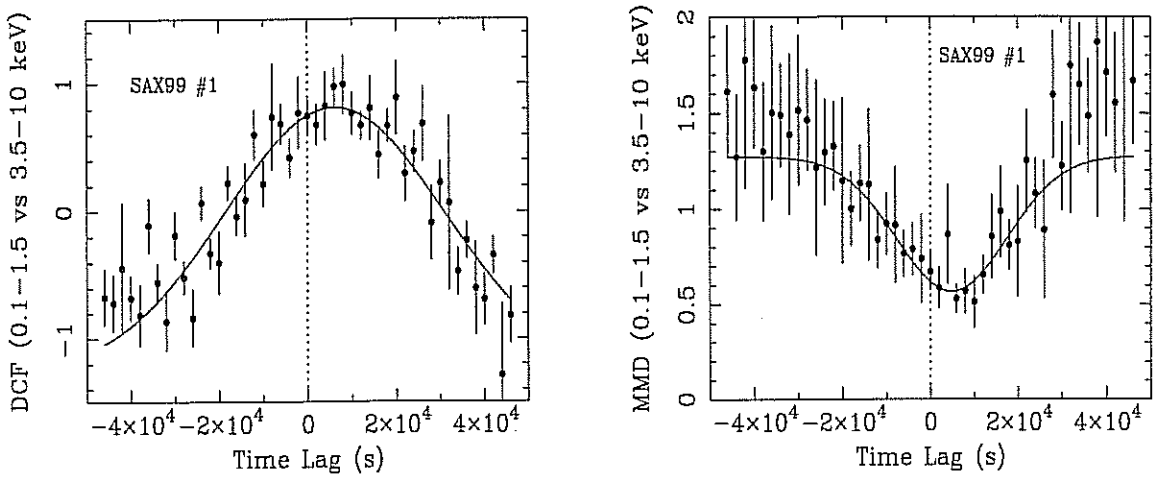

Figure 6.14: DCF and MMD between the 0.1–1.5 keV and 3.5–10 keV bands derived from the SAX99 #1 flare. The best fit consists of a Gaussian function plus a constant.

corresponding CCPDs suggest the soft lag with two-sided 1 σ error is $6.97^{+4.12}_{-4.31}$ ks (DCF) $5.72^{+4.45}_{-4.42}$ ks (MMD).

#2: this flare is weaker than #1. The derived DCF and MMD between the LE and ME2 bands and the corresponding CCPDs are displayed in Figure 6.15 and in the right panel of Figure 6.16. We note that time lags of #2 is similar to those of #1. The time lags estimated from the best fits to a Gaussian of the DCF and MMD is 6.56±1.13 ks and 9.29±2.40 ks, respectively, which is consistent with those estimated from the CCPDs: $5.80^{+5.23}_{-5.52}$ ks (DCF) and $8.57^{+5.15}_{-4.83}$ ks (MMD).

ASCA94

The DCF and MMD analysis between the 0.5–1.5 keV and 3.5–10 keV calculated from the whole light curve reveal soft lags of 3.17±1.08 ks (DCF) and 3.06±0.25 ks (MMD) (Figure 6.17), and the FR/RSS Monte Carlo simulations (see Figure 6.18) confirm these results with soft lags of $3.06^{+2.67}_{-2.52}$ ks (DCF) and $3.17^{+1.08}_{-1.08}$ ks (MMD). These results do not change significantly when we compute the DCF and MMD only for the flare #1.

* * *

To compare the time lags among different campaigns, we summarize the main results conducted in this section in Table 6.5 for the case between the 0.1–1.5 keV and the 3.5–10 keV bands.

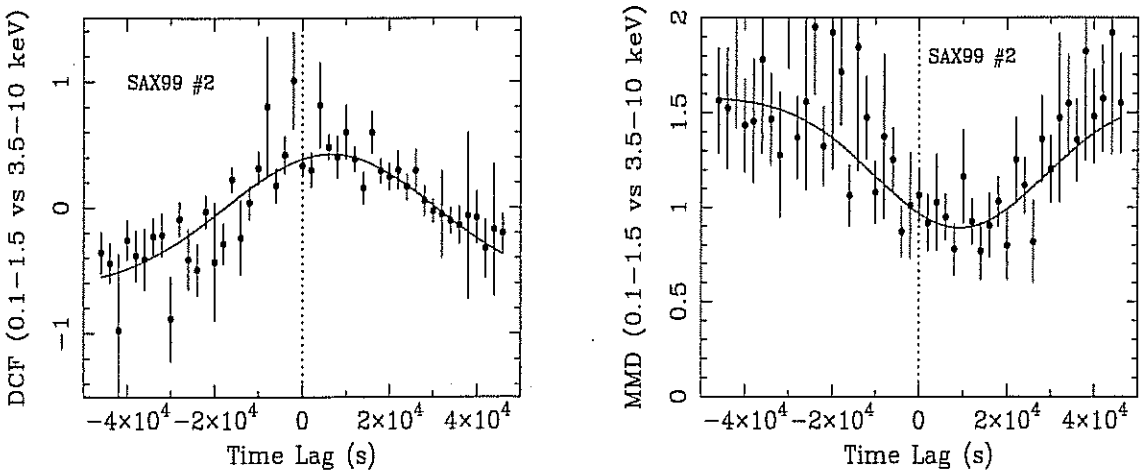

Figure 6.15: DCF and MMD between the 0.1–1.5 keV and 3.5–10 keV bands derived from the SAX99 #2 flare. The best fit consists of a Gaussian function plus a constant.

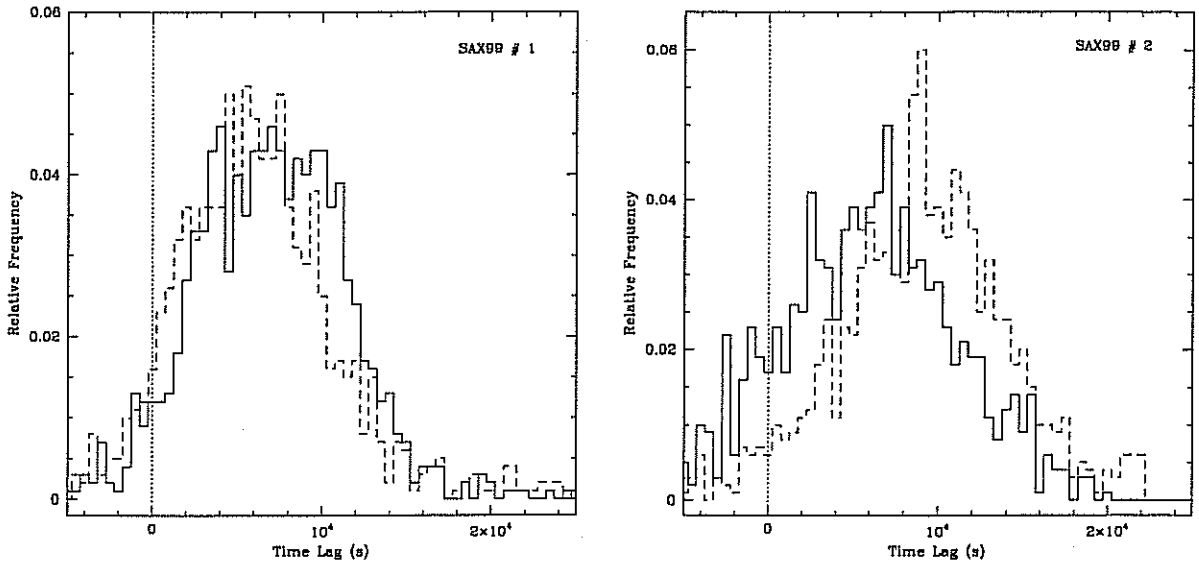

Figure 6.16: CCPD derived from the FR/RSS Monte Carlo simulations for the SAX99 #1 (left) and #2 (right) flare. The solid and dashed lines refer to DCF and MMD results, respectively.

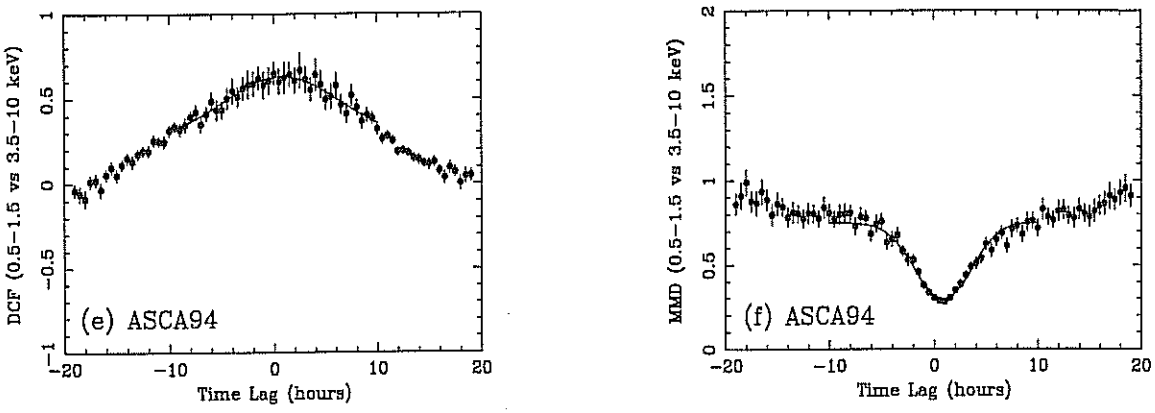

Figure 6.17: DCF and MMD between the 0.1–1.5 keV and the 3.5–10 keV from the ASCA94. The best fit consists of a Gaussian function plus a constant.

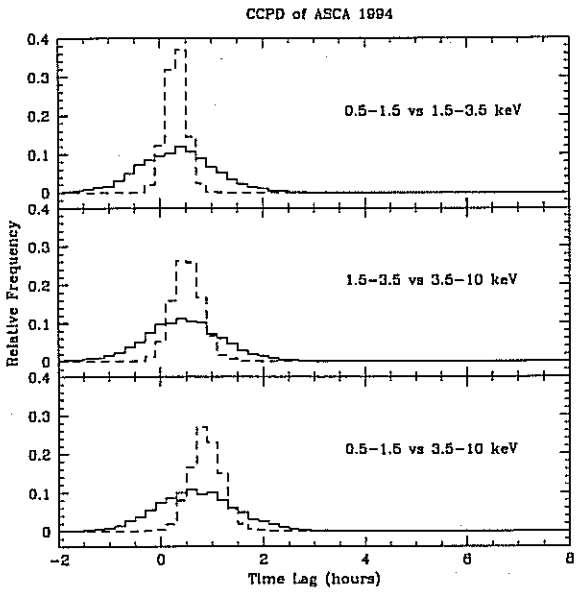

Figure 6.18: CCPD derived from the FR/RSS Monte Carlo simulations for the ASCA94. The solid and dashed lines refer to DCF and MMD results, respectively.

Table 6.5: Results of cross-correlation analysis (ks)

Date(UTC)	DCF	MMD	CCPD	
			DCF	MMD
SAX96 all	14.7±0.58	14.7±1.30	$15.4^{+3.71}_{-3.82}$	$15.4^{+4.68}_{-4.57}$
#2	5.60±0.64	5.50±2,12	...	...
SAX97 all	1.66±0.25	1.08±0.22	$1.15^{+0.97}_{-0.94}$	$1.13^{+0.50}_{-0.54}$
SAX99 # 1	6.07±0.76	4.93±1.28	$6.97^{+4.12}_{-4.31}$	$5.72^{+4.45}_{-4.42}$
# 2	6.56±1.13	9.29±2.40	$5.80^{+5.23}_{-5.52}$	$8.57^{+5.15}_{-4.83}$
ASCA94 all	3.17±1.08	3.06±0.25	$3.06^{+2.67}_{-2.52}$	$3.17^{+1.08}_{-1.08}$
#1	2.51±0.37	3.14±0.51	...	...

6.7 Energy-dependence of time lags

In last section, the issue to probe any possible time lag have been studied for the case of the 0.1–1.5 keV versus 3.5–10 keV energy bands. Among the 6 well defined flares, 4 are found to show pronounced soft lags, and 2 zero lags. We further quantify in this section the energy-dependence of time lags of PKS 2155−304 by dividing the 0.1–10 keV energy range into 6 narrow energy bands and measure the soft lags for each flare with respect to the 4–10 keV energy band. Both the DCF and MMD techniques are used, but we do not show the practical DCF and MMD distributions with their best fits to a Gaussian to determine the time lags. Moreover the FR/RSS simulations are not to be conducted.

The results of the energy-dependence of soft lags calculated for the SAX96 # 2 and ASCA94 # 1 are shown in Figure 6.19. Figure 6.20 is the energy-dependent soft lags against the energies for the SAX99 #1 and #2 flare, both show quite similar soft lags. The energy-dependence of soft lags for the three flares in SAX97 are not well constrained due to both the short duration and short soft lags, we will not discuss them any more in the following.

As in MKN 421, we discuss in the following the fitting results of the energy-dependent soft lags by using the synchrotron cooling time scale (equation [5.1]).

SAX96 #2: First we piont out the visible problems of DCF and MMD calculations. The first point in the figure (DCF between the 0.1–0.5 keV and 4–10 keV) is considerably below the fitting trend, and the corresponding MMD point is not shown because it even suggest hard lag. Given very poor representations of DCF and MMD, we can not discuss its insights. There is another MMD point (between LECS 1.5–2 keV and MECS 4–10 keV), the same problem as the above. In the

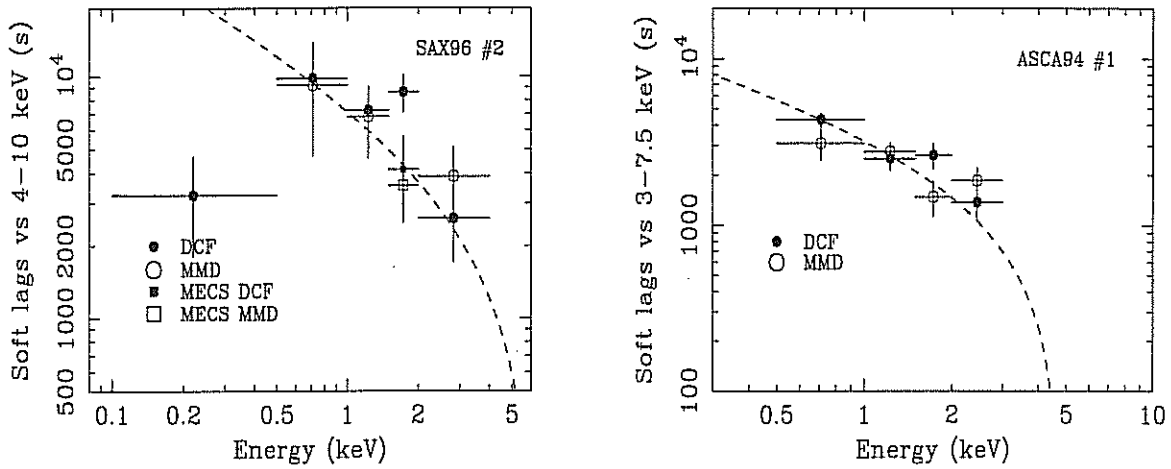

Figure 6.19: Energy-dependent soft lags of various X-ray energies compared to the 4–10 keV band photons, calculated from both the DCF (solid circles) and MMD (open circles). Left: SAX96 #2 flare; Right: ASCA94 #2 flare. The dashed line is the best fit with the energy dependence of the synchrotron cooling time scale.

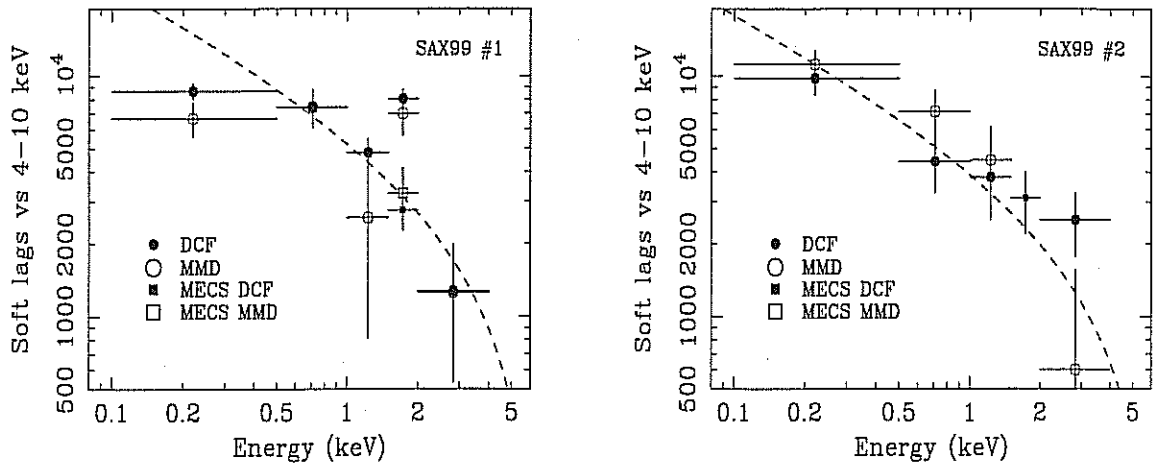

Figure 6.20: Energy-dependent soft lags of various X-ray energies compared to the 4–10 keV band photons, calculated from both the DCF (solid circles) and MMD (open circles). Left panel: SAX99 #1 flare (soft lag); right panel: SAX99 #2 flare (soft lag). The dashed line is the best fit with the energy dependence of synchrotron cooling time scale.

fitting we do not consider these points.

The best fit suggests that $B\delta^{1/3} = 0.40$ Gauss, and the fitting result is shown in the same figure as indicated by the dashed line. If we assume a typical value of $\delta = 25$ which accounts for the SED of this source (e.g., Kataoka et al. 2000), we have $B = 0.14$ Gauss.

SAX99 #1: we first point out that this flare happened in a quite faint brightness level, then the lags are not well determined due to poor statistics of photons in some cases, as seen from the left panel of Figure 6.20 (larger scatter of points appeared). The best fit suggests that $B\delta^{1/3} = 0.37$ Gauss, and the fitting result is shown in the same figure indicated by the dashed line. If assuming $\delta = 25$, we get $B = 0.13$ Gauss. The first point is not included during the fitting processes, as this point well below the dashed line, which is similar to the behavior in MKN 421 that the observed energy-dependence of soft lags flatten in the lowest energy. It is seen two times in MKN 421.

SAX99 #2: this flare shows very similar soft lags to its cousin flare #1. This flare is even fainter than #1, the problem of poor photon statistics works also in this flare. We then perform the fits with the energy-dependent synchrotron cooling time scale to this flare with the same initials of B and δ of #1 flare. The best fit gives $B\delta^{1/3} = 0.40$ Gauss. $B = 0.14$ Gauss is suggested if assuming $\delta = 25$. The magnetic field is same to that in #1 flare, if uncertainties of lags are considered. Another difference is that the energy-dependence of soft lags do not show clear flattening towards to the lowest energies, this is expected if the synchrotron peak frequency moves to lower frequency.

ASCA94 #1: in the case of ASCA94 #1 flare, we cut the energy bands as the exactly same way as in Kataoka et al. (2000) in order to compare properly each other, and the figure is also plotted in the same way (compare with Figure 4d of Kataoka et al. 2000). The DCF and MMD results are fully consistent with their results.

The best fit suggests that $B\delta^{1/3} = 0.65$ Gauss, and the fitting result is shown in the same figure as indicated by the dashed line. If $\delta = 25$ is assumed, we have $B = 0.22$ Gauss. We point out the difference between ours and theirs is different average coefficient in the equation of synchrotron cooling time scale (compare equation [5.1] and the equation appeared in § 2.2.1 of Kataoka et al. 2000), and they obtain $B = 0.13$ Gauss. After considering this difference, the two results agree completely even we only use the GIS2 data.

6.8 Discussion

The high degree of correlation and time lags between variations at different wavelengths provide strong constraints on the physical parameters of blazars. The previous multiwavelength monitoring campaigns of PKS 2155−304 found different variability behaviors (Edelson et al. 1995; Urry et al. 1997). In particular, the 1991 campaign showed the soft X-ray leading the UV by just $\sim$ 2 hours (the result of the cross correlation analysis was recently confirmed by Peterson et al. (1998) on the basis of simulations similar to those used in this thesis). However, during the 1994 campaign the UV lagged the X-ray by $\sim$ 2 days. Soft lags of $\sim$ 1 hour between the soft and the hard X-rays were first definitely quantified by the ASCA observations of MKN 421 (Takahashi et al. 1996) and PKS 2155−304 (i.e., ASCA94 data presented in this chapter; also see Makino et al. 1996, Kataoka et al. 2000), while EXOSAT observations of PKS 2155−304 showed no evidence of lags, with upper limits of a few hundred seconds (Tagliaferri et al. 1991). As we have stated at the beginning of this chapter, PKS 2155−304 is another HBL and shows very similar variability and SED behavior to MKN 421. It is thus of great importance to compare their variability (and SEDs) behavior in a systematic way: similar datasets sampled and same techniques. We have concentrated temporal X-ray variability behavior of these two HBLs with the same techniques, and dataset sampling are, at least on time scale of flare duration, comparable. They indeed show similar X-ray variability behaviors, supporting the idea that the same physical processes are taking place in their jets, but some differences also exist. In the following we will discuss the results of PKS 2155−304 presented in this chapter, and compare with those of MKN 421 from last chapter.

Structure of light curves: like MKN 421, *Beppo*SAX observations also demonstrate that PKS 2155−304 may repeatedly flare over time scales of about one day or over even faster time scales (ref. Figure 6.2). The quasi-symmetric structure of flares is also seen in most cases, and the duration of the flare is nearly independence of the energy. We explain that this kind of behavior can be accounted for by the fact that rapid local variability is relaxed (smoothed) by a light-crossing time scale (e.g., Chiaberge & Ghisellini 1999; Giommi et al. 1998) if the cooling time is shorter than light crossing time. In this scenario, the rising and falling phases of the flare are characterized by the same time scale $R/c\delta$ in the observer's frame, forming a quasi-symmetric shape of the flares. The best example of this behavior is clearly seen during the flare of the ASCA94 campaign (#1), from which the flare rising or decaying time scale is estimated to be $\sim$ 40 ks, and particularly the synchrotron

cooling time is $\sim$ 7.2 ks at 1 keV if using the best fit physical parameters from the energy-dependent soft lags, $B = 0.22$ Gauss and δ=25 (see 6.7). It can been seen that the synchrotron cooling time is much shorter than the light-crossing time, confirming that the flare is dominated by the light crossing time. However, at lower energies, e.g., 0.1 keV, where $t_{\rm cool} \geq R/c\delta$, it is possible that the symmetry of the light curves is broken and a longer decay time scale could be observed.

There are other effects that could also make the flares symmetric and have constant duration independent of the photon energies. We show here one example. Dermer (1998) found, assuming that the electron injection event continues for at least a light-crossing time, that the flare can become symmetric, with energy-dependent lag in the average time of the flare in various energy bands, and the average flare times can be nearly energy-independent if $t_{\rm cool}$ is less than or comparable to the injection time scale. However, it is very important to note that the above behaviors can be reproduced only when the particular electron injection distribution of $s = 2$ is selected (see equation [2] of Dermer 1998).

We thus believe that relaxing of rapid, local variability by light crossing-time effects must generally be important in blazar variability. In this scenario, as detailed simulations by Chiaberge & Ghisellini (1999), two of the most important variability behaviors, symmetric flares and soft lags, can be easily reproduced in spite of injection electrons features. This is consistent with the observations, in which flares with quasi-symmetric rising and decaying time scales have been observed many times from PKS 2155−304 in various states of activity with significant changes of X-ray spectral indices ranging from 1.0 to 2.5 (e.g., Sembay et al. 1993; Edelson el al.1995; Most flares from this chapter and see also Giommi et al. 1998, Chiappetti et al. 1999 and Kataoka et al. 2000). Symmetric flares have also been commonly found in other HBLs, e.g., MKN 421 discussed in last chapter, and PKS 2005−489 (Permann et al. 1999). To account for the general variability trends of PKS 2155−304, it thus seems that light-crossing time effects is preferablely included, as it is the case, we believe, to account for the inconsistence of the soft lags–fluxes trend between the observed one and the predicted one by simple homogeneous synchrotron model (see below). However, an important issue which have not been properly considered before is that energy-dependence of light-crossing time is necessary to account for phenonmenology of both the quasi-symmetric profiles and time lags from a flare.

Variability amplitude: the fractional *rms* variability parameter, $F_{\rm var}$, in the 0.1–2 keV and 2–10 keV for each campaign is shown in Table 6.2. It is clear that PKS 2155−304 is more variable in the hard energy band than in the soft energy band, regardless of sampling pattern and source brightness. This "normal" variability

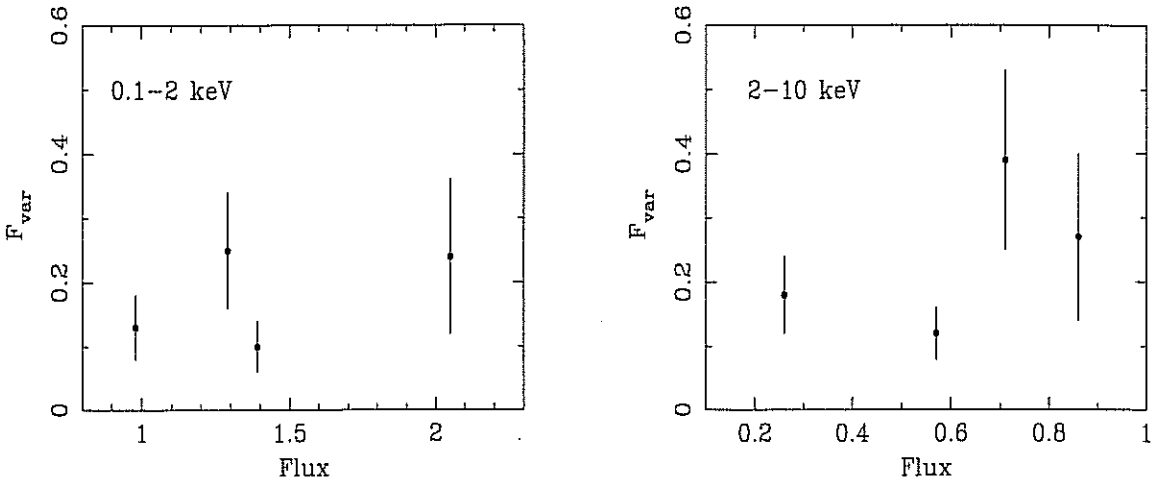

Figure 6.21: F_{var} is plotted against the flux of each campaign. Flux is in unit of 10^{-10} erg cm^{-2} s^{-1}.

behavior claimed before for HBLs have been confirmed with high quality *Beppo*SAX data by their two "classic" members, MKN 421 and PKS 2155−304.

We further show in Figure 6.21 the variability amplitude against the flux to see if there is positive correlation between variability amplitude and the source intensities. We find weak evidence that PKS 2155−304 is more variable when the source becomes brighter, this is somewhat *different* from the behavior found in MKN 421 (see §5.8), but need further studies and to be interpreted.

Variability time scales: like MKN 421, PKS 2155−304 shows shorter variability time scales with increasing energies, as quantified with the minimum doubling time scales in the 0.1–2 keV and 2–10 keV band light curves (Table 6.2), respectively, and this behavior is also independence of sampling pattern and source brightness.

Dependence of the minimum time scale on the source brightness is shown in Figure 6.22. There is weak evidence that the source shows faster time scale as the brightness increases, while SAX96 is always an exception.

In summary, the positive/anti- correlation between the variability amplitude/time scale and the source brightness is not well defined in MKN 421 and PKS 2155−304, though PKS 2155−304 shows weak evidence on such correlations.

SFs: the SFs of PKS 2155−304 are similar to those of MKN 421, also characterized by a relatively steep slop, $\beta_{SF} \sim 1.2$ (corresponding to $\alpha_{PDS} \sim 2.2$) in most cases, with a clear break at a characteristic time scale of ~ 1 day. It seems that this characteristic time scale for PKS 2155−304 is a little bit larger than that for MKN 421, this may relate to the source luminosity, as the luminosity of PKS 2155−304 is slightly

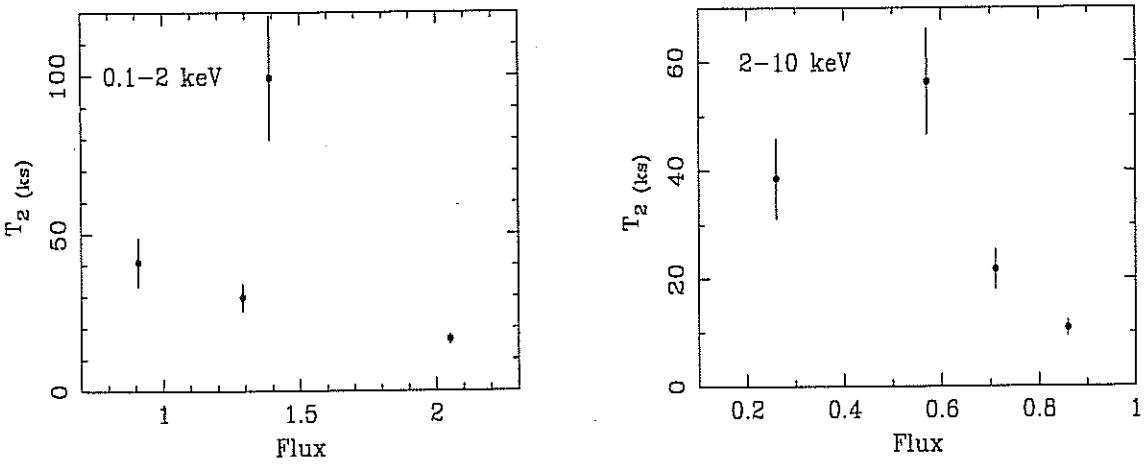

Figure 6.22: T_2 is plotted against flux of each campaign. Flux is in unit of 10^{-10} erg cm^{-2} s^{-1}.

higher than that of MKN 421.

As PKS 2155−304 is in very low state in SAX96 and SAX99, we may detected another time scale, minimum variability time scale, which the source variability emerge from the noise level, as seen from the fact that the SFs flatten at time scale of ~ 7 and ~ 5 ks, respectively. This feature is not present in SAX97 and ASCA94, also in all MKN 421 observations, may indicate the minimum variability time scales of shorter than 1000 s as they are brighter and the light curves are binned over 1000 s.

PDS: the powerful technique to statistically characterize the variability of a source is to derive its PDS. It should be noted that with the available data it is not easy to determine through the PDS the variability properties, e.g., dependence of variability on the frequency (or time scale) and typical variability time scale (e.g., characteristic time scale), as the light curves are usually sampled on a limited length with "serious" gap, and becomes very noisy over small time bins. Although the SF technique is more efficient than PDS when dealing with uneven sampled data, we still make an effort to derive the PDS of SAX96, SAX97 and ASCA94 data, as it is also important to compare the results from both methods. In general, the amplitude of variability decreases steeply as the time scales (temporal frequencies) become shorter (higher). Previous studies, mainly of Seyfert galaxies, show that their PDS can be approximated by power laws with slopes ranging between 1.5 and 2.0 (e.g., M^{c}Hardy 1999), providing valuable constraints to discriminate among possible models. However, the PDS of BL Lac objects has not yet been well studied in the X-ray band. The best determined PDS has been derived by Tagliaferri et al. (1991) for PKS 2155−304 us-

ing EXOSAT observations. An average power law slope of $\alpha \sim 2.5$ was obtained for the PDS in the 1−6 keV band, which however reduced to 1.9 after the removal of the linear trend (as required in that case). Our analysis shows, over the same temporal frequencies, that the slope of the average PDS from each observation is consistent within 1σ with that of the "de–trended" PDS derived from EXOSAT data. The fastest variability time scale inferred from the PDS may reach $\sim$ 1000 s, although this is largely uncertain because of the noisy PDS. We note that this time scale is consistent with that estimated from the PDS of the EXOSAT observations (Tagliaferri et al. 1991). Moreover, Paltani (1999) recently determined a similar minimum time scale ($\sim 600s$) from the EXOSAT data by using the structure function. Interestingly, the most rapid variability estimated from the "doubling time" in these observations occurred on a similar time scale ($\sim$ 1 hour), at least in SAX97. Of course, longer and uninterrupted X-ray monitoring will be crucial for constraining the PDS of blazars.

When comparing the results from the PDS and those from SFs, we find that the PDS slop is entirely consistent with those derived from the SF, by the relation of $\alpha_{\rm PDS} = \beta_{\rm SF} + 1$, for SAX97 and ASCA94 respectively. But for SAX96 PDS slope is flatter than that estimated from SF, with $\alpha_{PDS} - (\beta_{SF} + 1) = -0.7$, which may come from weak photon statistics in the PDS calculation of SAX96, as the source is fainter in this period.

Compared to the SFs, we do not see the characteristic time scale from the PDS analysis, which should be clearly seen from the "knee" (flattening) of the PDS at low frequencies. Since the light curves are folded to 3 or 4 intervals when calculating the PDS in order to improve the statistic significance, this making the lowest frequency (largest time scale) reached in the PDS smaller than the characteristic time scale detected in the SFs, and the "knee" in PDS corresponding to the "turn over" in SF can not been seen.

Recently, a good PDS is derived by Cagnoni, Papadakis & Fruscione (2000) for MKN 421 in the EUVE band with an extremely large database, and they have shown the PDS with power slope of $\sim 2.14 \pm 0.28$, also confirmed by the SF. This results is fully consistent with our results in the X-rays within 1σ, supporting that the same emitting mechanism, we believe the high energy tail of synchrotron process, operates in both energy bands. More importantly, the characteristic time scale, $\sim$ 3 days, derived in the EUVE from both the PDS and the SF, is larger than the those derived in the X-rays, this is a signature that the EUVE emission comes from the cooled energetic electron population with larger emitting region.

Time lag: the most significant results from this chapter is the detection of soft

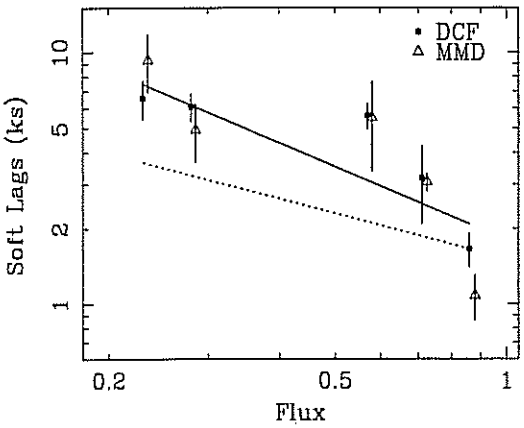

Figure 6.23: Soft lags (0.1−1.5 keV vs 3.5−10 keV) are plotted against the mean 2−10 keV fluxes. In order to show individual errors on lags of each flare from DCF and MMD respectively a small shift is applied to the fluxes. Solid line represent the best fit to a power law of the correlation, of which the best fit slop is ~ 0.97, with SAX96 clearly above the line. Dotted line refers to the relation predicted by the homogeneous synchrotron model, of which the slope is 0.6. It is clear that the observed slop is steeper than the predicted one. See text for details.

lags in all *Beppo*SAX and ASCA observations, and no hard lags found, and the soft lags in PKS 2155−304 are somewhat larger than those in MKN 421. However, it is important to note that hard lags have been detected in PKS 2155−304 from the RXTE observations (Sambruna 1999). The energy-dependence of soft lags in different flares are well fitted by the energy-dependence of synchrotron cooling time scales, and magnetic field B is constrained to be small values within a factor 2 changes.

We show in Figure 6.23 the dependence of soft lags (0.1–1.5 keV vs 3.5–10 keV) on the flare mean fluxes (2–10 keV). Interestingly, the correlation between the soft lags and the source fluxes is quite evident, indicating the lower intensity flares show larger soft lags. It is of great importance to note that this correlation is not found in MKN 421, where both soft and hard lags exist.

Obviously, the homogeneous SSC model is the simplest interpretation for the X-ray emission and overall spectral energy distribution (SED) of PKS 2155−304 (e.g., Chiappetti et al. 1999). According to this picture a quasi-stationary population of particles is responsible for a "quiescent" flux level, while flares result from a uniform injection and/or acceleration of relativistic electrons over a time interval Δt. The evolution of the particle distribution is governed by the radiative cooling through synchrotron emission which dominates in the X-ray band of HBLs, like PKS 2155−304. As the radiative losses are energy-dependent, that is, radiative

lifetime of electrons is inversely proportional to the emitted frequency, low energy photons are expected to lag high energy ones (e.g., Urry et al. 1997; Takahashi et al. 1996). In particular, within this simple scenario, it is possible to relate the observed time lag to the physical parameters of the source (see equation [2.43]; see also Tavecchio, Maraschi & Ghisellini 1998), and in the observer's frame this relation can be rewritten as (energy in unit of keV):

$$B\delta^{1/3} = 223.5 \left(\frac{1+z}{E_l}\right)^{1/3} \left[\frac{1-(E_l/E_h)^{1/2}}{\tau_{\rm obs}}\right]^{2/3} \text{(Gauss)} \qquad (6.1)$$

where E_l and E_h refer to the low and high X-ray energies (in unit of keV), and $\tau_{\rm obs}$ (s) is the observed lag between E_l and E_h photons. Under the synchrotron cooling assumption, the observed time lag τ_{obs} depends only on the magnetic field intensity B and the bulk Doppler factor δ of the radiating region. Although $B\delta^{1/3}$ can be obtained with a specific soft lag derived from two particular energy bands of a flare, it may largely change within a flare by using soft lags from different energy bands. We thus fit, more accurate, the energy-dependent soft lags to constrain $B\delta^{1/3}$ (see last section). Our results would imply $B\delta^{1/3} \sim 0.40$, 1.49, 0.37, 0.40, and 0.65 Gauss for SAX96 #2, SAX97, SAX99 #1 and #2, and ASCA94 #1 flares, respectively. Note that the value for SAX97 is only derived from soft lag between 0.1–1.5 keV and 3.5–10 keV energy bands of the whole observation, as explained in last section. Interestingly, Chiappetti et al. (1999) found that the model parameters derived through the fitting of the broad band spectrum during the SAX97 observation are consistent with that estimated from the observed soft lag.

A further piece of information is given by the trend between observed soft time lags and fluxes (see Figure 6.23). If we, for example, assume that δ has not changed, the simplest scenario would suggest that B varied by a factor ~ 4 from SAX96 to SAX97. Although qualitatively consistent with the variation in the flux, this can not quantitatively reproduce the observed correlation. In fact, under the (simplistic) assumptions of variations occurring only in the magnetic field, one would expect $F \sim B^{1+\alpha_{\rm x}}$ and $B\delta^{1/3} \sim \tau_{\rm obs}^{-2/3}$, thus implying that the relation between intensity and lag is given by $F \sim \tau_{\rm obs}^{-2(1+\alpha_{\rm x})/3}$ (assuming δ constant), where $\alpha_{\rm x}$ is the X-ray spectral index. For PKS 2155−304 the average $\alpha_{\rm x} \sim 1.5$, we then have $\tau_{\rm obs} \sim F^{-0.6}$. The predicted relation between the lags and the fluxes under this hypothesis is also shown in Figure 6.23 (dotted line), where it can be clearly seen that this is much flatter than that of the observed one between all of the observations. To compare the trend between the predicted and observed slope, we fit the observed trend with a power law, and the best fit is also shown in the same figure (solid line) with a slop of 0.97. Therefore, as one might expect, other physical quantities, such as the density

and energy spectra of the electron population and/or the Doppler factor, have to vary if the observed relation between flux and lag holds within the homogeneous SSC scenario.

We (qualitatively) stress again that the fact that the observed flux–soft lags trend is steeper than the predicted one by homogeneous synchrotron model could be associated with the importance of light-crossing effects with respect to the cooling time (ref. above). A more intense flux could be associated with relatively efficient dissipation, e.g., occurring at a shock front, which for a quasi–planar geometry (shock-in-jet model, in which a thin shock wave moves down a cylindrically symmetric jet, Marscher & Gear 1985) could imply that light-crossing effects do not dominate, and thus small time lags. A low source state, more similar to the quiescent underlying jet emission, might be associated with an acceleration/injection of particles in a larger region: due to significant light-crossing effects, the observed variability would be smoother and result in larger time lag between different frequencies. Interestingly the characteristic time scales estimated from SFs indeed suggest larger size of the emitting region when the source is fainter, and SAX96 deviate the observed trend with largest amplitude, suggesting larger emitting region is possible. The role of light-crossing time in producing soft lags is that this effect may indicate larger magnetic fields than the ones derived from fitting the energy-dependent soft lags where this effect is not considered.

In order to interpret the inter-band variable time lags, the development of time dependent models taking into account the effects of particle injection/acceleration, cooling and diffusion would be required. However, the time dependent problem is in general very complicated and only some simplified and specific cases have been considered so far. Mastichiadis & Kirk (1997) showed that, within the assumptions of a homogeneous SSC model, an increase in the maximum energy of the injected electron population can reproduce the rapid X-ray flares as well as the spectral evolution of blazars like MKN 421. Interestingly, they also show that these features cannot be due to changes of both the magnetic field and the amount of injected electrons. In addition, Chiaberge & Ghisellini (1999) pointed out the importance, for both spectral evolution and time lags, of delays due to light crossing the radiating region. This effect is superposed to the wavelength dependent time scales due to the different cooling times of radiating electrons. In contrast to the above studies, Georganopoulos & Marscher (1998) modeled, using a time-dependent inhomogeneous accelerating jet model, the evolution of flares during the two multiwavelength campaigns on PKS 2155−304 . Within this scenario, the different variability features could be reproduced by assuming that plasma disturbances with different physical

properties occur in an underlying jet characterized by the same physical parameters. The small time lag between the UV and X-ray bands in the 1991 November campaign would indicate quasi-co-spatiality of the regions radiating at these frequencies, assuming an injected electron distribution similar to that characterizing the underlying jet emission. However, the clear time lag between these same bands in the 1994 May campaign are interpreted as an indication of spatial separation of the emitting regions. The separation can be due to the propagation downstream of the electrons while progressively radiating at lower frequencies. This however also requires the injected electrons to be narrower in energy than during the 1991 November event.

* * *

Clearly, in order to pin down the origin and nature of variations, both systematic observational trends and a thorough analysis with the different models are needed. In this work, we have concentrated on the first aspect, but let us show here as an example the simulated results by Kataoka et al. (2000) for the ASCA94 flare behavior, to have an initial impression on how the soft lags can be reproduced from the energy-dependent cooling time scale and the role of the light-crossing time in producing symmetric flares and soft lags. Another similar example is given by Chiaberge & Ghisellini (1999) for the MKN 421 1994 flare observed by ASCA (Takahashi et al. 1996).

The time-dependent model is qualitatively similar to the one used in MKN 421 in §5.8, but without acceleration term to account for soft lags (ref. §2.6.1) with following assumptions: a one-zone homogeneous and spherical symmetric SSC emitting region, incorporating radiative cooling processes, particle injection and escape. Electrons are injected uniformly throughout a homogeneous emission region, which is possible if the injection duration is comparable to R/c, but not physical for shorter injection time scale since the particle injection process itself should take (at least) $\sim R/c$ to influence the whole emitting region. A more realistic picture for particles injection is a thin shock front which may propagate through the emission region with a finite velocity v_s, supplying freshly accelerated electrons only in the front's vicinity (Kirk, Rieger & Mastichiadis 1998).

Light crossing time effects are simply incorporated by dividing the whole source into $(t_{\rm crs}/\Delta t)$ slices of equal ΔR thickness, where $t_{\rm crs}$ $(= R/c)$ is the source light-crossing time and Δt is the time-step of the calculation. The interval Δt must be shorter than the shortest relevant time scales, e.g., the synchrotron or Compton cooling time scales or the injection time scale.

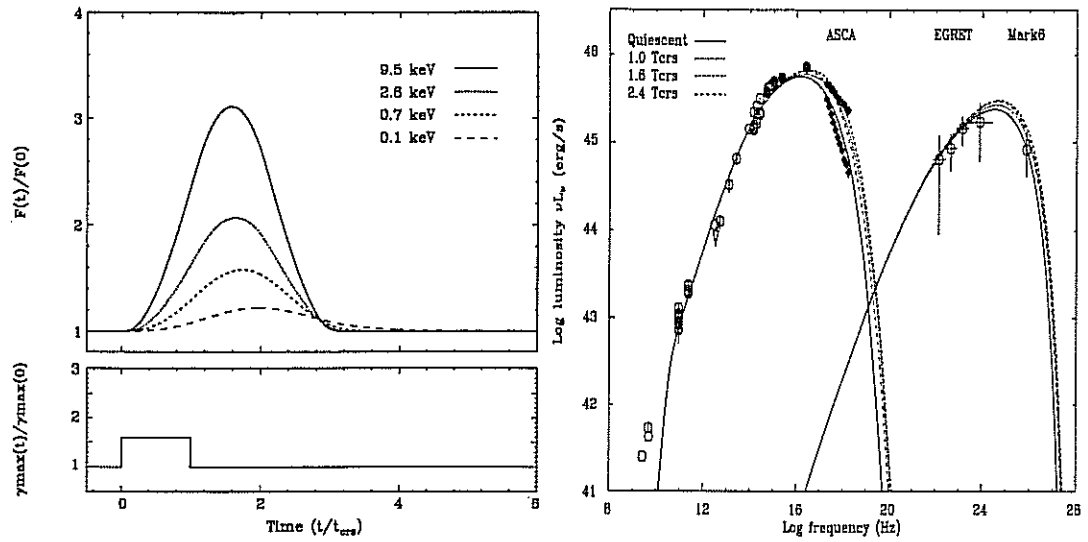

Figure 6.24: Left: simulated light curves at different X-ray energies, reproducing the rapid ASCA94 flare; Right: simulated multi-wavelength spectra at $t/t_{\rm crs}$ =0, 1.0, 1.6 and 2.4 are shown respectively. See Kataoka et al. (2000) for detailed observed data descriptions. Quoted from Kataoka et al. (2000).

All the physical parameters for the emitting region were self-consistently determined from seven observables (See Table 1 of Takaoka et al. 2000) in order to produce first a steady source state. The ASCA94 flare is then modeled as an increasingly extension of steady injection electron spectrum with $\gamma_{\rm max}$ to $1.6\gamma_{\rm max}$ for a flare, but electron spectral index is reserved, which continues for one source light-crossing time scale, $t_{\rm inj} = t_{\rm crs}$. If the injection results from a shock propagating with velocity $v_{\rm s}$ through the emission region, the duration of the injection event should be characterized by the shock crossing time scale, $R/v_{\rm s}$ (e.g., Kirk, Rieger & Mastichiadis 1998). Thus the assumption of $t_{\rm inj} = t_{\rm crs}$ corresponds to a highly relativistic shock, $v_{\rm s} \sim c$. Furthermore this kind of injection may also correspond to a new population of electrons injected with an electron distribution available up to higher energies during a flare, since electrons with larger γ require a longer time to be accelerated (e.g., Kirk, Rieger, & Mastichiadis. 1998), so the assumption of an increase in $\gamma_{\rm max}$ can be a good approximation as long as the acceleration time scale $t_{\rm acc}$ at $\gamma_{\rm max}$ is well shorter than $t_{\rm cool}$. Other scenarios for the flare, such as increasing the injected density $q_{\rm e}$ or the magnetic field strength B, can not reproduce well the flare (see also Mastichiadis & Kirk 1997 for MKN 421 case). In a more realistic scenario, of course, all of these parameters probably vary simultaneously, for example, increasing magnetic field B when the source increase the intensity, which is seen from the fitting results of the energy-dependent soft lags in different flares. But the most essential parameter to be changed during a flare should be $\gamma_{\rm max}$.

The simulated light curves and spectral evolution are shown in Figure 6.24. It can be seen that the symmetric flare is reproduced quite well, and it is clear that the peaking time of the flare at lower energies lags behind that at higher energies, with the flare amplitude becomes larger as the photon energy increases, which agree qualitatively with the observational data. To make a quantitative comparison of the variability behaviors between the observed and modeled flare in different energy bands, the simulated light curves and spectra are analyzed in the same way as that for the observational data, they match well each other, in particular a soft lag where the 0.1–1 keV photons lag behind 5 keV photons about $\sim$ 4 ks, implying that the observed soft lag is well represented by an incorporation of the energy-dependent synchrotron cooling time scales and light-crossing time.

>>>>>>

Chapter 7

X-ray Variability of Blazars

In the last two chapters, §5 and §6, we have performed a comprehensive temporal analysis for MKN 421 and PKS 2155−304 by the *Beppo*SAX observations. One clear question one may ask is how other blazars behaves and whether there is any variability trend in blazars. To answer this question, we start, by using public *Beppo*SAX database, to study and compare temporal and spectral variability of blazars.

7.1 Introduction

X-ray variability has long been known to be a common property of AGNs, which is observed on time scales from $\sim$ a thousand seconds to years and variability amplitude of up to an order of magnitude are observed in the $\sim$ 0.1–10 keV band (e.g., M$^{\rm c}$Hardy 1990; Grandi et al. 1992; Mushotzky, Done & Pounds 1993 for a review). In particular, there are a series of papers dedicated to the studies of the X-ray variability trend in AGNs. Barr & Mushotzky (1986) suggested the X-ray (flux) doubling time scale of an AGN to be proportional to its luminosity, this study involved a small sample of BL Lac objects. Lawrence & Papadakis (1993) confirmed the variability-luminosity relationship, quantifying variations seen in EXOSAT light curves by using the time scale above which the integrated *rms* variation should be 10%. Green, M$^{\rm c}$Hardy & Lehto (1993) also confirmed the correlation using the "normalized variability amplitude" and further, suggested sources with steeper X-ray spectra showed the highest amplitude of variability.

Recently *excess variance*, $\sigma^2_{\rm rms}$, has been suggested to be a good indicator to quantify the X-ray variability of AGNs. Edelson, Krolik & Pike (1990) previously used this quantity in the ultraviolet time series of AGNs and found an anti-correlation between excess-variance and luminosity. Nandra et al. (1997) examined ASCA

observations for a sample of Seyfert 1 galaxies with predominantly broad permitted lines (BLS1), and found an inverse correlation between X-ray variability and luminosity. In comparison, Leighly (1999) found the excess variance from ASCA observations of narrow-line Seyfert 1 galaxies (NLS1) is inversely correlated with their X-ray luminosity, and the excess variance of NLS1 is typically an order of magnitude larger than those of BLS1 at a particular X-ray luminosity. Turner et al. (1999) combined the above two studies and find similar correlations, and confirm that the sources with steeper spectra show stronger variability.

The same correlation is also found in radio-quiet quasars (RQQs). Fiore et al. (1998) studied the soft X-ray variability of six low redshift, radio-quiet PG quasars using ROSAT HRI observations, finding steep-spectrum, narrow-line quasars to show larger amplitude of X-ray variability in the 0.1–2 keV band than the flat-spectrum broad-line quasars. George et al. (2000) used ASCA observations to show that the variability characteristics of the PG RQQs is consistent with Seyfert 1 galaxies. A flux limited sample of faint QSOs with large redshift range, selected from the ROSAT survey, showed that variability amplitude declines sharply with luminosity, but with a suggestive upturn for the most powerful sources (Almaini et al.). We would remind the reader that the above studies are almost for radio-quiet AGNs.

Rapid variability has been reported to be a characteristic of blazars, but how common is it in the *Beppo*SAX observations? Is there any variation trend? In contrast to those of Seyfert galaxies and other radio-quiet AGNs, the X-ray variability trend of blazars, also other radio-loud AGNs, are not known in much detail. In contrast, SED trend of blazars is well established (e.g., Fossati et al. 1998), but it is not still clear about their variability trend. An earlier study by Giommi et al. (1990) with EXOSAT data failed to derive the variation trend in blazars due to very sparsely data and short duration, and they found no obvious differences in the X-ray variability properties of HBLs and LBLs. In order to characterize the X-ray properties of blazars we have started a systematic analysis of archival *Beppo*SAX data, in particular to see if some variability trends seen in radio-quiet AGNs also exist in blazars.

The information of the X-ray properties in blazars is of particular relevance, since in this band both the synchrotron and inverse Compton processes can contribute to the emission, in a way of single or a mixture of two components, possibly depending on the source's total luminosity. It is clear that in this band the two components have different spectral and variability properties, synchrotron emission is characterized by a steep continuum ($\alpha > 1$), and strong and rapid variations of intensity, while

low energy end of inverse Compton component in the X-rays of blazars, regardless of seed photon origins, would give rise to a flat X-ray spectrum with low amplitude of variability. Therefore, the spectral and temporal properties in this band can give a fundamental hint for disentangling the two components, and correlations of variability and spectral parameters is of particular relevance.

On the other hand, as we have shown in last two chapters, X-ray variability of MKN 421 and PKS 2155−304 is dominated by the light-crossing time scale. The inverse correlation between variability amplitude and luminosity found in radio-quiet AGNs might be explained if more luminous sources are physically larger in size, and examination of such a trend in blazars will show whether the size in blazars are luminosity dependent, and what dominate variability of blazars.

*Beppo*SAX observations are conducted continuously, in particular a sizable observations over a long time scale (e.g., days) exist, therefore they present an opportunity to systematically investigate the X-ray variability properties of blazars, although such studies are not without difficulty due to the gaps imposed by earth occultation and periods of high background.

One main goal of this chapter is to look for the X-ray variability trend in blazars. As the study is in progress, we can only present here a part of very preliminary results from such an analysis.

We organize this chapter as follows. The sample and data collection is described in §7.2; In §7.3 we perform a simple χ^2 test and calculate *excess variance* on each light curve. Spectral analysis is performed in §7.4; we show some correlations of variability and spectral parameters in §7.5; A brief discussion on our results is given in §7.6.

7.2 The sample and data

The publically available observations of blazars by 31 December 1999 were analyzed. All of the data had undergone various revision as reprocessed at *Beppo*SAX SDC, and were reduced individually using *Xselect* from the unfiltered events files. The source name, redshift, and *Beppo*SAX sequence are given in the first three columns of Table 7.1–7.5 for TeV sources, HBLs, LBLs, HPQs and LPQs, respectively.

In the following analysis we first use data from the MECS instruments only, and the light curves and spectra are selected from the merged event files of 2 or 3 MECS units.

7.3 Timing analysis

The light curves are rebinned over 5700 s ($\sim$ 1 orbit), and required that time series included in our analysis have at least 20 counts per time bin. The reason for choosing large time bin is that most of LBLs and FSRQs are quite faint and analysis using a small time bin (e.g., 256s) would have lead to the exclusion of many potentially interesting sources, while this would have resulted in too few bins for many datasets. The background level was not subtracted from these light curves.

7.3.1 χ^2 test

We first make a simple χ^2 test on each individual light curve to test for variability against the null hypothesis that the flux is constant. The resulting χ^2 is shown in the 8th column in Table 7.1–7.5, respectively.

For MKN 421, 8 of the 10 light curves show variability at greater than 99.9% confidence, 1 at greater than 98% confidence, and 1 non-variable. In MKN 501, 6 of the 10 light curves show variability at greater than 99.9% confidence, 4 at greater than 95% confidence. All the three observations of PKS 2155−304 show variability at greater than 99.9% confidence. Two observations in 1ES 2344+514 are variable at greater than 99.9% confidence, and others are not variable.

Among 19 observations of HBLs, only one show variability at greater than 95% confidence. For LBLs, 7 of 19 light curves show variability at greater than 95% confidence. In 14 observations of HPQs, only one is variable at greater than 95% confidence. One of 8 observations in PKS 0528+134 is variable at greater than 98% confidence, and 2 of 5 light curves of 3C 273 show variability at greater than 99.9% confidence.

It is important to stress that the non-detection of variability in many sources does not imply that no variations is occurring since intrinsic variations which are present are simply overwhelmed by photon noise. The detection of significant variability depends on the amplitude of intrinsic variations and on the signal to noise. As expected, it can been seen that the fraction of significantly variability increases with higher flux.

7.3.2 Excess variance

The excess variance quantifies amplitude of intrinsic variability of a source in excess of that expected from statistical fluctuations in the background level. To compare light curves with different count rate in a meaningful way, all light curves are first

normalized by their mean count rates. The excess variance is calculated by numerically solving Equation 4.13 for each light curve. The maximum likelihood estimates for the excess variance (with 68% confidence ranges) are displayed in the 6th column in Table 7.1–7.5, respectively. As expected, for most faint sources individually we can only estimate upper limits for the excess variance. The correlations of excess variance with other parameters is discussed in §7.5.

We note that for perfect comparison between sources, the excess variance should be calculated using observations of the same duration (T_d). However, in practice this would limit the analysis by reducing the number of sequences we could consider, or would require truncation of light curves to match the shortest observation. We note many of our light curves were constructed from observations of duration close to 50 ks. The data includes observations both a factor of 2 smaller and larger than this, and very few observations with very short or long duration. As the duration of an observation is random with respect to the parameters of interest then the effect of allowing a range of observation durations is to introduce scatter, which could hide some weak correlations but which should not introduce false correlations, if assuming that T_d is not correlated with excess variance, photon index Γ, and luminosity.

7.4 Spectral analysis

It is evident that blazars with different X-ray spectra may have different variability characteristics, which may occur between different observations of individual sources, and between sources. To search for correlations between X-ray spectra and luminosity/variability amplitude we determine the photon index of our sample by perform a spectral fit to the 2–10 keV energy range.

Although many of the spectra have been published by other authors in a comprehensive way, we re-calculated all the energy spectrum parameters ourselves in the same manner in order to retain continuity throughout the work. We derived the spectral parameters by fitting a single power law spectrum with a free absorbed column density to the background-subtracted MECS spectra in the 2–10 keV energy range extracted from the *Beppo*SAX data base. Although this model is not necessarily the best-fitting model it does enable us to obtain a reasonable value for the average photon index, flux and hence luminosity, which can be used in correlations. Choosing a free column density to the spectral fits, while unphysically, do reduce χ^2 significantly.

The MECS spectra have been rebinned using the grouping templates available at *Beppo*SAX SDC, and the background has been evaluated from the blank fields pro-

vided by the *Beppo*SAX SDC, using an extraction region similar in size and position to the source extraction region. The November 1998 release of public calibration files, matrices and effective areas was used [1].

The 2–10 keV energy range flux (10^{-12} erg cm^{-2} s^{-1}), luminosity (erg s^{-1}), and photon index (with 90% confidence errors) are given in 4th, 5th and 7th columns of Table 7.1–7.5, respectively. The luminosity was calculated by using the following cosmological parameters: $H_0 = 50$ km s^{-1}Mpc^{-1} and $q_0 = 0.5$.

7.5 Results

While we have showed parameters for all observations, we first stress two aspects in the following discussion: (a) all individual observations of 4 TeV sources, regardless of duration, this result in total 29 observations; (b) the observations with duration greater than 80 ks, regardless of source classification, and this produce total 17 observations. Other aspects of the analysis will be discussed in the future, since we need to analyze all data in a more rational way.

7.5.1 TeV blazars

The results for the 4 TeV blazars, with different symbols, are shown in Figure 7.1 in three correlations respectively: (a) excess variance against luminosity; (b) photon index against luminosity; (c) excess variance against photon index.

In Figure 7.1a, it is clear that there is no significant anti-correlation between excess variance and luminosity, in contrast with the "normal" trend seen in radio-quiet AGNs, if any trend exists, that suggest excess variance positively correlate with luminosity, it is more pronounced when examing individual sources.

Figure 7.1b show that in individual sources the (average) 2–10 keV spectra flatten with the increasing luminosity (flux), this property does not depend duration of the observations, which may have at least a factor 5 differences. However, when we compare different sources, this dependence does not exist, since at same luminosity the spectra of MKN 501 and 1ES 2344+514 is much flatter than those of MKN 421, and PKS 2155−304 show steeper spectra than those in MKN 421 even the luminosity of PKS 2155−304 is higher than those of MKN 421. This figure also demonstrate that the synchrotron peak energy in MKN 501 and 1ES 2344+514 will be in or larger than 2–10 keV energy in the brightest state, and the 2–10 keV band studied

[1] spectral grouping templates, blank fields event files, matrices and effective areas files are available at relevant subdirectories of the anonymous ftp site `ftp://www.sdc.asi.it/pub/sax/cal/`.

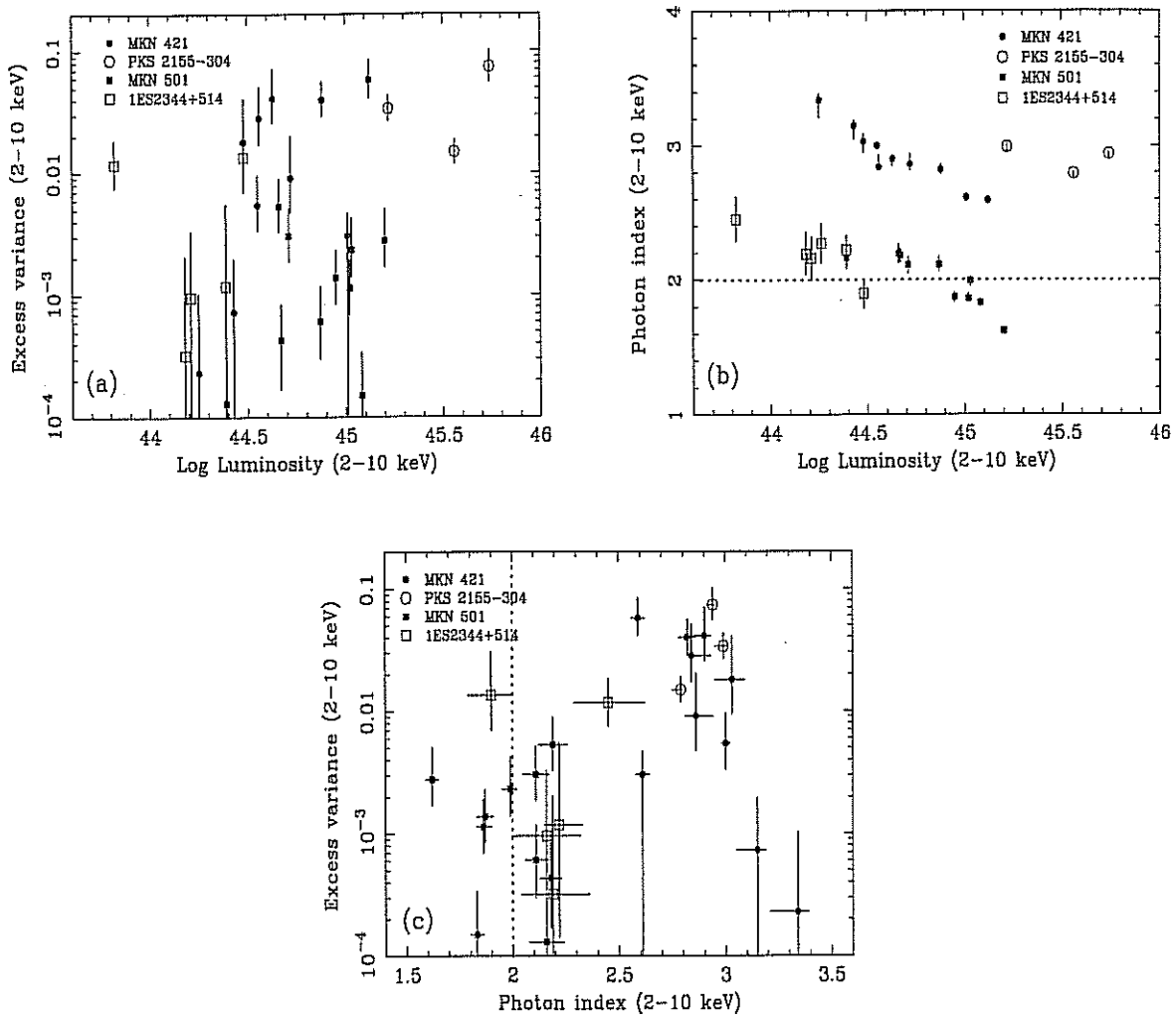

Figure 7.1: Correlations for TeV blazars in the 2–10 keV band, different source is indicated by different symbols as shown in the box. (a) excess variance is plotted against luminosity; (b) photon index against luminosity; (c) excess variance against photon index. In b and c the photon index corresponding to synchrotron peak in the SED is $\Gamma = 2$, which is shown by the dotted line.

here for these two sources is just around their synchrotron peak energy ranges. In contrast, 2–10 keV energy band of MKN 421 and PKS 2155−304 is well above their synchrotron peak energy even in their brightest states. This clearly indicates that the variability characteristics of MKN 501 and 1ES 2344+514 will be significantly different from those of MKN 421 and PKS 2155−304 , as seen from Figure 7.1a that the excess variance of the former two objects is much smaller than those of the latter two ones. This difference is expected by the fact that different change rate of the electron distribution at different relative electron energies, because electrons at the high energy tail of the distribution (in MKN 421 and PKS 2155−304) cool faster than those well above the high energy tail (as in MKN 501 and 1ES 2344+514).

In Figure 7.1c the excess variance is plotted against the photon index. This figure suggest that the source with steeper spectra shows larger excess variance, this is exactly a signature of synchrotron component, and can be easily imaged in the same source with a continuously steepening spectrum as increasing energy. In such an assumption, higher energy band with steeper spectrum will show larger variability. It is clear that MKN 501 and 1ES 2344+514 have systematically flatter spectra and show smaller variability. We note large scatter in this correlation, in particular in MKN 421 the two observations with steepest spectra show smallest variations. As we have stated above, this scatter is probably caused by different observation duration, and in particular when the duration is too short to sample larger variations, or the processes to produce variability are non-stationary.

In summary, as for TeV sources, in which the 2–10 keV energy range is dominated by the high energy end of the low energy synchrotron component, the differences and some correlations can be easily understood with the signature of variations caused by synchrotron emission.

7.5.2 Blazars

As we have stated, the continuity of properties among different classes of blazars is expected in terms of a unified view of blazar phenomenon. One of the systematic trends have been well constructed with the SEDs as a function of luminosity, in the sense that both the synchrotron and Compton peak frequencies move to low frequencies as increasing luminosities (Fossati et al. 1998). The SEDs trend definitely introduce different variability properties when we look at blazars at the same rest frame energy band, and a trend of variability with luminosity is expected. To identify this trend, the X-rays band, specifically 2–10 keV energy range shown here, is the best SED range to conduct such a study, as different emission components (with different variability signatures), either different relative position of synchrotron and

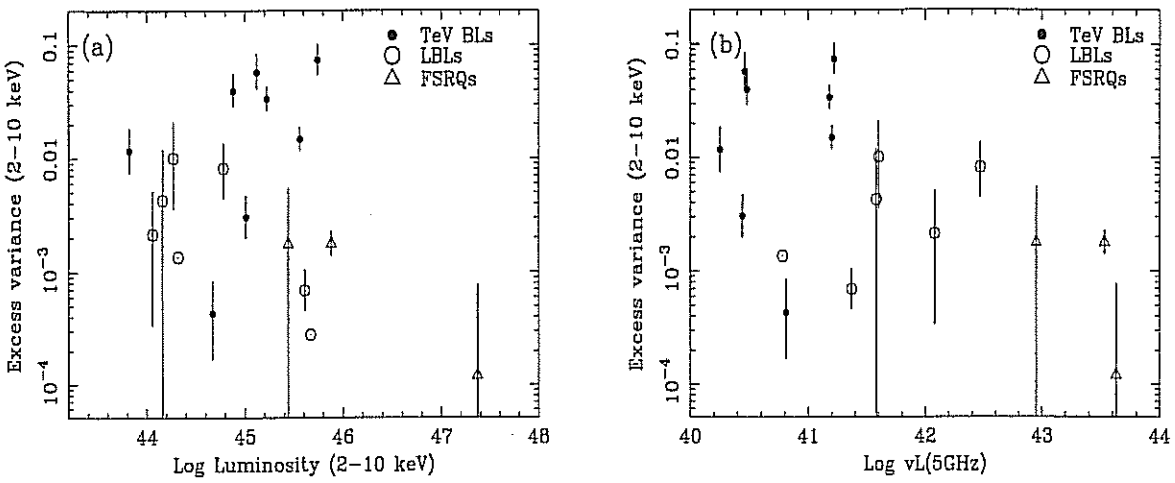

Figure 7.2: Excess variance in the 2–10 keV is plotted against 2–10 keV luminosity (a) and 5 GHz luminosity (b). Only observations with duration greater than 80 ks are shown. There is a small offset of radio luminosity to the different observations of MKN 421 and PKS 2155−304.

Compton or different combination of both components, may dominate in this energy range for different sources, and hence variety and complexity of behavior is shown in the X-rays. We thus perform a variability trend analysis in the 2–10 keV energy band.

Figure 7.2a shows the correlation between the excess variance and luminosity, both in the 2–10 keV energy band. It is clear that the X-ray excess variance does not depend well on the X-ray luminosity, We argue that the X-ray luminosity is not a good quantity to show the dependence of excess variance on it because the X-ray luminosity at the same energy may come from different components with different variability amplitude, and it does not in general represent blazar continuity. As suggested by Fossati et al. (1998) that radio luminosity is adopted as the key parameter characterizing the SEDs trend, we thus turn to look for the dependence of the excess variance on the radio luminosity. The disadvantage to use radio luminosity as an indicator is the nonsimultaneous radio data with the X-ray data and only an average radio data is reasonable for the sources which are observed several times by *Beppo*SAX. But given very small variations of blazars in the radio band, we assume that this is not a serious problem.

We computed the 5GHz radio luminosity in the rest frame for each selected source, and the radio data is taken from Fossati et al. (1998) as they are the average value if more than one data is found in the references. We plot again in Figure 7.2b the excess variance against νL at 5GHz radio frequency. It is evident that anti-correlation between excess variance (in 2–10 keV) and radio luminosity exist, while

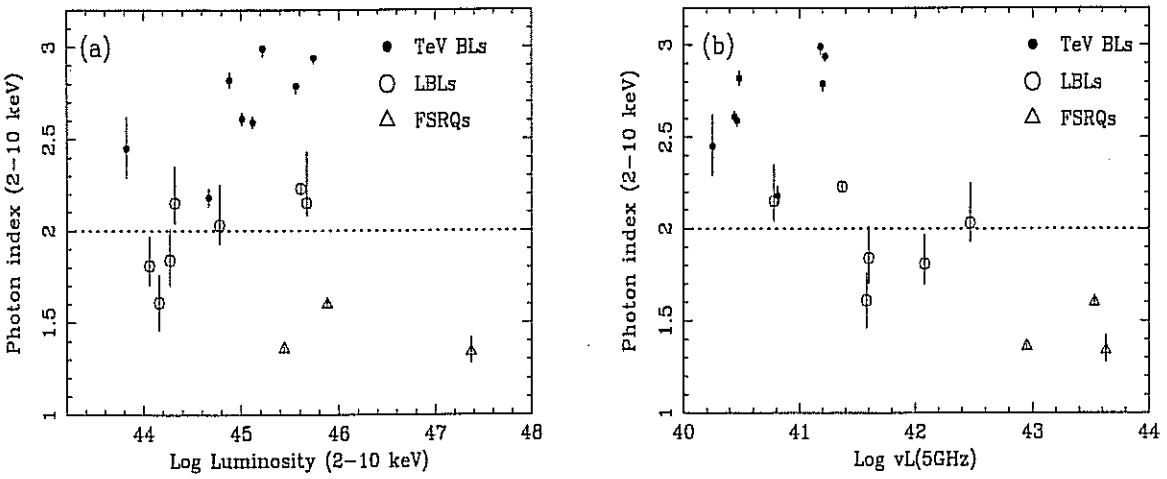

Figure 7.3: Photon index in the 2–10 keV is plotted against 2–10 keV luminosity (a) and 5 GHz luminosity (b). Only observations with duration greater than 80 ks are shown. There is a small offset of radio luminosity to the different observations of MKN 421 and PKS 2155−304. Dotted line have same meaning as in Figure 7.1b.

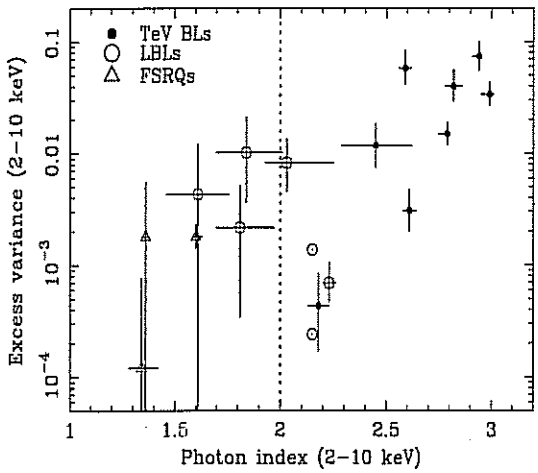

Figure 7.4: Excess variance in the 2–10 keV is plotted against 2–10 keV photon index. Only observations with greater than 80 ks are shown. Dotted line have same meaning as in Figure 7.1c.

large scatter is clear, in particular MKN 501 and 1741+196 which show relative small excess variance and upper limit respectively at their radio luminosity. One reason for this deviation is that there is large scatter in the anti-correlation between synchrotron peak frequency and radio luminosity (Figure 7a of Fossati et al. 1998), and very small excess variance may be accounted if the 2–10 keV energy band is just around or below the synchrotron peak energy. One caution in explaining this correlation is that TeV sources are different from LBLs and FSRQs because of different emission components.

Similarly, in Figure 7.3a,b we show the 2–10 keV photon index against 2–10 keV and 5GHz luminosity respectively. It can be seen that the 2–10 keV photon index inversely correlate with 5GHz luminosity, but not with 2–10 keV luminosity. This suggests that many properties of blazars may correlate well with radio luminosity.

In Figure 7.4 the excess variance is plotted against the photon index. Here we clearly see again that the source with steeper spectra shows larger excess variance, as seen in TeV sources only. However we note that two separate correlation lines is evident, one include TeV sources and three LBLs, and another one LBLs and FSRQs. The former anti-correlation can be accounted for if the 2–10 keV energy band emission is pure synchrotron component, and steeper spectrum relate with higher energy tail of synchrotron emission. The latter anti-correlation may be accounted for if the 2–10 keV emission is a mixture of synchrotron and Compton component, with flatter spectrum accompanied by less variability is caused by higher fraction of Compton component.

7.6 Discussion

The continuity of blazar SEDs with the luminosity, in particular the peak synchrotron frequency inversely correlating with the luminosity, which in turn is constrained by the intrinsic physical parameters, dictates the probable classification of an object. This is also of great relevance for the study of variability patterns of blazars. Specifically speaking, the SED of a source determine changes of variability characteristics along different energy range, and at the same energy range the variability patterns are different along the different blazars as the emission at the same energy is from various combination of different components, a continuity of variability pattern is expected with the luminosity.

Our results for the variability trend of blazars are qualitatively consistent with the predictions of the SEDs continuity. The excess variance and photon index in the 2–10 keV inversely correlate with the radio luminosity, and not correlate well

with the X-ray luminosity. We also find blazars with steeper X-ray spectra in the 2–10 keV band show relatively larger amplitude of X-ray variability (when sampled on 5700 s) than do the sources with flatter X-ray spectra.

In contrast, a survey of ultraviolet variability in blazars by Edelson (1992) showed the positive-correlation of ultraviolet variability amplitude (but over time scales of years, much longer than those discussed here) with the ultraviolet luminosity, and accounted for this correlation by different beaming factors, instead of intrinsic luminosity. Sources with larger Doppler boosting factors would have especially strongly contracted apparent time scale and hence larger variations. This scenario have been disproved by the recent analysis which show all blazars generally have identical Doppler factors (e.g., Ghisellini et al. 1998), so the correlation found by Edelson and his explanation is somewhat ambiguous if the SEDs continuity of blazars is not considered. In the ultraviolet range, higher variability with higher luminosity is reasonably accounted for by the fact that faster variable synchrotron component moves into this energy band. As we have stated above, the key parameter to correlate variability is the total bolometric intrinsic luminosity, but in fact radio luminosity is the best choice because of unknown total luminosity in general. A proper comparison of the X-ray variability with UV one over similar time scales is possible by using several years of *Beppo*SAX observations for a subsample of blazars, which forms a part of our future work.

It is interesting to note that our findings are qualitatively consistent with those found in radio-quiet AGNs, both show anti-correlation between the variability amplitude and luminosity, and steeper sources showing larger variations, while our results is less confident and need to further analysis. The difference in the correlation is that the X-ray variability variance correlate with the radio luminosity rather than with the X-ray luminosity itself. In radio-quiet AGNs, the X-ray variability inversely correlate well with the X-ray luminosity, and have been usually interpreted with the size of the emitting region. However, we are cautious that different physical processes are responsible for blazars and radio-quite AGNs in the X-rays.

Finally, the other effects should be taken into account when comparing variability properties of blazars. The most important one is light-crossing effect which will smooth out the fastest variations and reduce the amplitude of variability, the observed anti-correlation between variability amplitude and luminosity can also be accounted for by more luminous sources having larger emitting regions. It is currently unclear whether this is due to a single, coherent but erratically varying source or a large number of independent flaring regions. It is reasonable to assume that more luminous sources have larger physical size or more (even lager) flaring regions,

and hence the *rms* fluctuations will be smaller.

>>>>>>

Table 7.1: X-ray parameters for TeV blazars

(1) IAU name	(2) z	(3) Sequence	(4) Flux	(5) Log L	(6) $10^{-3}\sigma^2$	(7) Γ	(8) χ^2	(9) T_d/T_e
1101+384	0.031	50032001	85.35	44.56	$28.3^{+22.8}_{-11.1}$	$2.84^{+0.09}_{-0.02}$	156(7)	38.0/23.3
		50032002	83.34	44.55	$5.44^{+4.12}_{-2.10}$	$3.00^{+0.02}_{-0.03}$	28.7(8)	40.0/24.1
		50032003	100.2	44.63	$41.0^{+30.1}_{-15.3}$	$2.90^{+0.03}_{-0.05}$	252(8)	40.0/23.8
		50160002	123.9	44.72	$9.05^{+11.3}_{-4.33}$	$2.86^{+0.08}_{-0.06}$	53.5(4)	19.0/11.4
		50160003	70.86	44.48	$18.0^{+22.5}_{-8.58}$	$3.03^{+0.06}_{-0.08}$	61.5(4)	21.0/11.7
		50160004	41.11	44.25	$0.23^{+0.80}_{-...}$	$3.34^{+0.05}_{-0.13}$	1.59(4)	23.0/12.2
		50160005	62.87	44.43	$0.73^{+1.24}_{-...}$	$3.15^{+0.04}_{-0.10}$	3.57(4)	22.0/11.9
		50686002	310.3	45.12	$57.8^{+26.5}_{-16.5}$	$2.59^{+0.03}_{-0.03}$	362(16)	91.0/29.5
		50686001	177.8	44.88	$39.8^{+16.4}_{-10.6}$	$2.82^{+0.04}_{-0.04}$	138(19)	110./34.6
		50765001	239.3	45.01	$3.04^{+1.66}_{-1.04}$	$2.61^{+0.03}_{-0.03}$	27.6(13)	69.0/32.5
1652+398	0.034	50377001	214.2	45.03	$2.33^{+1.93}_{-0.94}$	$1.99^{+0.03}_{-0.04}$	25.7(7)	38.0/20.7
		50377002	238.8	45.08	$0.15^{+0.19}_{-0.09}$	$1.83^{+0.03}_{-0.03}$	2.77(7)	38.0/20.4
		50377003	320.5	45.20	$2.78^{+2.27}_{-1.10}$	$1.62^{+0.03}_{-0.03}$	46.7(7)	39.0/17.3
		50529001	176.4	44.95	$1.38^{+0.95}_{-0.53}$	$1.87^{+0.04}_{-0.04}$	6.67(11)	63.0/21.9
		50529002	208.5	45.02	$1.14^{+0.80}_{-0.45}$	$1.86^{+0.04}_{-0.03}$	6.00(11)	59.0/21.4
		50529003	146.3	44.87	$0.61^{+0.57}_{-0.31}$	$2.11^{+0.06}_{-0.05}$	3.00(10)	53.0/19.0
		50666001	49.16	44.39	$0.13^{+0.49}_{-...}$	$2.16^{+0.08}_{-0.08}$	1.16(11)	63.0/25.9
		50666002	103.0	44.71	$3.05^{+2.08}_{-1.18}$	$2.11^{+0.06}_{-0.06}$	7.14(11)	62.0/18.9
		50666003	90.40	44.66	$5.30^{+3.67}_{-2.01}$	$2.19^{+0.07}_{-0.07}$	11.1(10)	56.0/15.9
		50666004	82.66	44.67	$0.43^{+0.41}_{-0.26}$	$2.18^{+0.05}_{-0.05}$	1.91(17)	92.0/30.9
2155−304	0.116	50016001	55.85	45.56	$14.9^{+4.11}_{-3.03}$	$2.79^{+0.01}_{-0.04}$	46.4(38)	220./107.
		50160008	82.87	45.74	$73.8^{+27.7}_{-18.5}$	$2.94^{+0.01}_{-0.03}$	217(22)	120./59.5
		50880001	24.6	45.22	$33.8^{+9.48}_{-6.97}$	$2.99^{+0.02}_{-0.04}$	30.1(38)	220./104.
2344+514	0.044	50320001	17.58	44.18	$0.32^{+1.73}_{-...}$	$2.19^{+0.17}_{-0.15}$	1.32(4)	19.0/13.1
		50320002	18.98	44.21	$0.96^{+2.35}_{-0.89}$	$2.16^{+0.16}_{-0.16}$	2.00(4)	22.0/13.2
		50320003	28.76	44.39	$1.18^{+4.35}_{-1.04}$	$2.22^{+0.11}_{-0.07}$	2.46(3)	13.0/8.04
		50320004	36.27	44.48	$13.5^{+17.3}_{-6.59}$	$1.90^{+0.10}_{-0.11}$	28.6(4)	23.0/14.0
		50320005	21.57	44.26	$0.00^{+0.45}_{-0.00}$	$2.27^{+0.15}_{-0.15}$	0.54(5)	23.0/13.0
		50760001	7.765	43.82	$11.7^{+6.82}_{-4.23}$	$2.45^{+0.17}_{-0.16}$	4.81(16)	90.0/50.6

Table 7.2: X-ray parameters for HBLs

(1) IAU name	(2) z	(3) Sequence	(4) Flux	(5) Log L	(6) $10^{-3}\sigma^2$	(7) Γ	(8) χ^2	(9) T_d/T_e
0145+138	0.125	50064008	0.415	43.50	...	$2.55^{+0.94}_{-0.79}$	...	51.0/12.4
0158+002	0.299	50064004	2.661	45.08	$0.00^{+8.97}_{-0.00}$	$2.32^{+0.39}_{-0.24}$	1.2(5)	26.0/12.5
0317+186	0.190	50064007	6.926	45.07	$0.00^{+0.86}_{-0.00}$	$2.45^{+0.28}_{-0.27}$	0.3(5)	28.0/14.9
0323+022	0.147	50064011	3.149	44.51	$19.1^{+31.5}_{-13.3}$	$2.34^{+0.45}_{-0.23}$	2.9(5)	26.0/14.4
0414+009	0.287	50064003	8.380	45.58	$0.00^{+0.93}_{-0.00}$	$2.69^{+0.30}_{-0.20}$	0.3(5)	23.0/11.1
0502+675	...	50064013	18.96	45.57	$0.00^{+0.94}_{-0.00}$	$2.58^{+0.20}_{-0.18}$	0.7(5)	20.0/11.0
0737+747	0.315	50064015	1.404	44.90	$3.19^{+14.3}_{-...}$	$2.79^{+0.53}_{-0.31}$	1.3(5)	26.0/16.4
0927+500	0.188	50519006	6.606	45.04	$0.00^{+1.27}_{-0.00}$	$2.29^{+0.26}_{-0.26}$	0.6(8)	44.0/22.7
1028+511	0.239	50064009	10.06	45.47	$0.00^{+0.99}_{-0.00}$	$2.68^{+0.25}_{-0.24}$	0.5(5)	23.0/12.7
1101–232	0.186	50064017	37.20	45.78	$0.00^{+????}_{-0.00}$	$2.17^{+0.11}_{-0.11}$	0.4(5)	25.0/13.9
		50726001	25.12	45.62	$0.00^{+????}_{-0.00}$	$2.44^{+0.12}_{-0.13}$	0.7(10)	56.0/24.9
1118+424	0.124	50064012	2.673	44.30	$0.00^{+2.83}_{-0.00}$	$3.11^{+0.84}_{-0.66}$	0.3(4)	20.0/10.1
1133+704	0.046	50064010	5.019	43.68	$2.65^{+6.19}_{-2.23}$	$2.85^{+0.41}_{-0.29}$	2.2(4)	20.0/18.2
1218+301	0.130	50750001	7.217	43.74	$8.40^{+27.2}_{-....}$	$1.99^{+0.01}_{-0.01}$	1.1(8)	61/31.3
1255+244	0.141	50064001	11.13	45.01	$5.72^{+13.5}_{-4.35}$	$2.24^{+0.35}_{-0.19}$	2.9(3)	17.0/6.91
1312–423	0.108	50064016	4.055	44.34	$0.66^{+11.6}_{-....}$	$3.18^{+0.80}_{-0.67}$	1.0(2)	9.6/5.6
1517+656	...	50064014	9.720	45.30	$0.12^{+2.65}_{-....}$	$2.60^{+0.16}_{-0.15}$	0.9(4)	17.0/11.1
1553+113	0.360	50064005	12.87	45.98	$0.00^{+0.86}_{-0.00}$	$3.38^{+0.15}_{-0.28}$	0.3(5)	23.0/10.6
1959+650	0.048	50064002	13.22	44.14	$0.00^{+0.42}_{-0.00}$	$2.76^{+0.24}_{-0.16}$	0.6(4)	20.0/12.6

Table 7.3: X-ray parameters for LBLs

(1) IAU name	(2) z	(3) Sequence	(4) Flux	(5) Log L	(6) $10^{-3}\sigma^2$	(7) Γ	(8) χ^2	(9) T_d/T_e
0048–097	...	500460031	1.374	44.40	...	$2.34^{+0.11}_{-0.68}$	...	27/9.8
0219+428	0.444	50750003	1.987	45.29	$12.9^{+17.2}_{-9.20}$	$2.31^{+0.16}_{-0.14}$	1.9(10)	52/26.35
0235+164	0.940	50482001	0.762	45.48	...	$2.17^{+0.57}_{-0.42}$	...	170/29.1
0521–365	0.055	50497001	8.752	44.06	$2.14^{+2.96}_{-1.80}$	$1.81^{+0.16}_{-0.11}$	1.5(15)	83.0/41.1
0716+714	0.3?	50160001	1.360	44.78	$8.22^{+5.39}_{-3.75}$	$2.03^{+0.22}_{-0.10}$	2.0(28)	160.0/122.5
		50750002	2.564	45.02	$8.64^{+13.1}_{-6.66}$	$1.85^{+0.22}_{-0.15}$	2.0(9)	52.0/31.3
0851+202	0.306	50046002	2.175	44.99	$0.00^{+11.5}_{-0.00}$	$2.01^{+0.71}_{-0.28}$	0.8(5)	25.0/10.7
1144–379	1.048	50046006	0.696	45.44	$35.2^{+45.4}_{-21.7}$	$2.31^{+1.37}_{-0.74}$	2.4(8)	42.0/23.2
1219+285	0.102	50503001	4.030	44.27	$10.1^{+10.9}_{-6.52}$	$1.84^{+0.17}_{-0.14}$	1.8(14)	82.0/24.8
		505030011	3.233	44.16	$4.27^{+7.72}_{-4.27}$	$1.61^{+0.15}_{-0.15}$	1.4(13)	79.0/31.8
1519–273	...	50046007	0.603	44.03	$0.00^{+20.6}_{-0.00}$	$1.71^{+1.00}_{-0.56}$	0.5(4)	49.0/26.9
1741+1936	0.083	50470001	6.783	44.32	$0.00^{+1.36}_{-0.00}$	$2.15^{+0.20}_{-0.11}$	0.8(16)	86.0/38.7
1803+784	0.684	50482004	2.143	45.57	$0.00^{+5.47}_{-0.00}$	$1.62^{+0.36}_{-0.24}$	0.9(11)	59.0/40.4
1807+698	0.051	50482002	1.766	43.30	$0.00^{+3.43}_{-0.00}$	$1.75^{+0.21}_{-0.26}$	0.6(10)	57.0/33.9
1823+568	0.664	50046005	9.732	45.30	$0.00^{+13.9}_{-0.00}$	$2.00^{+0.71}_{-0.62}$	0.5(4)	26.1/13.4
2005–489	0.071	50046001	59.58	45.13	$0.21^{+0.75}_{-...}$	$2.41^{+0.10}_{-0.10}$	1.5(4)	19.9/9.91
		50503002	179.0	45.61	$0.69^{+0.36}_{-0.23}$	$2.23^{+0.03}_{-0.03}$	5.4(18)	98.1/52.5
2200+420	0.069	50046004	21.84	44.66	$18.4^{+16.0}_{-8.24}$	$1.92^{+0.17}_{-0.17}$	4.5(9)	50.7/13.7
2356–309	...	50493007	24.28	45.67	$0.00^{+0.24}_{-0.00}$	$2.15^{+0.28}_{-0.07}$	0.7(14)	80.0/41.0

Table 7.4: X-ray parameters for HPQs

(1) IAU name	(2) z	(3) Sequence	(4) Flux	(5) Log L	(6) $10^{-3}\sigma^2$	(7) Γ	(8) χ^2	(9) T_d/T_e
0836+710	2.172	50497003	26.36	47.37	$0.12^{+0.65}_{-...}$	$1.34^{+0.08}_{-0.06}$	1.1(14)	84.0/42.6
1253–055	0.538	50237016	5.558	45.83	$0.00^{+1.02}_{-0.00}$	$1.70^{+0.24}_{-0.11}$	0.5(8)	45.0/21.8
		50237017	5.640	45.84	$0.00^{+1.95}_{-0.00}$	$1.70^{+0.22}_{-0.11}$	0.8(9)	47.0/23.9
		50237018	6.101	45.87	...	$1.83^{+0.38}_{-0.39}$	...	5.7/2.6
		50237019	5.428	45.83	$0.00^{+2.15}_{-0.00}$	$1.84^{+0.32}_{-0.19}$	0.6(4)	21.0/11.7
		50237020	5.576	45.84	$1.84^{+3.86}_{-...}$	$1.75^{+0.13}_{-0.11}$	1.5(8)	43.0/24.7
1510-089	0.361	50497004	5.299	45.44	$1.78^{+3.72}_{-...}$	$1.36^{+0.01}_{-0.01}$	1.2(15)	86.0/43.9
2223–052	1.404	50181006	2.620	46.21	$0.00^{+17.6}_{-0.00}$	$2.31^{+0.70}_{-0.60}$	0.7(6)	40.0/16.1
2230+114	1.037	50237021	5.468	46.31	$0.00^{+1.41}_{-0.00}$	$1.63^{+0.29}_{-0.14}$	0.5(8)	45.0/23.8
		50237022	5.818	46.33	$0.00^{+1.26}_{-0.00}$	$1.83^{+0.29}_{-0.27}$	0.4(9)	51.0/22.2
		50237023	5.995	46.33	$3.97^{+7.06}_{-3.62}$	$1.63^{+0.12}_{-0.15}$	1.8(9)	51.0/25.7
		50237024	5.844	46.31	$0.00^{+2.60}_{-0.00}$	$1.67^{+0.39}_{-0.28}$	0.4(5)	25.0/12.2
		50237025	6.009	46.33	$8.23^{+10.7}_{-5.36}$	$1.53^{+0.17}_{-0.16}$	2.3(8)	46.0/19.3
2243–123	0.630	50727005	1.811	45.46	$0.00^{+3.42}_{-0.00}$	$1.77^{+0.56}_{-0.27}$	0.5(11)	59.0/27.4

Table 7.5: X-ray parameters for LPQs

(1) IAU name	(2) z	(3) Sequence	(4) Flux	(5) Log L	(6) $10^{-3}\sigma^2$	(7) Γ	(8) χ^2	(9) T_d/T_e
0528+134	2.070	50237001	2.373	46.24	$0.00^{+3.71}_{-0.00}$	$1.84^{+0.60}_{-0.53}$	0.5(5)	25.0/14.4
		50237002	2.430	46.25	$0.00^{+4.22}_{-0.00}$	$1.89^{+0.60}_{-0.54}$	0.5(5)	24.0/13.3
		50237003	2.220	46.27	$14.5^{+36.9}_{-11.8}$	$1.51^{+0.01}_{-0.01}$	2.5(3)	14.0/7.32
		50237004	2.458	46.28	$0.76^{+9.88}_{-...}$	$1.46^{+0.46}_{-0.36}$	1.0(5)	24.0/13.5
		50237005	2.256	46.20	$0.67^{+8.51}_{-...}$	$1.42^{+0.48}_{-0.40}$	0.9(5)	25.0/14.1
		50237006	2.390	46.29	$0.00^{+8.30}_{-0.00}$	$1.50^{+0.60}_{-0.34}$	0.9(4)	20.0/11.2
		50237007	2.153	46.22	$0.00^{+3.20}_{-0.00}$	$1.84^{+0.58}_{-0.51}$	0.3(5)	25.0/12.7
		50237008	2.067	46.22	$24.0^{+41.6}_{-15.7}$	$1.73^{+0.67}_{-0.44}$	3.6(4)	20.0/11.4
1226+023	0.158	50021001	67.76	45.88	$1.78^{+0.49}_{-0.37}$	$1.60^{+0.03}_{-0.01}$	6.2(50)	280/131.1
		50237011	118.8	46.11	$0.09^{+0.09}_{-...}$	$1.57^{+0.07}_{-0.02}$	1.5(6)	47.0/23.5
		50237012	113.9	46.09	$0.06^{+0.20}_{-...}$	$1.61^{+0.04}_{-0.05}$	1.3(9)	47.0/24.0
		50237013	107.7	46.07	$0.08^{+0.20}_{-...}$	$1.67^{+0.04}_{-0.05}$	1.5(9)	48.0/27.3
		50237015	103.0	46.05	$1.78^{+1.53}_{-0.78}$	$1.56^{+0.04}_{-0.03}$	7.2(9)	46.0/22.3

Chapter 8

Conclusions and Perspectives

8.1 Summary of main results

The main results of the research work presented in this thesis include two parts, the first is the comprehensive X-ray variability analysis of the two TeV bright sources, MKN 421 and PKS 2155−304. The second is the studies of the X-ray variability trend in blazars.

8.1.1 MKN 421 and PKS 2155−304

*Beppo*SAX has observed MKN 421 between 1997 and 2000, and we have conducted a comprehensive temporal analysis for the energy-dependent X-ray variability characteristics. When combing our results with those from ASCA observations, we can conclude that the source is characterized by the intra-day X-ray variations, and has shown a large variety of complex variability behaviors. These results have provided us a great wealth of information on the physical processes operating in jets, but at the present time these complex variability behaviors have been not well interpreted yet, though some efforts have been done. We have also (qualitatively) probed some fresh constraints on the radiative processes, in particular on the issue of particles acceleration.

We have also considered four (three by *Beppo*SAX and one by ASCA) long-duration (on time scale of two days) X-ray light curves of PKS 2155−304 with high time resolution, and performed detailed time series analysis on them. The intensities in soft and medium X-rays are always well correlated, but with significantly different soft lags, suggesting that variability properties are time dependent and/or different mechanisms responsible for the variability may be at work. The four light curves presented here, which are sampled over short time scales, do not seem to show

any direct correspondence with the overall/long term variability properties of the source, as suggested by the two closely similar ROSAT light curves with about 5 years separation discussed by Brinkmann & Siebert (1999).

To conclude, we summarize in the following the main results of this study, compare variability properties of MKN 421 and PKS 2155−304, and infer their physical constraints on the emitting regions.

Both MKN 421 and PKS 2155−304 are violently variable, characterized by recurrent flares. Flares typically have duration of about one day and show quasi-symmetric profiles in most cases, indicating a signature of light-crossing time dominating the emitting regions. The fact that flares frequently occur dictates that particles acceleration/injection must often take place to account for very fast cooling of the energetic electrons. The comprehensive temporal analyses presented in this thesis thus give us precious information on the acceleration and cooling process operating in the jets, and more importantly, the exchanging role of both processes which may produce complex energy-dependent variability.

The first information we obtained is about variability amplitude and time scales. In both sources, variability amplitude is higher at higher energies, independence of both the sampling patterns and the state of the source; the minimum doubling time scales are shorter at higher energies than at the lower energies, also independence of both the sampling patterns and the brightness state of the source. This simple energy-dependent variability amplitude and time scales is easily explained as synchrotron emission. In general, variability amplitude and time scales at a given energy do not correlate with the source brightness, while a weak correlation may exist in PKS 2155−304.

The SFs show relatively steep slopes, $\beta_{SF} \sim 1.2$, in both sources, with a significant turn-over at a characteristic time scale of ~ 0.5 days, after which the SFs flatten significantly. This shows that these sources is much less variable on very short time scales and the variations will not significantly strengthen above this characteristic time scale. Furthermore the pronounced characteristic time scale gives a constraint on the size of the emitting region ($\sim 10^{16}$ cm) and presumably the distance ($\sim 10^{17}$ cm) from the jet base, where particles acceleration may take place. The PDS analysis for PKS 2155−304 is, in general, consistent with the results from the SFs. Probable flaring periodicity of $\sim$ one day in MKN 421 suggests an ejection frequency of emitting plasma from the central black hole.

The most important results presented in this thesis are the detection of time lags. In MKN 421, time lags are detected in each isolated flare, and constrained to a small range from flare to flare ($\sim$ 1 hour between the 0.1–1.5 keV and 3.5–10 keV

bands) with various attributes: soft lags, hard lags or zero lags. For PKS 2155−304, only soft time lags are detected in each flare, and also within a small range from flare to flare ($\sim$ 1.5 hour between the 0.1–1.5 keV and 3.5–10 keV bands). A difference between the two sources is that in PKS 2155−304 the soft lags appears correlate to the flare intensities, i.e., the larger soft lags the lower flare intensities, but no correlation between time lags and source intensities is found in MKN 421. However we point out that this difference needs to be tested using better quality data. To account for variable time lags, relative changes of values between different time scales involved must occur in order to produce a variety of complex energy-dependent variability behaviors. The soft lags in the X-rays of a HBL is interpreted as related to the energy-dependent synchrotron cooling time scale of the relativistic emitting electrons. Within the simple homogeneous SSC model, the predicted dependence of soft lag on flux is much flatter than the observed one (assuming δ constant) in PKS 2155−304, underlining other factors must be at work to produce larger soft lags with lower fluxes (e.g., reduction in the Doppler factor). The light-crossing time will introduce larger soft lags when it dominates.

The energy-dependence of time lags can be well constrained for the flares in which a large enough time lag is detected. In a simplified scenario, soft and hard lag are due to the energy-dependent synchrotron cooling and acceleration time scales, respectively, and can be used to constrain the magnetic field and Doppler factor of the emitting region. Magnetic fields have been constrained to be 0.15–3.0 Gauss in MKN 421 (assuming $\delta = 20$) and 0.14–0.22 Gauss in PKS 2155−304 ($\delta = 25$ is assumed). Different acceleration mechanisms may take place in different flares. Note that at least in 2000a #2 flare of MKN 421 the diffusive shock acceleration does not work well when fitting the energy-dependent hard lags.

The fact that the light-crossing time dominates and energy-dependent time lags are detected suggests that light-crossing times (i.e., emission region sizes) are energy-dependent, as when the region size is determined by the cooling length. In the case of soft lags, lower energy emission may come from larger size of region than higher energy one does, if energetic electrons are first injected at highest energy with a narrow energy distribution and lower energy emission comes from the cooled electrons. As for hard lags, higher energy emission probably come from larger region size, as when electrons need longer time to accelerate to the radiative window. Future simulations should take into account the effects of the energy-dependent light-crossing times.

8.1.2 Blazars

The continuity of blazar SEDs with the luminosity suggests probable variability and spectral continuity in a particular waveband, as studied in Chapter 7. Although our results are very preliminary, we do find some trends residing in blazars. The 2–10 keV excess variance and photon index inversely correlate with the radio luminosity, and blazars with steeper X-ray spectra exhibit relatively larger amplitude of X-ray variability than do the ones with flatter X-ray spectra. Our findings are qualitatively consistent with the predictions of blazars SED continuity.

From the analysis of blazars, the complex variability patterns may relate to the different synchrotron peak frequencies from flare to flare and from source to source. The determination of such dependence forms a part of our future work. It is also of relevance to compare the variability characteristics in the X-rays of HBLs and in the optical/IR bands of LBLs/FSRQs, respectively, to determine the characteristic time scales and time lags. More specifically, it is necessary to compare the variability behaviors of the high energy part of the synchrotron emission, which appears in the different wavelengths along the SED continuity of blazars. Such comparisons are much informative to know whether similar physical processes are taking place in all blazars.

8.2 Future work and perspectives

It is always evident that more and better data are needed to characterize blazar variability, which in turn is one of the most efficient ways to constrain blazars models and unification schemes. As we have stated before, SEDs and their trends are much better known than variability. The availability of uniform data archives like ASCA, RXTE and *Beppo*SAX and the new satellites like Chandra and XMM with higher resolutions (in time, spectrum and space) provide us with an opportunity to conduct a comprehensive study for blazar variability in the X-rays. We outline in the following the main work to be done in order to strengthen our findings.

1. To search for time lags between different energy bands in other bright blazars. Up to now, we have such wealthy information only in MKN 421 and PKS 2155–304, the two bright sources in the X-rays which is the high energy tail of the synchrotron component. It is of great interests to search for the time lags of the Compton component, although it could be difficult because in general the X-ray emission of blazars is the low energy end of this component and thus less variable. The most important issue is to determine whether hard/soft lags

relate with the rise/decay of a flare, and do such study on the basis of "digs" rather than "peaks" as we have presented in this thesis. It is thus essential to get high quality data on the rise and decay profiles of flares in order to better understand the acceleration and cooling mechanisms.

2. Variability (amplitude) trend on various time scales should be properly studied. Rapid variability events can be studied for bright sources. A limited number of sources is multiply observed with similar sampling pattern. It is of great relevance to compare variability trends over different energy range: trends in the soft X-rays (0.1–2 keV) will be studied and compared with those in the 2-10 keV. More importantly, correlation between the variability and the synchrotron peak frequency is needed to account for the complex variability behaviors.

3. An important step is to measure and compare the characteristic physical time scales in blazars, and determine whether the time scales are longer in more luminous blazars, as in radio-quiet AGNs, possibly suggesting larger emitting regions and larger black hole masses. Such time scales can be obtained for example from the low- and high-frequency turn over of the PDS, or identically, turn over of long- and short-time scale in the SFs. Such analysis requires both long term monitoring, as performed by RXTE for a number of objects, and high throughout (high signal-to-noise on short time scales), such as will be available from XMM.

4. The structure of blazar light curves should be studied, to determine whether the light curves are stationary, linear and Gaussian or not, and the duty cycles. The fact that particular blazars can be distinguished on the basis of the shape of their light curves is very important for the study of X-ray variability in blazars in general. It is also important to compare the characteristic time scales, which is meaningful if the processes producing the variations are the same, and therefore a search for time scales must be combined with studies of the structure of light curves.

5. As significantly different spectra in the same band of blazars, a more meaningful way to compare variability amplitude, time scales and time lags could be studied in the corresponding peak frequency region of each blazar because of most of emission there, since large optical data are available for some LBLs and FSRQs.

6. A strong correlation has been found between hard X-ray variability and Hβ

FWHM of Seyfert 1 galaxies (Turner et al. 1999). An interesting step in blazars studies is thus to examine the correlation between broad emission line luminosity and the variability properties. The main problem is that many HBLs and LBLs have no detectable broad line emission and the upper limits in many cases are unlikely to be very informative. The clear physical connection between the BLR and the jet is the central black hole, the prime cause of all AGN phenomena. The correlation between the BLR and the variability could provide a clue on the relationship between blazars phenomenology and the central black hole masses, which can be studied for FSRQs only.

7. Further spectral analysis to get a better correlation between variability and spectral parameters. Of primary importance is the determination of the synchrotron peak frequency and the position of the Compton component emerging in the 0.1–10 keV band, as these two parameters are connected with the variability behavior of a blazar. The correlation of variability properties with the synchrotron peak frequencies will be studied in detail.

8. The relationships of blazars with other AGNs is, in any sense, worthing to probe. For example the similarity between blazars and Seyfert 1 galaxies in the correlation of variability with luminosity and spectra is intriguing, as the origin of the X-ray emission is different.

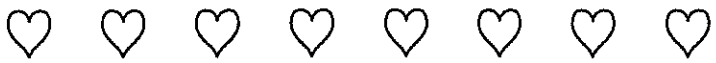

Thank you very much for reading!
Suggestions and comments are warmly welcome!

Bibliography

[1] Aharonian, F.A., et al. 1999a, A&A, 342, 69

[2] Aharonian, F.A., et al. 1999b, A&A, 350, 757

[3] Almaini, O., et al. 2000, MNRAS, 315, 325

[4] Angel, J.R.P., & Stockmann, H.S. 1980, ARA&A, 18, 321

[5] Antonucci, R. 1993, ARA&A, 31, 473

[6] Aiso, S., et al. 1997, in Proc. 25th Internat. Cosmic Ray Conf. (Durban, South Africa), ed. M. S. Potgeier, B. C. Raubenheimer, & D. J. van der Walt, 3, 261

[7] Bednarek, W. 1998, A&A, 336, 123

[8] Beloborodov A.M., Stern, B.E., & Svensson, R. 2000, ApJ, 535, 158

[9] Bertone, E., et al. 2000, A&A, 356, 1

[10] Bhat, C. L., et al. 1997, IAUC, 6709

[11] Barr, P., & Mushotzky, R.F. 1986, Nature 320, 421

[12] Blandford, R.D., & Levinson, A. 1995, ApJ, 441, 79

[13] Blandford, R., & Eichler, D. 1987, Phys. Rep., 154, 1

[14] Blandford, R.D., & Königl, A. 1979, ApJ, 232, 34

[15] Blandford, R.D., & Rees, M.J. 1978, in Pittsburgh Conference on BL Lac objects, ed. A.N. Wolfe (Pittsburgh University Press), P. 328

[16] Böttcher, M. 1999, ApJ, 515, L21

[17] Boella, G., et al. 1997a, A&AS, 122, 299

[18] Boella, G., et al. 1997b, A&AS, 122, 327

[19] Bradbury, S.M., et al. 1997, A&A, 320, L5

[20] Bregman, J.N., et al. 1986, ApJ, 301, 698

[21] Brinkmann, W., & Siebert, J., 1999, Proc. of the BL Lac Phenomenon meeting, Turku, Finland, 22-26 June 1998, ed. L.O. Takalo, PASP Conf. Series, 159, 168

[22] Brinkmann, W., et al. 1995, A&AS, 109, 147

[23] Buckley, J.H., et al. 1997, in Proc. of the Fourth Compton Symp., ed. C. D. Dermer, M. S. Strickman, & J. D. Kurfess (New York: AIP), AIP Conf. Proc. 410, 1381

[24] Buckley, J.H., et al. 1996, ApJ, 472, L9

[25] Cagnoni, I., Papadakis, I.E., & Fruscione, A. 2000, ApJ, in press (astro-ph/0006255)

[26] Cappi, M., et al. 1994, MNRAS, 271, 438

[27] Catanese, M., & Sumbruna, R.M. 2000, ApJ, 534, 39

[28] Catanese, M., et al. 1998, ApJ, 501, 616

[29] Catanese, M., et al. 1997, ApJ, 487, L143

[30] Chadwick, P.M., et al. 1999, ApJ, 513, 163

[31] Chiaberge, M., & Ghisellini, G. 1999, MNRAS, 306, 551

[32] Chiappetti, L., et al. 1999, ApJ, 521, 552

[33] Celotti A., Fabian, A.C., & Rees, M.J. 1998, MNRAS, 293, 239

[34] Celotti A., Maraschi, L., & Treves, A. 1991, ApJ, 377, 403

[35] Ciliegi, P., Bassani, L., & Caroli, E. 1995, ApJ, 439, 80

[36] Colmar, W. 1996, in Gamma-Ray Emitting AGN, Ed. J.G., Kirk, M. Camenzind, C. von Montigny, S. Wagner, P. 9

[37] Comastri, A., et al. 1997, ApJ, 480, 534

[38] Comastri, A., Molendi, S., & Ghisellini, G. 1995, MNRAS, 277, 297

[39] Dar, A., & Laor, A, 1997, ApJ, 478, L5

[40] Deeming, T.J. 1975, Ap&SS, 36, 137

[41] Dermer, C.D. 1998, ApJ, 501, L157

[42] Dermer, C.D., & Gehrels, N. 1995, 1995, ApJ, 447, 103

[43] Dermer, C.D. 1995, ApJ, 446, L63

[44] Dermer, C.D., Sturner, S.J., & Schlickeiser, R. 1993, ApJS, 109, 103

[45] Dermer, C.D., & Schlickeiser, R. 1993, ApJ, 416,458

[46] Dermer, C.D., Schlickeiser, R., & Mastichiadis, A. 1992, A&A, 256, L27

[47] Drury, L.O'C. 1983, Rep. Prog. Phys., 46, 973

[48] Edelson, R., & Nandra, K. 1999, ApJ, 514, 682

[49] Edelson, R., et al. 1995, ApJ, 438, 120

[50] Edelson, R. 1992, ApJ, 401, 516

[51] Edelson, R. et al. 1991, ApJ, 372, L9

[52] Edelson, R., Krolik, J.H., Pike, G.F. 1990, ApJ, 359, 86

[53] Edelson, R., & Krolik, J.H. 1988, ApJ, 333, 646

[54] Fanaroff, B.L., & Riley, J.M. 1974, MNRAS, 167, L31

[55] Fiore, F., Guainazzi, M., & Grandi, P. 1999, Cookbook for *Beppo*SAX NFI Spectral Analysis, version 1.2

[56] Fiore, F., et al. 1998, ApJ, 503, 607

[57] Fossati, G., et al. 2000a, ApJ, 541, 153

[58] Fossati, G., et al. 2000b, ApJ, 541, 166

[59] Fossati, G. 1998, PhD thesis, SISSA, Trieste

[60] Fossati, G., et al. 1998, MNRAS, 299, 433

[61] Fossati, G., et al. 1997, MNRAS, 289, 136

[62] Frontera, F., et al. 1997, A&AS, 122, 357

[63] Fugmann, W., 1988, A&A, 205, 86

[64] Gaidos, J. A., et al. 1996, Nature, 383, 319

[65] Gear, W.K., Robson E.I., & Brown, L.M.J. 1986, Nature, 324, 546

[66] Georganopoulos, M., & Marscher, A. P. 1998, ApJ, 506, L11

[67] George, I.M., et al. 2000, ApJ, 531, 52

[68] George, I.M., Warwick, R.S., & Bromage, G.E. 1988, MNRAS, 232, 793

[69] Ghisellini, G. 1999, in Proc. of 4th ASCA Symp. in press (astro-ph/9906111)

[70] Ghisellini, G., et al. 1998, MNRAS, 301, 451

[71] Ghisellini, G., et al. 1997, A&A, 327, 61

[72] Ghisellini, G., Maraschi, L., & Dondi, L. 1996, A&A, 120, 503

[73] Ghisellini, G., & Madau, P. 1996, MNRAS, 280, 67

[74] Ghisellini, G. 1989, Ph.D. thesis, SISSA, Trieste

[75] Ghisellini, G., Maraschi, L., & Treves, A. 1985, A&A, 146, 204

[76] Giommi, P., et al. 2000, in X-ray Astronomy 1999 (astro-ph/0003021)

[77] Giommi, P., Padovani, P., & Perlman, E. 2000, MNRAS, in press (astro-ph/9907377)

[78] Giommi, P., et al. 1999, A&A, 351, 59

[79] Giommi, P., & Padovani, P. 1994, MNRAS, 286, L51

[80] Giommi, P., et al. 1998, A&A, 333, L5

[81] Giommi, P., Ansari, S.G., & Micol, A. 1995, A&AS, 109, 267

[82] Giommi, P., et al. 1990, ApJ, 356, 432

[83] Giovannini, G., et al. 1994, ApJ, 435, 116

[84] Grandi, P., et al. 1992, ApJS, 82, 93

[85] Green, A., McHardy, I.M., & Lehto, H.J. 1993, MNRAS, 265, 664

[86] Guainazzi, M., et al. 1999, A&A, 342, 124

[87] Hartman, R.C., et al. 1999, ApJS, 123, 79

[88] Hartman, R. C., et al. 1996, ApJ, 461, 698

[89] Hartman, R.C., et al. 1993, ApJ, 407, L41

[90] Hayashida, K., et al. 1998, ApJ, 500, 642

[91] Hayashida, N., et al. 1998, ApJ, 504, L71

[92] Heidt, J. 1996, in Blazar Continuum Variability, H.R. Miller, J.R. Webb, J.C. Noble (Eds.), P.64

[93] Hillas, A. M. 1999, in TeV Astrophysics of Extragalactic Objects, ed. M. Catanese & T. C. Weekes, Astropart. Phys., in press

[94] Hufnagel, B. R., & Bregman, J. N. 1992, ApJ, 386, 473

[95] Hunter, S.D., et al. 1993, ApJ, 409, 134

[96] Impey, C.D., & Tapia, S. 1990, ApJ, 354, 124

[97] Impey, C.D., & Neugebauer, G. 1988, AJ, 95, 307

[98] Inoue, S., & Takahara, F. 1996, ApJ, 463, 555

[99] Jannuzi B.T., Smith, P.S., & Elston R. 1994, ApJ, 428, 130

[100] Jannuzi B.T., Smith, P.S., & Elston R. 1993, ApJs, 85, 265

[101] Jones, T.W., O'Dell, S.L., & Stein, W.A. 1974a, ApJ, 188, 353

[102] Jones, T.W., O'Dell, S.L., & Stein, W.A. 1974a, ApJ, 192, 261

[103] Kardashev, N.S., 1962, Soviet Astronomy-AJ, 6, 317

[104] Kataoka, J. et al. 1999, ApJ, 514, 138

[105] Kataoka, J. et al. 2000, ApJ, 528, 243

[106] Kazanas, D., & Mastichiadis, A. 1999, ApJ, 518, L17

[107] Kedziora-Chudcer, L. et al. 1997, in Radio Emission from Galactic and Extragalactic Compact Sources, J.A. Zensus, J.M. Wrobel, & G.B. Talor (Eds.), ASP, in press

[108] Kellermann, K.I., et al. AJ, 98, 1195

[109] Kirk, J.G., Rieger, F.M., & Mastichiadis, A. 1998, A&A, 333, 452

[110] Kirk, J.G. 1997, in Proc. of the Workshop on Relativistic Jets in AGNs, eds. M. Ostrowski, M. Sikora, G. Madejski, M. Begelman, Cracow (Poland), P. 145

[111] Kirk, J.G., & Mastichiadis, A. 1992, Nature, 360, 135

[112] Kniffen, D. A., et al. 1993, ApJ, 411, 133

[113] Kohmura, Y., et al. 1994, PASJ, 46, 131

[114] Kollgaard, R.I. 1994, Vistas in Astronomy, 38, 29

[115] Kollgaard, R.I., et al. 1992, AJ, 104, 1687

[116] Königl, A. 1981, ApJ, 243, 700

[117] Kraus, A., Krichbaum, T.P., Witzel, A. 1997, in Radio Emission from Galactic and Extragalactic Compact Sources, J.A. Zensus, J.M. Wrobel, & G.B. Talor (Eds.), ASP, in press

[118] Kusunose, M., Takahara, F., & Li, H. 2000, ApJ, 536, 299

[119] Lamer, G., & Wager, S.J. 1999, A&A, 331, L13

[120] Laurent-Muehleisen, S.A., et al. 1998, ApJ, 525, 127

[121] Laurent-Muehleisen, S.A., 3t al. 1993, AJ, 106, 875

[122] Lawrence,A., & Papadakis, I. 1993, ApJ, 414, L85

[123] Ledden, J.E., & O'Dell, S.L. 1985, ApJ, 298, 630

[124] Leighly, K.M. 1999, ApJS, 125, 297

[125] Levinson, A. 1996, ApJ, 459, 520

[126] Lin, Y.C., et al. 1999, ApJ, 525, 191

[127] Lin, Y.C., et al. 1997, in Proc. Fourth Compton Symp., ed. C.D. Dermer, M.S. Strickman, & J.D. Kurfess (New York: AIP), P. 1371

[128] MacLeod, J.M., et al. 1971, Ap. Letters, 9, 19

[129] MacLeod, J.M., & Andrew B. 1968, Ap. Letters, 1, 19

[130] Macomb, D.J., et al. 1995, ApJ, 449, L99; 1996, ApJ, 459, L111 (Erratum)

[131] Makino, F., et al. 1996, Röngtenstrahlung from The Universe, Ed. Zimmermann, H.U., Trumper, J.E., Yorke, H., MPE Report 263, 413

[132] Malizia, A., et al. 2000, MNRAS, 312, 123

[133] Mannheim, K. 1996, Space Sci. Rev., 75, 331

[134] Mannheim, K. 1993, A&A, 269, 67

[135] Mannheim, K., et al. 1991, A&A, 251, 723

[136] Manzo, G., et al. 1997, A&AS, 122, 341

[137] Maoz, D., & Netzer, H. 1989, MNRAS, 236, 21

[138] Maraschi, L., et al. 1999, ApJ, 526, L81

[139] Maraschi, L., et al. 1995, ApJ, 443, 578

[140] Maraschi, L., Ghisellini G., & Celotti A. 1992, ApJ, 397, L5

[141] Maraschi, L., et al. 1986, 304, 637

[142] Margon, B., et al. 1976, ApJ, 207, 359

[143] Marscher, A.P., & Travis J.P. 1996, A&AS, 120C, 537

[144] Marscher, A., & Gear, W. 1985, ApJ, 198, 114

[145] Mastichiadis, A. & Kirk, J. G. 1997, A&A, 320, 19

[146] Mattox, J.R., et al. 1997, ApJ, 476, 692

[147] Mattox, J.R., et al. 1993, ApJ, 410, 609

[148] M^{c}Hardy, I.M., et al. 1999, MNRAS, 310, 571

[149] M^{c}Hardy, I.M. 1999, Proc. of the BL Lac Phenomenon meeting, Turku, Finland, 22-26 June 1998, ed. L.O. Takalo, PASP Conf. Series, 159, 155

[150] M^{c}Hardy, I.M. 1996, in Blazars Continuum Variability, P. 293

[151] M^{c}Hardy, I.M., et al. 1990, MNRAS, 246, 305

[152] M^{c}Hardy, I.M. 1989, in ESA, The 23rd ESLAB Symposium on two Topics in X-ray Astronomy, Volume 2: AGN and the X-ray backgroud, P1111

[153] McLaughlin, M.A., et al. 1996, ApJ, 473, 763

[154] McNaron-Brown, K., et al. 1995, ApJ, 451, 575

[155] Mirabel, I.F., & Rodríguez, L.F. 1999, ARA&A, 37, 409

[156] Morganti, R., et al. 1995, MNRAS, 274, 393

[157] Mushotzky, R., Done, C., & Pounds, K. 1993, ARA&A, 31, 717

[158] Mushotzky, R., et al. 1978, in Pittsburgh Conference on BL Lac objects, ed. A.N. Wolfe (Pittsburgh University Press), P. 169

[159] Mukherjee, R. 1999, in Observational Evidence for Black Holes in the Universe, ed. S.K. Chakrabarti (Dordrecht: Kluwer), P. 215

[160] Mukherjee, R., et al. 1997, ApJ, 490, 116

[161] Mukherjee, R., et al. 1996, ApJ, 470, 831

[162] Nandra, K., et al. 1997, ApJ, 476, 70

[163] Ostriker, J.P., & Vietri, M. 1985, Nature, 318, 446

[164] Padovani, P., Giommi, P., & Fiore, F. 1997, MNRAS, 284, 569

[165] Padovani, P., & Giommi, P. 1996, MNRAS, 279, 526

[166] Padovani, P., & Giommi P., 1995a, ApJ, 444, 567

[167] Padovani, P., & Giommi P., 1995b, MNRAS, 277, 1477

[168] Padovani, P., 1992, MNRAS, 257, 404

[169] Paltani, S. 1999, Proc. of the BL Lac Phenomenon meeting, Turku, Finland, 22-26 June 1998, ed. L.O. Takalo, PASP Conf. Series, 159, 293

[170] Parmar, A. N., et al. 1997, A&AS, 122, 309

[171] Perlman, E.S., et al. 1999, ApJ, L119

[172] Perlman, E.S., et al. 1998, AJ, 115, 1253

[173] Perlman, E.S., & Stocke, J.T. 1993, ApJ, 406, 430

[174] Pesce, J. E., et al. 1997, ApJ, 486, 770

[175] Peterson B. M., et al. 1998, PASP, 110, 660

[176] Petry, D., et al. 2000, ApJ, 536, 742

[177] Petry, D., et al. 1996, A&A, 311, L13

[178] Pian, E., et al. 1998, ApJ, 492, L17

[179] Pian, E., et al. 1997, ApJ, 486, 784

[180] Press, W., et al. 1992, Numerical Recipes: The Art of Scientific Computing, 2nd Edition, (Cambridge University Press)

[181] Press, W. 1978, Comments on Astrophysics, 7, 103

[182] Protheroe, R. J., & Biermann, P. L. 1997, Astropart. Phys., 6, 293

[183] Protheroe, R. 1997, in *Accretion Phenomena and Related Outflows*, ed. D. Wickramasinghe *et al.*, IAU Colloquium 163, p. 585

[184] Punch, M. 1997, in Proc. 25th Internat. Cosmic Ray Conf. (Durban, South Africa), eds. M. S. Potgeier, B. C. Raubenheimer, & D. J. van der Walt, 3, 253

[185] Punch, J., et al. 1992, Nature, 358, 477

[186] Quinn, J., et al. 1999, ApJ, 518, 693

[187] Quinn, J., et al. 1996, ApJ, 456, L83

[188] Ricketts, M.J., Cooke, B.A., & Pounds, K.A. 1976, Nature, 259, 546

[189] Rybicki, G.B., & Lightman, A.P. 1979, Radiative Processes in Astrophysics, John Wiley & Sons, (New York): John Wiley & Sons

[190] Sambruna, R.M., et al. 2000, ApJ, 538, 127

[191] Sambruna, R.M. 1999, in Frascati Workshop (astrop-ph/9912060)

[192] Sambruna, R.M., et al. 1997, 474, 639

[193] Sambruna, R.M., Maraschi, L., & Urry C. M. 1996, ApJ, 463, 444

[194] Sambruna, R.M., et al. 1994, ApJ, 434, 468

[195] Samuelson, F. W., et al. 1998, ApJ, 501, L17

[196] Schmitt, J. 1968, Nature, 218, 663

[197] Sembay, S., et al. 1993, ApJ, 404, 112

[198] Sikora, M., et al. 1997, ApJ, 484, 108

[199] Sikora, M., et al. 1996, MNRAS, 280, 781

[200] Sikora, M., Begelman, M.C., & Rees, M.J. 1994, ApJ, 421, 153

[201] Simonetti, J.H., Cordes, J.M., & Heeschen, D.S. 1985, ApJ, 296, 46

[202] Sinitsyna, V. G., et al. 1997, in Proc. 25th Internat. Cosmic Ray Conf. (Durban, South Africa), ed. M. S. Potgeier, B. C. Raubenheimer, & D. J. van der Walt, 3, 273

[203] Sreekumar, P., & Vestrand, W. T. 1997, IAU Circ, 6774, 2

[204] Sreekumar, P., et al. 1996, ApJ, 464, 628

[205] Stecker, F.W., de Jager, O.C., & Salamon, M. 1992, ApJ, 390, L49

[206] Stevens, J., et al. 1994, ApJ, 460, 644

[207] Stickel, M., Meisenheimer, K., & Kühr, H. 1994, A&AS, 105, 211

[208] Stickel, M., Padovani, P., Urry, C. M., Fried, J. W., Kühr, H. 1991, ApJ, 374, 431

[209] Stocke, J.T., et al. 1991, ApJS, 76, 813

[210] Stocke, J. T., Liebert J., Schmidt G., Gioia I. M., MaccacaroT., Schild R. E., Maccagni D., Arp H. C. 1985, ApJ, 298, 619

[211] Strittmatter, P.A., et al. 1972, ApJ, L7

[212] Swanenburg, B.N., et al. 1978, Nature, 275, 298

[213] Tagliaferri, G., et al. 2000, 354, A&A, 431

[214] Tagliaferri, G., et al. 1996, ApJ, 465, 181

[215] Tagliaferri, G., et al. 1991, ApJ, 380, 78

[216] Takahashi, T., et al. 2000, ApJ Letters, in press (astro-ph/0008505)

[217] Takahashi, T., et al. 1996, ApJ, 470, L89

[218] Tanaka, Y., Inoue, H., & Holt, S.S. 1994, PASJ, 46, L37

[219] Tashiro, M., et al. 1995, PASJ, 47, 131

[220] Tavecchio, F., Maraschi, L., & Ghisellini, G. 1998, ApJ, 509, 608

[221] Thompson, D. J., et al. 1995, ApJS, 101, 259

[222] Treves, A., et al. 1989, ApJ, 341, 733

[223] Turner, T.J., et al. 1999, ApJ, 524, 667

[224] Ulrich, M.-H., Maraschi, L., & Urry, C.M. 1997, ARA&A, 35, 445

[225] Ulrich, M.-H., et al. 1984, ApJ, 276, 466

[226] Ulrich, M.-H. 1973, Astrophys. Lett., 14, 89

[227] Urry, C.M., et al. 1997, ApJ, 486, 799

[228] Urry, C.M., et al. 1996, ApJ, 463, 424

[229] Urry, C.M., & Padovani, P. 1995, PASP, 107, 803

[230] Urry, C.M., et al. 1993, ApJ, 411, 614

[231] Urry, C.M., et al. 1988, ApJ, 330, 791

[232] Vagnetti, F., & Spera, R. 1994, ApJ, 436, 611

[233] Vagnetti, F., Giallongo, E., & Cavaliere, A. 1991, ApJ, 368, 366

[234] Vermeulen, R.C., & Cohen, M.H. 1994, ApJ, 430, 467

[235] Vestrand, W. T., Stacy, J. G., & Sreekumar, P. 1995, ApJ, 454, L93

[236] von Montigny, C., et al. 1997, ApJ, 483, 161

[237] von Montigny, C., et al. 1995, ApJ, 440, 525

[238] Wagner, S.J. 1997, in Relativistic Jets in AGNs, eds. M. Ostrowski et al. (Krakow: Poligrafia ITS), P. 208

[239] Wagner, S.J., et al. 1996, AJ, 111, 2187

[240] Wagner, S.J., et al. 1995, ApJ, 454, L97

[241] Wagner, S.J., & Witzel,A. 1995, ARA&A, 33, 163

[242] Wehrle, A. et al. 1998, ApJ, 497, 178

[243] Wolter, A. et al. 2000, A&A, 357, 429

[244] Wolter, A. et al. 1998, A&A, 335, 899

[245] Worrall, D.M., & Wilkes, B.J. 1990, ApJ, 360, 396

[246] Zhang, Y.H., et al. 1999, ApJ, 527, 719